

Copyright is owned by the Author of the thesis. Permission is given for a copy to be downloaded by an individual for the purpose of research and private study only. The thesis may not be reproduced elsewhere without the permission of the Author.

Hetero-Interpenetrated Metal-Organic Frameworks

Supramolecular interactions between ligands in
metal-organic framework formation

A thesis presented in fulfilment of the requirements of the degree of

Doctor of Philosophy

in

Chemistry

At Massey University, Manawatū, New Zealand

David Perl

2020

*Pulchra sunt quae videntur, pulchriora quae sciuntur,
longe pulcherrima quae ignorantur.*

*Fair is what we see, fairer what we have perceived,
fairest what is still in veil.*

Abstract

Metal-organic frameworks are an exciting class of materials formed through the self-assembly of their metal ion and organic ligand components into ordered, nanoporous lattice structures whose pore spaces are open to solvent, gas, and other guest molecules. Their consequently high surface areas render them suitable for diverse applications including gas storage, separations, and catalysis. The ability to precisely engineer the chemistry of the pores in framework materials and thus tune their properties is one of their most attractive features. Interpenetration, a phenomenon where multiple lattices are woven through each other, is an important handle on tuning their properties, mediating between pore shapes and volumes, chemistries, and robustness.

In this thesis new frameworks are presented where two chemically distinct lattices are interpenetrated, a longstanding target in the field. These frameworks therefore have two orthogonal handles on both pore shape and functionalisation and have been applied to asymmetric organocatalysis by embedding an achiral catalytic site within a chiral pore space. Additionally, some insight is gained into the underlying principles of the formation of complex types of interpenetration through the exploitation of several analogous novel ligands.

Contributions

All of the work in this thesis was completed by David Perl

Acknowledgements

The world is a cold, dark, hostile place, each of its wretched inhabitants an island unto itself. None may trust or depend on another, lest they become a mere object, sacrificial to the storm. Life in civilisation is no less solitary, poor, nasty, brutish, and unbearably long than otherwise, and death is the only release. All one has, until then, is what one has achieved alone.

Just kidding.

Science depends on shared observations, and at its very deepest level is a collaborative enterprise, meaningless without context given by others' experience. I am immensely thankful to many people for the support necessary to have completed this PhD, and all the discussions along the way that helped shape it. This thesis has my name on the front of it, but it belongs as much to those named here and countless others from whom I beg forgiveness for having left them out.

Much of this work was possible thanks to beamtime at, and support from, the Australian Synchrotron, part of ANSTO, for which I am extremely thankful. Beamlines MX1 and MX2 were used in the course of this work, and at MX2 we made use of the Australian Cancer Research Foundation (ACRF) detector.

To my primary supervisor, Prof. Shane Telfer, I am grateful for being given a fascinating project to work on, quick and comprehensive review of that work, and the funding of my stipend and conference attendances. To my secondary supervisor, Prof. Geoff Jameson, I am thankful for sage advice on crystallography, as well as inspiration in many different fields of science beyond the narrow area of my work.

To all of my colleagues past and present, in the Telfer group: Dr. Sebastian Blackwood, Dr. Lujia Liu, Dr. Tian-you Zhou, Dr. Adil Alkas, Dr. Omid Taheri, Dr. Heather Jameson, Subo Lee, Joel Cornelio, Nisansala Bandara, Shikeale Harris, Dr. John Clements, Bernard Auer, Tim Craig. In other groups or positions at Massey

University: David Lun, Sam Brooke, Dr. Lauren Macreadie, Dr. Pat Edwards, Dr. Sean Bisset , in the MacDiarmid Institute student association MESA: Erin Service, Dr. Kyle Webster, Dr. Geoffry Laufersky Edoardo Galli, Dr. Kathryn Schroeder, Jackson Miller, and many others, thank you all very much for being who you are.

To my friends, Heather, Sarah, Josh, Tom, Grace, Brier, Ben, Hadee and many others without whose emotional support and kind feigning of interest I might have given up.

To my mother Eveline, for whom the value of education and scholarship is second only to love, and to whom I am forever grateful for having instilled those values in me.

To everyone who reads this.

Thank you.

Publications

Publications relevant to this thesis

Ferguson, A.; Liu, L.; Tapperwijn, S. J.; Perl, D.; Coudert, F.-X.; Van Cleuvenbergen, S.; Verbiest, T.; van der Veen, M. A.; Telfer, S. G., Controlled partial interpenetration in metal–organic frameworks. Nat. Chem. **2016**, 8 (3), 250-257. DOI: 10.1038/nchem.2430

Additional publications by the author

Perl, D.; Bisset, S. W.; Telfer, S. G., Postcomplexation synthetic routes to dipyrroin complexes. Dalton Trans. **2016**, 45 (6), 2440-2443. DOI: 10.1039/C5DT04466A

Abbreviations

AAS	Atomic absorption spectroscopy
BPDC	4,4'-biphenyldicarboxylic acid or 4,4'-biphenyldicarboxylate
CCDC	Cambridge crystallographic data centre
CCTBX	Computational crystallography toolbox
DBF	N,N-di-n-butylformamide
DEF	N,N-diethylformamide
DFT	Density functional theory
DIF	N,N-diisopropylformamide
DMF	N,N-dimethylformamide
DMSO	Dimethylsulfoxide
DOI	Digital object identifier
EDS	Energy-dispersive X-ray spectroscopy
DPF	N,N-di-n-propylformamide
ESI	Electrospray ionisation
FFT	Fast Fourier transform
HKL	Indices of crystallographic reflections, and filetype for crystallographic data
HKUST	Hong Kong University of Science and Technology
HOF	Hydrogen-bonded organic framework
HPLC	High-pressure liquid chromatography
IRMOF	Isorecticular metal-organic framework
KOH	Potassium hydroxide
MAD	Multiwavelength anomalous dispersion
MIR	Multiple isomorphous replacement
MOF	Metal-organic framework
MS	Mass spectrometry
MUF	Massey University Framework
MX	Macromolecular crystallography
NFP	N-formylpiperazine
NMP	N-methylpyrrolidone
NMR	Nuclear magnetic resonance
PCP	Porous coordination polymer
PDPE	Polydifluoroethylene
PDMS	Polydimethylsilane
PIP	Partially interpenetrated
PIZOF	Porous imidazolate framework
PTFE	Polytetrafluoroethylene
PXRD	Powder X-ray diffraction

RMSD	Root mean squared deviation
SBU	Secondary building unit
SCXRD	Single-crystal X-ray diffraction
SEM	Scanning electron microscopy
TEM	Tunneling electron microscopy
TFA	Trifluoroacetic acid
THF	Tetrahydrofuran
TLC	Thin layer chromatography
XANES	X-ray absorption (near edge) spectroscopy
XRD	X-ray diffraction

List of Figures

Figure 1.1: An illustration of the basic features of MOFs, using MOF-5⁶ as an example. (A) scheme of the synthetic preparation of many carboxylate MOFs. (B) A structural diagram of MOF-5. Grey spheres represent carbon, red, oxygen, cyan tetrahedra represent zinc (II) ions. The large yellow sphere represents the void space in the pore. (C) an enlarged view of the $[\text{Zn}_4\text{O}(\text{COO})_6]$ cluster which forms the SBU of MOF-5 among many zinc carboxylate MOFs, (D) a simplified illustration of the primitive cubic (**pcu**) lattice 2

Figure 1.2: The structures of some historically important MOFs. A) MOF-5: left, the $[\text{Zn}_4\text{O}(\text{COO})_6]$ cluster; right, the framework with a yellow sphere indicating the pore. B) UiO-66: left, the $\text{Zr}_6\text{O}_4(\text{COO})_8$ cluster; right, a $2 \times 2 \times 2$ supercell. C) HKUST-1: left, the $\text{Cu}_2(\text{COO})_4$ paddlewheel; right, a $2 \times 2 \times 2$ supercell. D) Cr-MIL-101: left, (1,0,0) view of the unit cell; right, (1,1,0) view of the unit cell. Carbon is coloured grey, oxygen red, zinc cyan, copper green, zirconium magenta, chromium orange. E) The “first MOFs”, described¹⁰ by Hoskins and Robson. Left, tetra(cyanophenyl)methane copper(I), right, $\text{ZnCu}(\text{CN})_4$. F) MOF-74, $[\text{Mg}_2(\text{dobdc})]$, notable for its one dimensional channels..... 4

Figure 1.3: An illustration of the isorecticular principle, by which frameworks with the same SBU and topology but varying pore size and functionality can be produced by varying the ligand length and/or functionalisation. 6

Figure 1.4: (A) An illustration of *interpenetration* using the simple example of two **pcu** lattices, with the nodes of each lattice perfectly centred in the pores of the other. (B) As before, but with the lattices offset from each other, maximising van der Waals contacts between lattices. 12

Figure 1.5: Illustration of guest and pore size comparisons for (A) non-interpenetrated and (B) interpenetrated versions of SIFSIX-2-Cu. Atom colours are indicated in the legend; red spheres represent the oxygen atoms of a modelled CO_2 molecule which closely match the pore size of SIFSIX-2-Cu-i. 13

Figure 1.6: A diagrammatic illustration of the main handles on interpenetration control in MOFs. 16

Figure 1.7: (A) A partially interpenetrated framework (NOTT-202¹⁰⁰) where the interpenetrating lattice is disordered over two incompatible sites. (B) A partially interpenetrated lattice where a continuum of degrees of interpenetration is possible. In both cases, the blue (primary) lattice is complete, while the secondary lattice (orange and yellow in A, blue in B) exists only in some regions and not in others... 18

Figure 1.8: An illustration of the structure of a hetero-interpenetrated MOF formed from 1D ladders interpenetrating through 2D sheets to form a 3D structure, reported by Carlucci¹⁰⁴ et al. A) One type of sublattice, 1D chains in a ladder-like arrangement. B) The other type of sublattice, 2D sheets in a brick-like pattern. C) An illustration of how the two types of network interpenetrate. D) The components of both lattices are manganese(II) ions with the depicted ligand. 20

Figure 2.1: MUF-9 structures and components. A) various representations of **L1**: first, a cartoon as a simple blue rod, second, a skeletal structure, third, a 3D atomic representation showing the twisted backbone. Only one enantiomer of **L1** is shown, but MUF-9 is made from the racemic ligand. B) various representations of the cluster in MUF-9, first, a blue sphere used in structural cartoons, second, the formula, third, a 3D visualisation of the tetrahedral, 6-coordinate cluster. C) an illustration of the range of structures from α -MUF-9 to β -MUF-9. 32

Figure 2.2: PXRD patterns of α - (top, blue), PIP- (middle, purple), and β -MUF-9 (bottom, red). 33

Figure 2.3: The structure of γ -MUF-9. Top: γ -MUF-9 can be prepared both by direct synthesis in DIF, as well as by heating α -MUF-9 in DIF. Bottom: a close-up view of a small section of the γ -MUF-9 lattice shown as both a cartoon representation and a ball-and-stick representation, from which side chains and hydrogens have been removed for clarity. 34

Figure 2.4: An illustration of the contacts between the lattices in MUF-9. Side chains have been removed from most ligands, and all hydrogens have been removed for clarity. One cell of the primary lattice is shown, where grey atoms are carbon, dark blue nitrogen, red oxygen, and light blue zinc. One ligand of an interpenetrating (secondary) lattice is shown in different colours for clarity, where yellow atoms are carbon, teal nitrogen, orange oxygen.	35
Figure 2.5: A) At any given site, L1 can take one of four orientations, and B) each one of those orientations is compatible with three orientations of the neighbouring ligand. C) An illustration of a single lattice where ligands are oriented in the same direction. D) Where ligands in both lattices are oriented in the same direction the pore size in β -MUF-9 is approximately 4 Å, indicated by the yellow sphere.	36
Figure 2.6: Optical micrographs showing a crystal undergoing autocatenation from α -MUF-9 to β -MUF-9 via PIP-MUF-9 by heating in DMF. Despite losing optical transparency, the crystal diffracts well at all stages of the conversion. PIP levels correspond to the occupancy of the interpenetrating lattice, as determined by SCXRD. Figure reproduced from reference 1.	37
Figure 2.7: An optical micrograph of “rafts” of intergrown α -MUF-9	39
Figure 2.8: Images of microcrystalline powder of MUF-91. Left, a dark-field optical micrograph. Right, an SEM image.....	39
Figure 2.9: A plot of the PIP % of nanocrystalline MUF-9 as it varies with synthesis temperature.	40
Figure 2.10: PXRD patterns of MUF-9 after exposure to various solvents at 85 °C for different periods of time. DMF = N,N'-dimethylformamide, DEF = N,N'-diethylformamide, DBF = N,N'-dibutylformamide, tBuF = N-tert-Butylformamide, DIF = N,N'-diisopropylformamide, NMP = N-methylpyrrolidinone, NFP = N-formylpyrrolidine, NFPip = N-formylpiperidine.	42
Figure 2.11: Plot of percentages of zinc(II) replaced by cobalt(II) in α -MUF-9 over time. Black squares represent percentage exchange at 2 mg mL ⁻¹ cobalt nitrate concentration while red circled represent exchange at 20 mg mL ⁻¹ cobalt nitrate concentration.....	44
Figure 2.12: Plot of percentages of L1 replaced by BPDC in α -MUF-9 as determined by ¹ H NMR spectroscopy of digested samples, over time.....	45
Figure 2.13: Plot of percentages of L1 replaced by BPDC-NH ₂ in α -MUF-9 as determined by ¹ H NMR spectroscopy of digested samples, over time.....	45
Figure 2.14: PXRD patterns of α -MUF-9 exposed to 2 mg mL ⁻¹ Co(NO ₃) ₂ ·6H ₂ O in DBF at 95 °C.	50
Figure 2.15: PXRD patterns α -MUF-9 exposed to 20 mg mL ⁻¹ Co(NO ₃) ₂ ·6H ₂ O in DBF at 95 °C.	50
Figure 2.16: PXRD patterns of α -MUF-9 exposed to BPDC	51
Figure 2.17: PXRD patterns of α -MUF-9 exposed to BPDC-NH ₂	51
Figure 2.18: PXRD diffractograms of MOF synthesis reactions in a variety of formamide solvents, using the same concentrations of starting materials as the standard syntheses of α - and β -MUF-9.	52
Figure 2.19: PXRD patterns of nanocrystalline MUF-9 synthesised at varying temperatures, from L1 and Zn(OAc) ₂ ·6H ₂ O in DBF.....	53
Figure 3.1: Illustration of the synthetic conditions for the synthesis of MUF-91 by secondary growth.	57
Figure 3.2: PXRD diffractograms of MUF-91 at various stages of growth.	58
Figure 3.3: Optical micrographs of MUF-91 at various stages of growth. The image taken after fifteen hours (lower left) most clearly shows the epitaxial growth of a transparent shell layer around the crystals.....	60

Figure 3.4: A) the structure of MUF-91. Hydrogens and disordered orientations of the side chain of L1 are omitted for clarity. Carbons are coloured grey, nitrogen blue, oxygen red, zinc cyan. B) the same structure, with the primary lattice (complete occupancy) coloured blue and the secondary lattice (partial occupancy) coloured red.....	63
Figure 3.5: an optical micrograph of crystals of MUF-91 taken through crossed polarisers, in which the outer IRMOF-9 shell is clearly distinguished from the MUF-91 core.....	65
Figure 3.6: Plot of complementary characterisation data for MUF-91. Black squares represent the PIP% values obtained from SCXRD datasets collected at various time points in the growth of MUF-93. Red circles represent the ratio of BPDC to L1 as determined by ¹ H-NMR. The grey line is drawn through the mean PIP% (from all SCXRD datasets) and the error bars correspond to the 95% confidence interval for the mean PIP% value for the sample.....	66
Figure 3.7: A ¹ H NMR spectrum for a digested sample of MUF-91 in 0.2M NaOD in D ₂ O, showing a 0.42:1 ratio of BPDC:L1. The peak used to determine the amount of BPDC is at 7.85 ppm and coloured red. The peak used to determine the amount of L1 is at 7.32 and coloured blue.	67
Figure 3.8: ¹ H NMR spectra of digested samples of MUF-91 as the secondary lattice grows in over time. Spectra 1-8 were taken after 1, 3, 6, 9, 12, 15, 18, and 21 hours of secondary growth respectively. Spectrum 9 was measured after 30 hours. Spectra were measured in 0.2M NaOD in D ₂ O.	68
Figure 3.9: Growth over time of [Zn ₄ O(bpdc) ₃] in powder MUF-9. Black squares represent the interpenetration percentage determined from the PXRD pattern and red circles represent the ratio of BPDC to L1 as determined by ¹ H-NMR spectroscopy on digested samples.....	71
Figure 3.10: PXRD patterns for MUF-91 grown as large crystals (top, red) or powder (bottom, black) after reaching the plateau of secondary growth.....	71
Figure 3.11: Baseline-corrected and scaled PXRD patterns for microcrystalline MUF-91.....	72
Figure 3.12: PXRD diffractograms of the MUF-91 shell with other phases for comparison. The small peak at 2θ = 8.9 is from incomplete separation of the shell from MUF-92. The shoulder on the low angle side of the peak at 2θ = 7.3, as well as the broader peak at 2θ = 11.5 distinguish the shell as IRMOF-9 rather than IRMOF-10.	76
Figure 3.13: ¹ H NMR spectrum of a digested sample of the shell of MUF-91, in 0.2M NaOD in D ₂ O, manually separated from the core.....	77
Figure 4.1: Whether or not the side chain of a ligand interacts with the metal of choice can strongly influence MOF formation.	82
Figure 4.2: The structure of SL3 when used for an interpenetrating lattice through α-MUF-9. A) the combination of all orientations of the ligand, from different views. B) A single orientation of the ligand, from different views.....	86
Figure 4.3: Illustration of the synthetic method to produce MUF-92.....	88
Figure 4.4: PXRD patterns of MUF-92 at various stages of growth.....	89
Figure 4.5: Optical micrographs of MUF-92 at various stages of growth.....	90
Figure 4.6: Plot of complementary characterisation data for MUF-92. Black squares represent the PIP% values obtained from SCXRD datasets collected at various time points in the growth of MUF-93. Red circles represent the ratio of BPDC-NH ₂ to L1 as determined by ¹ H-NMR. The grey line is drawn through the mean PIP% (from all SCXRD datasets) and the error bars correspond to the 95% confidence interval for the mean PIP% value for the sample.....	91
Figure 4.7: The placement of BPDC-NH ₂ in MUF-92, in various orientations. The NH ₂ side chain is disordered over four positions and the two backbone phenyl rings are arranged orthogonally. For	

clarity, hydrogens and all but one side chain from L1 have been removed. Carbons are grey, oxygen red, nitrogen blue, and zinc cyan.	91
Figure 4.8: Growth over time of $[\text{Zn}_4\text{O}(\text{bpdc-NH}_2)_3]$ in powder MUF-9. Black squares represent the interpenetration percentage determined from PXRD patterns (Figure 4.17) and red circles represent the ratio of BPDC-NH ₂ to L1 as determined by ¹ H-NMR, for digested samples of powder MUF-91.	93
Figure 4.9: Illustration of the synthetic method to produce MUF-93.	94
Figure 4.10: A) An illustration of a crystal of MUF-93 showing regions with different interpenetration properties. B) a photograph showing the crystal of MUF-93 and the section scanned along. C) a plot of PIP values determined from SCXRD datasets collected at various points along a scan across a single crystal of MUF-93.	95
Figure 4.11: Optical micrographs of MUF-93 at various stages of growth.	97
Figure 4.12: ¹ H NMR spectra of digested samples of MUF-93 as the secondary lattice grows in over time. Spectra 1-8 were taken after 3, 6, 9, 12, 15, and 18 hours of secondary growth respectively. Spectra were measured in 165 mM DCl in d ₆ -DMSO.	98
Figure 4.13: Plot of complementary characterisation data for MUF-93. Black squares represent the PIP% values obtained from SCXRD datasets collected at various time points in the growth of MUF-93. Red circles represent the ratio of BPDC to L1 as determined by ¹ H-NMR and blue triangles represent the ratio of Co to Zn as determined by flame AAS, for the same digested samples of MUF-93. The grey line is drawn through the mean PIP% (from all SCXRD datasets) and the error bars correspond to the 95% confidence interval for the mean PIP% value for the sample.	99
Figure 4.14: A plot of complementary characterisation data for MUF-93 prepared from powder α -MUF-9. Black squares represent the percentage of interpenetration of the sample as determined by PXRD, blue triangles represent the ratio of Co : Zn as determined by flame AAS and red circles represent the ratio of BPDC : L1 as determined by ¹ H-NMR, in the digested samples of powder MUF-93.	100
Figure 4.15: Plot of the growth of $[\text{Mg}_4\text{O}(\text{bpdc})_3]$ in α -MUF-9 over time. Black squares represent the PIP% values determined from single crystal datasets, while green circles represent the percentage of zinc in the primary lattice replaced by magnesium, determined from the same single crystal datasets.	107
Figure 4.16: PXRD patterns of representative results of synthesis of MOFs with cobalt and BPDC (top, black), zinc and BPDC-NH ₂ under ordinary synthetic conditions (middle, red), and at low concentration in DBF (bottom, blue).	107
Figure 4.17: Baseline-corrected PXRD patterns of MUF-92 grown from powder α -MUF-9.	108
Figure 4.18: PXRD patterns of MUF-93 at various stages of growth.	108
Figure 4.19: Baseline-corrected and scaled PXRD patterns of powder MUF-93 as used for interpenetration percentage determination.	109
Figure 4.20: ¹ H NMR spectra of digested samples of MUF-92 as the secondary lattice grows in over time. Spectra 1-5 were taken after 3, 6, 9, 12, and 15 hours of secondary growth respectively. Spectra were measured in 0.2M NaOD in D ₂ O.	110
Figure 5.1: Illustration of the conditions of Bragg diffraction.	114
Figure 5.2: Vector representation of a structure factor.	116
Figure 5.3: Scattering factor vectors are modified under anomalous scattering conditions. Because f'' is 90 ° out of phase with f_0 , the result is that Friedel mates have different intensities and phases in non-centrosymmetric crystals.	119

Figure 5.4: The upper panel shows intensities of x-ray reflections in MUF-93, by d-spacing, for data collected at high energy (17500 eV, 0.7084 Å) and at the cobalt(II) absorption edge (7500 eV, 1.653 Å). The lower panel shows the difference between the two datasets in the upper panel – the remaining signal is only the anomalous scattering from cobalt atoms.	122
Figure 5.5: Theoretical curves of f'' (upper) and f' (lower) for zinc (red) and cobalt (black). Note that these theoretical values are not accurate very near and above the absorption edge, not least because of the effects of neighbouring atoms.	124
Figure 5.6: A diagram of a hypothetical MUF-9 and MUF-93 unit cell, indicating the two crystallographic sites occupied by metal atoms	126
Figure 5.7: An illustration showing the location of the [Zn ₄ O] cluster in two space groups. Left, the non-centrosymmetric space group of α -MUF-9 and its partially interpenetrated derivatives, P -4 3 m. Right, the centrosymmetric space group of β -MUF-9, P m -3 m.....	127
Figure 5.8: Slice of (Fobs, Φ calc) electron density map of β -MUF-9, difference data between 17440 eV and zinc edge at 9670 eV.....	127
Figure 5.9: Slice of (Fobs, Φ calc) electron density map of MUF-93 at the plateau of secondary growth after 60 hours, difference data between 17440 eV and cobalt edge at 7500 eV.	129
Figure 5.10: Slice of (Fobs, Φ calc) electron density map of MUF-93 beyond the plateau of secondary growth after 168 hours, difference data between 17440 eV and cobalt edge at 7500 eV.....	130
Figure 5.11: Slice of (Fobs, Φ calc) electron density map of α -MUF-9 exchanged with cobalt (as described in Chapter 2, section 2.2.5, page 43), difference data between 17440 eV and cobalt edge at 7500 eV..	131
Figure 6.1: An illustration of the two classes of metal catalysis in MOFs. A) catalysis by structural metal atoms includes this example ^{131, 177} of MFU-1. B) catalysis by non-structural metals includes this example ¹⁶⁸ of UiO-bpydc where the catalytic metal is coordinated to the bipyridyl backbone of the ligand.....	141
Figure 6.2 An example of modulated organocatalysis in a MOF. Figure reproduced from reference ¹⁸⁶ with permission. The catalytic unit is directed into the pore space, and other parts of the framework can be used to tune the pore properties and the resulting catalytic outcome.....	142
Figure 6.3: A) an inhibitor (coloured green) bound to the active site of the protein chymotrypsin. The protein surface is coloured grey for carbon, red for oxygen, blue for nitrogen, and hydrogens are omitted for clarity. The residues at the binding site are shown as sticks and coloured blue. B) the catalytic intermediate ⁶⁹ [Rh(L)(CH ₃ CN) ₂ (CH ₃ CO)I] ⁺ in a MOF pore, observed by SCXRD. The overall MOF structure is drawn as the van der Waals surface while the catalytic complex is shown as sticks. Carbons are grey, hydrogens white, oxygens red, nitrogens blue, rhodium cream, iodine brown. C) An enamine adduct of proline, an intermediate in a homogeneous organocatalytic reaction.....	143
Figure 6.4: Enantiomers of L1	145
Figure 6.5: PXRD diffractograms of α -MUF-9 and α -MUF-10 heated in various solvents. Note that DBF and DPF do not cause phase changes in MUF-9 respectively, whereas smaller solvents do.....	147
Figure 6.6: Illustration of MUF-101, showing the role of each component lattice.....	148
Figure 6.7: PXRD patterns of MUF-101 as it grows over time.....	149
Figure 6.8: ¹ H NMR spectra of digested samples of MUF-101 at various stages of growth. Spectra were recorded in a solution of 165 mM DCl in d ₆ -DMSO.	150
Figure 6.9: HPLC UV absorbance traces (λ = 254 nm) of the results of the Henry reaction between nitromethane or nitroethane and m-nitrobenzaldehyde, catalysed by L2 in MUF-101. The peak at 17	

minutes is the nitrobenzaldehyde starting material. The peaks between 9 and 15 minutes are the products. 152

Figure 6.10: HPLC chromatograms of the results of the Henry reaction between nitrocyclopentane and m-nitrobenzaldehyde, catalysed by **L2** in MUF-101. The suffix ‘-ac’ indicates the catalyst has been rendered fully interpenetrated through autocatenation. The peak at 26.4 minutes corresponds to the m-nitrobenzaldehyde starting material. The peaks at 27.8 and 31.0 minutes correspond to the product enantiomers, as indicated by the MS chromatogram. 154

Figure 6.11: HPLC UV absorbance traces ($\lambda = 254$ nm) of various controls. Top, nitrocyclopentane in dioxane, identifying its position at 18.4 minutes. Second, m-nitrobenzaldehyde in dioxane, identifying its position at 26.4 minutes. Third, the stock solution used for the reaction, after 24 hours. Fourth, the solvent used for the reaction. The scale shows that there are no peaks. Fifth, the dioxane used to wash the MOF for the final time, showing that no material is leached from the MOF. 160

Figure 6.12: PXRD patterns of MUF-101 before and after catalysis. 161

Figure 7.1: An illustration of the general ideas presented in this chapter – changing either the ligand side chain or the donor group to look at their respective influences on the resulting MOF structures. 167

Figure 7.2: A) 3D model of **L3** as present in MOF-L3. B) the cell of MOF-L3. Disordered orientations of side chains and hydrogens have been removed for clarity. Carbon is coloured grey, oxygen red, nitrogen blue, zinc cyan. 174

Figure 7.3: A) A simplified representation of MOF-L4 viewed from the (1,0,0) direction. B) A simplified representation of MOF-L4 viewed from the (0,1,0) direction. C) A simplified view of MOF-L4 from near the (0,0,1) direction. In panels A and B, pink circles represent the Zn_2 SBUs and the ligands, respectively. In panel C, each layer is given a different colour. D) A close-up illustration of the SBU in MOF-L4. Only the first phenyl ring of each ligand is shown. Grey spheres are carbon; blue, coordinated DMF; red, oxygen; cyan, zinc. 175

Figure 7.4: A) Stick-representation illustration of α -MOF-L4 showing the edge-face interactions as yellow sticks between side chains of **L4**. B) Space-filling illustration of α -MOF-L4 showing the offset face-face interactions between side chains of **L4**. Coordinated solvent and solvent in the pores has been omitted for clarity. For both A and B, carbon is dark grey, oxygen pale red, nitrogen blue, zinc cyan, and hydrogen white. 176

Figure 7.5: Comparison of the PXRD patterns of β -MOF-L4 (the material obtained from **L4** in DBF) and α -MUF-9. 177

Figure 7.6: An illustration of the crystal structure of **P1**, showing the aryl embrace between the side chain on one molecule and the backbone of its neighbour. Carbons are coloured grey, nitrogen blue, hydrogen pink, and bromine brown. 179

Figure 7.7: A and B) illustration of the contacts between the two lattices in MOF-L11, with hydrogens removed for clarity. In panel A, carbons are coloured grey, oxygens red, nitrogens blue. In panel B, one ligand is coloured red and the other blue. B) Overall structure of the lattices in MOF-L11, with sidechains and hydrogens removed for clarity. 180

Figure 7.8: A) Simplified view of the coordination network in MOF-L21- α from the (0,1,0) view. Side chains and hydrogens are omitted for clarity. B) Simplified view of the coordination network in MOF-L21- γ at an angle, showing the alignment of ligands above and below the plane. C) and D) are views from the (1,0,0) and (0,0,1) directions respectively, showing the interdigitation of the layers in alternate directions. Side chains have been removed for clarity. E) Illustration of the fourfold phenyl embrace which joins the layers together. F) A closeup view of the $Zn_3(\text{pyz})_4\text{Cl}_2(\text{H}_2\text{O})_2$ cluster. 182

Figure 7.9: An illustration of β -MOF-21. A) the cubic Zn_8 cluster is illustrated with a cube, and the coordination of the ligands at each edge of the cube is shown. B) The overall connectivity of the lattice.	183
Figure 7.10: PXRD patterns of β -MOF-21 (top) and $Ni_8(bdp)_6(OH)_4(H_2O)_n$ (bottom).....	183
Figure 7.11: Experimental and calculated PXRD patterns for MOF-L11	193
Figure 7.12: Experimental and calculated PXRD patterns for MOF-L21- α	193

List of Schemes

Scheme 1.1: Top: hydrolysis of formamide solvents results in the slow build-up of dialkylamines in solvothermal MOF synthesis reactions. R = Me, Et, i-Pr, n-Pr, t-Bu, n-Bu, etc. Bottom: amines slowly generated from solvent decomposition deprotonate ligands. The example is an aromatic carboxylate, but it can be many other deprotonatable groups. The deprotonated ligand coordinates to available metals or metal clusters to form a MOF.	7
Scheme 2.1: Synthesis of L1	48
Scheme 2.2: Synthesis of α -MUF-9.....	48
Scheme 6.1: A generic scheme for the Henry reaction between a nitroalkane and an aldehyde.....	151
Scheme 6.2: The Henry reaction between nitromethane and an aldehyde.....	151
Scheme 6.3: The Henry reaction between m-nitrobenzaldehyde and nitrocyclopentane, as catalysed by L2 in MUF-101.....	153
Scheme 6.4: Synthesis of L2	157
Scheme 7.1: Synthesis of L3	173
Scheme 7.2: Synthesis of L4	174
Scheme 7.3: Synthesis of extended analogues of L1 with carboxylate donor groups. Full synthetic details are presented in section 7.4.3, page 187.....	178
Scheme 7.4: Synthesis of L21 . Full synthetic details in section 7.4.3.6, page 191.	181
Scheme 7.5: Synthesis of L11'	188

List of Tables

Table 2.1: Results of MOF syntheses with L1 and $\text{Zn}(\text{NO}_3)_2 \cdot 4\text{H}_2\text{O}$ in various formamide solvents at 85°C.....	41
Table 3.1: Crystallographic results for selected datasets obtained from MUF-91.....	62
Table 4.1: Different ligands trialled for secondary growth in α -MUF-9. The maximum PIP% observed is indicated in parentheses after each ligand name.	84
Table 4.2: Crystallographic data for representative samples of MUF-92	92
Table 4.3: Crystallographic results for selected datasets obtained from MUF-93.....	101
Table 4.4: Percentages of BPDC-NH ₂ (MUF-92) or BPDC (MUF-91) to L1 as determined by ¹ H NMR spectroscopy of digested samples which were prepared from a microcrystalline powder of α -MUF-9	110
Table 5.1: SHELXL refinement results and calculated statistics for anomalous difference datasets. Integrated values at each metal atom site are proportional to the electron count of the specified metal at each site but are not absolute values, as F(000) values were not determined for difference datasets.	135
Table 6.1: Results from catalysis with MUF-101 and control reactions	155
Table 7.1: All examples of MOFs with pyrazolate linkers greater than 13 Å in length in the CSD.....	169
Table 7.2: Crystallographic data for MOF-L3.....	194
Table 7.3: Crystallographic data for MOF-L4.....	195
Table 7.4: Crystallographic data for MOF-L11.....	196
Table 7.5: Crystallographic data for MOF-L21- α	197

Table of Contents

Abstract.....	i
Contributions.....	ii
Acknowledgements	iii
Publications.....	v
Abbreviations	vi
List of Figures	viii
List of Schemes.....	xv
List of Tables.....	xvii
Table of Contents.....	xix
Chapter 1: Introduction	1
1.1. Metal-organic frameworks.....	1
1.1.1. Coordination, polymers, and frameworks.....	1
1.1.2. MOF terminology.....	3
1.1.3. Geometry and topology	4
1.1.4. Early MOFs, and the development of the field	5
1.1.5. Synthesis and growth of MOFs.....	7
1.1.6. Applications of MOFs	8
1.1.7. Characterisation methods for MOFs	10
1.2. Interpenetration in metal-organic frameworks.....	12
1.2.1. Interpenetration and porosity	13
1.2.2. When is interpenetration useful and when isn't it?.....	14

1.2.3. Control of interpenetration.....	15
1.2.4. Partial interpenetration	17
1.2.5. Interpenetration of heterogeneous frameworks.....	19
1.3. A brief description of this work	21
1.4. references.....	23
Chapter 2: MUF-9	31
2.1. Introduction	31
2.2. Results	38
2.2.1. Improved and varied syntheses of α -MUF-9	38
2.2.2. Rapid synthesis of MUF-9 nanocrystals at different temperatures	40
2.2.3. Behaviour of MUF-9 precursors in different solvents	41
2.2.4. Behaviour of α -MUF-9 when heated in various solvents.....	42
2.2.5. Metal and ligand exchange in MUF-9.....	43
2.3. Conclusions	46
2.4. Experimental details and supplementary data	48
2.4.1. Synthesis of L1.....	48
2.4.2. Synthesis of α -MUF-9	48
2.4.3. PXRD patterns	50
2.5. References.....	54
Chapter 3: MUF-91 – [Zn₄O(bpdc)₃] in MUF-9	55
3.1. Introduction	55
3.2. Conditions for secondary growth of a nonidentical interpenetrating lattice	57
3.3. Characterisation of hetero-interpenetrated MOFs through complementary techniques.....	60

3.4. Powder MUF-91.....	70
3.5. Conclusions	73
3.6. Experimental details and supplementary data.....	75
3.6.1. General crystallographic methods and strategy.....	75
3.7. References.....	78
Chapter 4: Hetero-interpenetrated MOFs with Different metals and Functionalised ligands	81
4.1. Introduction	81
4.2. Initial results with different ligands and metals.....	84
4.3. MUF-92	88
4.4. MUF-93	94
4.5. Conclusions	102
4.6. Experimental details	104
4.6.1. MOF Protocols.....	104
4.6.2. [Mg ₄ O(bpdc) ₃] in MUF-9	107
4.6.3. PXRD patterns	107
4.6.4. ¹ H NMR data	110
4.7. References.....	111
Chapter 5: Site-specific metal identification in single-crystal X-ray diffraction structures using anomalous dispersion	113
5.1. Introduction	113
5.1.1. Single-crystal X-ray diffraction (SCXRD)	113
5.1.2. Powder X-ray diffraction (PXRD).....	117
5.1.3. Contemporary synchrotron techniques.....	117

5.1.4. Anomalous scattering.....	118
5.2. Method and results	120
5.2.1. Development of a method for site-specific metal identification using multiwavelength single-crystal x-ray diffraction data.....	120
5.2.2. Results from the application of this method to MUF-93 and control materials.....	125
5.3. Discussion.....	132
5.4. Additional experimental methods and data	133
5.4.1. Python codes.....	133
5.4.2. Determination of appropriate wavelength	133
5.4.3. Generation of difference dataset and Patterson map	134
5.4.4. Solution and refinement of difference data.....	134
5.4.5. Generation of Plots	135
5.4.6. Tabulated statistics from difference datasets.....	135
5.5. References.....	136
Chapter 6: applying hetero-interpenetrated Metal-organic frameworks to catalysis.....	139
6.1. Introduction	139
6.1.1. Pore engineering of MOFs.....	139
6.1.2. MOF catalysis	140
6.1.3. MUF-10, a chiral analogue to MUF-9.....	144
Further characterisation of MUF-10	147
6.2. Synthesis and characterisation of MUF-101	148
6.3. Application of MUF-101 to catalysis	151

6.4. Conclusions	156
6.5. Experimental details and supplementary data	157
6.5.1. Synthesis of L2	157
6.7. References	162
Chapter 7: Derivative ligands.....	167
7.1. Introduction	167
7.1.1. Supramolecular interactions and binding motifs.....	169
7.1.2. Prediction of crystal structures	171
7.2. Results	173
7.2.1. Phenanthraquinone-bpdc (L3)	173
7.2.2. Bis-benzil-bpdc (L4).....	174
7.2.3. Extended analogues of L1	178
7.2.4. Pyrazolate analogue of L11.....	180
7.3. Conclusions	184
7.4. Experimental details	186
7.4.1. Synthesis of L2.....	186
7.4.2. Synthesis of L4.....	186
7.4.3. Synthesis of L11 and L12.....	187
7.4.4. MOF syntheses and characterisation	192
7.4.5. Crystallographic data for MOFs	194
7.5. References.....	198
Chapter 8: Perspective and conclusions.....	201
8.1. Chapters 2 & 3 – what further information could we get?.....	201
8.2. Chapters 4 & 5 – how could these techniques be extended?	203

8.2.1. Chapter 4	203
8.2.2. Chapter 5	203
8.3. Chapter 6 – how could these materials be further exploited	204
8.4. Chapter 7 – what more can we find out about ligand-ligand interactions	205
8.5. Final words	206
8.6. References	207
Appendix A - Python codes	A-1
Appendix B - OTHER experimental data	B-1

Chapter 1: INTRODUCTION

1.1. METAL-ORGANIC FRAMEWORKS

1.1.1. Coordination, polymers, and frameworks

Metal-organic frameworks¹⁻³ (MOFs) are a class of materials with pores at nanometre size ranges. They are a subset of coordination polymers, built from organic linkers and metal ions.

Coordination polymers are where a ligand capable of coordinating to a metal atom (or polycationic cluster) in two or more divergent directions mediates between repeating metal centres. They have been known and studied since shortly after the beginning of coordination chemistry in the early twentieth century.⁴ The first usage of the term and reviews appeared in the 1960s, but these early coordination polymers were often one-dimensional chains, and/or lacked a well-defined structure, like traditional organic polymers.

MOFs are almost always crystalline, as a consequence of their construction. To build up MOF structures, one or more metal atoms in a cluster act as framework nodes. Since metal atoms tend to form bonds in specific directions, and the ligands tend to be either rigid, or flexible only in limited ways, the resulting structures are usually very regular.

These rigid clusters, considered together with the ligand donor atoms, are referred to in the field as secondary building units (SBUs), an abstraction analogous to talking about “building blocks” in broader supramolecular chemistry. Thinking about framework components in this way, e.g., thinking about ‘an octahedral SBU with connections at the edges’ instead of the $[\text{Zr}_6\text{O}_4(\text{OH})_4]$ cluster found in the popular UiO-66⁵ framework facilitates the design of new structures tailored to specific applications. The $[\text{Zn}_4\text{O}]$ hexacarboxylate SBU present in most of the MOFs presented in this thesis is illustrated in Figure 1.1C.

These SBUs are then linked by polytopic organic linkers² resulting in scaffold-like structures, illustrated in Figure 1.1D.

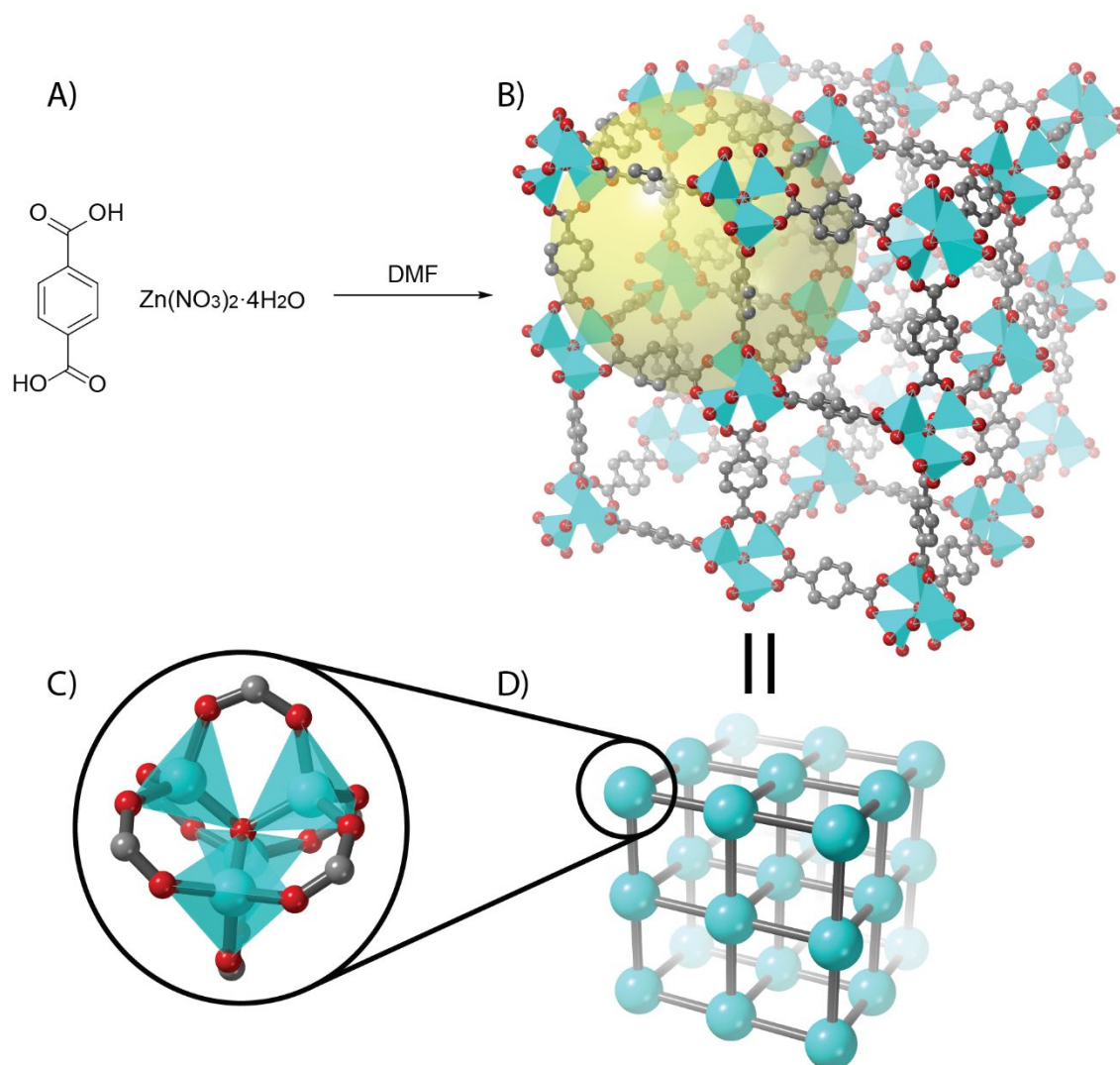


Figure 1.1: An illustration of the basic features of MOFs, using MOF-5⁶ as an example. (A) scheme of the synthetic preparation of many carboxylate MOFs. (B) A structural diagram of MOF-5. Grey spheres represent carbon, red, oxygen, cyan tetrahedra represent zinc (II) ions. The large yellow sphere represents the void space in the pore. (C) an enlarged view of the $[Zn_4O(COO)_6]$ cluster which forms the SBU of MOF-5 among many zinc carboxylate MOFs, (D) a simplified illustration of the primitive cubic (pcu) lattice

Since coordination complexes tend to have well-defined regular geometries, and each node in a MOF can be seen as a coordination complex, the overall structures also tend to be regular and well-defined, and to a certain extent, the resulting structure tends to be predictable from the precursors. Since the components are well separated and their structures are at least partially rigid, MOFs are highly porous, allowing the entrance

and removal of fluid and solute guest molecules. The transparent yellow sphere in Figure 1.1B illustrates the space between the lattice components.

1.1.2. MOF terminology

MOFs are defined by the International Union of Pure and Applied Chemistry to be “coordination polymers with an open framework containing potential voids”⁷ and are commonly referred to in two main ways. One way is by their chemical formula, in the style of traditional coordination chemistry. For example, in Figure 1.1B is a structural depiction of $[\text{Zn}_4\text{O}(\text{bdc})_3]$, where ‘bdc’ stands for the benzene dicarboxylate ligand. MOFs are also commonly referred to by individual names given to them by the research group which reports them, the material in Figure 1.1B being called ‘MOF-5’.

Some “famous” MOFs are depicted in Figure 1.2. A, MOF-5,⁶ which was the first 3-dimensional MOF with demonstrated gas uptake capability. B, UiO-66,⁵ on which thousands of articles have been published by hundreds of research groups, thanks to its extraordinary stability towards acidic and basic aqueous environments. C, HKUST-1,⁸ which was the first MOF reported where coordinated solvents could be removed to reveal uncoordinated metal sites. D, MIL-101,⁹ because of the remarkable geometry arising from such simple components. E, the “first MOFs” as reported by Hoskins and Robson¹⁰ in 1990. F, MOF-74,¹¹ in which the pores are one-dimensional channels, which allowed analogues to be synthesised with very wide pores, since interpenetration (section 1.2.) is not possible.

Throughout this introduction, I sometimes refer alternately to MOFs and “framework materials” interchangeably, partially for the sake of linguistic variety. I use this language especially when discussing general properties of, and approaches to working with, this class of materials. Despite being a little imprecise, I argue that this is a valid way to discuss them, because those other synthetic nanoporous framework materials, such as covalent organic frameworks (COFs¹²⁻¹⁴) and hydrogen-bonded

organic frameworks (HOFs^{15, 16}), share most of their synthetic and design strategies, characterisation methods, and applications with MOFs.

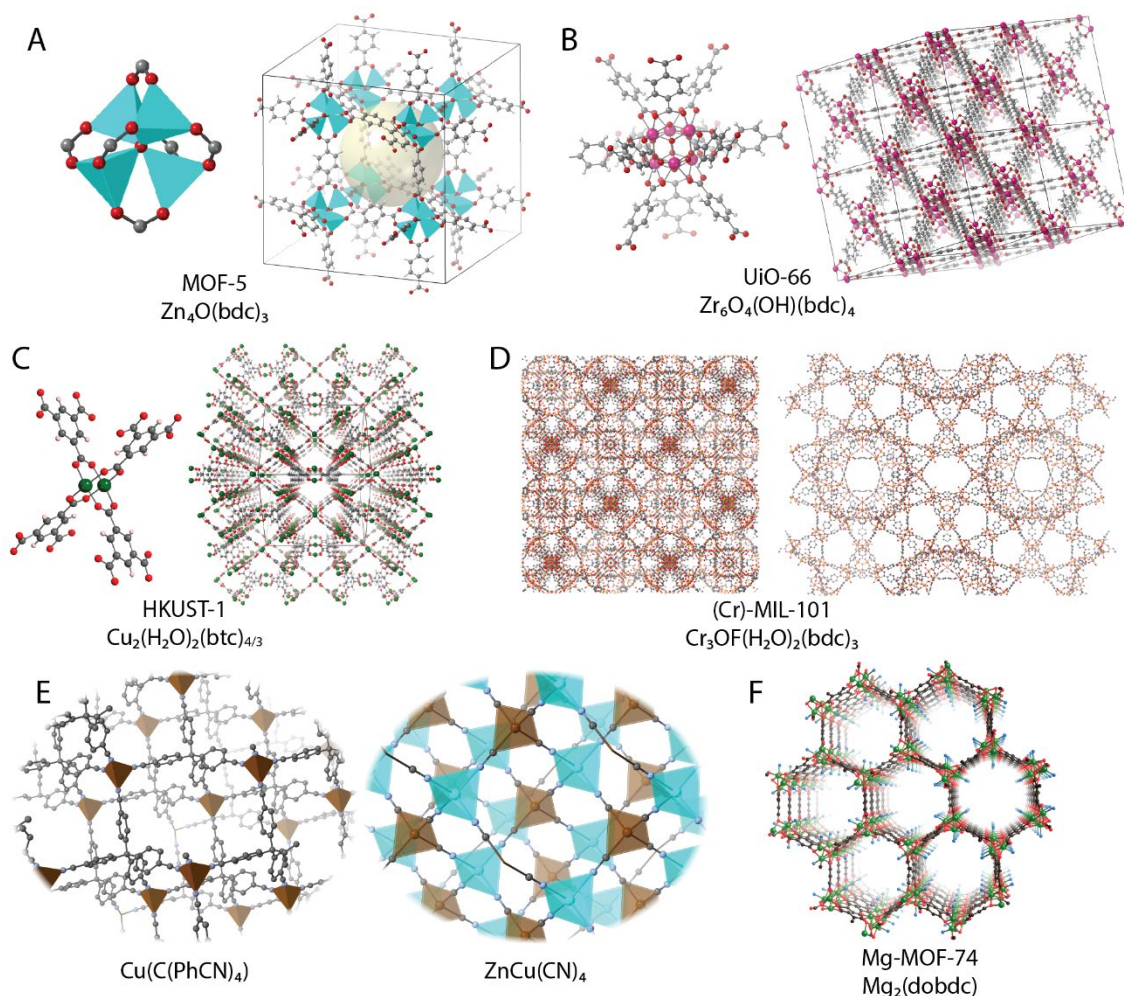


Figure 1.2: The structures of some historically important MOFs. A) MOF-5: left, the $[Zn_4O(COO)_6]$ cluster; right, the framework with a yellow sphere indicating the pore. B) UiO-66: left, the $Zr_6O_4(COO)_8$ cluster; right, a $2 \times 2 \times 2$ supercell. C) HKUST-1: left, the $Cu_2(COO)_4$ paddlewheel; right, a $2 \times 2 \times 2$ supercell. D) Cr-MIL-101: left, (1,0,0) view of the unit cell; right, (1,1,0) view of the unit cell. Carbon is coloured grey, oxygen red, zinc cyan, copper green, zirconium magenta, chromium orange. E) The "first MOFs", described¹⁰ by Hoskins and Robson. Left, tetra(cyanophenyl)methane copper(I), right, $ZnCu(CN)_4$. F) MOF-74, $[Mg_2(dobdc)]$, notable for its one dimensional channels.

1.1.3. Geometry and topology

MOF structures are often analysed from a topological^{17, 18} viewpoint. The crystallographer will determine, for a given MOF, the mathematical net¹⁹ which most simply describes the connectivity of the lattice. This is interesting in its own right as a way to describe and classify the many structures in the field, but also has some concrete uses. One is that these descriptions of the organisation of structures will help

us to rationally design and synthesise desirable materials. The other most important and related reason is that such descriptions are beneficial for the computational screening²⁰ and subsequent preparation²¹ of potential materials.

These topological nets are given a three-letter code, the short form of their name. These are often simple geometric descriptors, or minerals that share the net. For example, **pcu** stands for “primitive cubic” and indicates that every vertex is connected to six neighbours, while **dia** indicates a diamondoid network, and **nbo** the connectivity of NbO, niobium monoxide. Importantly, having a **pcu** net does not mean that the MOF unit cell or structure is a regular cube – only that the connectivity between nodes is the same as the connectivity between the vertices in a simple cubic lattice.

1.1.4. Early MOFs, and the development of the field

In 1989, a seminal paper by Hoskins and Robson¹⁰ showed that coordination polymers could form regular, three-dimensional frameworks with large void spaces. They replaced the ligands in the tetrahedral $[\text{Cu}^{\text{I}}(\text{CH}_3\text{CN})_4]^+$ complex with 4,4',4'',4'''-tetracyanotetraphenylmethane, yielding what is arguably the first metal-organic framework (it was at least the first to be identified as such – the pigment Prussian blue²², synthesised in the eighteenth century, has a cubic framework structure with many water molecules in the voids, and could be considered a MOF). Immediately, the possibilities inherent in such structures became apparent: the authors predicted that this new class of materials would be highly tuneable (by functionalisation of the organic component) and of interest in applications such as gas storage and separations, catalysis, and the isolation of otherwise unstable or reactive compounds to study them.

These predictions have largely come true (details on the application of MOFs in section 1.1.6, page 8). At the time of writing, a Scifinder search on metal-organic frameworks yields over 52,000 results, and this number is a conservative estimate of the number of publications as some authors use different terms (such as PCP – porous

coordination polymer) instead of MOF. Similarly, there are over 90,000 MOF crystal structures deposited in the Cambridge Structural Database²³ at the time of writing.

A few years later, the same group reported similar materials²⁴ based on tetraphenylporphyrin, establishing that it was possible to include a potentially catalytic component as part of a framework structure. Unfortunately, both of these materials were not stable to the removal of the solvent from their pores – the crystalline order was lost when the guest solvent was evaporated. In the early 1990s, several reports^{25, 26} of extended solids or crystalline coordination polymers were made. A notable study by Fujita et al.²⁷ showed that the pores could be used for catalysis, but none of these materials was stable to the evacuation of solvent either.

In the mid-1990s the first reports of such materials which were able to have their guests exchanged for others, and later, those which were stable to evacuation of solvents appeared^{6, 24, 28}. A particularly notable example is MOF-5²⁹ in 1999, which was the first three-dimensional MOF demonstrated to be capable of selectively adsorbing gases on its high surface area. This framework was inspired by the crystal structure of basic zinc acetate, where four tetrahedral zinc (II) ions around a central oxide form a cluster which is capped in an overall octahedral fashion by six acetate ligands. Instead of acetate, 1,4-benzenedicarboxylate was used, linking [Zn₄O] clusters together into a cubic lattice (this is the MOF illustrated in Figure 1.1).

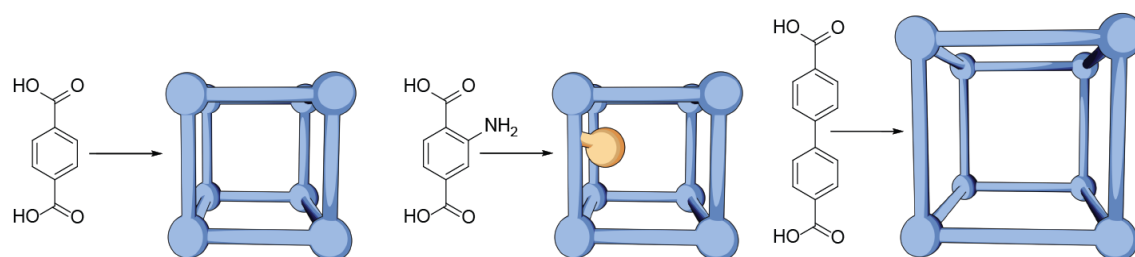


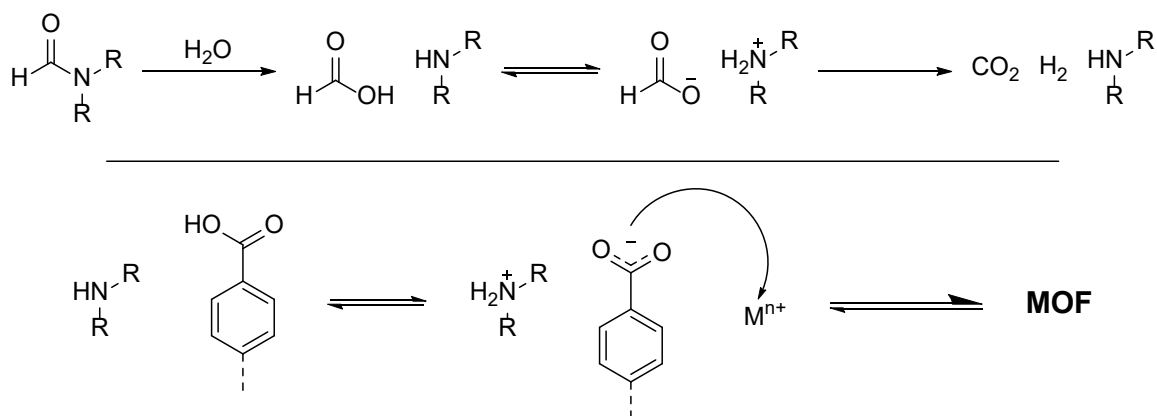
Figure 1.3: An illustration of the isorecticular principle, by which frameworks with the same SBU and topology but varying pore size and functionality can be produced by varying the ligand length and/or functionalisation.

By the early 2000s it was demonstrated that the pore sizes could indeed be tuned³⁰ by the use of the same types of SBUs with linkers of varying lengths. Yaghi and coworkers showed that a wide range of structures with the same topology as MOF-5

could be prepared by simply varying the length and substituents on the organic linker. Varying the length leads to a material with the same topology, but a different pore size. Varying the substituents leads to a material with the same topology but a different pore chemistry. This principle, ‘isorecticular chemistry’, illustrated in Figure 1.3, is used to guide MOF design³¹⁻³⁶ to create new materials with desired properties, a long-standing challenge in materials chemistry and science in general.

1.1.5. Synthesis and growth of MOFs

The historical examples of MOFs referred to in the previous section were synthesised through the traditional methods of coordination chemistry, namely vapour diffusion. The slow diffusion of triethylamine into a solution of benzene-1,4-dicarboxylic acid and zinc nitrate resulted in the slow deprotonation of the ligand, allowing the self-assembly of the MOF.



Scheme 1.1: Top: hydrolysis of formamide solvents results in the slow build-up of dialkylamines in solvothermal MOF synthesis reactions. R = Me, Et, i-Pr, n-Pr, t-Bu, n-Bu, etc. Bottom: amines slowly generated from solvent decomposition deprotonate ligands. The example is an aromatic carboxylate, but it can be many other deprotonatable groups. The deprotonated ligand coordinates to available metals or metal clusters to form a MOF.

MOFs can be synthesised through a wide range of techniques³⁷, but today they are most commonly prepared using solvothermal reactions^{38, 39} between protonated ligands and metal salts in amide-based solvents such as DMF. The gradual hydrolysis of the solvent produces amines (**Scheme 1.1**) which then deprotonate the ligand. The very gradual build-up of base allows the MOF to form slowly, and the temperature means that each metal-ligand bond is labile enough for “error correction” to occur and

high-quality crystals to result. These reactions are conveniently conducted in small (c. 2-20 mL) glass vials heated in an oven or heating block, which allow the crystal growth to be monitored easily. This is the synthetic method mostly employed in this work.

Like most crystallisation processes, MOF formation is still somewhat mysterious, and the details probably differ for every individual structure. Nonetheless, in-situ time-resolved NMR⁴⁰ and XRD⁴¹ experiments can reveal intermediate assemblies such as the metal cluster capped by solvent before the ligand coordinates.

1.1.6. Applications of MOFs

Potential applications for MOFs almost always exploit their accessible pores, and include gas storage² and separation,⁴² catalytic mitigation of toxic compounds,⁴³ and many other similar problems. Although the field is newly emerging, the first commercial products incorporating MOFs are starting to appear⁴⁴ and include storage solutions for dangerous gases used for semiconductor manufacture, and products that release inhibitors of the gases responsible for fruit ripening. In 2017, the prototype of a water harvesting device based on MOFs was featured in the news media.⁴⁵ A MOF adsorbent bed in the device is able to trap water at low humidity levels, and release it through the effect of heat. Enough heat is collected by average natural sunlight on a square metre to release approximately three litres of water from the device per day.

Many new potential applications for framework materials are being reported all the time, but I will pick a few of the most well-developed to describe with a little more detail.

1.1.6.1. *Gas storage*

The large surface area of a MOF provides many sites for gas molecules to physisorb⁴⁶⁻⁵⁰ and the energy associated with this adsorption reduces the kinetic energy of the molecules. This effect is strongest when the gas has a particularly good shape, size, or polarity match⁴⁶ to the pore or some part thereof. This means that within the MOF, the same number of gas molecules have a lower pressure than they would in a contiguous

space of the same volume – more gas can be stored at the same pressure as in a non-adsorbent-containing tank. The open nature of a framework similarly allows substrates for catalytic reactions to diffuse in and out of a MOF crystal, increasing the possible rate of a catalytic reaction by increasing the number of available catalyst sites. Compared to other commonly used porous materials, such as zeolites and porous carbons, MOFs and other framework materials often have higher surface areas and almost always have a wider scope for functionalisation².

1.1.6.2. *Separations*

Just as with gas storage, gas separation applications^{42, 47, 51-53} exploit the high surface areas of MOFs as well as, importantly, their specific pore shapes. Separations as fine as those of hydrogen isotopes⁵⁴ or xylene isomers^{55, 56} have been achieved. The highest profile gas separation is the capture of carbon dioxide⁵⁷ (CO₂) which has significant implications for climate change. Gas separations can be broadly classified on a spectrum from absorption to kinetics.

In absorptive⁵⁸ separations, the total gas uptake of the material, higher for one gas than another, is exploited. The adsorbent (in this case a MOF, but it could also be another porous material like a zeolite) is exposed to a mixture of gases, one or more of which the adsorbent has a higher affinity for than the others. The excess which is not absorbed is collected, and the gas which is absorbed is removed from the material by vacuum, heating, or a combination of the two.

Kinetic⁵⁹ separations, on the other hand, are based on some molecules diffusing more slowly through MOF pores. The extreme end of this spectrum is molecular sieving, where only one part of the mixture fits through the adsorbent pores at all, while the other is completely blocked from going through.

1.1.6.3. *Catalysis*

MOFs are an ideal platform for heterogeneous catalysis⁶⁰⁻⁶⁴ because they also provide many of the benefits of homogeneous catalysis. The dedicated materials scientist can control the specific chemical surroundings and pore spaces^{36, 65-67} in a MOF to influence

the catalytic outcome. In this case, each catalytic unit is identical, just as in homogeneous catalysis by transition metal complexes or organocatalysts. MOF catalysis is therefore unlike most traditional heterogeneous catalysis by, e.g. metal nanoparticles, which often do not have well-defined structures. The highly ordered structures of MOFs also facilitate study of the catalytic cycle, and some researchers have even observed catalytic intermediates by SCXRD⁶⁸⁻⁷⁰ to provide clear evidence for mechanisms.

A more detailed introduction to MOF catalysis is given in Chapter 6, where some MOFs designed and prepared as part of this work are applied to catalysis in a new way.

1.1.7. Characterisation methods for MOFs

1.1.7.1. *XRD*

X-ray diffraction (XRD) both of single-crystal (SCXRD) and powder (PXRD) samples is the most important characterisation method for MOFs. By comparison of the expected scattering calculated from a structural model with the real scattering observed when a MOF material is exposed to X-rays, the MOF's average atomic structure is revealed, including vital information about the sizes of pores and their windows. XRD is introduced in detail in Chapter 5.

1.1.7.2. *Gas sorption measurements*

To determine the surface area of a MOF experimentally, and to assess a given MOF's suitability for a gas storage or separation application, gas sorption measurements are performed. Measurements of amounts of a gas or vapour adsorbed to a MOF surface can be obtained gravimetrically, by measuring the weight of a sample as it changes with pressure or a gas at a fixed temperature, or volumetrically, by measuring the resultant pressure in a sample cell when a specific volume of gas is added.

1.1.7.3. *NMR spectroscopy*

MOFs are characterised by NMR spectroscopy both in the solid state, as well as after digestion of the frameworks and dissolution of their components, giving information very complementary⁷¹ to XRD.

NMR analysis of digested MOF samples, usually of the ^1H nucleus, provides information about the organic components after MOF synthesis. It is regularly used to confirm that the organic ligand remains intact during MOF synthesis, as well as to determine the ratio of multiple ligands in multivariate or multicomponent MOFs.

In the solid state, NMR allows information⁷² to be gained about the interaction of the framework with guests, such as the kinetics of guest diffusion and the adsorption sites⁷³ of gas molecules.

Solid state NMR also allows measurement of the dynamics of mobile parts of MOF components. As an example, in (very common) aromatic ligands the rings can often rotate, and solid state NMR can be used to measure the rate of this rotation. Sometimes one can even find out about the motion of molecular machines such as rotaxanes⁷⁴ when they have been used as MOF components.

1.1.7.4. *Electron microscopy*

Electron microscopy, both SEM and TEM, are commonly used for MOF characterisation, especially when the material of interest is nanocrystalline rather than large single crystals. Electron diffraction has provided the only reported single crystal structures¹⁴ of COFs, which are notoriously difficult to prepare in crystals larger than the nanoscale.

Since electron microscopy can not only provide imaging but also information about local symmetry (through electron diffraction) it has been used to directly identify locations with different crystal defects⁷⁵ (missing ligands and/or nodes) through the combination of imaging and diffraction.

1.2. INTERPENETRATION IN METAL-ORGANIC FRAMEWORKS

Interpenetration is a phenomenon known in MOFs,⁷⁶ supramolecular cages,⁷⁷ and many other kinds of network materials⁷⁸ such as organic polymers and hydrogels. In the context of MOFs and other crystalline materials, interpenetration means that two or more lattices are present in the same crystal. The number of lattices is typically an integer, usually under five, and the nodes of one lattice occupy the pores of the neighbouring lattice(s), so that the overall structure can be thought of as a catenane on a polymeric scale. This is illustrated with the simplest example, two-fold interpenetration, in Figure 1.4.

Interpenetration in MOFs is very common, occurring in some of the very earliest²⁶ examples. The highest level of interpenetration reported to date is a remarkable 54-fold⁷⁹. The probability of a given MOF being interpenetrated increases with increasing length of the organic linker, and thus with the void volume a non-interpenetrated framework would have had.

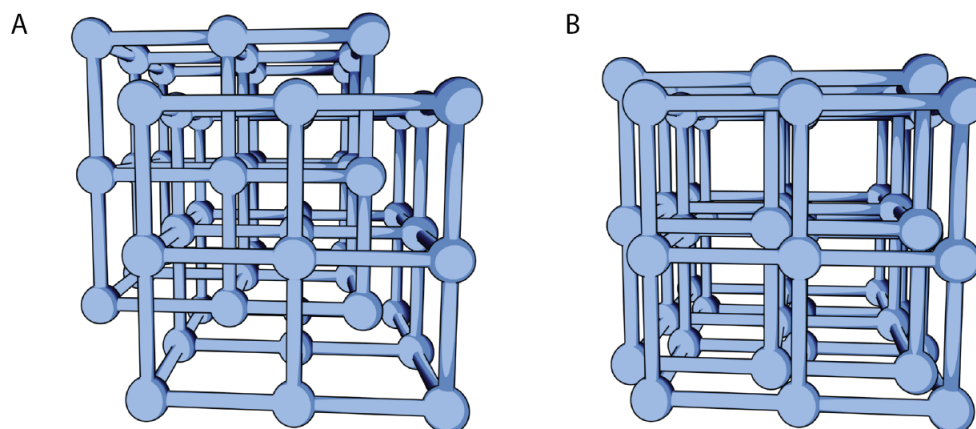


Figure 1.4: (A) An illustration of *interpenetration* using the simple example of two **pcu** lattices, with the nodes of each lattice perfectly centred in the pores of the other. (B) As before, but with the lattices offset from each other, maximising van der Waals contacts between lattices.

In most cases, notably the IRMOF series³⁰, interpenetrating lattices are not evenly distributed with nodes directly in the centres of the pores of the neighbouring lattice (Figure 1.4A). Instead they are usually offset (Figure 1.4B), to allow the maximum amount of van der Waals contact between the lattices. Although individual van der

Waals contacts are weak, over a large structure they sum to a significant amount of energy, and this is the primary reason for interpenetration being thermodynamically preferred.

1.2.1. Interpenetration and porosity

Interpenetration reduces the pore volume of a MOF, and thus reduces its surface area and in most cases its total uptake of gas, or porosity.⁸⁰

For any given gas storage or separation application, a match between the pore size and the desired guest is key. For example, the ideal pore diameter for hydrogen uptake has been calculated to be approximately 7 Å or 10 Å, corresponding to two or three hydrogen molecules without any excess space respectively⁸¹. If the interpenetration of a framework brings its pore diameter closer to such an ideal size, an improvement in separation properties (if not necessarily absolute gravimetric uptake) can be expected.

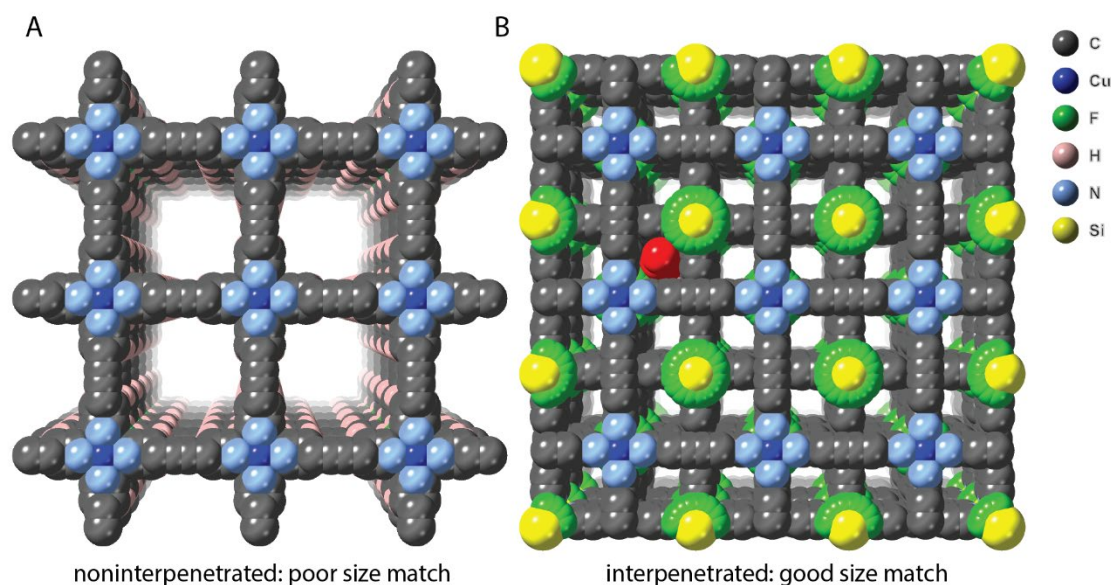


Figure 1.5: Illustration of guest and pore size comparisons for (A) non-interpenetrated and (B) interpenetrated versions of SIFSIX-2-Cu. Atom colours are indicated in the legend; red spheres represent the oxygen atoms of a modelled CO₂ molecule which closely match the pore size of SIFSIX-2-Cu-i.

In some cases, the absolute gravimetric uptake can also be higher in interpenetrated frameworks, under specific conditions. One example is the copper(II), 4,4'-dipyridylacetylene and hexafluorosilicate based framework SIFSIX-2-Cu⁴⁹ illustrated

in Figure 1.5. This material has a surface area of $3140 \text{ m}^2 \text{ g}^{-1}$ in its non-interpenetrated phase, while in its interpenetrated phase this is reduced to $735 \text{ m}^2 \text{ g}^{-1}$. The interpenetrated phase has a pore diameter closely matching the kinetic diameter of carbon dioxide.

The non-interpenetrated phase exhibits CO_2 uptake of $41.4 \text{ cm}^3 \text{ g}^{-1}$ at 298 K and 1 bar, but because of the aforementioned size match, the interpenetrated phase SIFSIX-2-Cu-i absorbs almost three times as much, taking up $121.2 \text{ cm}^3 \text{ g}^{-1}$ (5.41 mmol g^{-1} , 238 mg g^{-1}) under the same conditions. There are similar materials for hydrogen adsorption.⁸²

Interpenetration also allows for the possibility of dynamic behaviour of interpenetrated lattices. A two-fold interpenetrated nickel(II), 1,2-bis(4-pyridyl)ethane and dicyanamide based MOF synthesised by Kitagawa and coworkers⁸³ shows some remarkable behaviours. Exposure to CO_2 gas induces a shift in the arrangement of the two lattices, allowing the gas to enter and be adsorbed. N_2 and O_2 however, which are of a similar size, are entirely excluded from the pores. This makes the framework very highly selective for CO_2 uptake.

1.2.2. When is interpenetration useful and when isn't it?

Whether or not framework interpenetration is desirable is highly specific to the MOF and the application, but I will briefly mention a few examples which may illustrate the breadth of the range of situations in which one needs to consider it. The first example is the simple tuning of pore size (as described above) which produces new or different sites⁸⁴ for gas sorption.

Interpenetration increases the thermal conductivity⁸⁵ of MOFs by introducing vibrations of the framework relative to each other. Thermal conductivity is critical for gas sorption applications, as the adsorption and desorption of gases are energetic processes with large associated temperature swings which need to be mitigated to allow loading of the MOF pores in a reasonable timeframe.

Ligands in an interpenetrated MOF can structurally support⁸⁶ each other to prevent framework collapse on solvent removal. Large ligands (e.g. those based on porphyrins) can be brought closer together than they would be in a non-interpenetrated structure, for cooperative catalysis⁸⁷ between groups from both ligands. Ligand distances also have a strong influence over MOF luminescence properties, which can also be tuned⁸⁸ through the control of interpenetration.

1.2.3. Control of interpenetration

As the previous section hopefully indicated, control of interpenetration in framework materials is highly desirable, and indeed such control has been a popular target^{89,90} for MOF chemists. As described above, interpenetration can result in a variety of positive and negative effects on any particular MOF structure, but the effect depends on at least partially known features of the framework. Thus, the MOF chemist can use the control of interpenetration to tailor a MOF towards a specific purpose. A selection of the most common parameters by which interpenetration can be modulated are summarised in Figure 1.6.

The framework geometry determines, first of all, whether interpenetration is possible at all. In simple cubic or diamondoid networks (such as those illustrated in Figure 1.2A and E respectively) it is easy to understand how interpenetration could be possible. On the other hand, certain topologies can prevent interpenetration. One example of this is MOF-177⁹¹, where a doubling of the **qom** net would result in each network sharing some of its edges with the other: possible in a mathematical representation of a topology, but not in a chemical structure. The largest pores achieved to date are in analogues of MOF-74⁹², which has one-dimensional channels as pores. This allowed the linker length to be increased without resulting in interpenetration, giving rise to materials with pore diameters over 98 Å, large enough for the inclusion of whole proteins.

Ligand length is probably the most important factor among many determining the interpenetration of a given framework. As ligands become longer, the pore spaces and diameters of pore openings increase, and room is made available for additional lattices. For example, in similar synthesis conditions, the short 1,4-benzenedicarboxylate ligand produces non-interpenetrated materials while the longer 4,4'-biphenyldicarboxylate ligand produces interpenetrated frameworks³⁰. Bulky substituents on ligands tend to reduce the occurrence of interpenetration, simply through steric hindrance of the entry of additional ligands to the pores of the MOF. In one example, a bulky boc-protected proline substituent³⁵ resulted in a non-interpenetrated framework, while the bare backbone results in a two-fold interpenetrated framework.

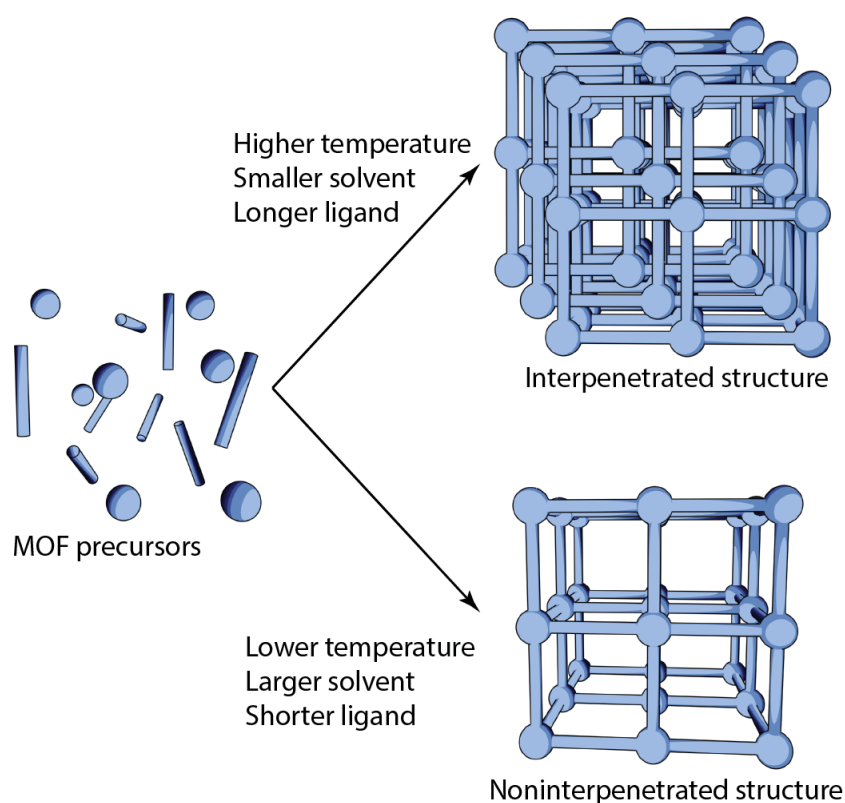


Figure 1.6: A diagrammatic illustration of the main handles on interpenetration control in MOFs.

Solvent choice has been effective in determining interpenetration levels in some cases. Solvents with larger molecular sizes tend to produce non-interpenetrated structures through the exclusion of additional ligand from the pores of a lattice. In one study⁹³

using formamide as the solvent generated fivefold interpenetrated structures, while in the bulkier DMF fourfold interpenetrated structures formed, and in the yet bulkier diethylformamide threefold interpenetrated structures formed, in each case from the same ligand and metal combinations.

Concentration of precursors³⁰ and synthesis through sonication at various energies⁹⁴ have also been used to discriminate between the formation of IRMOF-9 and IRMOF-10, the twofold interpenetrated and noninterpenetrated isomers of $[\text{Zn}_4\text{O}(\text{bpdc})_3]$, respectively.

Temperature has also been used to effectively control interpenetration. It is a feature of all types of chemical reaction that kinetic products tend to dominate at lower temperatures, while thermodynamic products are formed at higher temperatures. So it is with metal-organic frameworks, where at low temperatures less interpenetrated products are more common. For example⁹⁵ IRMOF-8, which was originally prepared in an interpenetrated form via solvothermal synthesis, could be synthesised in a non-interpenetrated form by performing the synthesis at room temperature over a longer time period. Electrostatic interaction between ligands and solvent has also been observed⁹⁶ to preclude interpenetration in a MOF family which is otherwise strongly predisposed to it.

1.2.4. Partial interpenetration

Partial interpenetration^{49, 97-100} is a recently observed and uncommon phenomenon where an interpenetrating lattice can have a fractional crystallographic occupancy. That is, some cells of the crystal contain a sublattice, while other cells are non-interpenetrated, resulting in a fractional value of interpenetration. Figure 1.7 shows two different ways in which partial interpenetration can be manifested.

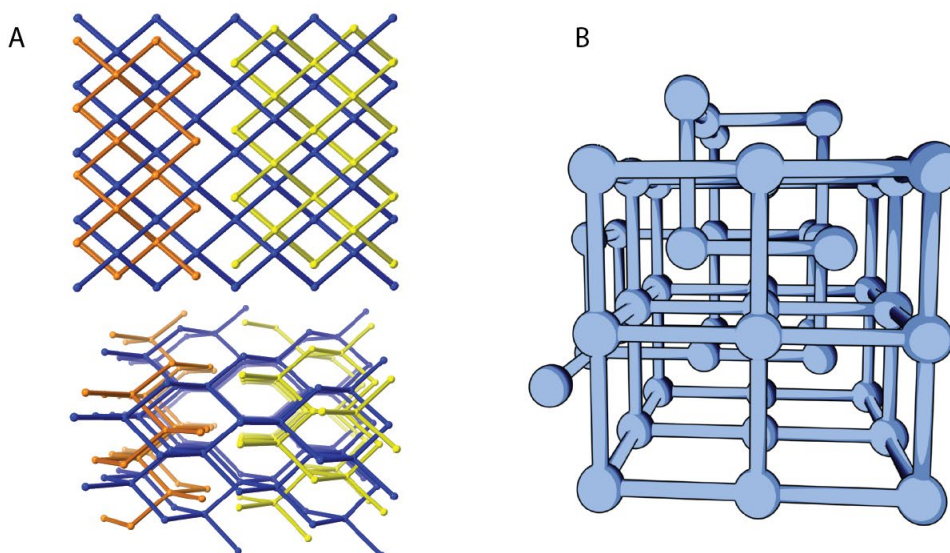


Figure 1.7: (A) A partially interpenetrated framework (NOTT-202¹⁰⁰) where the interpenetrating lattice is disordered over two incompatible sites. (B) A partially interpenetrated lattice where a continuum of degrees of interpenetration is possible. In both cases, the blue (primary) lattice is complete, while the secondary lattice (orange and yellow in A, blue in B) exists only in some regions and not in others.

The first kind of partial interpenetration (Figure 1.7A) is exemplified by NOTT-202¹⁰⁰ the first partially interpenetrated framework to be reported. It consists of a diamondoid lattice, where the second, interpenetrating lattice can occupy two different, incompatible positions relative to the primary lattice. The gaps between interpenetrated regions result in crystals which are only interpenetrated throughout 75% of their volume.

Ma et al. reported⁹⁸ the only known partially interpenetrated framework with more than two lattices. It has three, where the primary lattice is fully occupied while the secondary and tertiary lattices have occupancies of 50% and 25% respectively. This framework is partially interpenetrated for the same reason as NOTT-202, with each sublattice being disordered over incompatible positions.

Massey University Framework (MUF) 9 and its analogues⁹⁹ are materials which display *controlled* partial interpenetration. In MUF-9, a bulky side chain on the ligand only slows but does not prevent interpenetration. This results in a material with any possible fraction of lattices between one and two: any cell can either have a second lattice or not, as illustrated in Figure 1.7B. This is in contrast to the aforementioned

examples, where the partial occupancy of the interpenetrating lattices is fixed. MUF-9 was reported by the Telfer group and collaborators in 2016 and is the basis for this work. It will be introduced in detail in Chapter 2.

More recently, the Zaworotko group reported a MOF⁹⁷ where control over partial interpenetration is also displayed. They could vary the occupancy of the second lattice in their SIFSIX-14-Cu-i material between 99% and 70%, then demonstrated that decreasing the interpenetration percentage also decreased the C₂H₂/C₂H₄ separation performance in an otherwise identical material. For both MUF-9 and SIFSIX-14-Cu-i, the partial interpenetration results from a difference in growth rate between primary and secondary lattices, but has only one crystallographic site for the secondary lattice, which is what makes the continuum of degrees of partial interpenetration possible.

1.2.5. Interpenetration of heterogeneous frameworks

There are some examples, a list of which was collected in a recent review⁷⁶, of atypical cases of interpenetration where the interpenetrating lattices are *not* identical to each other. The two lattices often have different dimensionalities, such as 1D chains that interpenetrate through 2D grids, one nice example of which is the MOF depicted in **Figure 1.8**. However, in several isolated cases¹⁰¹⁻¹⁰³ they can be combinations of 3D lattices that have different topologies and compositions.

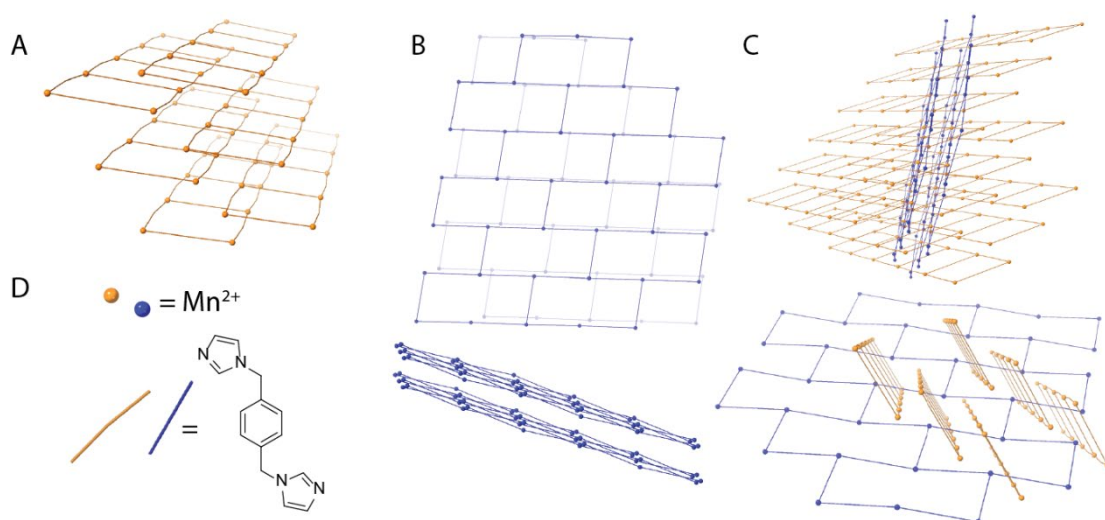


Figure 1.8: An illustration of the structure of a hetero-interpenetrated MOF formed from 1D ladders interpenetrating through 2D sheets to form a 3D structure, reported by Carlucci¹⁰⁴ et al. A) One type of sublattice, 1D chains in a ladder-like arrangement. B) The other type of sublattice, 2D sheets in a brick-like pattern. C) An illustration of how the two types of network interpenetrate. D) The components of both lattices are manganese(II) ions with the depicted ligand.

To date, the observation of interpenetrated MOFs that comprise two different lattices has been serendipitous. Rational synthetic strategies to produce such materials have not yet emerged, though recent computational efforts^{105, 106} have focused on identifying potentially compatible existing frameworks. This is the most fundamental question addressed in this thesis: can one purposefully produce hetero-interpenetrated MOF materials?

1.3. A BRIEF DESCRIPTION OF THIS WORK

This thesis has more (and shorter) Chapters than is usual, and has more introductory material spread throughout different Chapters than is common. For example, a detailed introduction to X-ray crystallography is presented in Chapter 5, where a new crystallographic technique is developed, and a detailed introduction to catalysis in MOFs is given in Chapter 6, where the subject is the application of a MOF to tuning a catalytic reaction. I have chosen this format in the hope that it will be easier to read when related pieces of information are nearer each other.

To boil it down to the simplest expression I can think of, this work is a case study of how the shape of the organic component of a MOF can influence its structure, and how the interactions between MOF components can be exploited to access difficult and useful structures. The example studied is the deliberate synthesis of hetero-interpenetrated MOFs in a stepwise process.

In Chapter 2, we will look at the MOF which is used as the starting material for much of the work of this thesis. I will describe this framework, MUF-9, and present some characterisation which furthers our understanding of it compared to what was presented in its original publication. This extra characterisation is in order to establish its viability for use as a starting material in the following Chapters, and the conditions under which it can be used in that capacity.

In Chapter 3, I present the first rationally designed hetero-interpenetrated MOF, prepared from MUF-9 in a stepwise synthesis. The conditions necessary for that synthesis are established, and a means of characterising such a complex material is described.

In Chapter 4, I expand the methods established in Chapter 3 to a range of different secondary lattices. Some of the limits of this method are shown, and two interesting examples of hetero-interpenetrated frameworks are characterised in detail.

In Chapter 5, I present a new method, using multiwavelength synchrotron techniques, to specifically determine the identities of metal atoms at selected crystallographic loci, something which is usually not possible with fixed-wavelength laboratory X-ray sources.

In Chapter 6, the method for producing hetero-interpenetrated MOFs is adapted to a closely related starting material, MUF-10, and then applied to produce a designer catalyst. This is a proof-of-concept demonstration of one kind of use which hetero-interpenetrated frameworks could have: materials where each of the two different lattices contribute orthogonally to the functionality of the material.

In Chapter 7, I present a few new frameworks using new ligands related to those used in Chapters 2-6. Our target here was to explore variations of MUF-9 which could elucidate the reasons for its unusual behaviour. I explore how the supramolecular interactions between the side chains of these ligands determine the structure of the resulting framework materials.

In Chapter 8, I summarise the overall results of this work and reiterate their place in the larger context of MOF chemistry and chemistry in general. I offer my perspective on directions the results of this work might lead.

1.4. REFERENCES

1. Furukawa, H.; Muller, U.; Yaghi, O. M., "Heterogeneity within order" in metal-organic frameworks. *Angew Chem Int Ed Engl* **2015**, *54* (11), 3417-30. DOI: 10.1002/anie.201410252
2. Furukawa, H.; Cordova, K. E.; O'Keeffe, M.; Yaghi, O. M., The Chemistry and Applications of Metal-Organic Frameworks. *Science* **2013**, *341* (6149), 1230444. DOI: 10.1126/science.1230444
3. Yaghi, O. M., Metal-organic Frameworks: A tale of two entanglements. *Nat. Mater.* **2007**, *6* (2), 92-93. DOI: 10.1038/nmat1824
4. Kitagawa, S.; Kitaura, R.; Noro, S.-i., Functional Porous Coordination Polymers. *Angew. Chem. Int. Ed.* **2004**, *43* (18), 2334-2375. DOI: 10.1002/anie.200300610
5. Cavka, J. H.; Jakobsen, S.; Olsbye, U.; Guillou, N.; Lamberti, C.; Bordiga, S.; Lillerud, K. P., A new zirconium inorganic building brick forming metal organic frameworks with exceptional stability. *J. Am. Chem. Soc.* **2008**, *130* (42), 13850-1. DOI: 10.1021/ja8057953
6. Yaghi, O. M.; Li, G.; Li, H., Selective binding and removal of guests in a microporous metal-organic framework. *Nature* **1995**, *378* (6558), 703-706. DOI: DOI 10.1038/378703a0
7. Batten, S. R.; Champness, N. R.; Chen, X.-M.; Garcia-Martinez, J.; Kitagawa, S.; Öhrström, L.; O'Keeffe, M.; Suh, M. P.; Reedijk, J., Coordination polymers, metal-organic frameworks and the need for terminology guidelines. *CrystEngComm* **2012**, *14* (9), 3001-3004. DOI: 10.1039/c2ce06488j
8. Chui, S. S.; Lo, S. M.; Charmant, J. P.; Orpen, A. G.; Williams, I. D., A chemically functionalizable nanoporous material. *Science* **1999**, *283* (5405), 1148-50. DOI: 10.1126/science.283.5405.1148
9. Ferey, G.; Mellot-Draznieks, C.; Serre, C.; Millange, F.; Dutour, J.; Surble, S.; Margiolaki, I., A chromium terephthalate-based solid with unusually large pore volumes and surface area. *Science* **2005**, *309* (5743), 2040-2. DOI: 10.1126/science.1116275
10. Hoskins, B. F.; Robson, R., Design and construction of a new class of scaffolding-like materials comprising infinite polymeric frameworks of 3D-linked molecular rods. A reappraisal of the zinc cyanide and cadmium cyanide structures and the synthesis and structure of the diamond-related frameworks $[N(CH_3)_4][CuI ZnII(CN)_4]$ and $CuI[4,4',4'',4''']$ -tetracyanotetraphenylmethane]BF₄.x C₆H₅NO₂. *J. Am. Chem. Soc.* **1990**, *112* (4), 1546-1554. DOI: 10.1021/ja00160a038
11. Rosi, N. L.; Kim, J.; Eddaoudi, M.; Chen, B.; O'Keeffe, M.; Yaghi, O. M., Rod packings and metal-organic frameworks constructed from rod-shaped secondary building units. *J. Am. Chem. Soc.* **2005**, *127* (5), 1504-18. DOI: 10.1021/ja045123o
12. Diercks, C. S.; Yaghi, O. M., The atom, the molecule, and the covalent organic framework. *Science* **2017**, *355* (6328). DOI: 10.1126/science.aal1585
13. Stewart, D.; Antypov, D.; Dyer, M. S.; Pitcher, M. J.; Katsoulidis, A. P.; Chater, P. A.; Blanc, F.; Rosseinsky, M. J., Stable and ordered amide frameworks synthesised under reversible conditions which facilitate error checking. *Nat Commun* **2017**, *8* (1), 1102. DOI: 10.1038/s41467-017-01423-5

14. Zhang, Y. B.; Su, J.; Furukawa, H.; Yun, Y.; Gandara, F.; Duong, A.; Zou, X.; Yaghi, O. M., Single-crystal structure of a covalent organic framework. *J. Am. Chem. Soc.* **2013**, *135* (44), 16336-9. DOI: 10.1021/ja409033p
15. Li, Y.; Tang, S.; Yusov, A.; Rose, J.; Borrforss, A. N.; Hu, C. T.; Ward, M. D., Hydrogen-bonded frameworks for molecular structure determination. *Nat Commun* **2019**, *10* (1), 4477. DOI: 10.1038/s41467-019-12453-6
16. Lin, R. B.; He, Y.; Li, P.; Wang, H.; Zhou, W.; Chen, B., Multifunctional porous hydrogen-bonded organic framework materials. *Chem. Soc. Rev.* **2019**, *48* (5), 1362-1389. DOI: 10.1039/c8cs00155c
17. O'Keeffe, M.; Yaghi, O. M., Deconstructing the crystal structures of metal-organic frameworks and related materials into their underlying nets. *Chem Rev* **2012**, *112* (2), 675-702. DOI: 10.1021/cr200205j
18. Kim, D.; Liu, X.; Lah, M. S., Topology analysis of metal-organic frameworks based on metal-organic polyhedra as secondary or tertiary building units. *Inorganic Chemistry Frontiers* **2015**, *2* (4), 336-360. DOI: 10.1039/c4qi00236a
19. Ockwig, N. W.; Delgado-Friedrichs, O.; O'Keeffe, M.; Yaghi, O. M., Reticular chemistry: occurrence and taxonomy of nets and grammar for the design of frameworks. *Acc. Chem. Res.* **2005**, *38* (3), 176-82. DOI: 10.1021/ar020022l
20. Yazaydin, A. O.; Snurr, R. Q.; Park, T. H.; Koh, K.; Liu, J.; Levan, M. D.; Benin, A. I.; Jakubczak, P.; Lanuza, M.; Galloway, D. B.; Low, J. J.; Willis, R. R., Screening of metal-organic frameworks for carbon dioxide capture from flue gas using a combined experimental and modeling approach. *J. Am. Chem. Soc.* **2009**, *131* (51), 18198-9. DOI: 10.1021/ja9057234
21. Farha, O. K.; Yazaydin, A. O.; Eryazici, I.; Malliakas, C. D.; Hauser, B. G.; Kanatzidis, M. G.; Nguyen, S. T.; Snurr, R. Q.; Hupp, J. T., De novo synthesis of a metal-organic framework material featuring ultrahigh surface area and gas storage capacities. *Nat Chem* **2010**, *2* (11), 944-8. DOI: 10.1038/nchem.834
22. Buser, H. J.; Schwarzenbach, D.; Petter, W.; Ludi, A., The crystal structure of Prussian Blue: Fe₄[Fe(CN)₆]₃·xH₂O. *Inorg. Chem.* **2002**, *16* (11), 2704-2710. DOI: 10.1021/ic50177a008
23. Groom, C. R.; Bruno, I. J.; Lightfoot, M. P.; Ward, S. C., The Cambridge Structural Database. *Acta Crystallogr B Struct Sci Cryst Eng Mater* **2016**, *72* (Pt 2), 171-9. DOI: 10.1107/S2052520616003954
24. Abrahams, B. F.; Hoskins, B. F.; Michail, D. M.; Robson, R., Assembly of porphyrin building blocks into network structures with large channels. *Nature* **1994**, *369* (6483), 727-729. DOI: 10.1038/369727a0
25. Kondo, M.; Yoshitomi, T.; Matsuzaka, H.; Kitagawa, S.; Seki, K., Three-Dimensional Framework with Channeling Cavities for Small Molecules: {[M₂(4,4'-bpy)₃(NO₃)₄·xH₂O]}_n (M = Co, Ni, Zn). *Angew. Chem., Int. Ed. Engl.* **1997**, *36* (16), 1725-1727. DOI: 10.1002/anie.199717251
26. Yaghi, O. M.; Li, G., Mutually Interpenetrating Sheets and Channels in the Extended Structure of [Cu(4,4'-bpy)Cl]. *Angew. Chem., Int. Ed. Engl.* **1995**, *34* (2), 207-209. DOI: 10.1002/anie.199502071
27. Fujita, M.; Kwon, Y. J.; Washizu, S.; Ogura, K., Preparation, Clathration Ability, and Catalysis of a Two-Dimensional Square Network Material Composed of Cadmium(II) and 4,4'-Bipyridine. *J. Am. Chem. Soc.* **1994**, *116* (3), 1151-1152. DOI: 10.1021/ja00082a055

28. Yaghi, O. M.; Li, H.; Groy, T. L., Construction of Porous Solids from Hydrogen-Bonded Metal Complexes of 1,3,5-Benzenetricarboxylic Acid. *J. Am. Chem. Soc.* **1996**, *118* (38), 9096–9101. DOI: DOI 10.1021/ja960746q
29. Li, H.; Eddaoudi, M.; O'Keeffe, M.; Yaghi, O. M., Design and synthesis of an exceptionally stable and highly porous metal-organic framework. *Nature* **1999**, *402* (6759), 276-279. DOI: 10.1038/46248
30. Eddaoudi, M.; Kim, J.; Rosi, N.; Vodak, D.; Wachter, J.; O'Keeffe, M.; Yaghi, O. M., Systematic Design of Pore Size and Functionality in Isoreticular MOFs and Their Application in Methane Storage. *Science* **2002**, *295* (5554), 469–472. DOI: DOI 10.1126/science.1067208
31. Yuan, S.; Chen, Y. P.; Qin, J. S.; Lu, W.; Zou, L.; Zhang, Q.; Wang, X.; Sun, X.; Zhou, H. C., Linker Installation: Engineering Pore Environment with Precisely Placed Functionalities in Zirconium MOFs. *J. Am. Chem. Soc.* **2016**, *138* (28), 8912-9. DOI: 10.1021/jacs.6b04501
32. Liu, L.; Telfer, S. G., Systematic ligand modulation enhances the moisture stability and gas sorption characteristics of quaternary metal-organic frameworks. *J. Am. Chem. Soc.* **2015**, *137* (11), 3901-9. DOI: 10.1021/jacs.5b00365
33. Dau, P. V.; Cohen, S. M., A bifunctional, site-isolated metal-organic framework-based tandem catalyst. *Inorg. Chem.* **2015**, *54* (7), 3134-8. DOI: 10.1021/ic502316v
34. Lu, W.; Wei, Z.; Gu, Z. Y.; Liu, T. F.; Park, J.; Park, J.; Tian, J.; Zhang, M.; Zhang, Q.; Gentle, T., 3rd; Bosch, M.; Zhou, H. C., Tuning the structure and function of metal-organic frameworks via linker design. *Chem. Soc. Rev.* **2014**, *43* (16), 5561-93. DOI: 10.1039/c4cs00003j
35. Lun, D. J.; Waterhouse, G. I.; Telfer, S. G., A general thermolabile protecting group strategy for organocatalytic metal-organic frameworks. *J. Am. Chem. Soc.* **2011**, *133* (15), 5806-9. DOI: 10.1021/ja202223d
36. Gascon, J.; Aktay, U.; Hernandezalonso, M.; Vanklink, G.; Kapteijn, F., Amino-based metal-organic frameworks as stable, highly active basic catalysts. *J. Catal.* **2009**, *261* (1), 75-87. DOI: 10.1016/j.jcat.2008.11.010
37. Stock, N.; Biswas, S., Synthesis of Metal-Organic Frameworks (MOFs): Routes to Various MOF Topologies, Morphologies, and Composites. *Chem. Rev.* **2012**, *112* (2), 933–969. DOI: 10.1021/cr200304e
38. Schaate, A.; Roy, P.; Godt, A.; Lippke, J.; Waltz, F.; Wiebcke, M.; Behrens, P., Modulated synthesis of Zr-based metal-organic frameworks: from nano to single crystals. *Chemistry* **2011**, *17* (24), 6643-51. DOI: 10.1002/chem.201003211
39. Hausdorf, S.; Baitalow, F.; Seidel, J.; Mertens, F. O. R. L., Gaseous Species as Reaction Tracers in the Solvothermal Synthesis of the Zinc Oxide Terephthalate MOF-5. *The Journal of Physical Chemistry A* **2007**, *111* (20), 4259-4266. DOI: 10.1021/jp0708291
40. Férey, G.; Haouas, M.; Loiseau, T.; Taulelle, F., Nanoporous Solids: How Do They Form? An In Situ Approach. *Chem. Mater.* **2013**, *26* (1), 299-309. DOI: 10.1021/cm4019875
41. Van Vleet, M. J.; Weng, T.; Li, X.; Schmidt, J. R., In Situ, Time-Resolved, and Mechanistic Studies of Metal-Organic Framework Nucleation and Growth. *Chem Rev* **2018**, *118* (7), 3681-3721. DOI: 10.1021/acs.chemrev.7b00582

42. Denny Jr, M. S.; Moreton, J. C.; Benz, L.; Cohen, S. M., Metal-organic frameworks for membrane-based separations. *Nature Reviews Materials* **2016**, 1 (12), 16078. DOI: 10.1038/natrevmats.2016.78
43. Vellingiri, K.; Deep, A.; Kim, K. H., Metal-Organic Frameworks as a Potential Platform for Selective Treatment of Gaseous Sulfur Compounds. *ACS Appl. Mater. Interfaces* **2016**, 8 (44), 29835-29857. DOI: 10.1021/acsami.6b10482
44. Frameworks for commercial success. *Nat. Chem.* **2016**, 8 (11), 987-987. DOI: 10.1038/nchem.2661
45. Kim, H.; Yang, S.; Rao, S. R.; Narayanan, S.; Kapustin, E. A.; Furukawa, H.; Umans, A. S.; Yaghi, O. M.; Wang, E. N., Water harvesting from air with metal-organic frameworks powered by natural sunlight. *Science* **2017**, 356 (6336), eaam8743. DOI: 10.1126/science.aam8743
46. Chen, Q.; Ma, Y.; Song, W. C.; Chang, Z.; Li, J. R.; Zhang, J.; Sun, H. W.; Balbuena, P. B.; Bu, X. H., Why Porous Materials Have Selective Adsorptions: A Rational Aspect from Electrodynamics. *Inorg. Chem.* **2017**, 56 (5), 2614-2620. DOI: 10.1021/acs.inorgchem.6b02746
47. Nandasiri, M. I.; Jambovane, S. R.; McGrail, B. P.; Schaef, H. T.; Nune, S. K., Adsorption, separation, and catalytic properties of densified metal-organic frameworks. *Coord. Chem. Rev.* **2016**, 311, 38-52. DOI: 10.1016/j.ccr.2015.12.004
48. Carrington, E. J.; Vitorica-Yrezabal, I. J.; Brammer, L., Crystallographic studies of gas sorption in metal-organic frameworks. *Acta Crystallogr. B* **2014**, 70 (Pt 3), 404-22. DOI: 10.1107/S2052520614009834
49. Nugent, P.; Belmabkhout, Y.; Burd, S. D.; Cairns, A. J.; Luebke, R.; Forrest, K.; Pham, T.; Ma, S.; Space, B.; Wojtas, L.; Eddaoudi, M.; Zaworotko, M. J., Porous materials with optimal adsorption thermodynamics and kinetics for CO₂ separation. *Nature* **2013**, 495 (7439), 80-4. DOI: 10.1038/nature11893
50. Yang, C.; Wang, X.; Omary, M. A., Crystallographic observation of dynamic gas adsorption sites and thermal expansion in a breathable fluorinated metal-organic framework. *Angew. Chem. Int. Ed.* **2009**, 48 (14), 2500-5. DOI: 10.1002/anie.200804739
51. Lin, R.-B.; Xiang, S.; Zhou, W.; Chen, B., Microporous Metal-Organic Framework Materials for Gas Separation. *Chem* **2019**. DOI: 10.1016/j.chempr.2019.10.012
52. Zhao, X.; Wang, Y.; Li, D. S.; Bu, X.; Feng, P., Metal-Organic Frameworks for Separation. *Adv Mater* **2018**, 30 (37), e1705189. DOI: 10.1002/adma.201705189
53. Senkovska, I.; Kaskel, S., Ultrahigh porosity in mesoporous MOFs: promises and limitations. *Chem. Commun.* **2014**, 50 (54), 7089-98. DOI: 10.1039/c4cc00524d
54. Kim, J. Y.; Oh, H.; Moon, H. R., Hydrogen Isotope Separation in Confined Nanospaces: Carbons, Zeolites, Metal-Organic Frameworks, and Covalent Organic Frameworks. *Adv Mater* **2019**, 31 (20), e1805293. DOI: 10.1002/adma.201805293
55. Huang, J.; Han, X.; Yang, S.; Cao, Y.; Yuan, C.; Liu, Y.; Wang, J.; Cui, Y., Microporous 3D Covalent Organic Frameworks for Liquid Chromatographic Separation of Xylene Isomers and Ethylbenzene. *J. Am. Chem. Soc.* **2019**, 141 (22), 8996-9003. DOI: 10.1021/jacs.9b03075

56. Alaerts, L.; Maes, M.; Giebel, L.; Jacobs, P. A.; Martens, J. A.; Denayer, J. F.; Kirschhock, C. E.; De Vos, D. E., Selective adsorption and separation of ortho-substituted alkylaromatics with the microporous aluminum terephthalate MIL-53. *J. Am. Chem. Soc.* **2008**, *130* (43), 14170-8. DOI: 10.1021/ja802761z
57. Yu, J.; Xie, L. H.; Li, J. R.; Ma, Y.; Seminario, J. M.; Balbuena, P. B., CO₂ Capture and Separations Using MOFs: Computational and Experimental Studies. *Chem Rev* **2017**, *117* (14), 9674-9754. DOI: 10.1021/acs.chemrev.6b00626
58. Pullumbi, P.; Brandani, F.; Brandani, S., Gas separation by adsorption: technological drivers and opportunities for improvement. *Current Opinion in Chemical Engineering* **2019**, *24*, 131-142. DOI: 10.1016/j.coche.2019.04.008
59. Adil, K.; Belmabkhout, Y.; Pillai, R. S.; Cadiau, A.; Bhatt, P. M.; Assen, A. H.; Maurin, G.; Eddaoudi, M., Gas/vapour separation using ultra-microporous metal-organic frameworks: insights into the structure/separation relationship. *Chem. Soc. Rev.* **2017**, *46* (11), 3402-3430. DOI: 10.1039/c7cs00153c
60. Pascanu, V.; Gonzalez Miera, G.; Inge, A. K.; Martin-Matute, B., Metal-Organic Frameworks as Catalysts for Organic Synthesis: A Critical Perspective. *J. Am. Chem. Soc.* **2019**, *141* (18), 7223-7234. DOI: 10.1021/jacs.9b00733
61. Jiao, L.; Wang, Y.; Jiang, H. L.; Xu, Q., Metal-Organic Frameworks as Platforms for Catalytic Applications. *Adv Mater* **2018**, *30* (37), e1703663. DOI: 10.1002/adma.201703663
62. Foo, M. L.; Matsuda, R.; Kitagawa, S., Functional Hybrid Porous Coordination Polymers. *Chem. Mater.* **2014**, *26* (1), 310-322. DOI: 10.1021/cm402136z
63. García-García, P.; Müller, M.; Corma, A., MOF catalysis in relation to their homogeneous counterparts and conventional solid catalysts. *Chemical Science* **2014**, *5* (8), 2979. DOI: 10.1039/c4sc00265b
64. Chen, T.-H.; Popov, I.; Kaveevivitchai, W.; Miljanić, O. Š., Metal-Organic Frameworks: Rise of the Ligands. *Chem. Mater.* **2014**, *26* (15), 4322-4325. DOI: 10.1021/cm501657d
65. Sun, Q.; Tang, Y.; Aguila, B.; Wang, S.; Xiao, F. S.; Thallapally, P. K.; Al-Enizi, A. M.; Nafady, A.; Ma, S., Reaction Environment Modification in Covalent Organic Frameworks for Catalytic Performance Enhancement. *Angew Chem Int Ed Engl* **2019**, *58* (26), 8670-8675. DOI: 10.1002/anie.201900029
66. Liu, L.; Zhou, T.-Y.; Telfer, S. G., Modulating the Performance of an Asymmetric Organocatalyst by Tuning Its Spatial Environment in a Metal-Organic Framework. *J. Am. Chem. Soc.* **2017**, *139* (39), 13936-13943. DOI: 10.1021/jacs.7b07921
67. Alkas, A.; Cornelio, J.; Telfer, S. G., Tritopic Triazatruxene Ligands for Multicomponent Metal-Organic Frameworks. *Chem. Asian. J.* **2019**, *14* (8), 1167-1174. DOI: 10.1002/asia.201801546
68. Liu, L.; Li, L.; DeGayner, J. A.; Winegar, P. H.; Fang, Y.; Harris, T. D., Harnessing Structural Dynamics in a 2D Manganese-Benzoquinoid Framework To Dramatically Accelerate Metal Transport in Diffusion-Limited Metal Exchange Reactions. *J. Am. Chem. Soc.* **2018**, *140* (36), 11444-11453. DOI: 10.1021/jacs.8b06774

69. Burgun, A.; Coghlan, C. J.; Huang, D. M.; Chen, W.; Horike, S.; Kitagawa, S.; Alvino, J. F.; Metha, G. F.; Sumby, C. J.; Doonan, C. J., Mapping-Out Catalytic Processes in a Metal-Organic Framework with Single-Crystal X-ray Crystallography. *Angew. Chem. Int. Ed.* **2017**, *56* (29), 8412-8416. DOI: 10.1002/anie.201611254
70. Metzger, E. D.; Comito, R. J.; Hendon, C. H.; Dinca, M., Mechanism of Single-Site Molecule-Like Catalytic Ethylene Dimerization in Ni-MFU-4l. *J. Am. Chem. Soc.* **2017**, *139* (2), 757-762. DOI: 10.1021/jacs.6b10300
71. Lucier, B. E. G.; Chen, S.; Huang, Y., Characterization of Metal-Organic Frameworks: Unlocking the Potential of Solid-State NMR. *Acc. Chem. Res.* **2018**, *51* (2), 319-330. DOI: 10.1021/acs.accounts.7b00357
72. Sutrisno, A.; Huang, Y., Solid-state NMR: a powerful tool for characterization of metal-organic frameworks. *Solid State Nucl. Magn. Reson.* **2013**, *49-50*, 1-11. DOI: 10.1016/j.ssnmr.2012.09.003
73. Wong, Y. T. A.; Martins, V.; Lucier, B. E. G.; Huang, Y., Solid-State NMR Spectroscopy: A Powerful Technique to Directly Study Small Gas Molecules Adsorbed in Metal-Organic Frameworks. *Chemistry* **2019**, *25* (8), 1848-1853. DOI: 10.1002/chem.201803866
74. Vukotic, V. N.; Harris, K. J.; Zhu, K.; Schurko, R. W.; Loeb, S. J., Metal-organic frameworks with dynamic interlocked components. *Nat Chem* **2012**, *4* (6), 456-60. DOI: 10.1038/nchem.1354
75. Liu, L.; Chen, Z.; Wang, J.; Zhang, D.; Zhu, Y.; Ling, S.; Huang, K. W.; Belmabkhout, Y.; Adil, K.; Zhang, Y.; Slater, B.; Eddaoudi, M.; Han, Y., Imaging defects and their evolution in a metal-organic framework at sub-unit-cell resolution. *Nat Chem* **2019**, *11* (7), 622-628. DOI: 10.1038/s41557-019-0263-4
76. Gong, Y.-N.; Zhong, D.-C.; Lu, T.-B., Interpenetrating metal-organic frameworks. *CrystEngComm* **2016**, *18* (15), 2596-2606. DOI: 10.1039/c6ce00371k
77. Zhu, R.; Ding, J.; Jin, L.; Pang, H., Interpenetrated structures appeared in supramolecular cages, MOFs, COFs. *Coord. Chem. Rev.* **2019**, *389*, 119-140. DOI: 10.1016/j.ccr.2019.03.002
78. Batten, S. R., Topology of interpenetration. *CrystEngComm* **2001**, *3* (18), 67-72. DOI: 10.1039/b102400k
79. Wu, H.; Yang, J.; Su, Z. M.; Batten, S. R.; Ma, J. F., An exceptional 54-fold interpenetrated coordination polymer with 10(3)-srs network topology. *J. Am. Chem. Soc.* **2011**, *133* (30), 11406-9. DOI: 10.1021/ja202303b
80. Schaate, A.; Roy, P.; Preusse, T.; Lohmeier, S. J.; Godt, A.; Behrens, P., Porous interpenetrated zirconium-organic frameworks (PIZOFs): a chemically versatile family of metal-organic frameworks. *Chemistry* **2011**, *17* (34), 9320-5. DOI: 10.1002/chem.201101015
81. Murray, L. J.; Dinca, M.; Long, J. R., Hydrogen storage in metal-organic frameworks. *Chem. Soc. Rev.* **2009**, *38* (5), 1294-314. DOI: 10.1039/b802256a
82. Ma, S.; Sun, D.; Ambrogio, M.; Fillinger, J. A.; Parkin, S.; Zhou, H. C., Framework-catenation isomerism in metal-organic frameworks and its impact on hydrogen uptake. *J. Am. Chem. Soc.* **2007**, *129* (7), 1858-9. DOI: 10.1021/ja067435s

83. Maji, T. K.; Matsuda, R.; Kitagawa, S., A flexible interpenetrating coordination framework with a bimodal porous functionality. *Nat. Mater.* **2007**, *6* (2), 142-8. DOI: 10.1038/nmat1827
84. Han, S. S.; Jung, D.-H.; Heo, J., Interpenetration of Metal Organic Frameworks for Carbon Dioxide Capture and Hydrogen Purification: Good or Bad? *J. Phys. Chem. C* **2012**, *117* (1), 71-77. DOI: 10.1021/jp308751x
85. Sezginel, K. B.; Asinger, P. A.; Babaei, H.; Wilmer, C. E., Thermal Transport in Interpenetrated Metal–Organic Frameworks. *Chem. Mater.* **2018**, *30* (7), 2281-2286. DOI: 10.1021/acs.chemmater.7b05015
86. Ma, L.; Lin, W., Unusual interlocking and interpenetration lead to highly porous and robust metal-organic frameworks. *Angew Chem Int Ed Engl* **2009**, *48* (20), 3637-40. DOI: 10.1002/anie.200806227
87. Lin, Z.; Zhang, Z. M.; Chen, Y. S.; Lin, W., Highly Efficient Cooperative Catalysis by Co(III) (Porphyrin) Pairs in Interpenetrating Metal-Organic Frameworks. *Angew Chem Int Ed Engl* **2016**, *55* (44), 13739-13743. DOI: 10.1002/anie.201605802
88. Wang, R.; Zhang, M.; Liu, X.; Zhang, L.; Kang, Z.; Wang, W.; Wang, X.; Dai, F.; Sun, D., Tuning the Dimensionality of Interpenetration in a Pair of Framework-Catenation Isomers To Achieve Selective Adsorption of CO₂ and Fluorescent Sensing of Metal Ions. *Inorg. Chem.* **2015**, *54* (13), 6084-6. DOI: 10.1021/acs.inorgchem.5b00934
89. Shekhah, O.; Wang, H.; Paradinas, M.; Ocal, C.; Schüpbach, B.; Terfort, A.; Zacher, D.; Fischer, R. A.; Wöll, C., Controlling interpenetration in metal–organic frameworks by liquid-phase epitaxy. *Nat. Mater.* **2009**, *8* (6), 481–484. DOI: 10.1038/nmat2445
90. Verma, G.; Butikofer, S.; Kumar, S.; Ma, S., Regulation of the Degree of Interpenetration in Metal-Organic Frameworks. *Top Curr Chem (Cham)* **2019**, *378* (1), 4. DOI: 10.1007/s41061-019-0268-x
91. Chae, H. K.; Siberio-Perez, D. Y.; Kim, J.; Go, Y.; Eddaoudi, M.; Matzger, A. J.; O’Keeffe, M.; Yaghi, O. M., A route to high surface area, porosity and inclusion of large molecules in crystals. *Nature* **2004**, *427* (6974), 523-7. DOI: 10.1038/nature02311
92. Deng, H.; Grunder, S.; Cordova, K. E.; Valente, C.; Furukawa, H.; Hmadeh, M.; Gandara, F.; Whalley, A. C.; Liu, Z.; Asahina, S.; Kazumori, H.; O’Keeffe, M.; Terasaki, O.; Stoddart, J. F.; Yaghi, O. M., Large-pore apertures in a series of metal-organic frameworks. *Science* **2012**, *336* (6084), 1018-23. DOI: 10.1126/science.1220131
93. Park, J. H.; Lee, W. R.; Kim, Y.; Lee, H. J.; Ryu, D. W.; Phang, W. J.; Hong, C. S., Interpenetration Control, Sorption Behavior, and Framework Flexibility in Zn(II) Metal–Organic Frameworks. *Cryst. Growth Des.* **2014**, *14* (2), 699-704. DOI: 10.1021/cg401583v
94. Kim, J.; Yang, S.-T.; Choi, S. B.; Sim, J.; Kim, J.; Ahn, W.-S., Control of catenation in CuTATB-n metal–organic frameworks by sonochemical synthesis and its effect on CO₂ adsorption. *J. Mater. Chem.* **2011**, *21* (9). DOI: 10.1039/c0jm03318a
95. Feldblyum, J. I.; Wong-Foy, A. G.; Matzger, A. J., Non-interpenetrated IRMOF-8: synthesis, activation, and gas sorption. *Chem. Commun.* **2012**, *48* (79), 9828-9828. DOI: 10.1039/c2cc34689c
96. Yazdanparast, M. S.; Day, V. W.; Gadzikwa, T., Hydrogen-Bonding Linkers Yield a Large-Pore, Non-Catenated, Metal-Organic Framework with pcu Topology. *Molecules* **2020**, *25* (3). DOI: 10.3390/molecules25030697

97. O'Nolan, D.; Madden, D. G.; Kumar, A.; Chen, K. J.; Pham, T.; Forrest, K. A.; Patyk-Kazmierczak, E.; Yang, Q. Y.; Murray, C. A.; Tang, C. C.; Space, B.; Zaworotko, M. J., Impact of partial interpenetration in a hybrid ultramicroporous material on C₂H₂/C₂H₄ separation performance. *Chem Commun (Camb)* **2018**, 54 (28), 3488-3491. DOI: 10.1039/C8CC01627E
98. Verma, G.; Kumar, S.; Pham, T.; Niu, Z.; Wojtas, L.; Perman, J. A.; Chen, Y.-S.; Ma, S., Partially Interpenetrated NbO Topology Metal–Organic Framework Exhibiting Selective Gas Adsorption. *Cryst. Growth Des.* **2017**, 17 (5), 2711-2717. DOI: 10.1021/acs.cgd.7b00198
99. Ferguson, A.; Liu, L.; Tapperwijn, S. J.; Perl, D.; Coudert, F.-X.; Van Cleuvenbergen, S.; Verbiest, T.; van der Veen, M. A.; Telfer, S. G., Controlled partial interpenetration in metal–organic frameworks. *Nat. Chem.* **2016**, 8 (3), 250-257. DOI: 10.1038/nchem.2430
100. Yang, S.; Lin, X.; Lewis, W.; Suyetin, M.; Bichoutskaia, E.; Parker, J. E.; Tang, C. C.; Allan, D. R.; Rizkallah, P. J.; Hubberstey, P.; et al., A partially interpenetrated metal–organic framework for selective hysteretic sorption of carbon dioxide. *Nat. Mater.* **2012**, 11 (8), 710–716. DOI: 10.1038/nmat3343
101. Ding, J.-G.; Yin, C.; Zheng, L.-Y.; Han, S.-S.; Li, B.-L.; Wu, B., Tuning cadmium coordination architectures using 1,4-bis(1,2,4-triazol-1-ylmethyl)benzene and sulfoisophthalate. *RSC Advances* **2014**, 4 (47), 24594. DOI: 10.1039/c4ra02291b
102. Yao, X.-Q.; Cao, D.-P.; Hu, J.-S.; Li, Y.-Z.; Guo, Z.-J.; Zheng, H.-G., Chiral and Porous Coordination Polymers Based on an N-Centered Triangular Rigid Ligand. *Cryst. Growth Des.* **2011**, 11 (1), 231–239. DOI: 10.1021/cg1011764
103. Xu, H.; Bao, W.; Xu, Y.; Liu, X.; Shen, X.; Zhu, D., An unprecedented 3D/3D hetero-interpenetrated MOF built from two different nodes, chemical composition, and topology of networks. *CrystEngComm* **2012**, 14 (18), 5720-5720. DOI: 10.1039/c2ce25739d
104. Carlucci, L.; Ciani, G.; Maggini, S.; Proserpio, D. M., A New Polycatenated 3D Array of Interlaced 2D Brickwall Layers and 1D Molecular Ladders in [Mn₂(bix)₃(NO₃)₄]·2CHCl₃[bix = 1,4-bis(imidazol-1-ylmethyl)benzene] That Undergoes Supramolecular Isomerization upon Guest Removal. *Cryst. Growth Des.* **2008**, 8 (1), 162-165. DOI: 10.1021/cg700884q
105. Kwon, O.; Park, S.; Zhou, H. C.; Kim, J., Computational prediction of hetero-interpenetration in metal-organic frameworks. *Chem. Commun.* **2017**, 53 (12), 1953-1956. DOI: 10.1039/c6cc08940b
106. Sezginel, K. B.; Feng, T.; Wilmer, C. E., Discovery of hypothetical hetero-interpenetrated MOFs with arbitrarily dissimilar topologies and unit cell shapes. *CrystEngComm* **2017**, 19 (31), 4497-4504. DOI: 10.1039/c7ce00290d

Chapter 2: MUF-9

2.1. INTRODUCTION

The MOFs that serve as the starting material for the investigations in chapters 3 – 6 are named MUF-9 and MUF-10. These MOFs were reported in a 2016 paper⁹⁹ by our research group, and I will summarise the important results from this paper here. I will focus on those aspects of MUF-9 which are most relevant to the work carried out in this thesis.

MUF-9 is formed from the racemic mixture of the biphenyl dicarboxylate (BPDC)-based ligand **L1** (Figure 2.1A) and [Zn₄O] SBUs (Figure 2.1B), the same as those found in the archetypal examples of MOF-5 and IRMOF-9. MUF-9 is a two-fold interpenetrated structure (labelled β) when synthesised in DMF, but when the bulkier dibutylformamide (DBF) is used as the reaction solvent a noninterpenetrated (α) phase is formed, as illustrated in Figure 2.1C. MUF-9 displays a primitive cubic (**pcu**) topology, with unit cell lengths of 17.2 Å, and a pore diameter of approximately 9 Å in the noninterpenetrated phase. The space group for α -MUF-9 is $P\bar{4}3m$, while for β -MUF-9 it is the centrosymmetric $Pm\bar{3}m$.

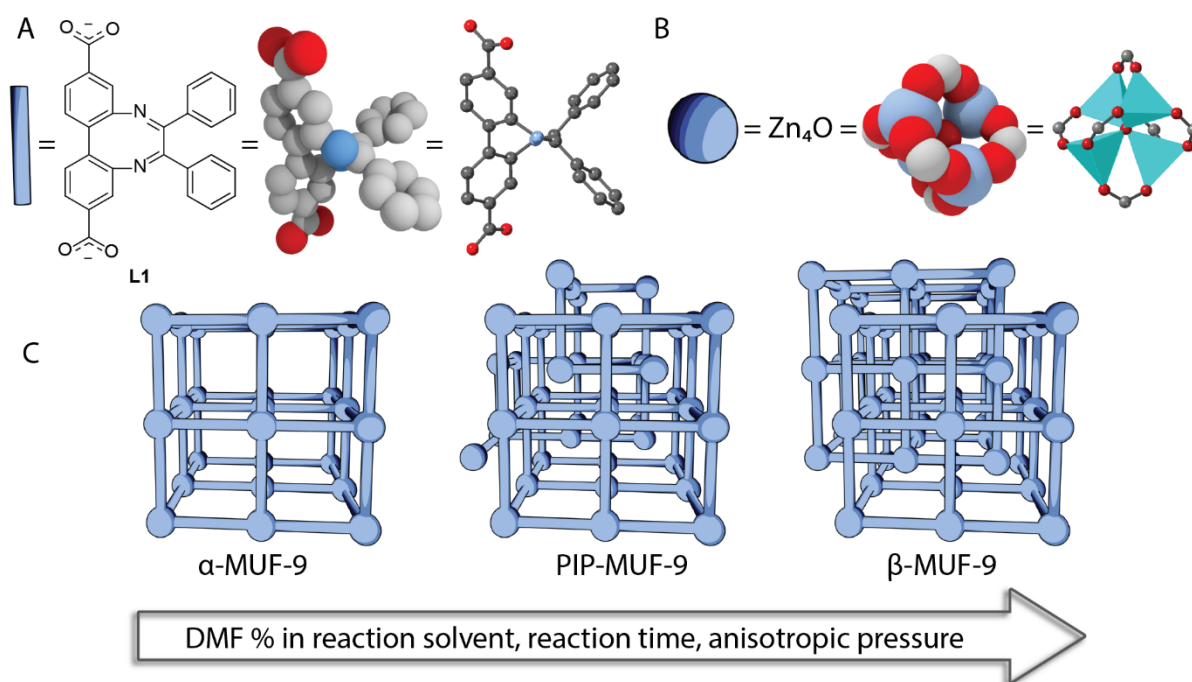


Figure 2.1: MUF-9 structures and components. A) various representations of **L1**: first, a cartoon as a simple blue rod, second, a skeletal structure, third, a 3D atomic representation showing the twisted backbone. Only one enantiomer of **L1** is shown, but MUF-9 is made from the racemic ligand. B) various representations of the cluster in MUF-9, first, a blue sphere used in structural cartoons, second, the formula, third, a 3D visualisation of the tetrahedral, 6-coordinate cluster. C) an illustration of the range of structures from α -MUF-9 to β -MUF-9.

MUF-9 can also be *partially* interpenetrated. What this means is that in some cells of the crystal, a second lattice is present, while in other cells it is not (Figure 2.1C). This phase is labelled PIP-MUF-9. A given sample of PIP-MUF-9 thus has a partial interpenetration percentage (PIP%), which is the proportion of cells which are interpenetrated.

As the interpenetration percentage of MUF-9 increases, the phase change can be tracked qualitatively by PXRD (Figure 2.2) with the decrease in intensity of the peak at $2\theta = 5.2^\circ$, while the peak at 7.3° increases in intensity. These peaks correspond to the (100) and (110) reflections respectively. Their intensities are thus most prominently determined by the proportion of cells which are interpenetrated. As the PIP% increases, the space group approximates that of the β phase, in which the (100) reflection is systematically absent. It is important that crystals are oriented randomly during the PXRD measurement to make this determination.

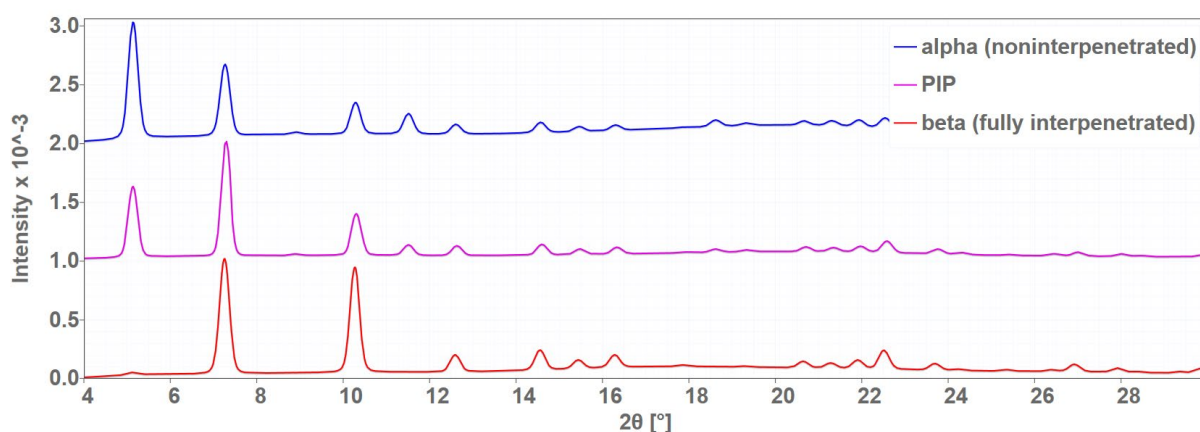


Figure 2.2: PXRD patterns of α - (top, blue), PIP- (middle, purple), and β -MUF-9 (bottom, red).

This diagnostic use of PXRD is the most important and consistent characterisation tool used throughout this entire work. In many experiments, significant information about the behaviour of MUF-9 in various conditions is gained simply from the ratio of those first two peaks. This was always the first characterisation method we would look at for any attempt at preparing a new material, in the way an organic synthetic chemist might check a TLC to see if something is happening in their reaction.

Using reaction solvents with intermediate size between DMF and DBF, including *N,N*-diisopropylformamide (DIF), result in a different phase, labelled γ -MUF-9, illustrated in **Figure 2.3**. This is a non-interpenetrated framework with a **bsn** topology, with cell dimensions of $a = b = 32.63 \text{ \AA}$ and $c = 17.13 \text{ \AA}$, in the tetragonal space group $I-4_2d$. In the **bsn** net (named for the bonding in the β phase of Sn), nodes are six-coordinate just as they are as in **pcu**, but the connectivity is different. Along the xy plane, the nodes form a square grid, but the connectivity between the layers of grids alternates direction. This connectivity results, given the constraint of fixed ligand and cluster sizes, in angles between ligands deviating from the 90° of the cubic lattices to 75.3° in one direction and 104.7° in the other. This means γ -MUF-9 has a structure where the ligands are brought closer together than in α -MUF-9, but further apart than in β -MUF-9, which makes sense given the intermediate solvent size.

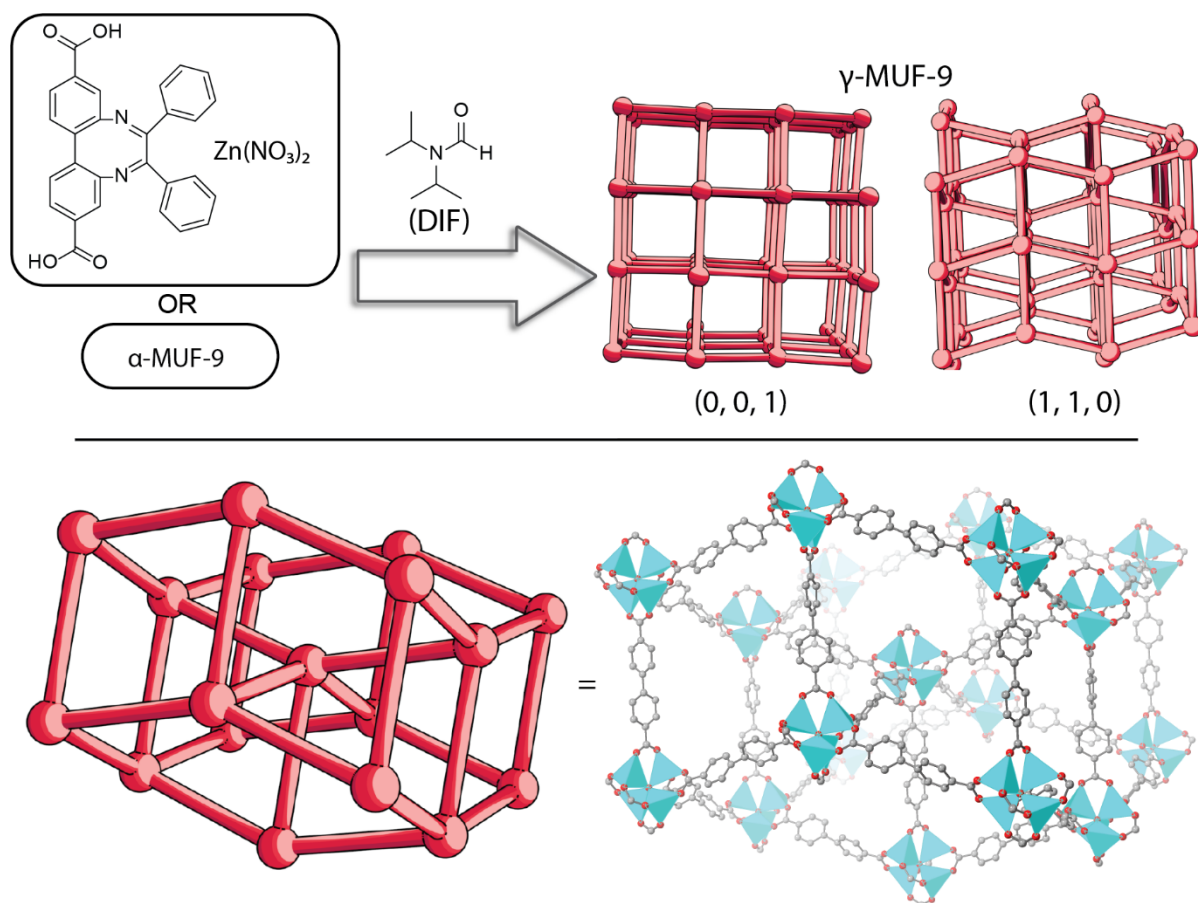


Figure 2.3: The structure of γ -MUF-9. Top: γ -MUF-9 can be prepared both by direct synthesis in DIF, as well as by heating α -MUF-9 in DIF. Bottom: a close-up view of a small section of the γ -MUF-9 lattice shown as both a cartoon representation and a ball-and-stick representation, from which side chains and hydrogens have been removed for clarity.

We originally anticipated that the bulky side chain on **L1** would prevent it from forming interpenetrated structures, as observed for many related ligands. One such example is a boc-protected proline-functionalised BPDC derivative used in earlier work by our group to synthesise noninterpenetrated frameworks³⁵. However, the pendant phenyl rings on the side chain of **1** form moderate π - π interactions with the backbone of the neighbouring lattice⁹⁹ which promote the formation of the interpenetrated structure. The non-interpenetrated structure (α -MUF-9) is therefore a metastable form of this material.

Figure 2.4 illustrates the interactions between the lattices in MUF-9. The pendant phenyl rings of the primary lattice wrap around the backbone of the secondary ligand, and the pendant phenyl rings of the secondary ligand wrap around the backbone of the next ligand along in the primary lattice, making a total of four offset face-to-face

noncovalent interactions between aromatic groups, for each ligand in the secondary lattice, one for each phenyl ring in the ligand.

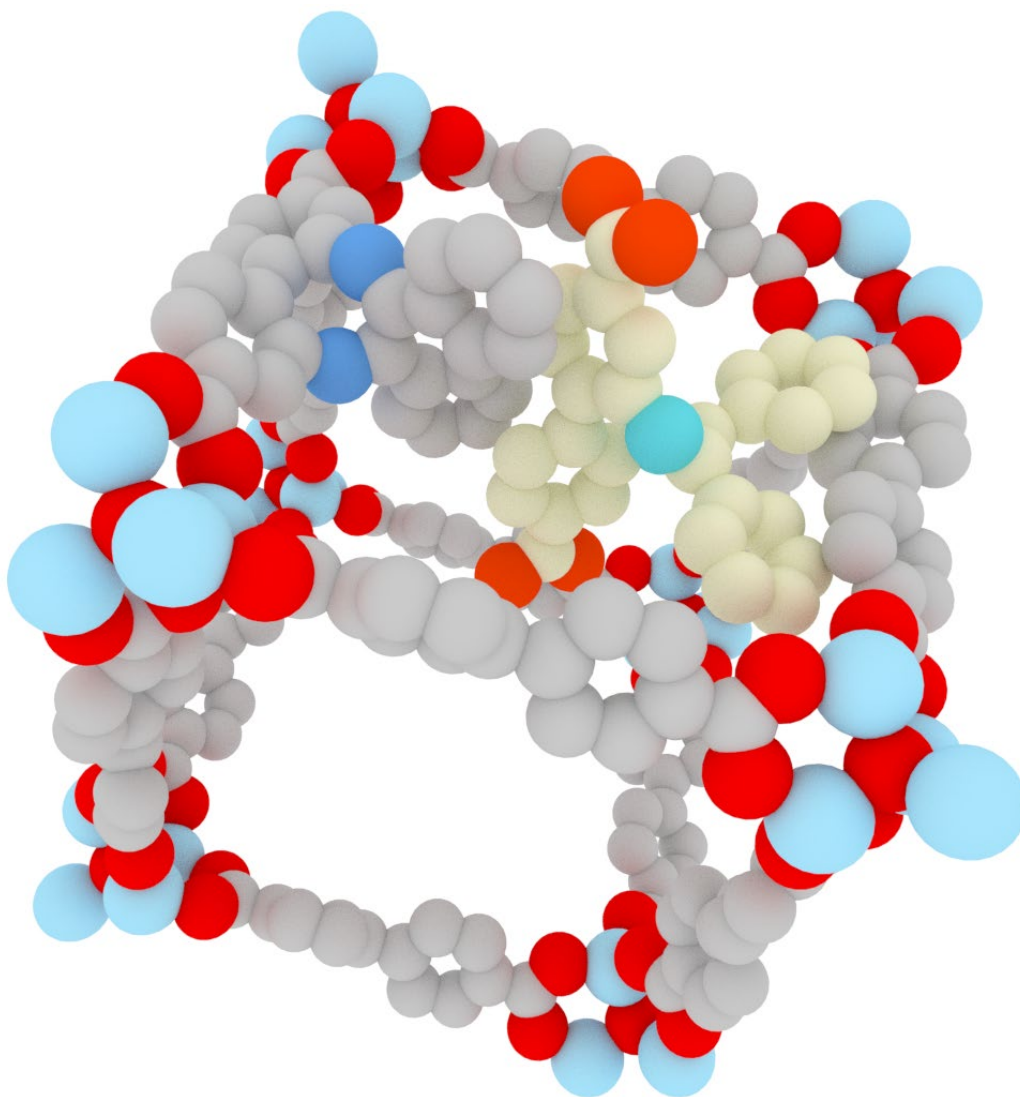


Figure 2.4: An illustration of the contacts between the lattices in MUF-9. Side chains have been removed from most ligands, and all hydrogens have been removed for clarity. One cell of the primary lattice is shown, where grey atoms are carbon, dark blue nitrogen, red oxygen, and light blue zinc. One ligand of an interpenetrating (secondary) lattice is shown in different colours for clarity, where yellow atoms are carbon, teal nitrogen, orange oxygen.

The interaction described above, with the side chain of each of two neighbouring ligands pointing in the same direction is the most favourable orientation for the ligands. This orientation was assumed for all pairs of ligands when calculating the ‘interpenetration enthalpy’ of 259 kJ mol^{-1} per $[\text{Zn}_4\text{O}]$ unit.

However, each ligand can be in any of four orientations (Figure 2.5A), and three of those are sterically compatible with any one orientation of their neighbour (Figure

2.5B) if the side chain of the neighbouring ligand is directed towards it. Figure 2.5C shows a single lattice with all ligands oriented in only one direction, which leads to pores of approximately 4 Å diameter (Figure 2.5D) in β -MUF-9.

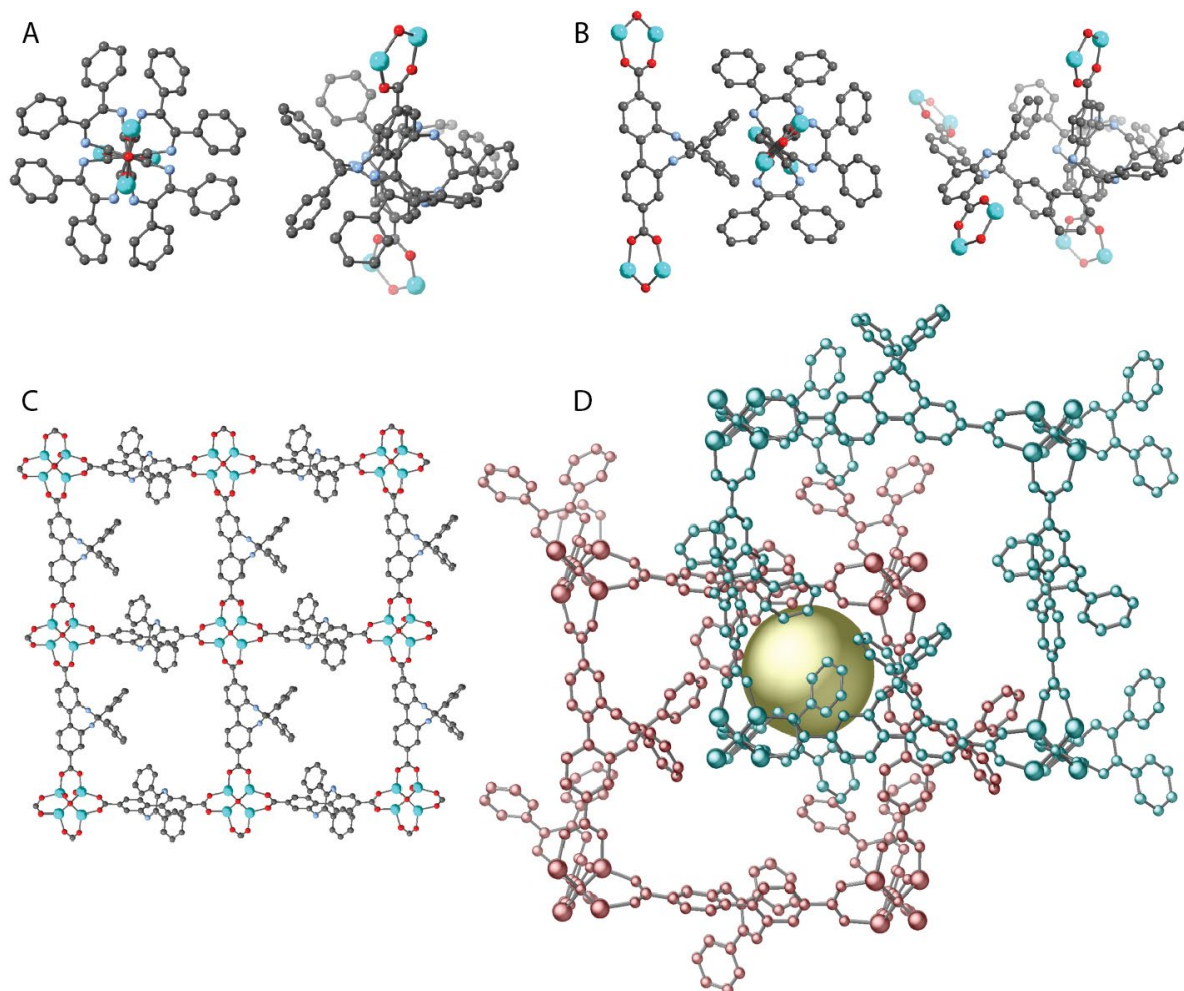
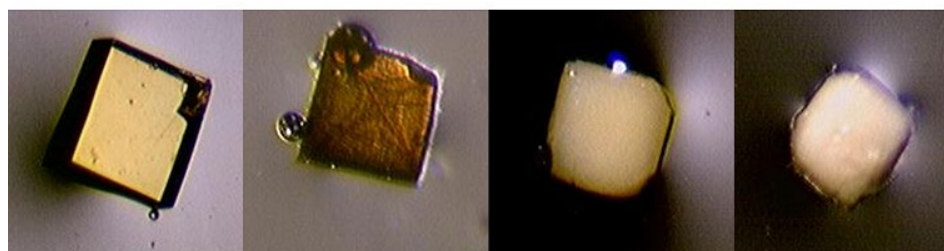


Figure 2.5: A) At any given site, **L1** can take one of four orientations, and B) each one of those orientations is compatible with three orientations of the neighbouring ligand. C) An illustration of a single lattice where ligands are oriented in the same direction. D) Where ligands in both lattices are oriented in the same direction the pore size in β -MUF-9 is approximately 4 Å, indicated by the yellow sphere.

We think that this situation predominates, but the symmetry of the overall structure indicates that all orientations are present throughout. At the putative boundaries between the domains where ligands are aligned with each other, there may be (slightly) smaller and larger pores present.

Because β -MUF-9 is the thermodynamic product, α - and PIP-MUF-9 are metastable. They display a behaviour we dubbed ‘autocatenation’ in which, through a variety of stimuli, they can be induced to transform into the fully interpenetrated phase in a

single-crystal-to-single-crystal process. These stimuli include heating in DMF or DEF, removal of the solvent trapped in the framework pores, heating in moderate concentrations of mineral or carboxylic acids, and anisotropic physical pressure such as grinding. **Figure 2.6** shows some optical micrographs of an individual single crystal which was induced to undergo autocatenation by heating in DMF over time.



Heating time:	0 hours	18 hours	36 hours	60 hours
PIP level:	0 %	27 %	92 %	100 %
Size (mm):	$0.50 \times 0.47 \times 0.34$	$0.48 \times 0.47 \times 0.29$	$0.45 \times 0.44 \times 0.28$	$0.43 \times 0.41 \times 0.25$
Volume (mm³):	0.080	0.065	0.055	0.044

Figure 2.6: Optical micrographs showing a crystal undergoing autocatenation from α -MUF-9 to β -MUF-9 via PIP-MUF-9 by heating in DMF. Despite losing optical transparency, the crystal diffracts well at all stages of the conversion. PIP levels correspond to the occupancy of the interpenetrating lattice, as determined by SCXRD. Figure reproduced from reference 1.

The autocatenation of MUF-9 from the α to the β phase is a single-crystal-to-single-crystal transformation, so the crystals do not dissolve and reform. Each crystal shrinks to about half its original size, as expected for one lattice rearranging to two lattices. The intensity of high angle X-ray diffraction peaks as the phase change progresses *increases*. That is, the material becomes more highly ordered over the course of this process. This trend will be observed throughout the following three chapters: materials with higher PIP% values are better ordered and give better diffraction.

The results presented in this chapter are some new characterisations of the behaviour of L1 and MUF-9. Many of these provide a foundation for the experimental work in later chapters and serve as control experiments – they establish the conditions in which it might be possible to work with MUF-9 as a starting material for further stepwise syntheses. Beyond that, the results here also give some additional basic insights into the behaviour of this rather unusual material.

2.2. RESULTS

2.2.1. Improved and varied syntheses of α -MUF-9

The outcome of a MOF synthesis reaction with $\text{Zn}(\text{NO}_3)_2 \cdot 4\text{H}_2\text{O}$ and **L1** can vary significantly with the batch of the ligand. This is unsurprising as trace additives are known to influence^{107, 108} crystallisation for a variety of MOFs. To overcome this, some effort was dedicated to producing **L1** as pure as possible, so that the additives could be carefully controlled. The procedure for producing **L1** (section 2.4.1) involves the coupling of benzil and 2,2'-diamino-4,4'-biphenyldicarboxylic acid in 1,4-dioxane with added trifluoroacetic acid instead of in glacial acetic acid, significantly increasing the yield over the literature procedure¹⁰⁹ (from ~25 % to over 80 %). A small excess of benzil (1.3 equivalents) is used to ensure that all the 2,2'-diamino-4,4'-biphenyldicarboxylic acid is consumed. This aids purification of the ligand, because benzil is significantly more soluble in medium-polarity organic solvents than either the carboxylic acid starting material or the ligand product.

For most purposes in Chapters 3 – 6, large single crystals are desirable, as they make it possible to obtain good quality single-crystal X-ray diffraction datasets, which are critical when dealing with the complex structures of hetero-interpenetrated MOFs. In general, MOFs have very low density due to their pores. This means that compared to a small molecule crystal of equivalent size, there is less ordered material to diffract X-rays, and therefore larger crystals are required for a good signal-to-noise ratio in a single-crystal diffraction experiment.

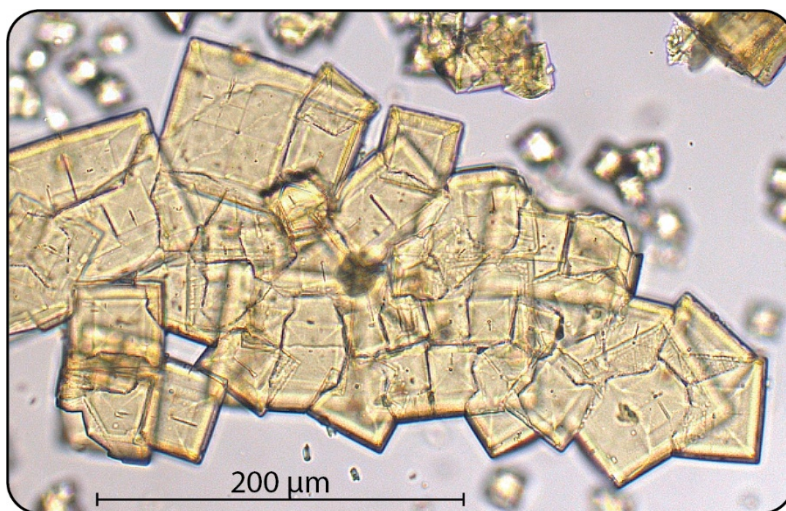


Figure 2.7: An optical micrograph of "rafts" of intergrown α -MUF-9

With some screening, it was found that the addition of 1 mg mL^{-1} of 2-fluorobenzoic acid to the synthetic mixture resulted in optimal crystals, with a size range of about $0.15 - 0.4 \text{ mm}$ in each dimension. This also reduced the formation of "rafts" of intergrown crystals (Figure 2.7) but did not avoid them entirely.

2.2.1.1. *Synthesis of microcrystalline powder MUF-91*

We also wanted to prepare smaller crystals of α -MUF-9, to be able to test the effect of the crystallite size of the starting material on the results of the syntheses in chapters 3 and 4.

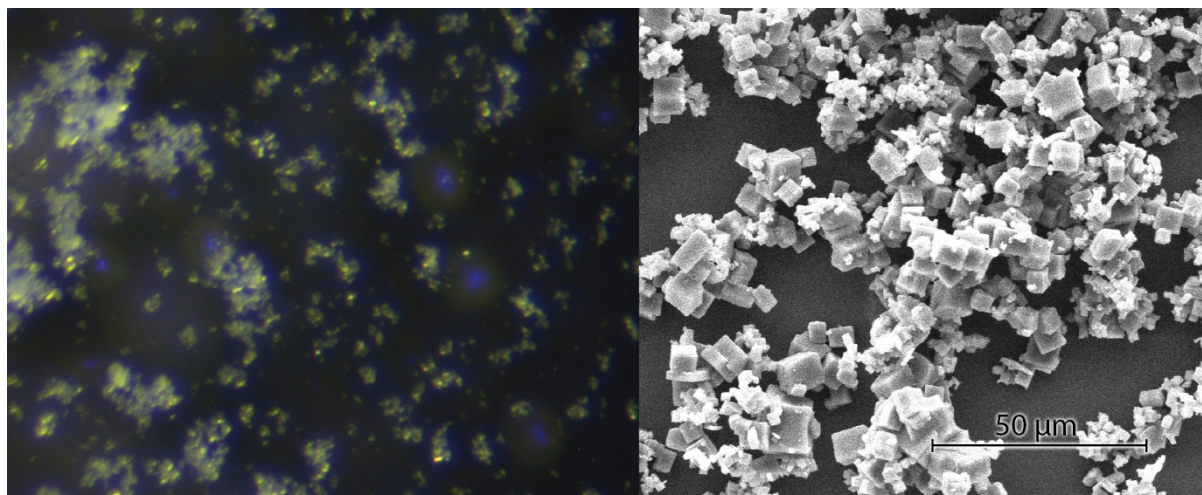


Figure 2.8: Images of microcrystalline powder of MUF-91. Left, a dark-field optical micrograph. Right, an SEM image.

Microcrystalline samples could be produced by adding H_2O ($5 - 10 \text{ } \mu\text{L}$) per vial and agitating the vial during synthesis. These crystals were too small for SCXRD analysis,

but were used to further characterise the hetero-interpenetrated materials presented in Chapters 3 and 4 (section 3.6.1.2, and sections 4.3. 4.4.). Their size range is about 1 – 5 μm , as shown in Figure 2.8.

2.2.2. Rapid synthesis of MUF-9 nanocrystals at different temperatures

Many $[\text{Zn}_4\text{O}(\text{L}_3)]$ MOFs, where L is a ditopic carboxylate linker such as 1,4-benzenedicarboxylic acid (bdc) or bpdc, can be synthesised as nanocrystals at room temperature^{67, 110, 111} by mixing solutions of ligand with zinc(II) acetate hexahydrate. With the more basic acetate counterion (compared to nitrate, which is typically used in solvothermal syntheses), the ligand is rapidly deprotonated and the solution has a high nucleation rate. The MOF can later be heated to improve its crystallinity.

In attempting to synthesise nanocrystals of α -MUF-9 at ambient temperatures, the formation of PIP-MUF-9 was observed even at those rapid time scales. Knowing that temperature is a factor^{112, 113} in the control of interpenetration, I repeated this experiment at a lower temperature, and obtained α -MUF-9. Then, we sought to prepare the full range of PIP-MUF-9 through varying the temperature (Figure 2.9), to add another method to the existing list of techniques for controlling interpenetration in this remarkable MOF.

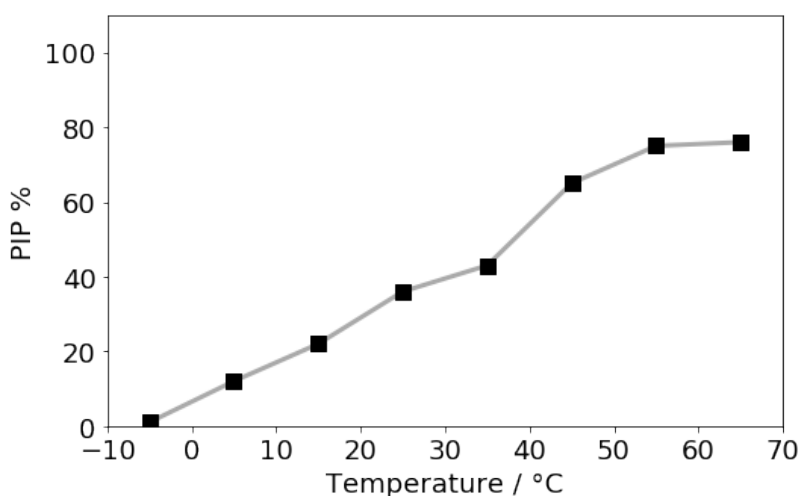


Figure 2.9: A plot of the PIP % of nanocrystalline MUF-9 as it varies with synthesis temperature.

The synthetic method for preparing nanocrystalline MUF-9 can be found in section 2.4.2.3, and the PXRD patterns in section 2.4.3.4. Figure 2.9 shows how the PIP% of samples of nanocrystalline MUF-9 increases approximately linearly with temperature, reaching a plateau of about 75% interpenetration, at 55 °C.

2.2.3. Behaviour of MUF-9 precursors in different solvents

Having already observed that different phases of MUF-9 could be obtained through solvothermal synthesis in various formamide solvents, we explored syntheses using the same starting materials in a few other solvents as well.

Table 2.1: Results of MOF syntheses with **L1** and $\text{Zn}(\text{NO}_3)_2 \cdot 4\text{H}_2\text{O}$ in various formamide solvents at 85°C.

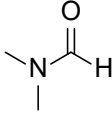
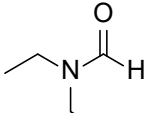
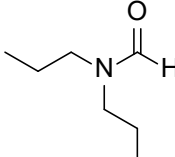
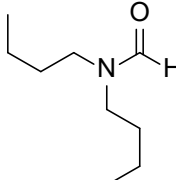
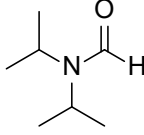
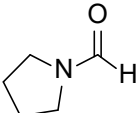
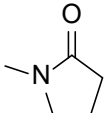
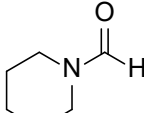
Solvent(s)	 DMF	 DEF	 DPF	 DBF	 DIF
	 NFP	 NMP			 NFPip
MOF obtained	β -MUF-9		PIP-MUF-9	α -MUF-9	γ -MUF-9

Table 2.1 shows the results of that study: ‘MOF obtained’ indicates the phase at the onset of crystallisation, although just as with MUF-9 in DBF, the PIP% of MUF-9 in DPF continues to increase over time if the reaction conditions are maintained. PXRD patterns are in section 2.4.3.3, page 52.

2.2.4. Behaviour of α -MUF-9 when heated in various solvents

Because the aim of the following chapters is to produce new materials from (without altering the existing structure of) α -MUF-9, the effect of different solvents on MUF-9 was investigated. For each condition, a few crystals of α -MUF-9 were added to a 2 mL vial, and 1 mL of the respective solvent was added. Each vial was then placed in an 85 °C oven for the indicated time and a PXRD pattern collected (Figure 2.10).

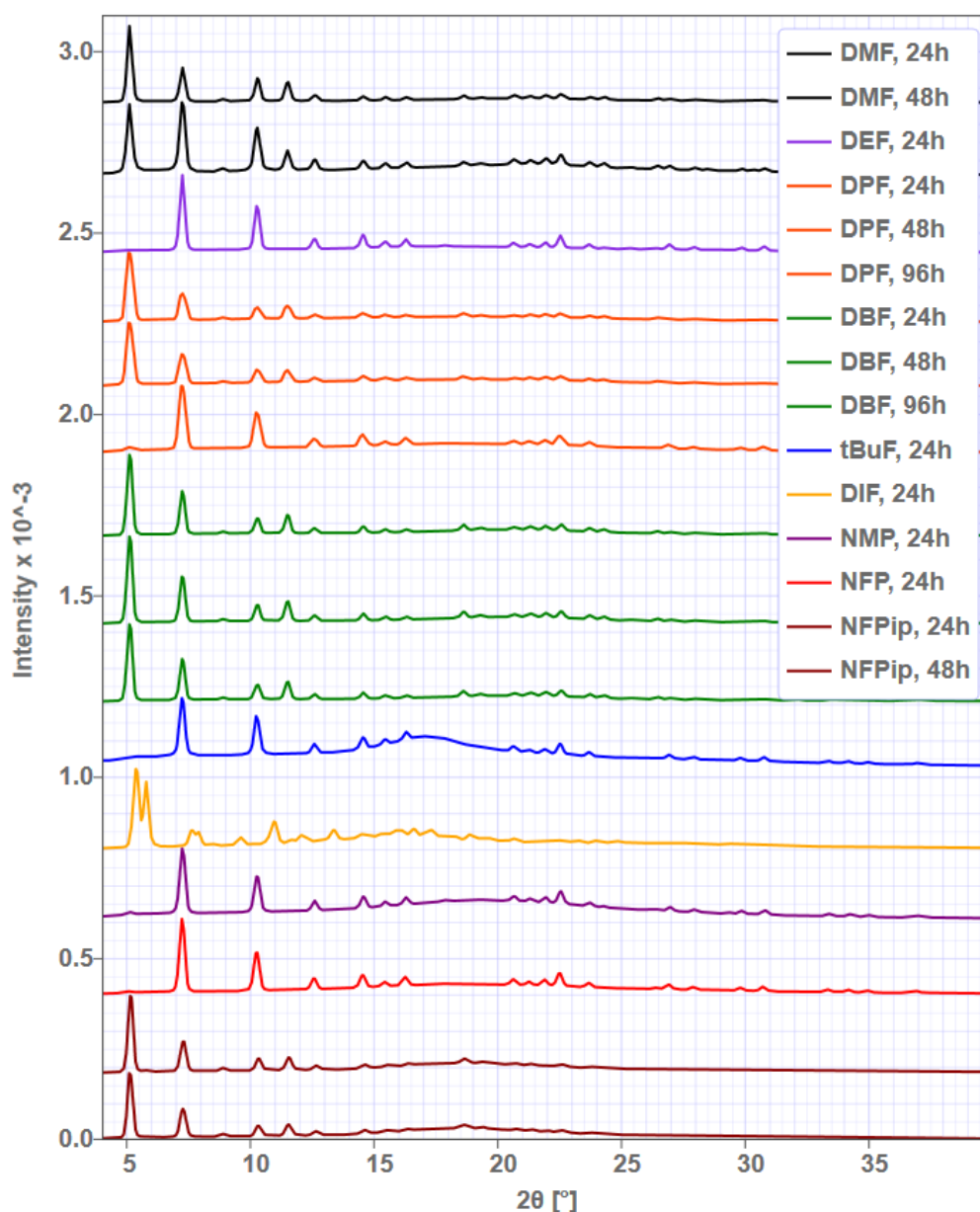


Figure 2.10: PXRD patterns of MUF-9 after exposure to various solvents at 85 °C for different periods of time. DMF = N,N'-dimethylformamide, DEF = N,N'-diethylformamide, DBF = N,N'-dibutylformamide, tBuF = N-tert-Butylformamide, DIF = N,N'-diisopropylformamide, NMP = N-methylpyrrolidinone, NFP = N-formylpyrrolidine, NFPip = N-formylpiperidine.

In most cases, the MOF changed to the phase which is obtained from direct synthesis in that solvent. DMF (as previously observed), DEF, tBuF, NMP, and NFP all resulted in a structural change to the fully interpenetrated β phase. N,N-diisopropylformamide (DIF, the yellow diffractogram in Figure 2.10) results in a change of phase to γ -MUF-9, while N-formylpiperidine (NFPip) does not result in a change of phase in the time period studied, even though γ -MUF-9 is obtained from direct synthesis in NFPip. DBF was the only solvent out of these which resulted in the α phase being formed.

2.2.5. Metal and ligand exchange in MUF-9

Metal and ligand exchange are common techniques to prepare otherwise inaccessible MOFs. It is often used when a target MOF cannot be prepared directly because the desired MOF components are sensitive to the MOF formation conditions (high temperature and mildly acidic or basic solutions), since exchange can often be observed under milder conditions than synthesis.

It is worthwhile to determine the conditions in which a MOF can undergo ligand or metal-exchange for its own sake, but in this work the purpose of these experiments are to serve as controls for the work in the following two chapters. There, MOFs will be exposed to solutions of ligands and metal salts, but the exchange of these components into the original lattice is not desired. These experiments have been conducted to establish an upper bound on the amount of exchange which we can expect MUF-9 to undergo in conditions like the ones used here.

2.2.5.1. *Exchange of cobalt(II) into α -MUF-9*

Samples of α -MUF-9 were exposed to solutions of $\text{Co}(\text{NO}_3)_2 \cdot 6\text{H}_2\text{O}$ in DBF at concentrations of 2 mg mL^{-1} and 20 mg mL^{-1} , and heated in each solution in a dry bath set to 95°C , then the samples analysed by PXRD, then digested with DCl in DMSO and analysed with flame AAS.

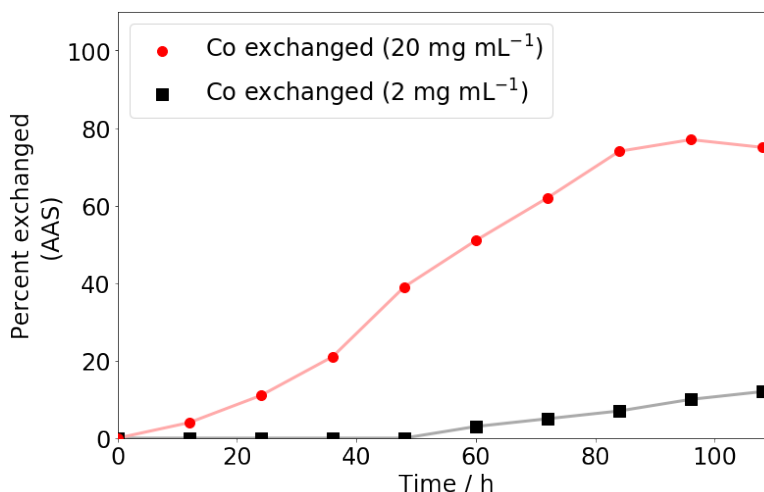


Figure 2.11: Plot of percentages of zinc(II) replaced by cobalt(II) in α -MUF-9 over time. Black squares represent percentage exchange at 2 mg mL⁻¹ cobalt nitrate concentration while red circles represent exchange at 20 mg mL⁻¹ cobalt nitrate concentration.

Unsurprisingly, concentration is hugely important in determining the rate of replacement of zinc(II) by cobalt(II) in α -MUF-9. At a concentration of 20 mg mL⁻¹ cobalt(II) nitrate hexahydrate, significant exchange is observed: Figure 2.11 shows that about half of the zinc(II) is replaced after two days, and a plateau is reached after four days, when three out of the four zinc ions have been replaced by cobalt – the [Zn₄O] clusters have become ZnCo₃O clusters. This is consistent with literature¹¹⁴ on many other [Zn₄O] MOFs.

At a concentration of 2 mg mL⁻¹ cobalt(II) nitrate hexahydrate, very low exchange is observed for the first 50 hours of the experiment. 2 mg mL⁻¹ ought therefore to be a safe concentration to use when trying to prepare new materials from α -MUF-9 in shorter timeframes.

2.2.5.2. Exchange of other ligands into MUF-9

Samples of α -MUF-9 were prepared by a standard method. Solutions of 0.5 mg mL⁻¹ BPDC or 1 mg mL⁻¹ BPDC-NH₂ with 3 mg mL⁻¹ 2-fluorobenzoic acid were prepared in DBF and added to vials of α -MUF-9. As established in section 2.2.4, no autocatenation is expected when heating α -MUF-9 in this solvent at this temperature. The vials were placed in a dry bath set to 85 °C and the solution replaced every 6 hours. PXRD patterns were obtained from each sample, which confirmed that the added ligand also

did not result in autocatenation or other phase changes. Then, the samples were washed with DMF (2 mL \times 3) and acetone (4 mL \times 5) and dried under high vacuum. Each sample was digested in 0.2 M NaOD in D₂O for ¹H NMR spectroscopic analysis.

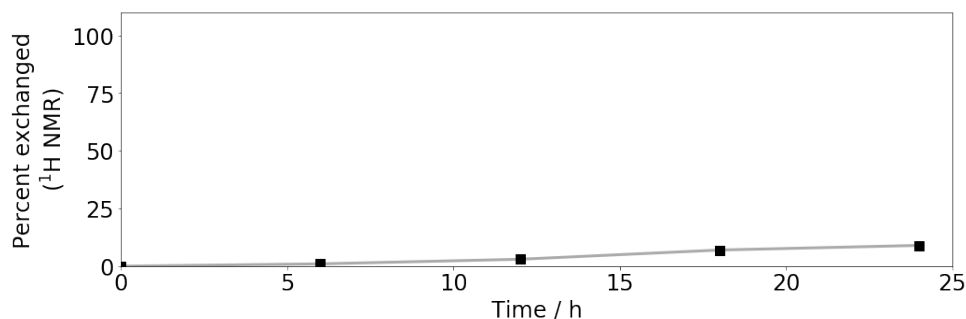


Figure 2.12: Plot of percentages of **L1** replaced by BPDC in α -MUF-9 as determined by ¹H NMR spectroscopy of digested samples, over time.

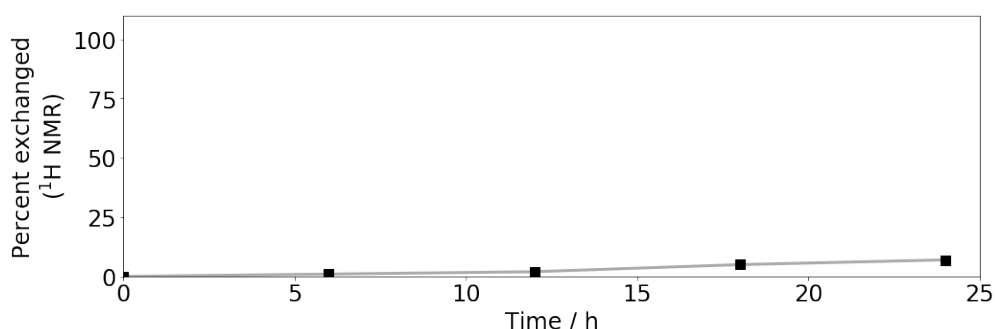


Figure 2.13: Plot of percentages of **L1** replaced by BPDC-NH₂ in α -MUF-9 as determined by ¹H NMR spectroscopy of digested samples, over time.

These plots, Figure 2.14 and Figure 2.15, show a similar amount of **L1** replaced by another ligand, BPDC in the former case, and BPDC-NH₂ in the latter case. This suggests that the NH₂ group doesn't significantly influence the rate of ligand exchange. In both cases, only a few percent of the **L1** is exchanged in the first few hours of the reaction, reaching roughly 7% after 24 hours. 7% of the primary lattice being replaced is higher than desirable in our proposed hetero-interpenetrated MOFs. However, when we try to use additional ligand to construct a secondary lattice, that additional ligand will be consumed during the reaction. That should reduce the amount of ligand available to replace the original framework. 7% is therefore an absolute upper bound of the amount of ligand exchange we expect to see.

2.3. CONCLUSIONS

In this chapter we have explored some of the interesting behaviour of MUF-9. Many of the results here aren't easily made to tell a neat story on their own, but simply expand our understanding of this unusual MOF.

The results from section 2.2.4, show that α -MUF-9 can change phase when heated in various solvents, which implies that the ligand-cluster bond remains somewhat labile at high temperatures. This will be important to keep in mind when determining the appropriate reaction conditions if we want to keep our primary MUF-9 lattice intact. Generally, MUF-9 is converted into whichever phase is obtained from direct synthesis in that solvent, except in the case of NFPip, which doesn't cause a phase change in the time period studied.

The most important thing these results do is set the stage for the following four chapters of this thesis. In order to use MUF-9 as a starting material for further reactions, we need to be confident about its behaviour under a range of conditions we might use for those reactions. Specifically, we want to know that the α -MUF-9 lattice itself will not be altered by the solvent, and that the components will not be replaced by the added ones. For this purpose, there are two key takeaways from sections 2.2.4 and 2.2.5 above:

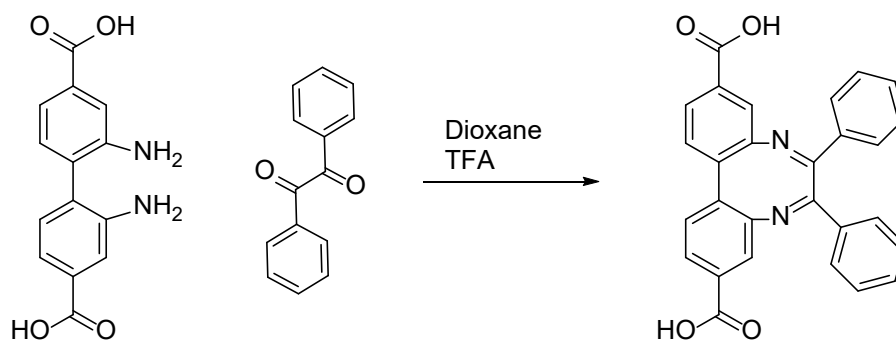
- It's possible to expose α -MUF-9 to temperatures up to at least 95 °C in several solvents, without causing the autocatenation behaviour observed when that solvent is DMF.
- It's possible to expose α -MUF-9 to low or moderate concentrations of alternative ligands and metals salts without them replacing large amounts of the original components or causing other changes to the structure.

These two results address two of the biggest potential roadblocks in the use of α -MUF-9 as the starting material for a hetero-interpenetrated framework. If significant exchange of new components into the original framework of α -MUF-9 or

autocatenation of the original framework had been observed, then those conditions would not be suitable for producing distinct hetero-interpenetrated frameworks. These experiments have established an upper bound for these background processes, and we can therefore be somewhat confident that it will be possible to add new components to α -MUF-9 in such a way that they go to construct a distinct secondary lattice, if those new components and the conditions under which they are introduced meet some criteria for suitability. Those criteria will be established in chapters three and four.

2.4. EXPERIMENTAL DETAILS AND SUPPLEMENTARY DATA

2.4.1. Synthesis of L1



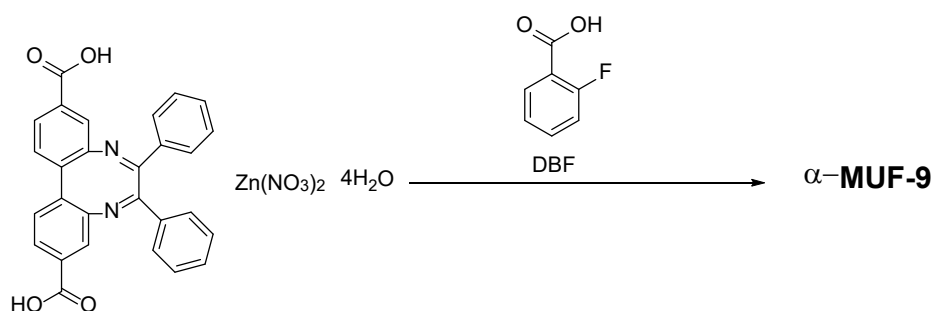
Scheme 2.1: Synthesis of L1

2,2'-Diaminobiphenyl-4,4'-dicarboxylic acid (300 mg, 1.10 mmol) and benzil (300 mg, 1.43 mmol) in dioxane (7.2 mL) and TFA (0.8 mL) were heated to 180 °C by microwave irradiation for 2 hours. The reaction mixture was transferred to a centrifuge tube and water (25 mL) was added to precipitate the product. The solid was collected by centrifugation at 4000 rpm for 15 minutes. The crude product was dissolved in 1 M aqueous NaOH (10 mL), and washed with CH₂Cl₂ (5 mL × 3). 2 M aqueous HCl was then added dropwise until a pale-yellow precipitate formed, which was collected by filtration and washed with H₂O to yield **L1** (420 mg, 1.10 mmol, 85%).

Characterisation data matched those previously reported.^{99, 109}

2.4.2. Synthesis of α-MUF-9

2.4.2.1. Large single crystals



Scheme 2.2: Synthesis of α-MUF-9

L1 (90 mg, 201 μmol), $\text{Zn}(\text{NO}_3)_2 \cdot 4\text{H}_2\text{O}$ (160 mg, 611 μmol , 3.04 eq.), and 2-fluorobenzoic acid were dissolved in DBF (10 mL) which was then split between ten 4 mL vials with PTFE-lined septum caps. The vials were heated to 85 °C in a convection oven for seven hours, then removed, allowed to attain room temperature, then the crystals washed with DBF.

2.4.2.2. *Microcrystals*

L1 (36 mg) and $\text{Zn}(\text{NO}_3)_2 \cdot 4\text{H}_2\text{O}$ (64 mg) were dissolved in DBF (4 mL) with H_2O (10 μL) in a 25 mL Schott bottle and heated in an 85°C oven for 6 hours, shaking the mixture every hour. The resulting small crystals were then transferred to a 4 mL vial which was packed into a 50 mL centrifuge tube and centrifuged at 1000 rpm for 30 seconds at speed.

2.4.2.3. *Rapid synthesis of MUF-9 nanocrystals*

$\text{Zn}(\text{OAc})_2 \cdot 2\text{H}_2\text{O}$ (160 mg, 0.71 mmol) was dissolved in DBF (5 mL). Benzil-bpdc (90 mg, 0.21 mmol) was dissolved separately in DBF (5 mL). The solutions were allowed to equilibrate in a temperature-controlled bath for 15 minutes. Metal salt solution (0.5 mL) was added dropwise to ligand solution (0.5 mL) with shaking, and the mixture left stirring at for 2 hours. The pale yellow powder that formed was collected by centrifugation (1 minute at 14k rpm) and the supernatant removed and replaced with clean dry DBF.

2.4.3. PXRD patterns

2.4.3.1. PXRD patterns of α -MUF-9 exposed to cobalt(II)

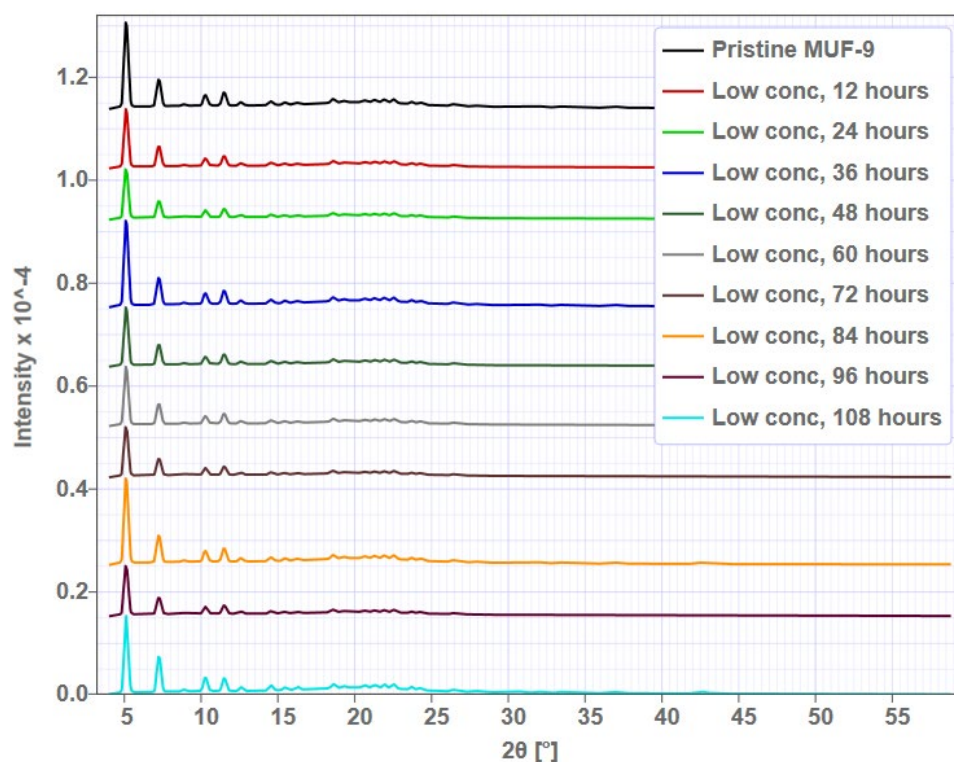


Figure 2.14: PXRD patterns of α -MUF-9 exposed to $2 \text{ mg mL}^{-1} \text{ Co(NO}_3)_2 \cdot 6\text{H}_2\text{O}$ in DBF at 95°C .

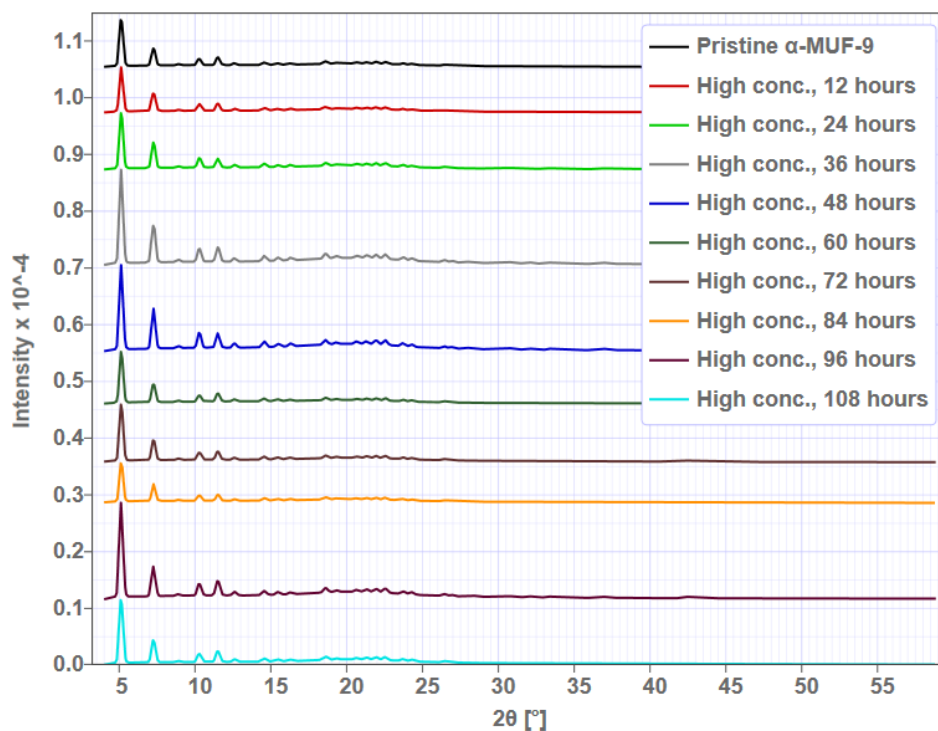


Figure 2.15: PXRD patterns α -MUF-9 exposed to $20 \text{ mg mL}^{-1} \text{ Co(NO}_3)_2 \cdot 6\text{H}_2\text{O}$ in DBF at 95°C .

2.4.3.2. PXRD patterns of α -MUF-9 exposed to BPDC and BPDC-NH₂

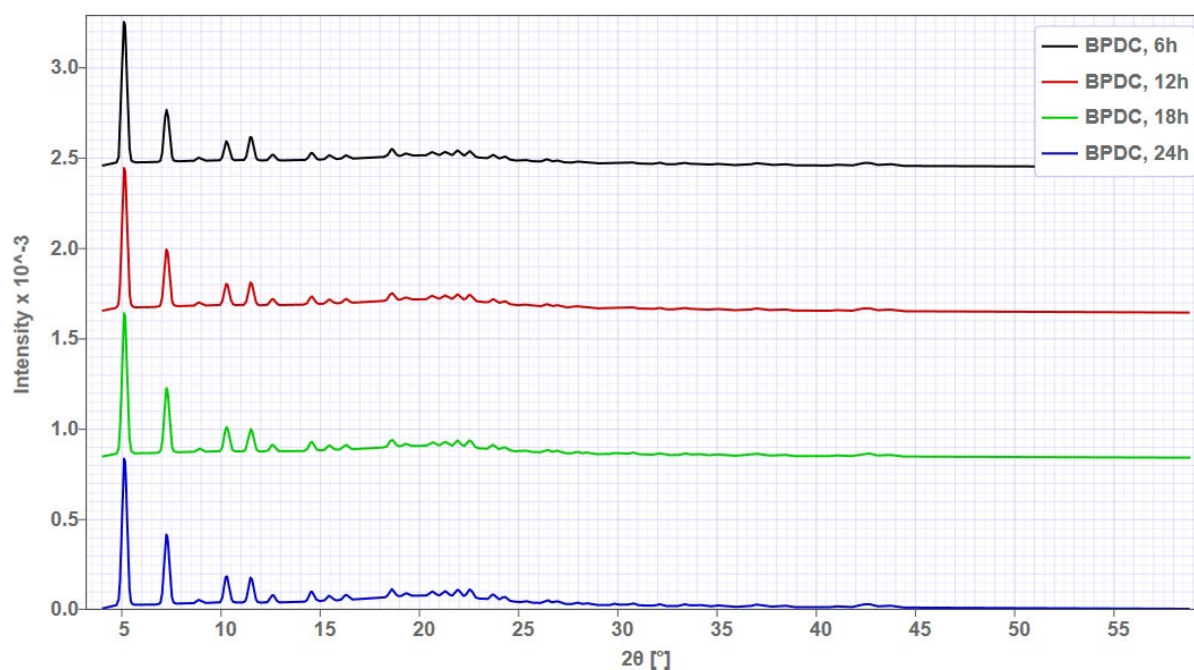


Figure 2.16: PXRD patterns of α -MUF-9 exposed to BPDC

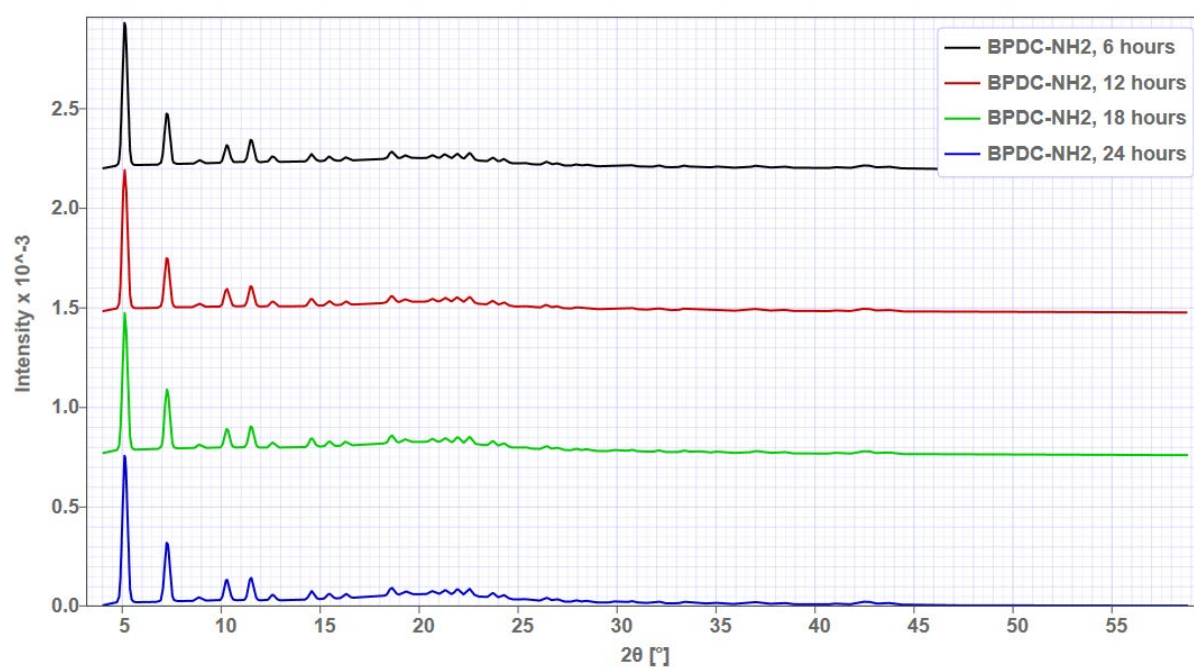


Figure 2.17: PXRD patterns of α -MUF-9 exposed to BPDC-NH₂

2.4.3.3. PXRD patterns of MOFs obtained from L1 in different solvents

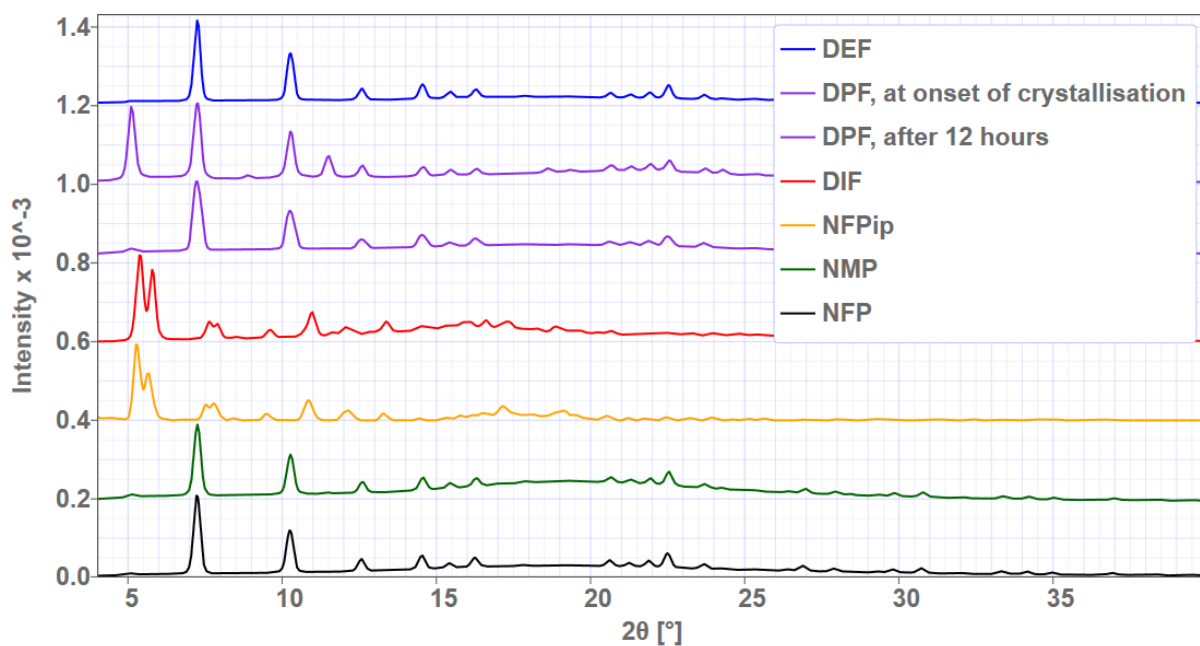


Figure 2.18: PXRD diffractograms of MOF synthesis reactions in a variety of formamide solvents, using the same concentrations of starting materials as the standard syntheses of α - and β -MUF-9.

2.4.3.4. *PXRD patterns of nanocrystalline MUF-9 synthesised at varying temperatures.*

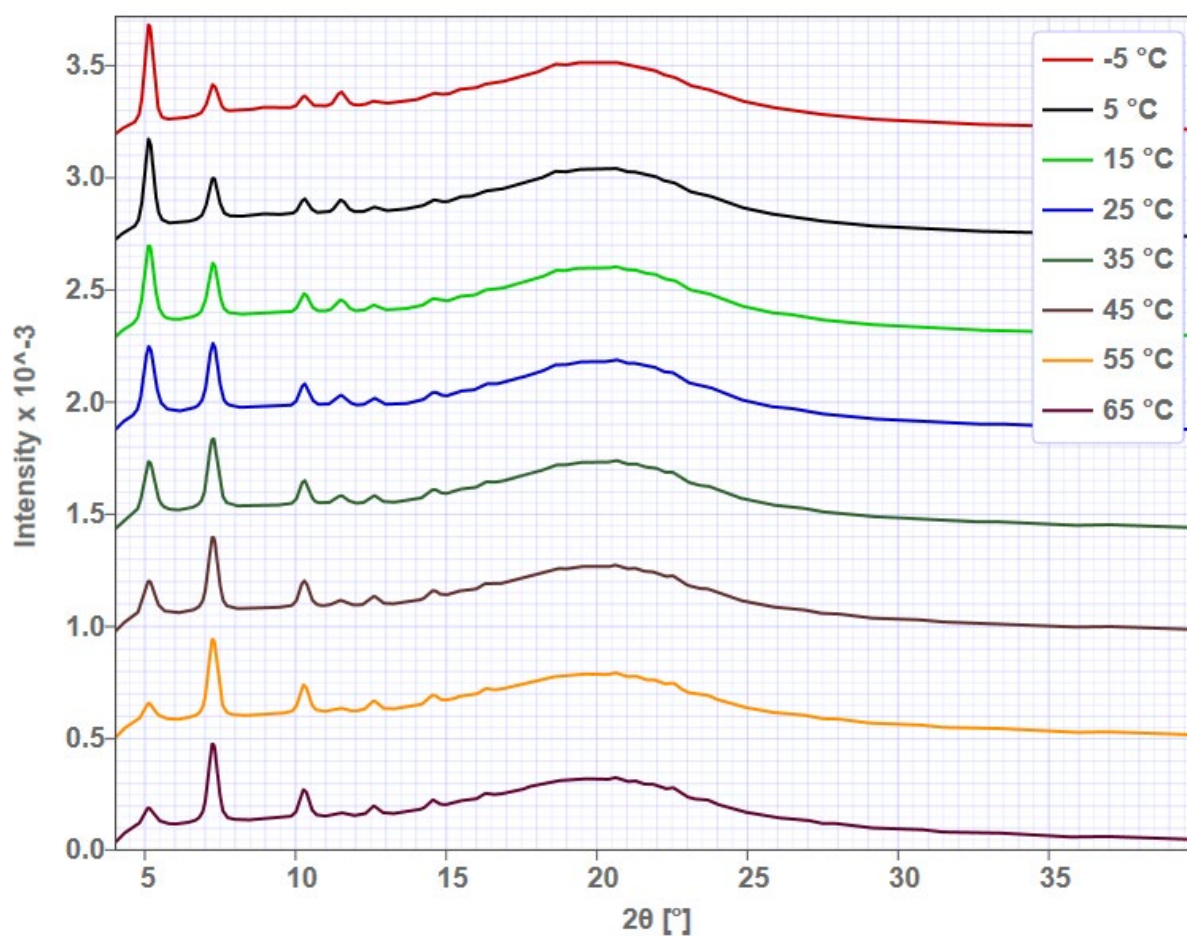


Figure 2.19: PXRD patterns of nanocrystalline MUF-9 synthesised at varying temperatures, from L1 and $\text{Zn}(\text{OAc})_2 \cdot 6\text{H}_2\text{O}$ in DBF.

2.5. REFERENCES

35. Lun, D. J.; Waterhouse, G. I.; Telfer, S. G., A general thermolabile protecting group strategy for organocatalytic metal-organic frameworks. *J. Am. Chem. Soc.* **2011**, *133* (15), 5806-9. DOI: 10.1021/ja202223d
67. Alkas, A.; Cornelio, J.; Telfer, S. G., Tritopic Triazatruxene Ligands for Multicomponent Metal-Organic Frameworks. *Chem.Asian.J.* **2019**, *14* (8), 1167-1174. DOI: 10.1002/asia.201801546
99. Ferguson, A.; Liu, L.; Tapperwijn, S. J.; Perl, D.; Coudert, F.-X.; Van Cleuvenbergen, S.; Verbiest, T.; van der Veen, M. A.; Telfer, S. G., Controlled partial interpenetration in metal-organic frameworks. *Nat. Chem.* **2016**, *8* (3), 250-257. DOI: 10.1038/nchem.2430
107. Yuan, S.; Feng, L.; Wang, K.; Pang, J.; Bosch, M.; Lollar, C.; Sun, Y.; Qin, J.; Yang, X.; Zhang, P.; Wang, Q.; Zou, L.; Zhang, Y.; Zhang, L.; Fang, Y.; Li, J.; Zhou, H. C., Stable Metal-Organic Frameworks: Design, Synthesis, and Applications. *Adv Mater* **2018**, *30* (37), e1704303. DOI: 10.1002/adma.201704303
108. Howarth, A. J.; Peters, A. W.; Vermeulen, N. A.; Wang, T. C.; Hupp, J. T.; Farha, O. K., Best Practices for the Synthesis, Activation, and Characterization of Metal-Organic Frameworks. *Chem. Mater.* **2016**, *29* (1), 26-39. DOI: 10.1021/acs.chemmater.6b02626
109. Allinger, N. L.; Youngdale, G. A., Reduction of 6,7-Diphenyldibenzo[e,g] [1,4]diazocine. An Unusual Nucleophilic Aromatic Substitution 1. *J. Org. Chem.* **1959**, *24* (3), 306-308. DOI: DOI 10.1021/jo01085a004
110. Cornelio, J.; Zhou, T. Y.; Alkas, A.; Telfer, S. G., Systematic Tuning of the Luminescence Output of Multicomponent Metal-Organic Frameworks. *J. Am. Chem. Soc.* **2018**, *140* (45), 15470-15476. DOI: 10.1021/jacs.8b09887
111. Tranchemontagne, D. J.; Hunt, J. R.; Yaghi, O. M., Room temperature synthesis of metal-organic frameworks: MOF-5, MOF-74, MOF-177, MOF-199, and IRMOF-0. *Tetrahedron* **2008**, *64* (36), 8553-8557. DOI: 10.1016/j.tet.2008.06.036
112. Wang, Y.; Cheng, L.; Wang, K. J.; Perry, Z.; Jia, W.; Chen, R.; Wang, Z. L.; Pang, J., Temperature-Controlled Degree of Interpenetration in a Single-Crystal-to-Single-Crystal Transformation within Two Co(II)-Triazole Frameworks. *Inorg. Chem.* **2019**, *58* (1), 18-21. DOI: 10.1021/acs.inorgchem.8b01339
113. Zhang, J.; Wojtas, L.; Larsen, R. W.; Eddaoudi, M.; Zaworotko, M. J., Temperature and concentration control over interpenetration in a metal-organic material. *J. Am. Chem. Soc.* **2009**, *131* (47), 17040-1. DOI: 10.1021/ja906911q
114. Brozek, C. K.; Dinca, M., Cation exchange at the secondary building units of metal-organic frameworks. *Chem. Soc. Rev.* **2014**, *43* (16), 5456-67. DOI: 10.1039/c4cs00002a

Chapter 3: MUF-91 – [Zn₄O(BPDC)₃] IN MUF-9

3.1. INTRODUCTION

Given the supramolecular interactions leading to the interesting behaviour of MUF-9 (Chapter 2, section 1), we had the idea that those behaviours could be exploited to give hetero-interpenetrated frameworks. The strategy, then, was to begin with the isolated α phases of MUF-9 and MUF-10 and replace the excess components in their synthesis mother liquor with different, but geometrically compatible, metals and ligands. In this way, the second lattice that forms would be chemically distinct from the first. We term this process 'secondary growth' and it is illustrated in Figure 3.1 (page 57).

In this chapter I will describe the determination of the conditions necessary for secondary growth in α -MUF-9, and how to characterise the hetero-interpenetrated materials which result. Several references will be made to the following chapter where this phenomenon is expanded upon – these are here to foreshadow the significance of the results here within the broader context of this work but shouldn't be necessary to understand the results in this chapter.

The first hetero-interpenetrated MOF presented in this thesis, MUF-91, has a [Zn₄O(bpdC)₃] lattice interpenetrated through α -MUF-9. [Zn₄O(bpdC)₃] (known on its own as IRMOF-10) is the simplest possible secondary lattice we could construct, with an identical metal to the primary lattice and the unfunctionalised BPDC ligand, to illustrate this concept.

IRMOF-10 is the noninterpenetrated analogue of IRMOF-9, approximately identical to α -MUF-9 without the side chains on **L1**. It is very famous, having been first described in Yaghi's seminal 2002 paper³⁰ which established isorecticular chemistry in MOFs. IRMOF-10 has been extensively studied computationally¹¹⁵⁻¹¹⁸ but was only experimentally reported as a single noisy PXRD pattern in the original paper. The

structure was inferred from similarity in the PXRD pattern to a related MOF in the same paper, IRMOF-12. IRMOF-12 replaces BPDC with 2,7-pyrenedicarboxylate, which can also be thought of as BPDC with its rings joined together on both sides by additional ethylene groups. IRMOF-10 has also been obtained by separation¹¹⁹ based on density, from a mixture with IRMOF-9. Analogues of IRMOF-10 have been reported^{35, 120} where large ligand substituents force a noninterpenetrated result, including IRMOF-12 itself.

3.2. CONDITIONS FOR SECONDARY GROWTH OF A NONIDENTICAL INTERPENETRATING LATTICE

When samples of α -MUF-9 are heated in solutions with relatively low concentrations of different ligands and metal salts (compared to those typical¹⁰⁸ for ordinary solvothermal MOF syntheses) an interpenetrating phase can grow at the exclusion of other processes. Examples of these other processes include the formation of separate phases by the new components, or the replacement of the components of the original framework by exchange¹²¹⁻¹²³ processes, which are common in MOFs. These were avoided by careful control of the reaction conditions.

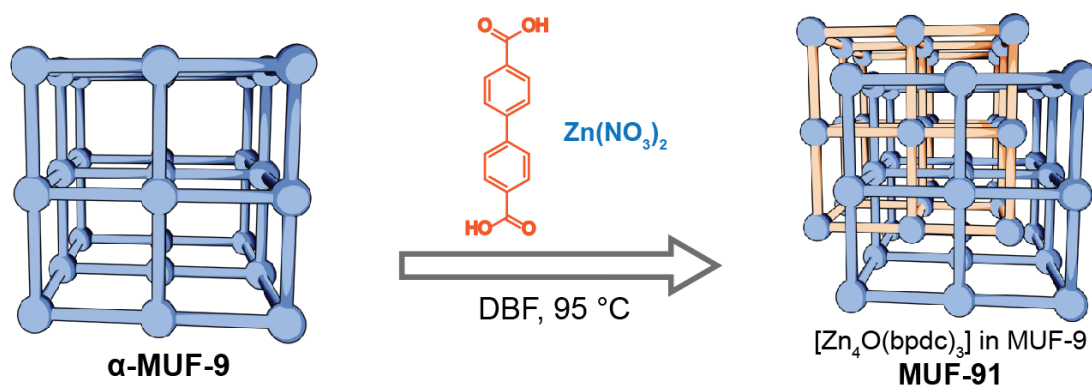


Figure 3.1: Illustration of the synthetic conditions for the synthesis of MUF-91 by secondary growth.

The growth of the secondary lattice reaches a plateau at approximately 60-70% PIP for MUF-91 as well as for the other frameworks presented in the following chapter. These percentages are determined from SCXRD structures, described in section 3.3. At this stage, the outer region of each crystal is fully interpenetrated and the transport of new components to the centre of the crystal is prevented, leading to a core-shell structure with highly interpenetrated regions near the surface and a less interpenetrated region in the centre of the crystal. Continued exposure to the secondary growth conditions beyond this plateau results in a second shell structure formed through epitaxial growth of a new phase. For now, this is simply inferred from the data we have, but in the following chapter there is an experiment which directly addresses this point.

Somewhat higher maximum PIP% values (70-90%) were achieved for samples prepared from microcrystalline MUF-9 powder than for large single crystals.

In many MOFs it is possible to replace^{62, 122-124} the components with new ones, simply by soaking the crystals in a concentrated solution of new ligands or metal salts. Clearly, it is possible that the methods we use here could result in such exchange, as demonstrated in Chapter 2, but our targets are hetero-interpenetrated frameworks where each lattice has only one ligand. This is why controlling the growth conditions precisely is critical to generating the products we want. The key factors in favouring secondary growth over component exchange turn out to be the concentration of the secondary components in the reaction solution, and the temperature at which secondary growth is conducted, within the confines established in Chapter 2. The optimum concentrations turn out to be about 2.0 mg mL⁻¹ or 7.6 μM for the metal salt, in this case Zn(NO₃)₂·4H₂O, and about 0.5 mg mL⁻¹ or 2.0 μM for the ligand, in this case BPDC. We didn't observe significant exchange of BPDC into the primary lattice at those concentrations with temperatures as high as 95 °C.

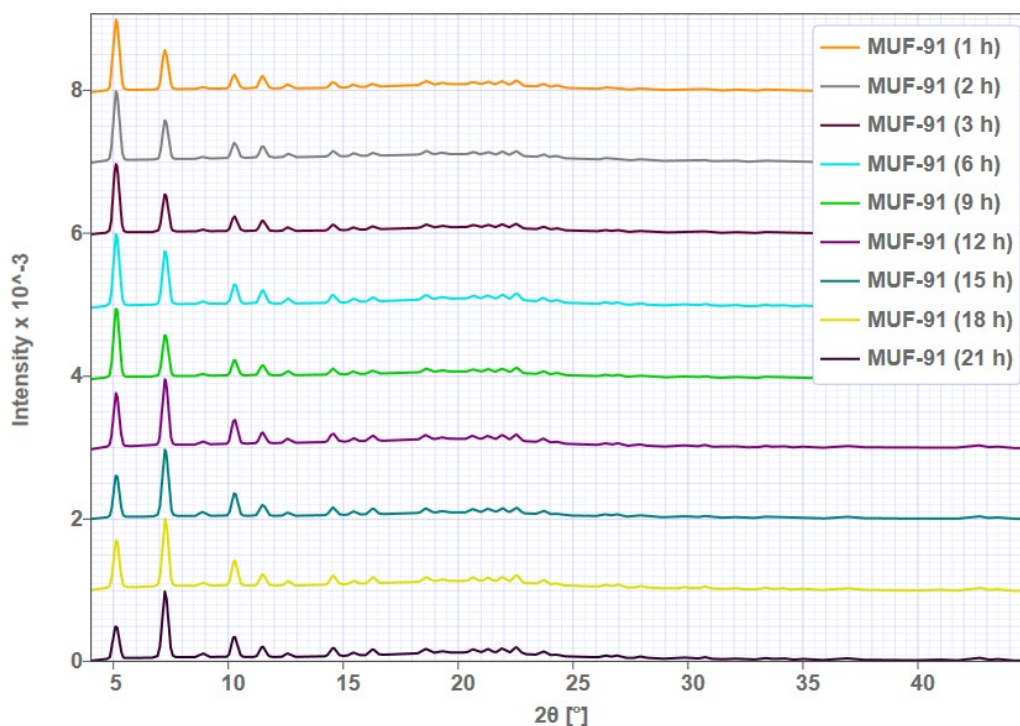


Figure 3.2: PXRD diffractograms of MUF-91 at various stages of growth.

After some of the new components in the secondary growth solution are consumed by the reaction forming the secondary lattice, the concentration of those components decreases. Therefore, the growth solution must be periodically replaced with fresh stock solution, keeping the concentration of the new components near its initial value throughout the entire period of growth of the secondary lattice.

The increase in interpenetration due to secondary growth over time can be tracked qualitatively by PXRD (Figure 3.2). As MUF-91 becomes more interpenetrated, we observe a decrease in intensity of the peak at $2\theta = 5.2^\circ$, while the peak at 7.3° increases in intensity, just as with MUF-9 itself. From the results in Chapter 2, we don't expect these changes to occur by simply heating MUF-9 in DBF, DBF with zinc nitrate, or DBF with BPDC. This gives us some confidence that the change in PXRD patterns over time shown in Figure 3.2 is due to the growth of a second lattice from the new precursors.

3.3. CHARACTERISATION OF HETERO-INTERPENETRATED MOFs THROUGH

COMPLEMENTARY TECHNIQUES

Changes to the MUF-9 crystals as they become MUF-91 are visually apparent. Optical micrographs in Figure 3.3 show darkening around the edges of the crystals in the initial stages, and later the growth of a shell phase around the crystals. The growth of this shell phase begins at around ten hours of secondary growth but is most clearly visible after fifteen hours.

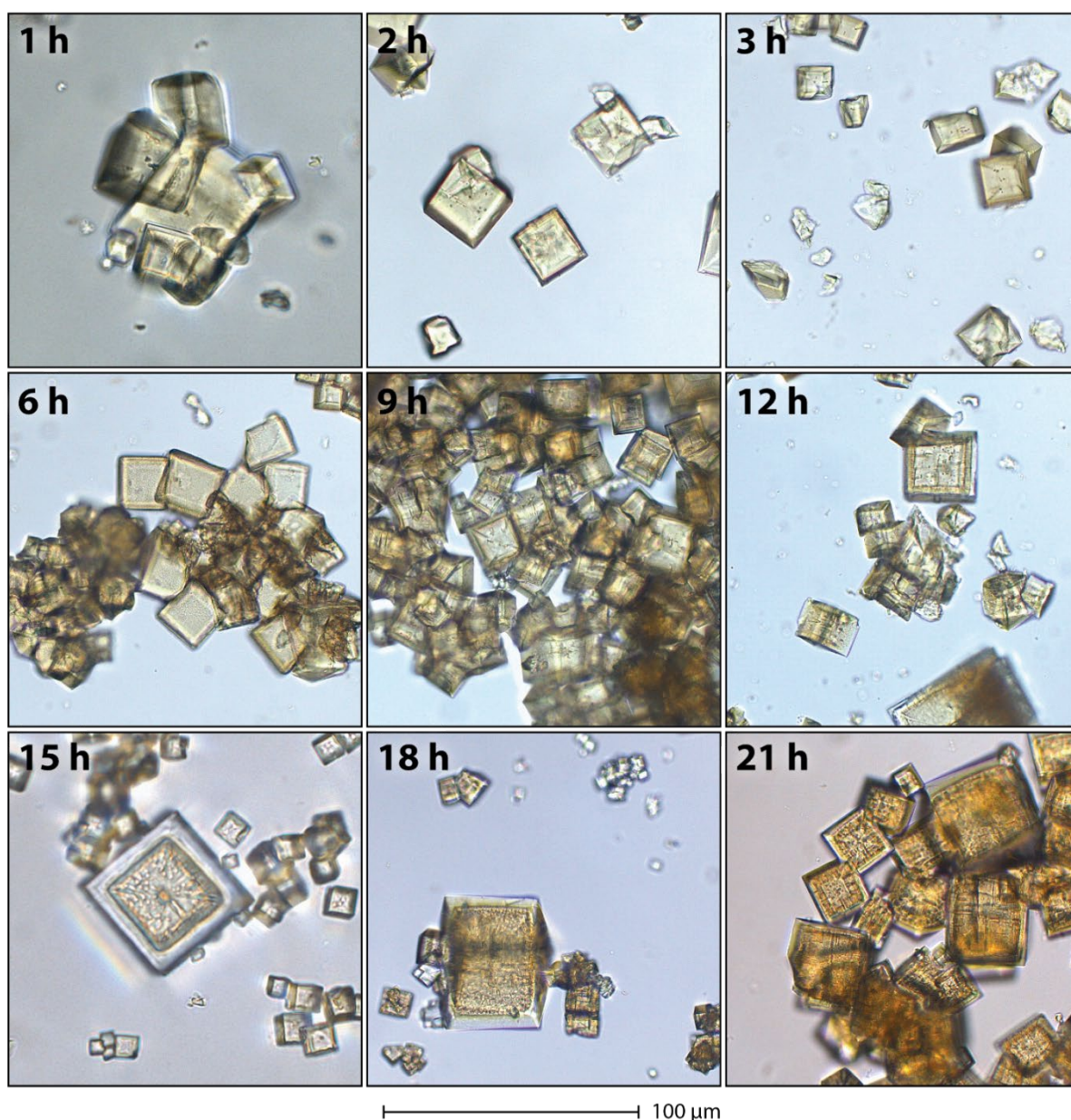


Figure 3.3: Optical micrographs of MUF-91 at various stages of growth. The image taken after fifteen hours (lower left) most clearly shows the epitaxial growth of a transparent shell layer around the crystals.

To characterise both the crystal-to-crystal variation as well as the bulk properties of MUF-91 as it grew over time, we collected several SCXRD datasets from each sample at each time point. The crystal-to-crystal variation turned out to be significant, something we were wary of from our experience with MUF-9. Figure 3.6 includes data derived from 18 individual SCXRD datasets obtained from two samples of MUF-91 prepared under the same conditions. We were able to collect so many datasets because of the rapid data collection available at the Australian Synchrotron – not including the time for mounting a crystal, setup, and processing of an experiment, a dataset could be collected in about two minutes, thanks to the high symmetry space group ($P\bar{4}3m$) of these materials. Table 3.1 summarises the crystallographic parameters for a selection of the SCXRD datasets.

Table 3.1: Crystallographic results for selected datasets obtained from MUF-91.

	Low PIP% (worst data)	Medium PIP% (representative data)	High PIP% (best data)
Identification code	MUF-91-1h-12pc	MUF-91-3h-41pc	MUF-91-9h-64pc
Empirical formula	C _{89.16} H _{56.96} N ₆ O _{14.6} Zn _{4.49}	C _{101.41} H _{57.95} N ₆ O _{18.39} Zn _{5.66}	C _{110.97} H _{69.41} N ₆ O _{21.35} Zn _{6.57}
Synthesis time	1 h	3 h	9 h
Interpenetration fraction (PIP%)	0.12	0.41	0.64
Formula weight	1739.38	2024.60	2257.80
Temperature / K	100(2)	100(2)	100(2)
Crystal system	cubic		
Space group	P-43m		
a,b,c / Å	17.036(12)	17.119(2)	17.1300(12)
α, β, γ / °	90		
Volume / Å ³	4944(10)	5016.9(18)	5026.6(11)
Z	1		
ρ_{calc} / g cm ⁻³	0.584	0.670	0.746
M / mm ⁻¹	0.566	0.699	0.808
F(000) / e ⁻	885.0	1025.0	1145.0
Radiation	Synchrotron ($\lambda = 0.71075$ Å)		
2 θ range for data collection / °	5.348 to 29.402	5.322 to 41.632	5.318 to 46.496
Index ranges	-12 ≤ h ≤ 12,	-17 ≤ h ≤ 17,	-15 ≤ h ≤ 19,
	-10 ≤ k ≤ 12,	-13 ≤ k ≤ 17,	-19 ≤ k ≤ 19,
	-11 ≤ l ≤ 7	-17 ≤ l ≤ 13	-19 ≤ l ≤ 13
Reflections collected	3170	9849	13590
Independent reflections	395 [R _{int} = 0.1314, R _{sigma} = 0.0587]	1046 [R _{int} = 0.0759, R _{sigma} = 0.0305]	1409 [R _{int} = 0.0512, R _{sigma} = 0.0237]
Data/restraints/parameters	395/81/33	1046/177/99	1409/75/33
Goodness-of-fit on F ²	1.623	2.253	1.420
Final R indexes [I ≥ 2σ (I)]	R ₁ = 0.1946, wR ₂ = 0.4512	R ₁ = 0.1752, wR ₂ = 0.4603	R ₁ = 0.1303, wR ₂ = 0.3261
Final R indexes [all data]	R ₁ = 0.2063, wR ₂ = 0.4618	R ₁ = 0.1860, wR ₂ = 0.4698	R ₁ = 0.1496, wR ₂ = 0.3555
Largest diff. peak/hole / e Å ⁻³	0.50/-0.51	1.88/-0.94	0.97/-0.38
Flack parameter	0.31(9)	0.620(18)	0.34(2)

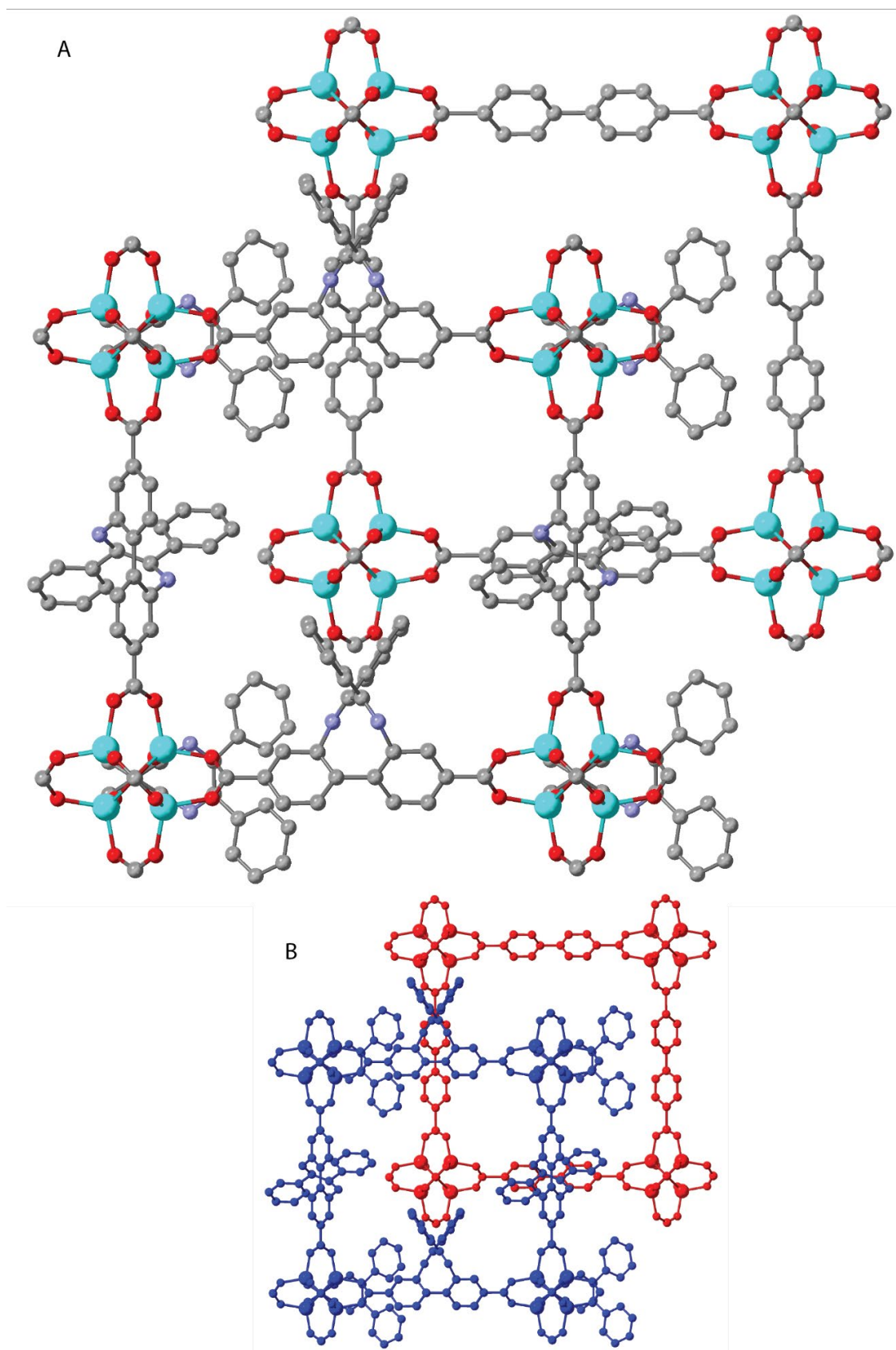


Figure 3.4: A) the structure of MUF-91. Hydrogens and disordered orientations of the side chain of **L1** are omitted for clarity. Carbons are coloured grey, nitrogen blue, oxygen red, zinc cyan. B) the same structure, with the primary lattice (complete occupancy) coloured blue and the secondary lattice (partial occupancy) coloured red.

The structure of MUF-91 is presented in Figure 3.4.

Processing datasets was sped up by the use of a Python script which identified successful data collections, retrieved refined cell parameters and reflection data from each XDS¹²⁵ output folder, set up SHELX¹²⁶-compatible model files for each dataset. A separate script executed the refinement routine for every dataset and returned PIP% values to the console. Each dataset was then checked by hand to ensure convergence of the refinement of the model, and relax the restraints on anisotropic displacement parameters to the maximum amount while preserving refinement stability. All Python codes are given in Appendix A.

A crystallographic model was developed from the highest-quality, most highly interpenetrated data set, with the occupancy of the secondary lattice assigned to a free variable. This model is illustrated in Figure 3.4. This model was then used for a dataset obtained from a low PIP% sample (which provide less than perfect data) adding tight restraints to preserve refinement stability and chemical correctness. The restrained model was adapted with the appropriate cell parameters for each individual data set, and then refined individually, loosening the restraints as much as possible for each sample given the data quality available. The refined occupancy of the secondary lattice was taken to be the PIP% value for each sample.

Samples with lower PIP% diffract poorly by nature, just as with the parent MUFs-9 and -10, due to their inhomogeneity, but for higher PIP% samples good data ($R_1 < 0.15$ with no corrections for solvent scattering and resolution better than 0.85 Å) could be obtained. The structural models we used were determined from these high-quality datasets and refined appropriately, resulting in good values for the statistics by which SCXRD structures are typically judged, as described above. These highest quality datasets are indicated in tables of crystallographic results (e.g. Table 3.1) as ‘best’ data. Many of the other datasets presented in this work have some data quality issues which would ordinarily limit their usefulness for SCXRD structure determination, exemplified by those indicated as ‘worst data’ in tables of crystallographic results.

Although there are *many* published MOF structures with worse statistics than even the worst data presented here, because MOFs are not dense and require large crystals for good diffraction, obviously for structure determination the best quality data available is preferred. In this work, it is strictly necessary to use these lower-quality datasets because they provide further information about the bulk properties of the same samples which produced the high-quality datasets. Relying exclusively only on good datasets would bias the results towards higher values of PIP% among other issues. It is also acceptable to use these datasets because, with atom positions fixed, these datasets still contain enough information to determine the single value of PIP% to reasonable accuracy and precision, and they are not used for structure determination. Even so, this result was only possible thanks to the use of the Australian Synchrotron. Despite many efforts, no datasets of MUF-91 obtained from our home diffractometer were suitable even for PIP% determination.

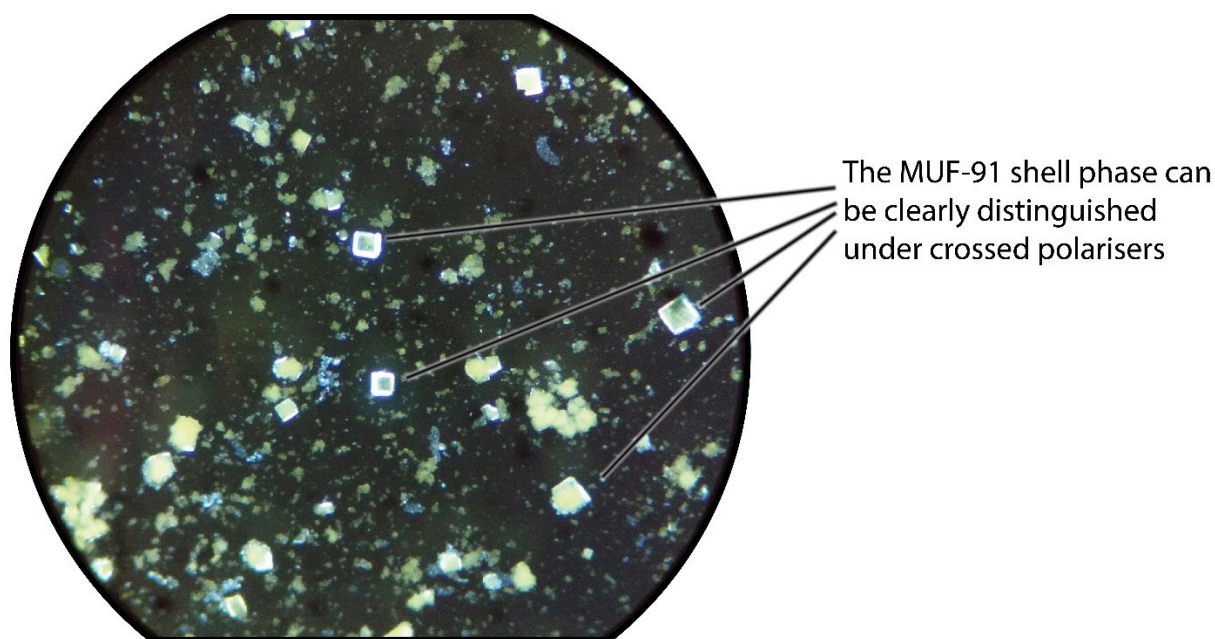


Figure 3.5: an optical micrograph of crystals of MUF-91 taken through crossed polarisers, in which the outer IRMOF-9 shell is clearly distinguished from the MUF-91 core.

The PIP% increases with reaction time, as expected for the slow growth of the secondary lattice, then reaches a plateau of about 60% interpenetration. At this point, the shell phase starts forming, the PXRD pattern stops changing (Figure 3.2) and the

PIP% determined from SCXRD stays relatively constant afterwards, or even appears to decrease a little (Figure 3.6).

We tried, but were not able, to collect a SCXRD structure for the shell phase, but identified it as IRMOF-9 by PXRD (experimental data in section 3.6.1.4, page 76). IRMOF-9 is an interpenetrated BPDC-only phase with similar geometry to MUF-9, although not cubic, displaying extinction under crossed polarisers (Figure 3.5). This structure for the shell would explain the apparent decrease in PIP% through the enhancement of intensity of the peaks corresponding to the noninterpenetrated phase, as IRMOF-9 has a strong peak in its PXRD pattern at $2\theta = 5.2^\circ$. That is the same position as the most intense peak for noninterpenetrated MUF-9, and the shell is likely aligned with the core due to its epitaxial formation.

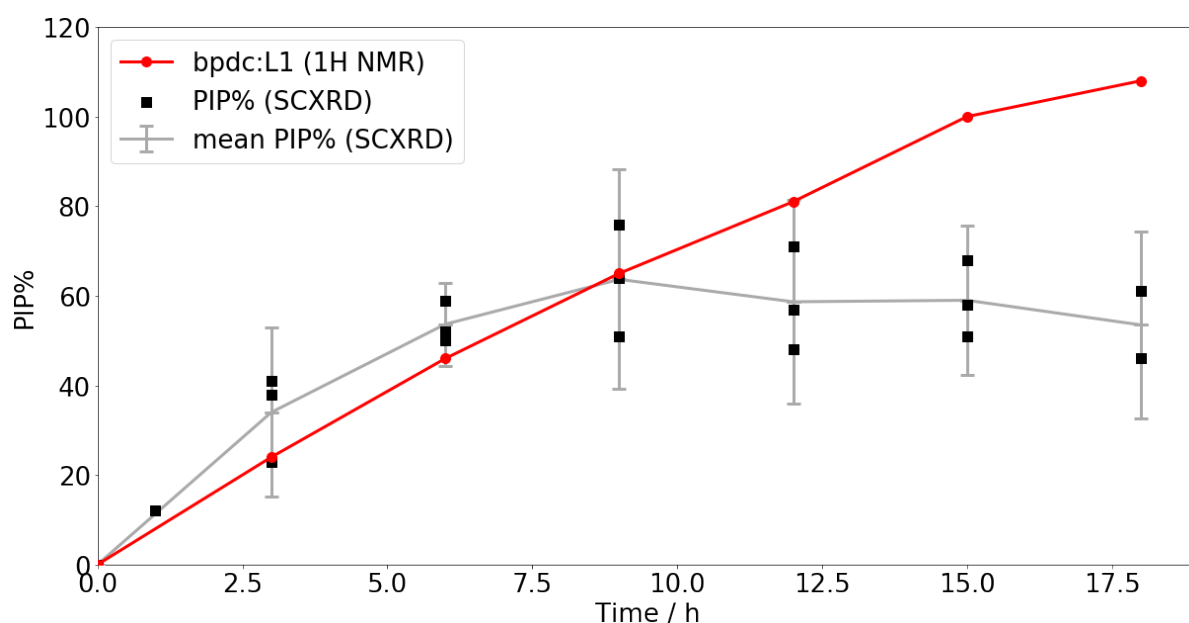


Figure 3.6: Plot of complementary characterisation data for MUF-91. Black squares represent the PIP% values obtained from SCXRD datasets collected at various time points in the growth of MUF-93. Red circles represent the ratio of BPDC to L1 as determined by ^1H -NMR. The grey line is drawn through the mean PIP% (from all SCXRD datasets) and the error bars correspond to the 95% confidence interval for the mean PIP% value for the sample.

A digested sample of the shell was analysed by ^1H NMR which showed it to contain mostly BPDC. There are small peaks from L1 visible in the NMR but I attribute those to imperfect manual separation of the core and shell phases. This is good evidence that

L1 does not leach from the primary framework in significant quantities under the conditions used for secondary growth.

^1H NMR spectroscopic analysis of digested samples show that the ratio of BPDC to **L1** in MUF-91 increases with time, as depicted in Figure 3.8. This ratio is calculated using the peak for H_2BPDC at 7.85 ppm, and the peak for **L1** at 7.32 ppm, as illustrated with an example spectrum in Figure 3.7. It is calculated by calibrating the integral of the peak for **L1** at 7.32 ppm at six protons and dividing the integral of the peak for H_2BPDC at 7.85 ppm by four to give the ratio of the ligands.

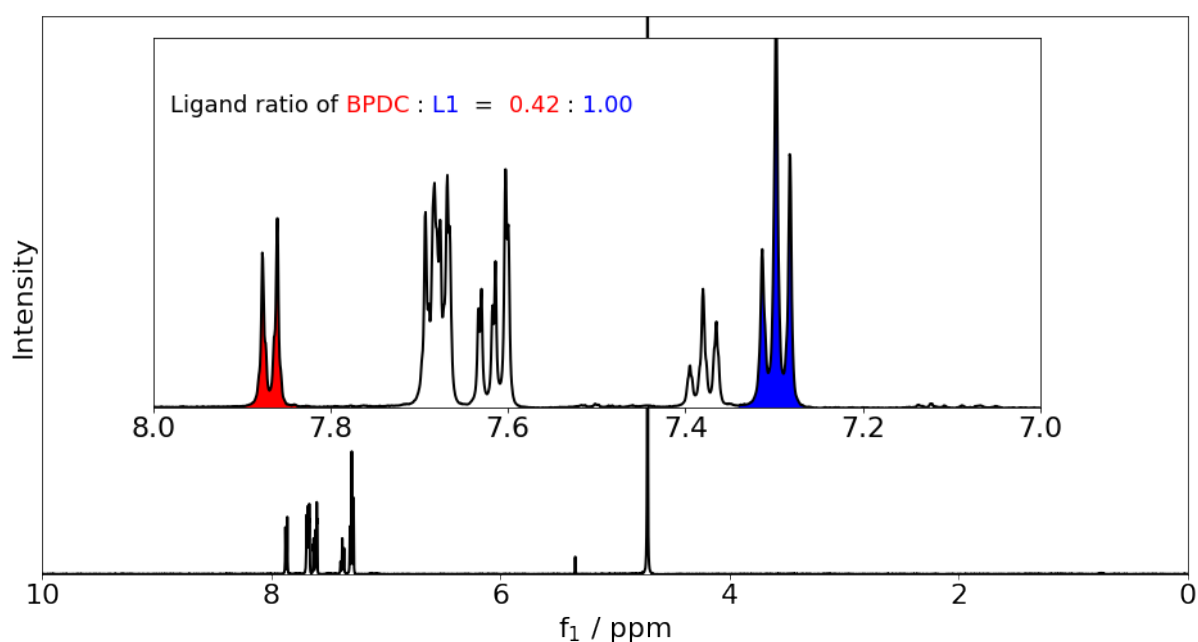


Figure 3.7: A ^1H NMR spectrum for a digested sample of MUF-91 in 0.2M NaOD in D_2O , showing a 0.42:1 ratio of BPDC:**L1**. The peak used to determine the amount of BPDC is at 7.85 ppm and coloured red. The peak used to determine the amount of **L1** is at 7.32 and coloured blue.

Assuming that **L1** content in the a-MUF-9 host is fixed, this is consistent with secondary growth of the $[\text{Zn}_4\text{O}(\text{bpdc})_3]$ lattice. After around 9 h of secondary growth, the ratio of BPDC to **L1** observed by ^1H NMR spectroscopy increases beyond the interpenetration percentage deduced by SCXRD (spectra 7-9 in Figure 3.8) as would be expected from the epitaxial growth of a shell phase with only BPDC as the ligand.

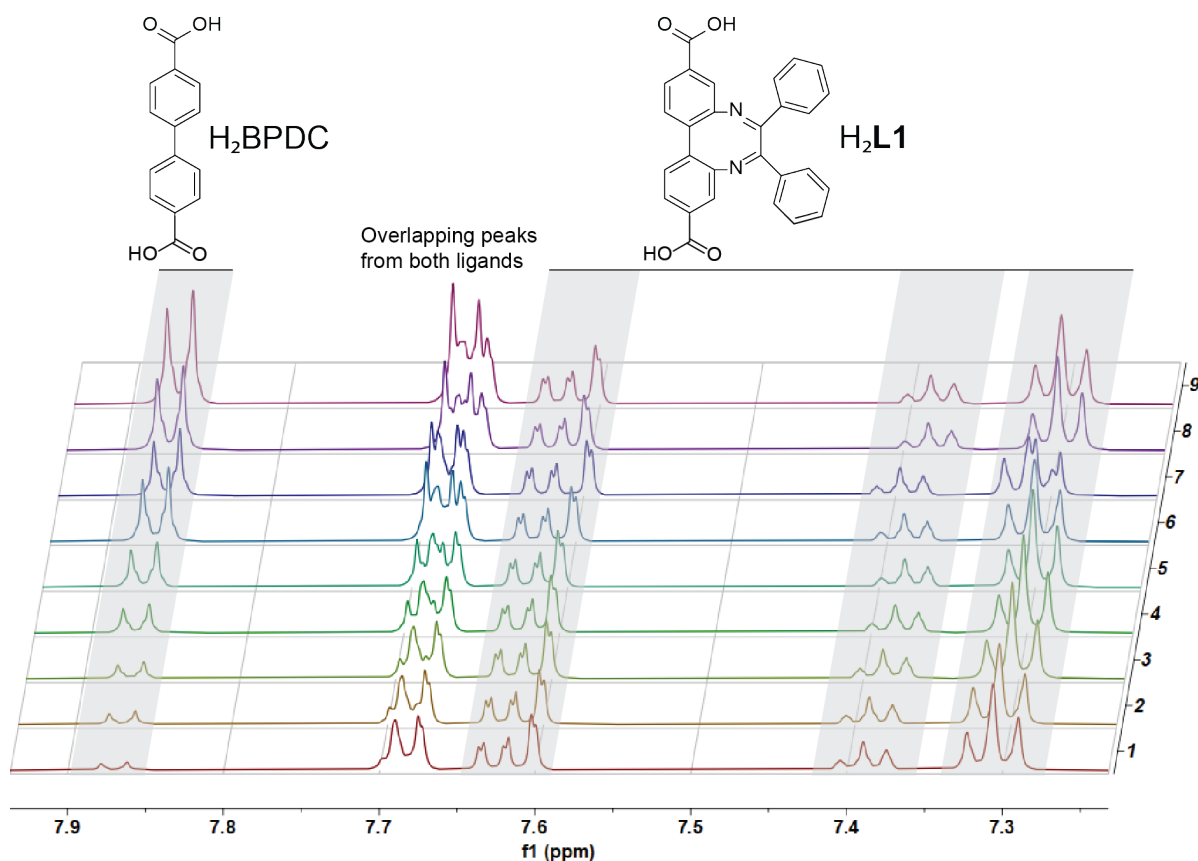


Figure 3.8: ^1H NMR spectra of digested samples of MUF-91 as the secondary lattice grows in over time. Spectra 1-8 were taken after 1, 3, 6, 9, 12, 15, 18, and 21 hours of secondary growth respectively. Spectrum 9 was measured after 30 hours. Spectra were measured in 0.2M NaOD in D_2O .

At first glance it appears that there is less than perfect agreement between these complementary methods of characterisation in the first 9 hours of secondary growth. The average PIP% determined by SCXRD is approximately 10 % higher than the ratio of the ligands determined by ^1H NMR spectroscopy. However, the overestimation of the percentage of interpenetration by single-crystal X-ray diffraction in the early stages of growth accounts for this. Highly interpenetrated samples diffract more strongly, even with the parent MUF-9, as do highly interpenetrated regions of samples. We collected many datasets which could not be processed, almost all of these taken from samples in the first two hours of secondary growth. We were only able to obtain data of good enough quality that it could be successfully processed from one sample with a PIP% below 20, out of tens of attempts. Doubtless, many samples with lower PIP% which would have brought the average values down were discarded in this process.

Combining all the data from individual crystal structures with the data obtained from ^1H NMR analyses, there is good agreement between both estimates of the interpenetration percentage, suggesting that BPDC does not substitute into the primary lattice. The ligand ratio as determined by NMR is within the 95% confidence interval for the mean interpenetration percentage for each sample as determined by SCXRD until the plateau of secondary growth at nine hours. The crystal-to-crystal variation can be as much as a difference of 40 percentage points in refined PIP% values from individual crystals from the same sample. This variation increases over the course of secondary growth, reaching a maximum spread after nine hours. Nine hours is also the point at which the PIP% reaches a plateau, as well as when the shell phase begins to grow.

3.4. POWDER MUF-91

We spent two or three years trying to increase the maximum PIP% of single crystals of MUF-91 as much as possible, initially with the aim of reaching full interpenetration. Ultimately, we realised it was inevitable that if the additional components for the secondary lattice entered the α -MUF-9 crystals from the outside, then as the second lattice formed it would always block the pores and prevent complete growth of a secondary lattice. We could think of no synthetic conditions in which the secondary lattice would grow from the inside of the crystal towards the outside.

Among the approaches to increasing the PIP% that we attempted were:

- Temperature for secondary growth reactions, ranging from 65 °C to 120 °C.
- Autocatenation of the secondary lattice by heating of the partially hetero-interpenetrated materials in NFPip.
- Modulator (2-fluorobenzoic acid) concentrations from 1 – 10 mg mL⁻¹.
- Microwave irradiation for heating of secondary growth reactions.

One observation we made in this process was that the maximum PIP% was significantly related to the particle size. To test this, we prepared microcrystalline samples of α -MUF-9 (section 2.2.1.1, page 39) and subjected them to the same procedure. The result was, indeed, a higher plateau of PIP%, around 80% (Figure 3.9).

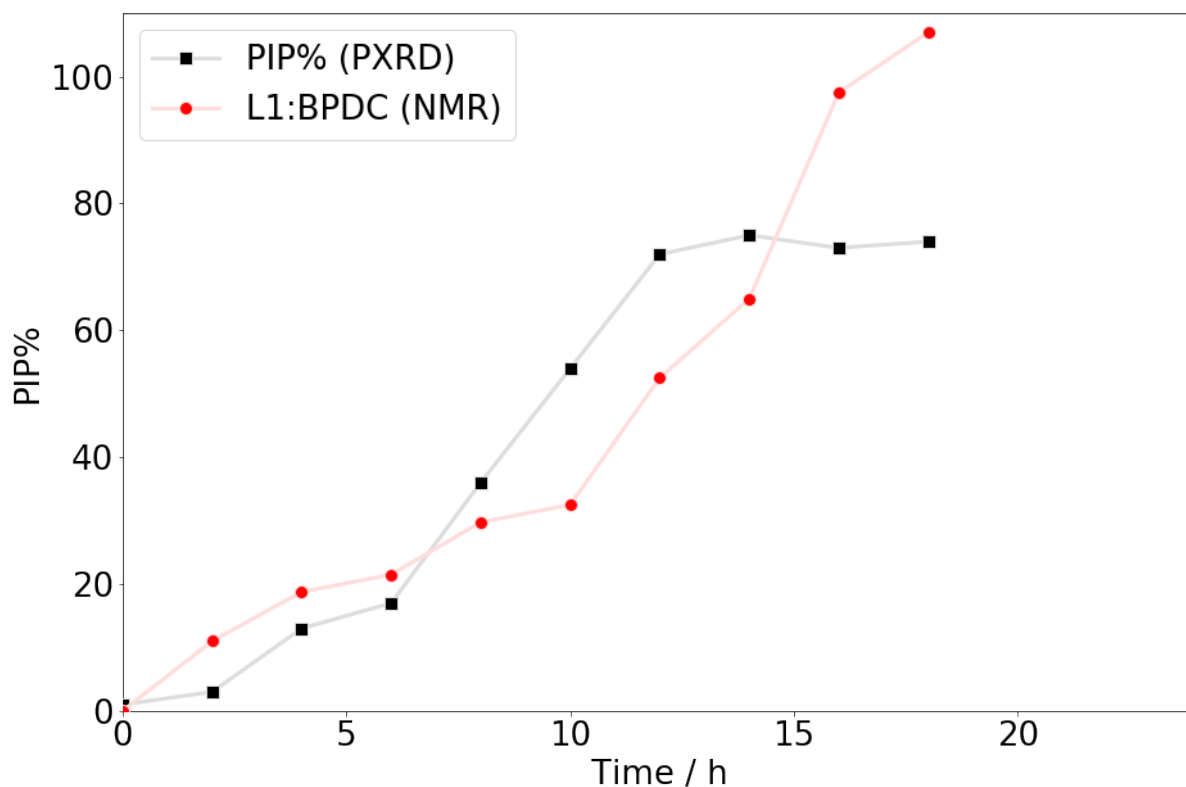


Figure 3.9: Growth over time of $[\text{Zn}_4\text{O}(\text{bpd})_3]$ in powder MUF-9. Black squares represent the interpenetration percentage determined from the PXR pattern and red circles represent the ratio of BPDC to L1 as determined by ^1H -NMR spectroscopy on digested samples.

The difference in final interpenetration percentages can easily be qualitatively observed from the PXR patterns. Figure 3.10 shows PXR pattern from both large crystals and powder after reaching the plateau of secondary growth. In the latter, the peak at $2\theta = 5.2^\circ$ is significantly lower in intensity, indicating a higher PIP%.

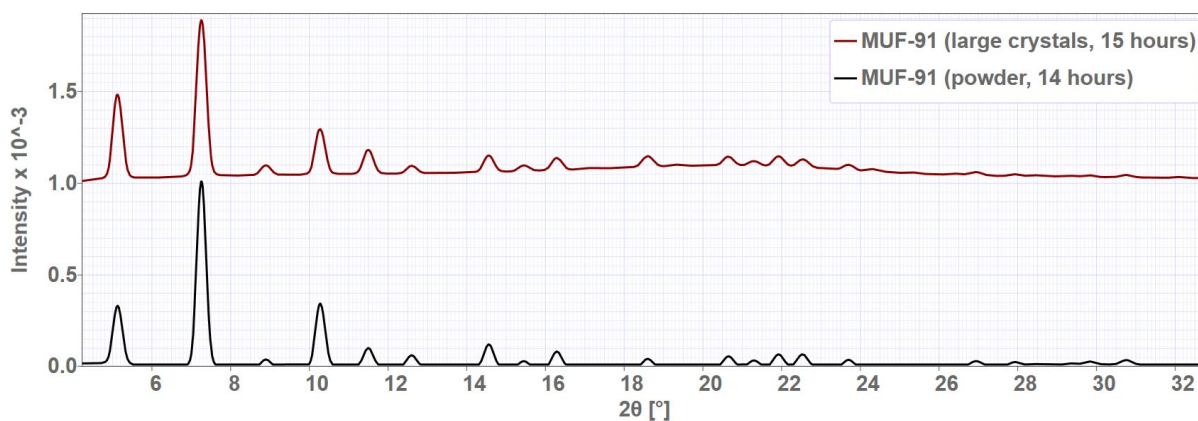


Figure 3.10: PXR patterns for MUF-91 grown as large crystals (top, red) or powder (bottom, black) after reaching the plateau of secondary growth.

Because these crystals were too small for SCXRD analysis, we determined the PIP% from their PXRD patterns. Baselines were removed from PXRD data using a custom implementation of the Sonneveld-Visser¹²⁷ Algorithm (Python code in Appendix A, page A-1). This algorithm removes a baseline by first finding points on the PXRD pattern where the gradient is low (i.e. points which are not on peaks), then fitting a polynomial to those points and subtracting it from the diffractogram.

The apparent PIP% for each sample was then obtained by calculating the contribution of each component in a linear combination of a fully interpenetrated and a noninterpenetrated sample of MUF-9 with the least-squares difference to the observed PXRD pattern (python code in Appendix A, page A-3). In other words, if the sum of the fully interpenetrated PXRD pattern scaled to 0.4 of its original size and a noninterpenetrated PXRD pattern scaled to 0.6 of its original size, was the sum which best approximated the observed PXRD pattern (by least-squared-differences) then the PIP% was said to be 40.

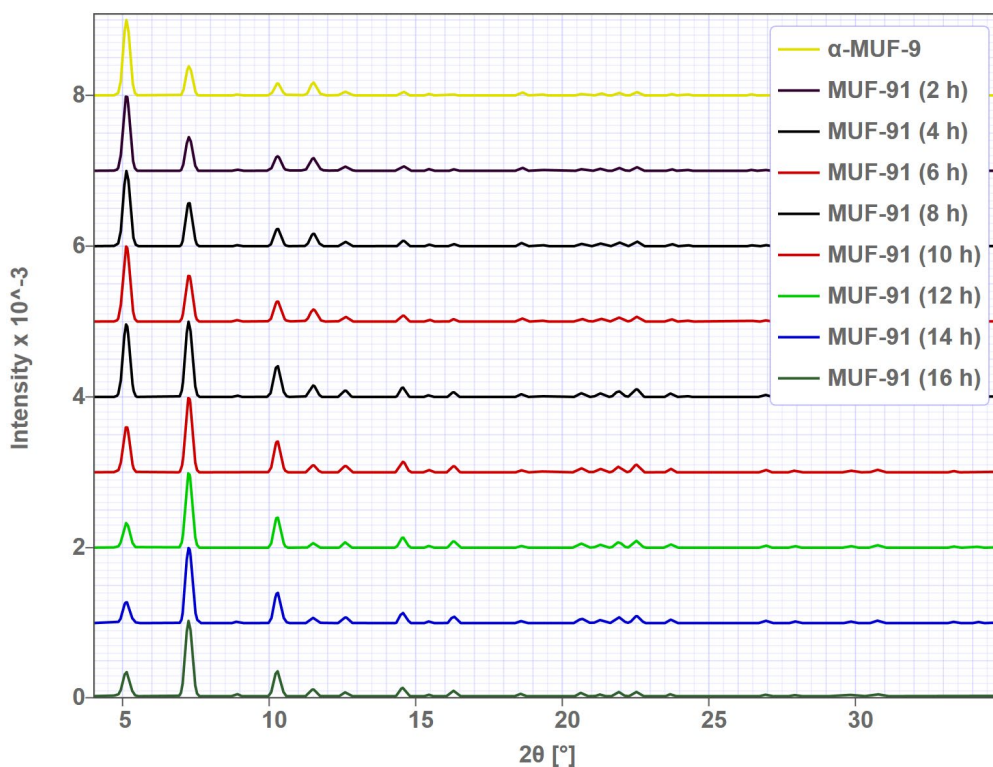


Figure 3.11: Baseline-corrected and scaled PXRD patterns for microcrystalline MUF-91

3.5. CONCLUSIONS

Fundamentally, our hypothesis that it is possible to produce hetero-interpenetrated frameworks using α -MUF-9 as a starting material has been shown to be correct. We have used the growth of a $[\text{Zn}_4\text{O}(\text{bpdc})_3]$ secondary lattice interpenetrated through α -MUF-9 to demonstrate that.

The fact that secondary growth of a lattice interpenetrated through α -MUF-9 is possible shines further light on α -MUF-9 itself as well. It further verifies our hypothesis that the increase in PIP% in α -MUF-9 at long synthesis times is due to the presence of extra components in the mother liquor. Although the control experiments in Chapter 2 had rendered any other possibility (such as rearrangement of the primary lattice stimulated by temperature, ligand, or metal ions) unlikely, the results presented in this chapter solidify that understanding.

In MUF-91 we have used the correlation between the ratio of BPDC to **L1** as determined by ^1H NMR and the PIP% determined by SCXRD to show that the new ligand goes to form the secondary framework. The control experiments from Chapter 2 imply that other explanations for the increase of PIP% and inclusion of a second ligand are unlikely.

We note significant variability in samples of MUF-91, both between batches and individual crystals. We also note that limited structural resolution is possible even with synchrotron SCXRD, but we have managed to obtain several datasets of very good quality that allow us to be confident in the structure assignment.

The drawbacks of this method notwithstanding, we consider it a success: to my knowledge this is the first example of a deliberately prepared hetero-interpenetrated MOF. This represents a step forward in MOF synthesis. It gives us access to frameworks where we have independent control over two ligands. This in turn gives

us a potential means of tuning pore chemistry more finely than in the case of frameworks with only one ligand.

The example of MUF-91, using only BPDC for the secondary lattice, is relatively simple. It tells us that preparing hetero-interpenetrated materials is possible, but does not tell us much about the generality of this technique. That will be explored in the following chapter.

3.6. EXPERIMENTAL DETAILS AND SUPPLEMENTARY DATA

All CIF files relevant to this chapter are listed in Appendix B, page B-7. The files are available electronically on the included CD-ROM.

3.6.1. General crystallographic methods and strategy

Powder X-ray diffraction data and some single crystal X-ray diffraction data were obtained using a Rigaku Spider. Other single crystal X-ray diffraction data were obtained¹²⁸ at the Australian Synchrotron MX1 and MX2 beamlines. In no cases have any solvent scattering contributions been taken into account. The crystallographic models used were adapted from that for MUF-91 which was originally solved with SHELXT¹²⁹, and SHELXL¹²⁶ was used for refinement, using OLEX2 as a graphical interface¹³⁰ and for the preparation of publication material.

A crystallographic model for each MOF was developed from the highest-quality, most highly interpenetrated data set. The coordinates of the atoms were then fixed, with the occupancy of the secondary lattice assigned to a free variable. This model was then used for a dataset obtained from a low PIP% sample (which provide less than perfect data) adding tight restraints to preserve refinement stability and chemical correctness. The restrained model was adapted with the appropriate cell parameters for each individual data set, and then refined individually, loosening the restraints as much as possible for each sample given the data quality available.

3.6.1.1. *Synthesis of single-crystal MUF-91*

α -MUF-9 was synthesised in a 4 mL glass vial with phenolic cap and PTFE-lined PDMS septum, by a literature⁹⁹ method. A solution of H₂-BPDC (0.5 mg mL⁻¹), Zn(NO₃)₂·4H₂O (2 mg mL⁻¹) and 2-fluorobenzoic acid (3 mg mL⁻¹) was prepared in DBF. The solvent was removed from a vial of α -MUF-9 and replaced with this stock solution, after which the vial was heated in a dry bath set to 95 °C. The stock solution was removed and replaced with fresh solution every three hours. At the desired stage

of growth, the crystals were removed from the dry bath, cooled to room temperature, and washed several times with DBF.

3.6.1.2. *Synthesis of microcrystalline powder MUF-91*

Microcrystals of α -MUF-9 were prepared as detailed in Chapter 2. The supernatant was replaced with 2 mL of a stock solution of H₂-BPDC (0.5 mg mL⁻¹), Zn(NO₃)₂·4H₂O (2 mg mL⁻¹) and 2-fluorobenzoic acid (3 mg mL⁻¹) in DBF, and the crystals were heated in a dry bath set at 95 °C. At intervals of two hours, the crystals were centrifuged, a sample taken out, and the solution exchanged for fresh stock solution, then heating continued.

3.6.1.3. *MOF Digests*

For digestion, MOF samples were washed with DMF three times, then acetone five times. Excess solvent was removed, and the MOF dried under vacuum overnight. To the dried MOF, 0.2 mL of a 375 mM solution of DCl in d₆-DMSO was first added, and the mixture sonicated until the MOF was dissolved, then a further 0.4 mL of d₆-DMSO added. This solution was then used for ¹H NMR analysis before being further used for AAS where relevant.

3.6.1.4. *Characterisation of shell phase of MUF-91*

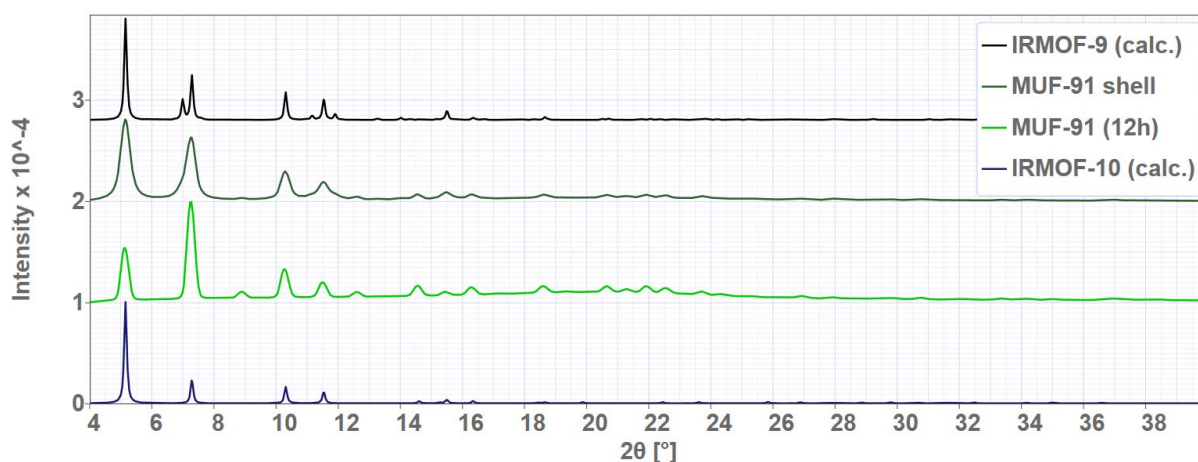


Figure 3.12: PXRD diffractograms of the MUF-91 shell with other phases for comparison. The small peak at $2\theta = 8.9$ is from incomplete separation of the shell from MUF-92. The shoulder on the low angle side of the peak at $2\theta = 7.3$, as well as the broader peak at $2\theta = 11.5$ distinguish the shell as IRMOF-9 rather than IRMOF-10.

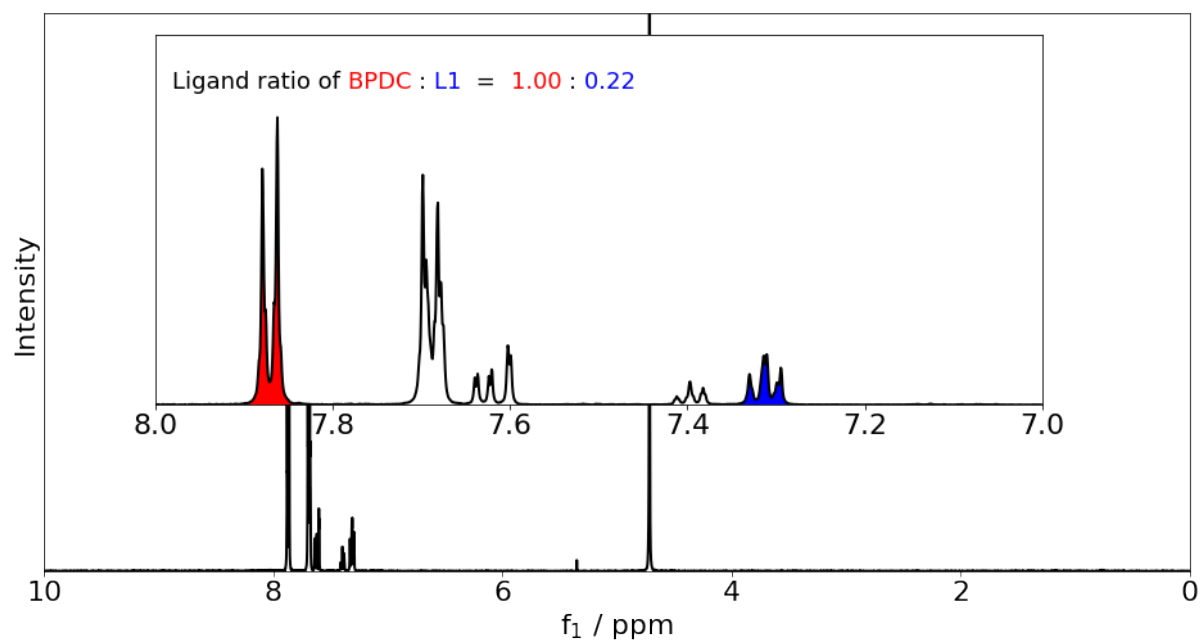


Figure 3.13: ^1H NMR spectrum of a digested sample of the shell of MUF-91, in 0.2M NaOD in D_2O , manually separated from the core.

3.7. REFERENCES

30. Eddaoudi, M.; Kim, J.; Rosi, N.; Vodak, D.; Wachter, J.; O'Keeffe, M.; Yaghi, O. M., Systematic Design of Pore Size and Functionality in Isoreticular MOFs and Their Application in Methane Storage. *Science* **2002**, 295 (5554), 469–472. DOI: DOI 10.1126/science.1067208
35. Lun, D. J.; Waterhouse, G. I.; Telfer, S. G., A general thermolabile protecting group strategy for organocatalytic metal-organic frameworks. *J. Am. Chem. Soc.* **2011**, 133 (15), 5806-9. DOI: 10.1021/ja202223d
62. Foo, M. L.; Matsuda, R.; Kitagawa, S., Functional Hybrid Porous Coordination Polymers. *Chem. Mater.* **2014**, 26 (1), 310–322. DOI: 10.1021/cm402136z
99. Ferguson, A.; Liu, L.; Tapperwijn, S. J.; Perl, D.; Coudert, F.-X.; Van Cleuvenbergen, S.; Verbiest, T.; van der Veen, M. A.; Telfer, S. G., Controlled partial interpenetration in metal-organic frameworks. *Nat. Chem.* **2016**, 8 (3), 250-257. DOI: 10.1038/nchem.2430
108. Howarth, A. J.; Peters, A. W.; Vermeulen, N. A.; Wang, T. C.; Hupp, J. T.; Farha, O. K., Best Practices for the Synthesis, Activation, and Characterization of Metal-Organic Frameworks. *Chem. Mater.* **2016**, 29 (1), 26-39. DOI: 10.1021/acs.chemmater.6b02626
115. Borycz, J.; Tiana, D.; Haldoupis, E.; Sung, J. C.; Farha, O. K.; Siepmann, J. I.; Gagliardi, L., CO₂ Adsorption in M-IRMOF-10 (M = Mg, Ca, Fe, Cu, Zn, Ge, Sr, Cd, Sn, Ba). *J. Phys. Chem. C* **2016**, 120 (23), 12819-12830. DOI: 10.1021/acs.jpcc.6b02235
116. Hicks, J. M.; Desgranges, C.; Delhommelle, J., Characterization and Comparison of the Performance of IRMOF-1, IRMOF-8, and IRMOF-10 for CO₂ Adsorption in the Subcritical and Supercritical Regimes. *J. Phys. Chem. C* **2012**, 116 (43), 22938-22946. DOI: 10.1021/jp307319u
117. Babarao, R.; Jiang, J., Molecular screening of metal-organic frameworks for CO₂ storage. *Langmuir* **2008**, 24 (12), 6270-8. DOI: 10.1021/la800369s
118. Yang, L.-M.; Ravindran, P.; Vajeeston, P.; Tilset, M., Ab initio investigations on the crystal structure, formation enthalpy, electronic structure, chemical bonding, and optical properties of experimentally synthesized isoreticular metal-organic framework-10 and its analogues: M-IRMOF-10 (M = Zn, Cd, Be, Mg, Ca, Sr and Ba). *RSC Adv.* **2012**, 2 (4), 1618-1631. DOI: 10.1039/c1ra00187f
119. Farha, O. K.; Mulfort, K. L.; Thorsness, A. M.; Hupp, J. T., Separating solids: purification of metal-organic framework materials. *J. Am. Chem. Soc.* **2008**, 130 (27), 8598-9. DOI: 10.1021/ja803097e
120. Lee, J. S.; Kapustin, E. A.; Pei, X.; Llopis, S.; Yaghi, O. M.; Toste, F. D., Architectural Stabilization of a Gold(III) Catalyst in Metal-Organic Frameworks. *Chem* **2020**, 6 (1), 142-152. DOI: 10.1016/j.chempr.2019.10.022
121. Deria, P.; Mondloch, J. E.; Karagiari, O.; Bury, W.; Hupp, J. T.; Farha, O. K., Beyond post-synthesis modification: evolution of metal-organic frameworks via building block replacement. *Chem. Soc. Rev.* **2014**, 43 (16), 5896-912. DOI: 10.1039/c4cs00067f

122. Karagiari, O.; Bury, W.; Mondloch, J. E.; Hupp, J. T.; Farha, O. K., Solvent-assisted linker exchange: an alternative to the de novo synthesis of unattainable metal-organic frameworks. *Angew Chem Int Ed Engl* **2014**, *53* (18), 4530-40. DOI: 10.1002/anie.201306923
123. Brozek, C. K.; Bellarosa, L.; Soejima, T.; Clark, T. V.; Lopez, N.; Dinca, M., Solvent-dependent cation exchange in metal-organic frameworks. *Chemistry* **2014**, *20* (23), 6871-4. DOI: 10.1002/chem.201402682
124. Yin, Z.; Zhou, Y.-L.; Zeng, M.-H.; Kurmoo, M., The concept of mixed organic ligands in metal-organic frameworks: design, tuning and functions. *Dalton Trans.* **2015**, *44* (12), 5258–5275. DOI: 10.1039/c4dt04030a
125. Kabsch, W., XDS. *Acta Crystallogr D Biol Crystallogr* **2010**, *66* (Pt 2), 125-32. DOI: 10.1107/S0907444909047337
126. Sheldrick, G., Crystal structure refinement with SHELXL. *Acta Crystallogr. C* **2015**, *71* (1), 3-8. DOI: doi:10.1107/S2053229614024218
127. Sonneveld, E. J.; Visser, J. W., Automatic collection of powder data from photographs. *J. Appl. Crystallogr.* **1975**, *8* (1), 1-7. DOI: doi:10.1107/S0021889875009417
128. McPhillips, T. M.; McPhillips, S. E.; Chiu, H.-J.; Cohen, A. E.; Deacon, A. M.; Ellis, P. J.; Garman, E.; Gonzalez, A.; Sauter, N. K.; Phizackerley, R. P.; et al., Blu-Ice and the Distributed Control System: software for data acquisition and instrument control at macromolecular crystallography beamlines. *J. Synchrotron Rad.* **2002**, *9* (6), 401–406. DOI: 10.1107/S0909049502015170
129. Sheldrick, G., SHELXT - Integrated space-group and crystal-structure determination. *Acta Crystallographica Section A* **2015**, *71* (1), 3-8. DOI: doi:10.1107/S2053273314026370
130. Dolomanov, O. V.; Bourhis, L. J.; Gildea, R. J.; Howard, J. A. K.; Puschmann, H., OLEX2: a complete structure solution, refinement and analysis program. *J. Appl. Crystallogr.* **2009**, *42* (2), 339-341. DOI: doi:10.1107/S0021889808042726

Chapter 4: HETERO-INTERPENETRATED MOFS WITH DIFFERENT METALS AND FUNCTIONALISED LIGANDS

4.1. INTRODUCTION

To expand on the concept of secondary growth established in the previous chapter and establish the generality of this approach to synthesising hetero-interpenetrated frameworks, we explored a range of combinations of metals and ligands for secondary lattices. Many of these showed positive preliminary results, and we selected two examples to characterise thoroughly.

The $[\text{Zn}_4\text{O}]$ unit is one of the most common building blocks for MOFs. There are several hundred examples in the CCDC at the time of writing, including the well-known IRMOF series³⁰. Their cobalt(II) analogues, on the other hand, are virtually unknown: only a cobalt(II) analogue of MOF-5 (IRMOF-1) has been reported¹³¹ using a complex preformed cluster as a starting material and without single-crystal formation. The $[\text{Co}_4\text{O}]$ cluster is found in a few pyrazolate MOFs¹³² but no SCXRD structures have been reported of $[\text{Co}_4\text{O}]$ hexacarboxylate materials.

Substituents on ligands can often influence¹³³ or interfere with MOF formation (Figure 4.1). This can be as simple as the geometry and steric bulk of a ligand leading to a particular structure¹³⁴ or topology. It can also be much more subtle, such as functional groups which can coordinate to metals making MOF formation impossible. This is difficult to predict: for example, take 2,2'-bipyridine-5,5'-dicarboxylic acid, a ligand which could be useful because it can coordinate through its carboxylates to form a MOF, leaving the nitrogen atoms free to coordinate a metal. A metal coordinated there could then be exploited, perhaps for catalysis. There are many MOFs reported with this ligand based on zirconium(IV)¹³⁵, aluminium(III)¹³⁶. However, a CSD search for zinc MOFs with this ligand yields no results. There is one example with 2,2'-bipyridine-4,4'-dicarboxylic acid, and in this case, the nitrogen coordination¹³⁷ is part of the ligand structure. We have also tried to incorporate 2,2'-bipyridine-5,5'-

dicarboxylic acid into many zinc and BPDC-based MOFs in our lab over several years, never with any success. We can infer that with 2,2'-bipyridine-5,5'-dicarboxylic acid, the ability of the nitrogen atoms to interact with the metals prevents the desired structure from forming.

BPDC-NH₂ (depicted as its conjugate acid in Table 4.1) is another such ligand: [Zn₄O(bpdc-NH₂)₃] does not form on its own under standard synthetic conditions compatible with other BPDC-based ligands. It has been obtained through increasing the metal-to-ligand ratio and temperature¹³⁸ compared to related MOFs without amine functionalities. In that case, it forms a doubly interpenetrated structure. It has also been prepared postsynthetically¹³⁹ from a MOF constructed with a ligand featuring a protecting group on the amine functionality.

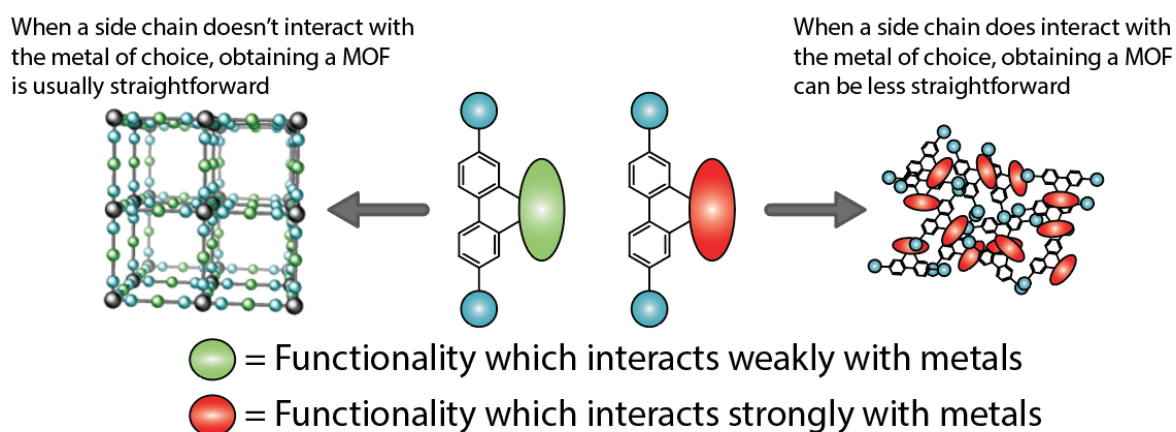


Figure 4.1: Whether or not the side chain of a ligand interacts with the metal of choice can strongly influence MOF formation.

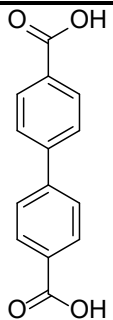
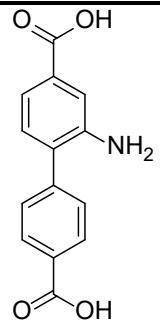
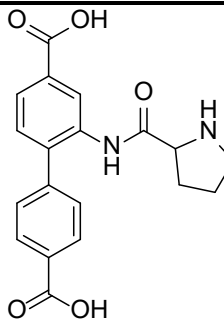
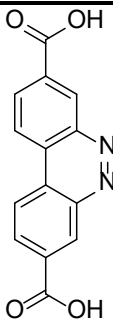
Among the results in this chapter, we obtain several unprecedented materials. It is not, however, the materials themselves which are interesting. As far as we know, they don't have any particularly outstanding properties regarding their application. What makes them exciting is the mechanism of their formation: α -MUF-9 templates the formation of these frameworks which would not otherwise form on their own. The pendant phenyl rings on α -MUF-9 create a pore space which is very accommodating to a BPDC-based lattice, as we have seen in the previous chapter. Here, we see that it is accommodating enough to encourage otherwise unfavourable frameworks to form.

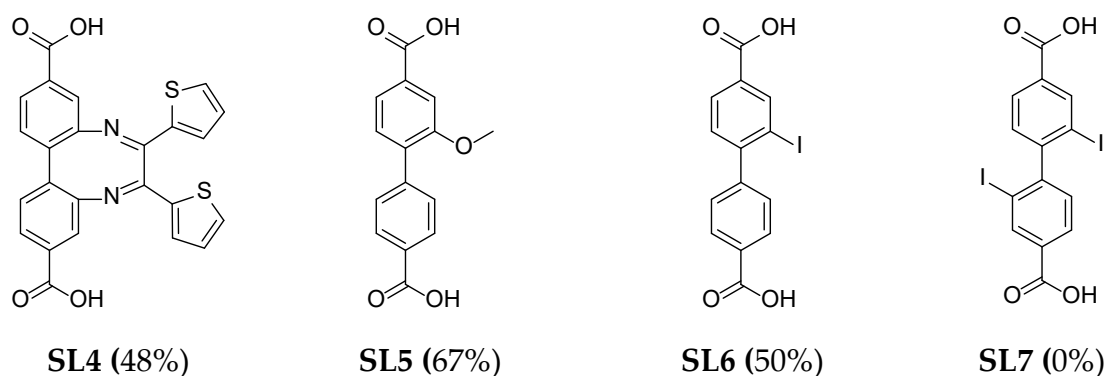
4.2. INITIAL RESULTS WITH DIFFERENT LIGANDS AND METALS

When we were first establishing the viability of our method to produce hetero-interpenetrated frameworks as described in Chapter 3, we tested the secondary growth reaction in MUF-9 with a range of different ligands chosen for different purposes. Table 4.1 shows a selection of those ligands for which we achieved some degree of successful secondary growth. SCXRD data were collected on hetero-interpenetrated MOFs made with **SL3** through **SL6** in MUF-9, crystallographic data for all of these can be found in Appendix B, Page B-10.

We also tested several different metals each with BPDC as the secondary ligand. We achieved secondary growth of interpenetrating lattices in α -MUF-9 with two of these: cobalt and magnesium. We obtained good quality SCXRD data from frameworks prepared with α -MUF-9, magnesium nitrate hexahydrate, and BPDC (section 4.6.2, page 107). From those SCXRD datasets we observed significant replacement of zinc in the original framework by magnesium, even in the early stages of the reaction. Because of this complication, and the fact that $[\text{Co}_4\text{O}]$ clusters are more unusual and potentially more interesting (unlike with cobalt, many $[\text{Mg}_4\text{O}]$ MOFs have been reported¹⁴⁰) we directed more focus on the material using cobalt. It should also be noted that the degree of atmospheric humidity strongly affected the outcome of the synthesis of $[\text{Mg}_4\text{O}(\text{bpdc})_3]$ in α -MUF-9, more so than with other secondary lattices.

Table 4.1: Different ligands trialled for secondary growth in α -MUF-9. The maximum PIP% observed is indicated in parentheses after each ligand name.

			
H₂BPDC (91%)	H₂BPDC-NH₂ (74%)	H₂BPDC-Pro (35%)	SL3 (61%)



The ligands with iodo groups (**SL6** and **SL7**) were prepared because they could help us understand the secondary growth process with SCXRD datasets obtainable with our laboratory diffractometer. Because of the large electron count of iodine, it should be discernible even at low occupancy and disordered over eight crystallographic sites. We prepared **SL7** first, but did not observe any change in the PXRD pattern of α -MUF-9 exposed to **SL7** and zinc(II) nitrate tetrahydrate. We tentatively attribute this to the shape of the ligand – it seems that with both iodine groups present, and the ligand adopting a conformation which keeps them far apart, the kinetic diameter of **SL7** is too big for it to enter the α -MUF-9 pores. This is counterintuitive when compared to the (in absolute terms) bulkier **SL4** for which some secondary growth *was* observed, but in **SL4** the steric bulk of the side chain is limited to only one side of the ligand.

BPDC-Pro was tested as a secondary ligand, in the hope that it could be used for catalysis. Some $\text{Zn}_4\text{O}(\text{bpdc-pro})_3$ could form as a secondary lattice within MUF-9 (see Table 4.1). But, when we observed no product formation in attempted reactions with substrates for which this ligand is usually an active catalyst,^{35, 66} we concluded that a side chain as bulky as proline excludes those substrates from the interpenetrated MOF pores, and abandoned this ligand. Instead, we pursued a ligand we designed to have a smaller catalytically active side chain, which is described in Chapter 6.

SL3 gave an interesting structure: due to the symmetry of neighbouring metal clusters, which have a 90° rotation between them, twice as many orientations of **SL3** are present compared to BPDC. Because of inherent symmetry in **SL3** from the rings being joined

by the side chain, however, the overall result is a structure with the same $P -4 3 m$ symmetry as α -MUF-9 and MUF-91. Figure 4.2 shows this ligand and illustrates its orientations. This can be compared to BPDC-NH₂ (depicted in Figure 4.7, page 91) which has the same *overall* symmetry, but only two orientation for each ring (the carbon atom remains in the same position, but the NH₂ group can be on either side). **SL3** has four orientations for each ring, but both **SL3** and BPDC-NH₂ have only one orientation for each carboxylate group.

When the two rings of the ligand of the interpenetrating lattice are not bridged through their side chains, they often adopt orthogonal orientations. This can be explained¹⁴¹ by such a conformation allowing the greatest distance between substituents at the 2, 6, 2' and 6' positions, as well as putting the rings coplanar with the carboxylate groups, allowing weak hydrogen bonding¹⁴¹ between the 2, 5, 2' and 5' hydrogens and the carboxyl oxygens.

SL4 appeared to work, but is difficult to distinguish from **L1** by X-ray diffraction, given the disorder of its side chain. For that reason **SL4** was not explored further as a secondary ligand.

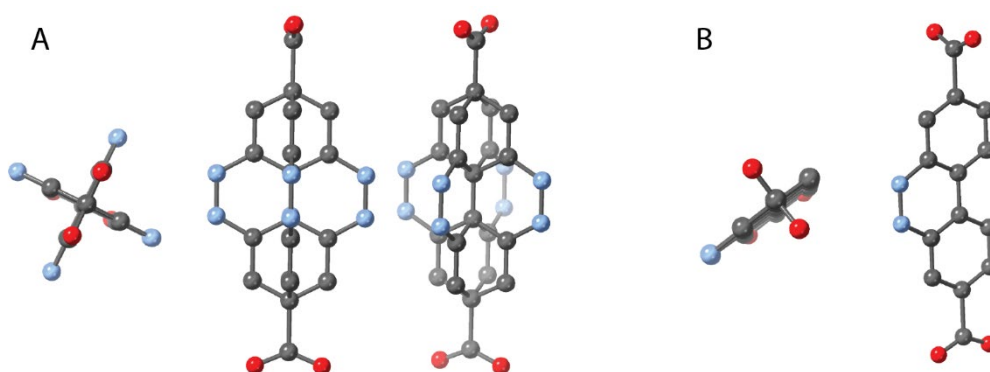


Figure 4.2: The structure of **SL3** when used for an interpenetrating lattice through α -MUF-9. A) the combination of all orientations of the ligand, from different views. B) A single orientation of the ligand, from different views.

SL5, when used for a secondary lattice in MUF-9, gives roughly the same result as BPDC in MUF-91, including the epitaxial growth of a shell phase after the plateau of interpenetration. That shell was observed by optical microscopy and was not

characterised, but it seems likely that it should be an analogue of IRMOF-9 where the ligand has a methoxy side chain. **SL5** is known¹⁴² to form such an analogue on its own.

We also prepared $[\text{Mg}_4\text{O}(\text{bpdc})_3]$ in MUF-9. We collected some good quality SCXRD datasets from this material, with which we could quantify both the growth of the second lattice as well as the replacement of zinc(II) in the primary lattice with magnesium(II). Replication of the synthesis of this material was not reliable, succeeding two or three out of ten times, so we decided to focus on others to characterise thoroughly. I wasn't able to determine exact reasons for the failure of those syntheses, but I can note that ambient humidity and precursor/solvent water content seemed important. Although we used carefully dried solvents and reagents, and limited the unnecessary exposure of samples to atmosphere, it was not practical to completely protect our samples from ambient humidity.

Ultimately, we selected two of these materials for which we carefully optimised the method, and which we thoroughly characterised as with MUF-91. These are MUF-92, which is prepared with zinc(II) as the metal and BPDC-NH₂ as the ligand, and MUF-93, which is prepared with cobalt(II) as the metal and BPDC as the ligand.

4.3. MUF-92

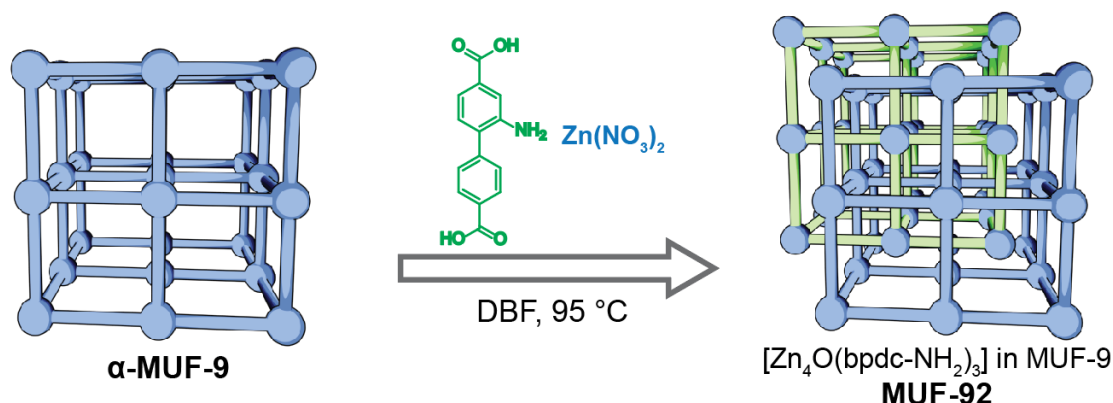


Figure 4.3: Illustration of the synthetic method to produce MUF-92.

Under similar conditions to MUF-91, but with an amino functional group on the secondary ligand, 2-amino-biphenyldicarboxylic acid (BPDC-NH₂), MUF-92 ([Zn₄O(bpdc-NH₂)₃] interpenetrated through MUF-9) is produced, illustrated in Figure 4.3. Full synthetic details are provided in Section 4.6.1.

[Zn₄O(bpdc-NH₂)₃] does not form on its own under standard synthetic conditions. I attempted synthesis of a MOF from H₂BPDC-NH₂ and Zn(NO₃)₂·4H₂O in DMF and DEF at concentrations ranging from 5-15 mg mL⁻¹ of the ligand and 10-25 mg mL⁻¹ of the metal salt. In DMF, the reaction did not form any solid material within several days and in DEF only an amorphous precipitate appeared. However, single crystals of doubly interpenetrated [Zn₄O(bpdc-NH₂)₃] were obtained from a low concentration solution of the precursors in DBF, the same solution as used for secondary growth. In this case, it is the templating effect of the primary framework which allows a single lattice of [Zn₄O(bpdc-NH₂)₃] and thus MUF-92 to form.

The changes in PXRD patterns (Figure 4.4) are similar to those in MUF-91. The peak at $2\theta = 5.2^\circ$ decreases in intensity, while the peak at 7.3° increases in intensity as the secondary lattice grows in. The rate of secondary lattice growth is similar to MUF-91. A plateau of PIP% is also reached after between 9 and 12 hours, and the PXRD pattern does not change much further beyond this point.

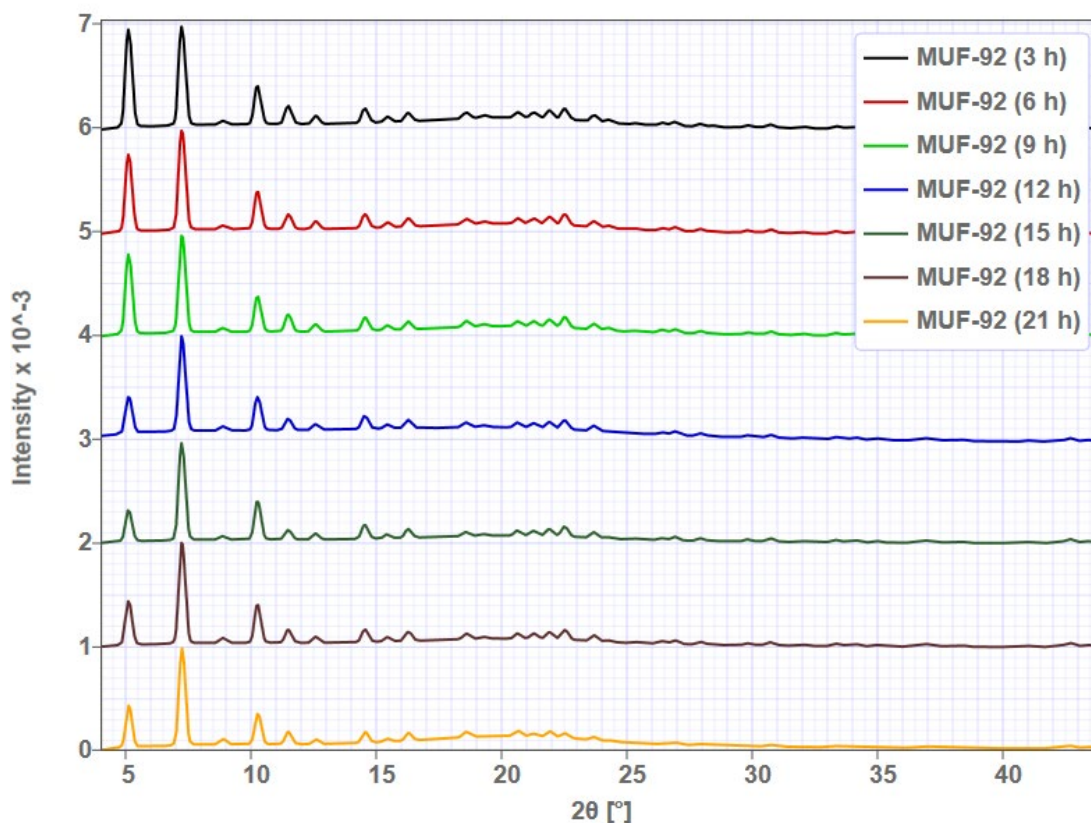


Figure 4.4: PXRD patterns of MUF-92 at various stages of growth.

As with MUF-91, visual changes to the crystals are apparent during MUF-92 synthesis. Selected micrographs depicting these changes are displayed in Figure 4.5. The interpenetrated regions around the edges darken and the crystals turn a deeper orange over time. Unlike MUF-91, however, no shell phase forms on the outside of the crystals.

Instead of the growth of a shell phase, the deposition of an uncharacterised amorphous phase occurs, increasing with time. This phase is removed whenever the crystals are washed with clean solvent, or when the secondary growth solution is refreshed. I think that the increase in how much of this phase forms over time is because as the sites for the second lattice become occupied, less of the new components can go to add to it. Seeding of the growth of this phase by some incompletely washed out remnants could also contribute.

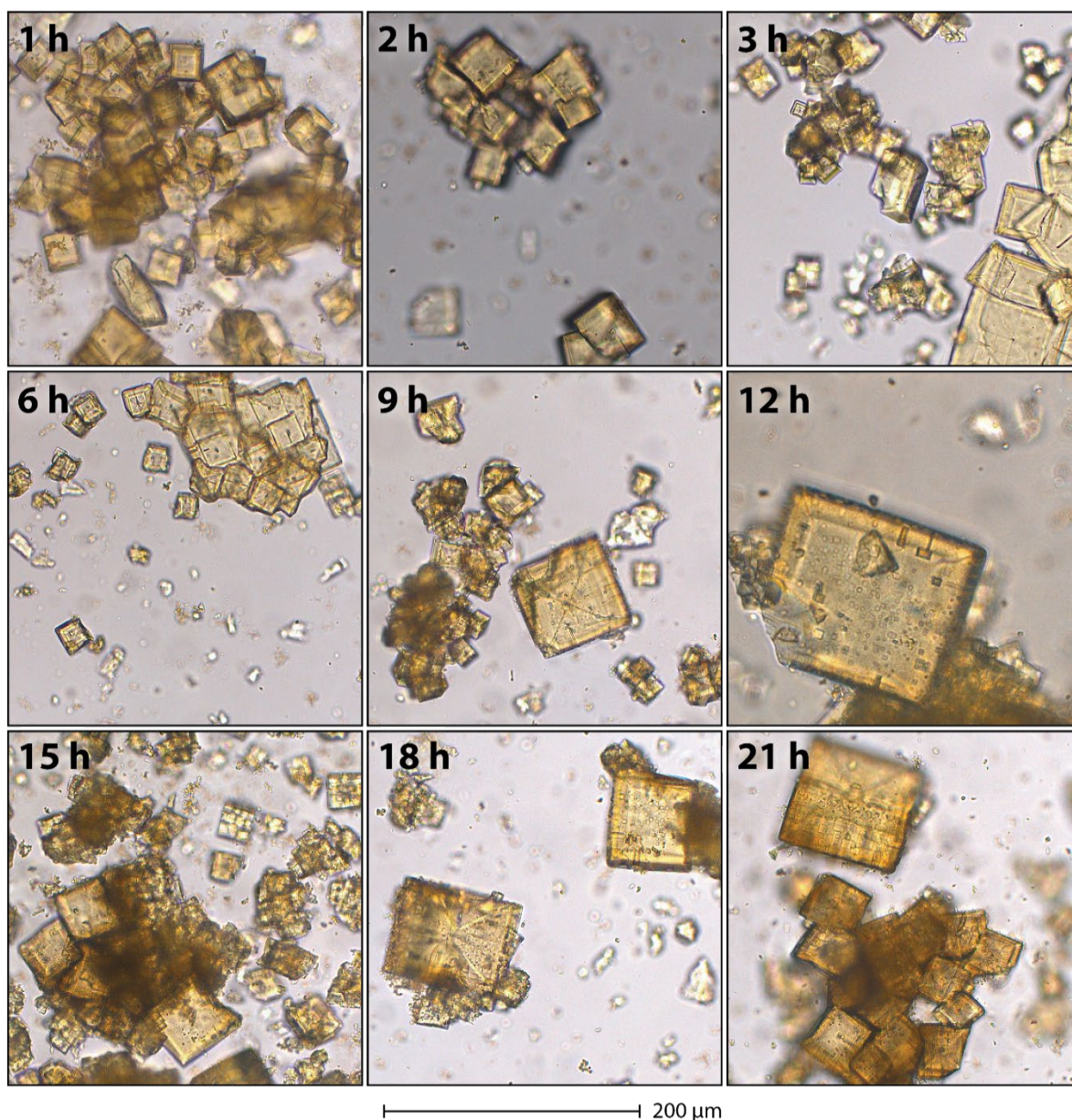


Figure 4.5: Optical micrographs of MUF-92 at various stages of growth.

We followed the growth of the secondary lattice in MUF-92 by both SCXRD and ^1H NMR spectroscopy (Figure 4.6), just as with MUF-91. Again, the two parameters closely track each other until the secondary lattice stops growing, at nine hours or three rounds of exposure to secondary growth conditions. After the growth of the secondary lattice reaches its plateau, the amount of BPDC-NH₂ in the sample increases rapidly, and the two measures diverge from each other. The increase in the amount of secondary ligand present after the plateau is faster than that for MUF-91, which I attribute to the uncharacterised amorphous phase mentioned above.

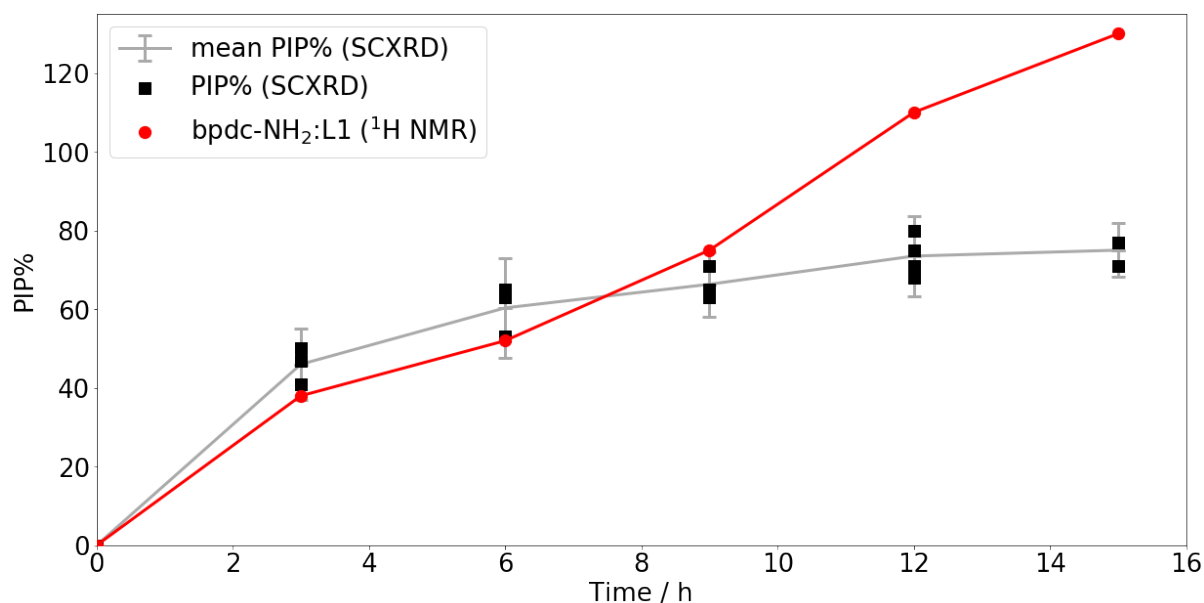


Figure 4.6: Plot of complementary characterisation data for MUF-92. Black squares represent the PIP% values obtained from SCXRD datasets collected at various time points in the growth of MUF-93. Red circles represent the ratio of BPDC-NH₂ to L1 as determined by ¹H-NMR. The grey line is drawn through the mean PIP% (from all SCXRD datasets) and the error bars correspond to the 95% confidence interval for the mean PIP% value for the sample.

The SCXRD structures of MUF-92 show (**Figure 4.7**) that the BPDC-NH₂ ligand adopts a conformation where its two phenyl rings are perfectly orthogonal. This is the preferred conformation for this ligand, putting the amino group as far away from other atoms as possible. This arrangement is impossible for L1, where the two backbone rings are bridged and offset by a maximum of 53 °, corroborating our view that there is little if any exchange of ligands between the two lattices.

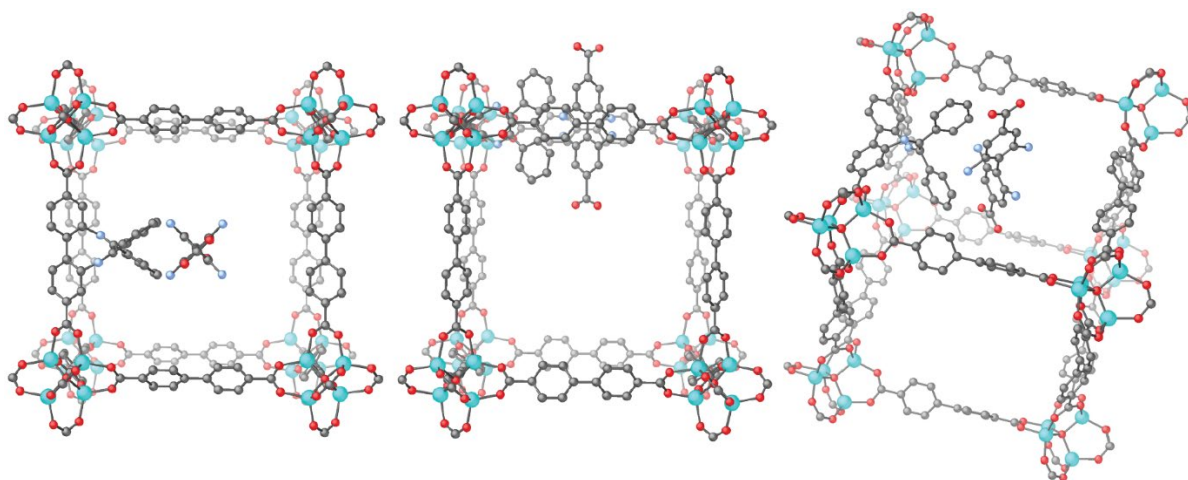


Figure 4.7: The placement of BPDC-NH₂ in MUF-92, in various orientations. The NH₂ side chain is disordered over four positions and the two backbone phenyl rings are arranged orthogonally. For clarity, hydrogens and all but one side chain from L1 have been removed. Carbons are grey, oxygen red, nitrogen blue, and zinc cyan.

Table 4.2 shows some representative results from the SCXRD datasets collected from MUF-92. At its best, the data we obtained from this MOF was very good, with final R_1 values around 11%. We tried unsuccessfully to obtain datasets at shorter time points and lower PIP% values (the lowest obtained was 41%) but despite many attempts we couldn't obtain any such datasets which were stable to refinement.

Table 4.2: Crystallographic data for representative samples of MUF-92

	Low PIP% (worst data)	Medium PIP% (representative data)	High PIP% (best data)
Identification Code	MUF-92-3h-41pc	MUF-92-6h-65pc	MUF-92-12h-71pc
Empirical formula	C _{101.13} H _{68.68} N _{8.45} O _{18.31} Zn _{5.63}	C _{111.48} H _{71.54} N _{7.96} O _{21.51} Zn _{6.62}	C _{113.92} H _{73.64} N _{8.14} O _{22.26} Zn _{6.85}
Interpenetration fraction (PIP%)	0.41	0.65	0.71
Formula weight	2063.14	2299.36	2360.33
Temperature / K		100(2)	
Crystal system		cubic	
Space group		P-43m	
a,b,c / Å	17.146(7)	17.140(3)	17.1190(7)
α, β, γ / °		90	
Volume / Å³	5041(6)	5035(3)	5016.9(6)
Z		1	
$\rho_{\text{calc}} / \text{g cm}^{-3}$	0.680	0.758	0.781
M / mm⁻¹	0.694	0.814	0.845
F(000) / e⁻	1050.0	1167.0	1198.0
Radiation	Synchrotron ($\lambda = 0.7108$ Å)		
2Θ range for data collection / °	5.312 to 32.93	5.314 to 37.634	5.322 to 52.694
Index ranges	-13 \leq h \leq 13, -13 \leq k \leq 13, -12 \leq l \leq 13	-15 \leq h \leq 15, -15 \leq k \leq 15, -14 \leq l \leq 15	-18 \leq h \leq 18, -13 \leq k \leq 20, -16 \leq l \leq 19
Reflections collected	6213	9105	15680
Independent reflections	558 [$R_{\text{int}} = 0.0781$, $R_{\text{sigma}} = 0.1066$]	795 [$R_{\text{int}} = 0.0950$, $R_{\text{sigma}} = 0.0373$]	1926 [$R_{\text{int}} = 0.0644$, $R_{\text{sigma}} = 0.0341$]
Data/restraints/parameters	558/120/66	795/120/66	1926/120/66
GooF on F²	1.764	1.633	1.212
Final R indexes [I \geq 2σ (I)]	$R_1 = 0.1844$, $wR_2 = 0.3888$	$R_1 = 0.1504$, $wR_2 = 0.3405$	$R_1 = 0.1098$, $wR_2 = 0.2979$
Final R indexes [all data]	$R_1 = 0.1993$, $wR_2 = 0.4183$	$R_1 = 0.1580$, $wR_2 = 0.3560$	$R_1 = 0.1495$, $wR_2 = 0.3300$
Largest diff. peak/hole / e Å⁻³	0.62/-0.50	0.89/-0.39	0.66/-0.52
Flack parameter	0.54(6)	0.27(4)	0.578(18)

MUF-92 was also prepared as a microcrystalline powder. In this case the plateau of interpenetration was not increased by as much as in MUF-91, reaching about 75% PIP (Figure 4.8). Correlation of the ligand ratio with the PIP% determined from PXRD is very good throughout most of the growth period (from 8 – 14 hours). In the early phase of growth there is notably more BPDC-NH₂ present than expected. This could be due to the adsorption of some BPDC-NH₂ into the pores of α -MUF-9. We don't have any direct evidence for this, but the noncovalent interactions which we know to be present between the ligands supports this interpretation.

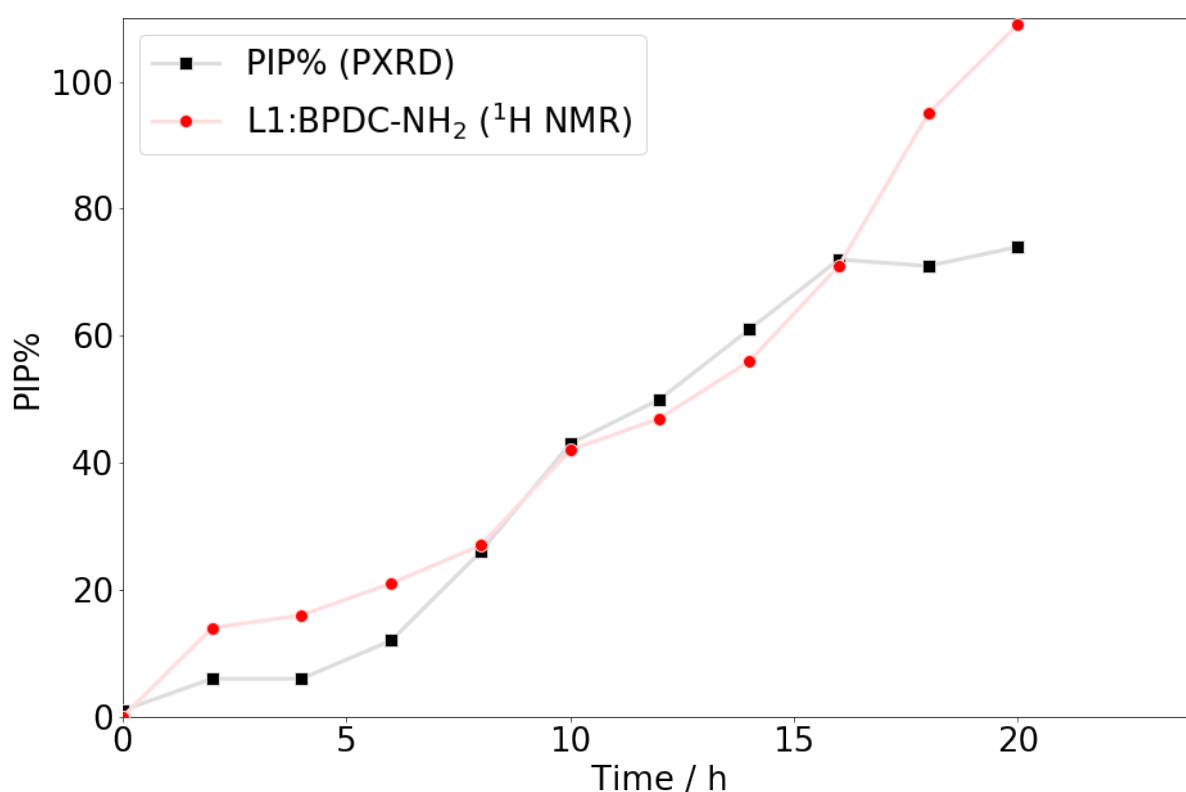


Figure 4.8: Growth over time of [Zn₄O(bpdc-NH₂)₃] in powder MUF-9. Black squares represent the interpenetration percentage determined from PXRD patterns (Figure 4.17) and red circles represent the ratio of BPDC-NH₂ to L1 as determined by ¹H-NMR, for digested samples of powder MUF-91.

4.4. MUF-93

In MUF-93, $[\text{Co}_4\text{O}(\text{bpdc})_3]$ is the interpenetrating secondary lattice templated by the primary MUF-9 lattice. This framework is not known to have been synthesised directly and does not form in similar reaction mixtures without the MUF-9 template. A PXRD of the result of such a reaction is presented in section 4.6.3.1

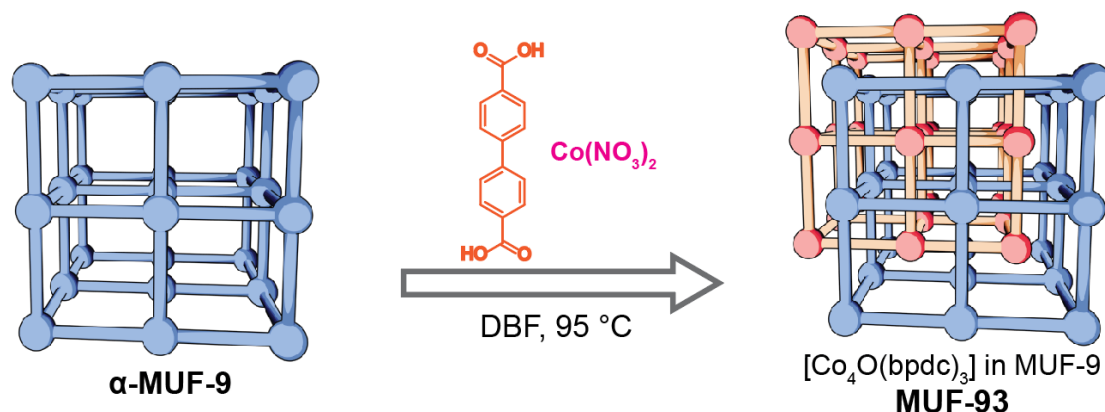


Figure 4.9: Illustration of the synthetic method to produce MUF-93

Similar visual changes to the crystals as with MUF-92 are apparent during MUF-93 synthesis – except they are even more distinct because of the purple colour of the cobalt(II) ions. As shown in Figure 4.11, the interpenetrated regions around the edges darken and the crystals turn a deeper purple over time.

As with MUF-92, no shell phase forms on the outside of the crystals. Instead, a similar amorphous phase deposits external to the MUF-93 crystals, in larger quantities over time, as with MUF-92. It seems likely that since this occurred for the combinations of cobalt with BPDC and the combination of zinc with BPDC- NH_2 , but wasn't observed in other trials, that such phases form when the additional components don't readily form a MOF themselves. This phase was analysed by SEM with EDS which showed only the presence of zinc, not cobalt, and by ^1H NMR after digestion, which showed almost exclusively BPDC. Its PXRD contains no peaks, so it is likely an amorphous coordination polymer of BPDC and cobalt. Those characterisation data are in Appendix B, page B-3.

Characterisation by PXRD is also identical to the other hetero-interpenetrated MOFs we have looked at, with the peaks at $2\theta = 5.2$ and 7.3 decreasing and increasing respectively as the secondary lattice forms. The PXRD data are shown in Section 4.6.3.3 (page 108).

We collected data on MUF-93 which directly shows the core-shell nature of hetero-interpenetrated materials. Figure 4.10A has a stylised rendition of a MUF-93 crystal, with highly interpenetrated regions around the outside and low interpenetration in the core of the crystal.

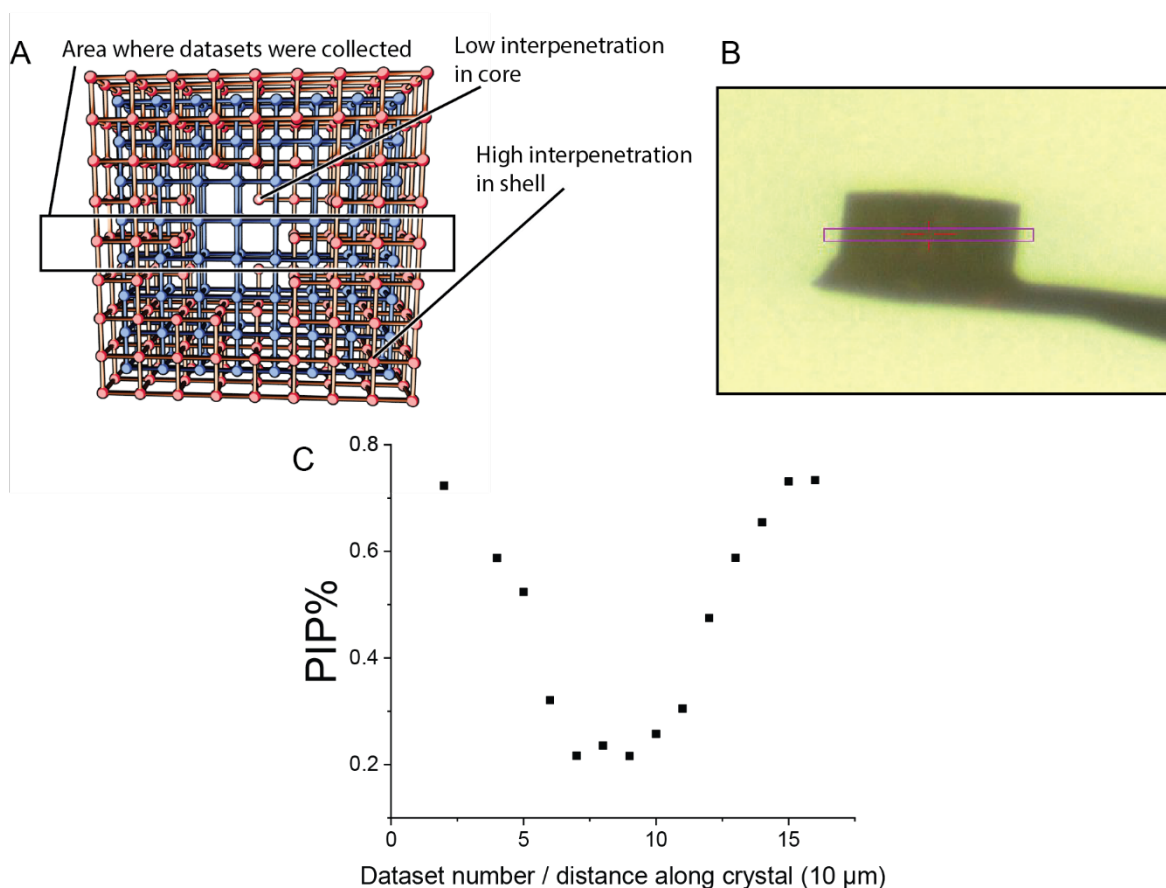


Figure 4.10: A) An illustration of a crystal of MUF-93 showing regions with different interpenetration properties. B) a photograph showing the crystal of MUF-93 and the section scanned along. C) a plot of PIP values determined from SCXRD datasets collected at various points along a scan across a single crystal of MUF-93.

We collected SCXRD datasets while scanning along a crystal of MUF-93 (a photo of this crystal is shown in Figure 4.10B) and determined the interpenetration percentage at each point. This was possible thanks to software at the Australian Synchrotron MX2 beamline which allows positioning of a mounted crystal along a predefined grid.

Thanks to the high symmetry of MUF-93, rotation on a single axis is sufficient to capture all orientations of the crystal. Therefore, we could collect a dataset at one position, move the crystal by 10 μm , collect another dataset, and so on.

These datasets show that the outer regions (20 – 30 μm) of the crystals are highly interpenetrated, as shown on by the outer points on Figure 4.10C. The points for dataset numbers 2 and 15 were taken near the outside of the crystal and show around 75 PIP%, while the points for datasets 6-8, near the centre of the crystal, show around 25 PIP%. This supports our proposed mechanism for the formation of secondary lattices in MUF-9, which is that they are formed by the additional components entering the MUF-9 pores, without the MUF-9 changing or rearranging itself. Following on from that, it explains why MUFs 91-93 all stop growing after a certain plateau, and why the plateau is higher for smaller crystal sizes. This plateau occurs because when the outer regions of the crystal are fully interpenetrated, no more new ligand molecules from the secondary growth solution can reach the centre of the crystal.

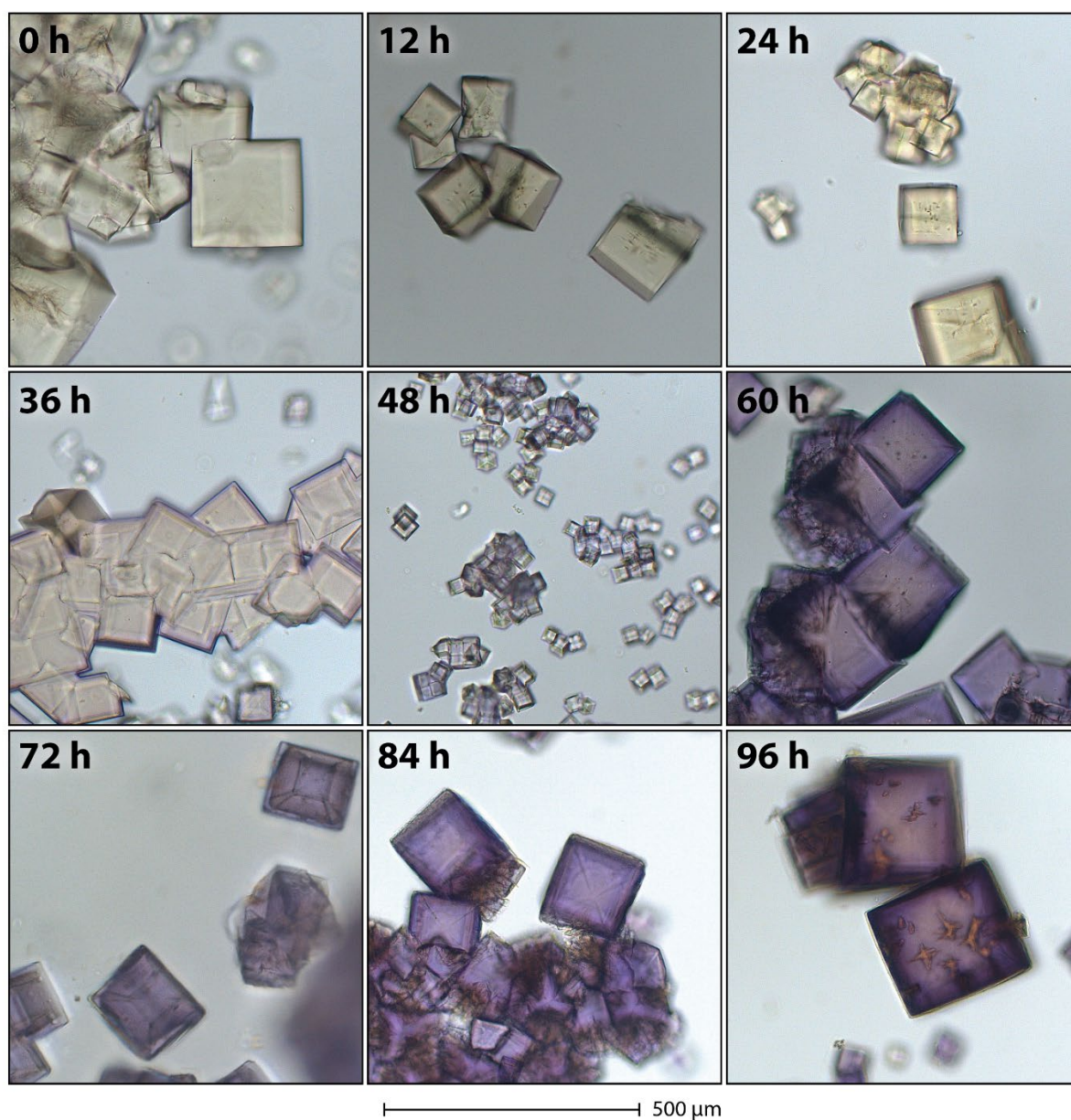


Figure 4.11: Optical micrographs of MUF-93 at various stages of growth

The growth of the secondary lattice in MUF-93 was also analysed by ^1H NMR spectroscopy of digested samples, in order to determine the ratio of BPDC to L1 for each sample. These spectra are displayed in Figure 4.12. In d_6 -DMSO, unlike in D_2O , all the peaks of both ligands are well separated. In this case, the ratio was calculated using the average of all the peak integrals.

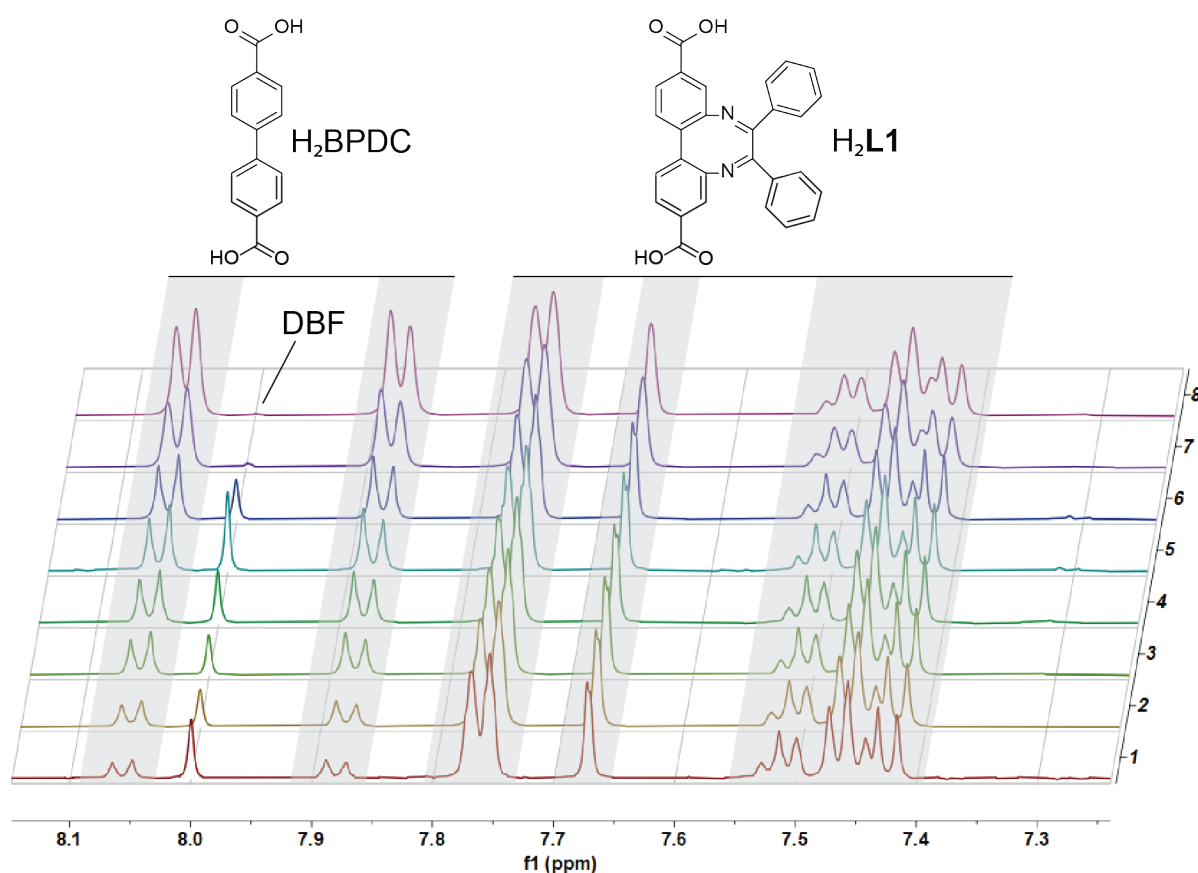


Figure 4.12: ^1H NMR spectra of digested samples of MUF-93 as the secondary lattice grows in over time. Spectra 1-8 were taken after 3, 6, 9, 12, 15, and 18 hours of secondary growth respectively. Spectra were measured in 165 mM DCl in d_6 -DMSO.

For MUF-93, we can add an additional characterisation method to track the growth over time. Just as NMR spectroscopy can tell us about the ligand ratio, atomic absorption spectroscopy (AAS) tells us about the ratio of cobalt to zinc in samples of MUF-93. We expect that the ratio of metals should track the interpenetration percentage if the secondary lattice forms exclusively from cobalt(II) and no cobalt(II) is integrated into the primary lattice.

We observe limited exchange of cobalt(II) into the original framework by displacement of the zinc(II) ions of the $[\text{Zn}_4\text{O}]$ clusters during the growth of $[\text{Co}_4\text{O}(\text{bpdc})_3]$ in MUF-9. This is evidenced by the match between the amount of cobalt determined by AAS and that expected based on the PIP% level determined by SCXRD assuming that no Co/Zn exchange takes place. We note that exchange of three out of four zinc(II) ions per node is possible through heating α -MUF-9 in concentrated

solutions of cobalt(II) nitrate in DBF (Chapter 1), which is in agreement with the literature¹⁴³ on other MOFs with $[\text{Zn}_4\text{O}]$ nodes.

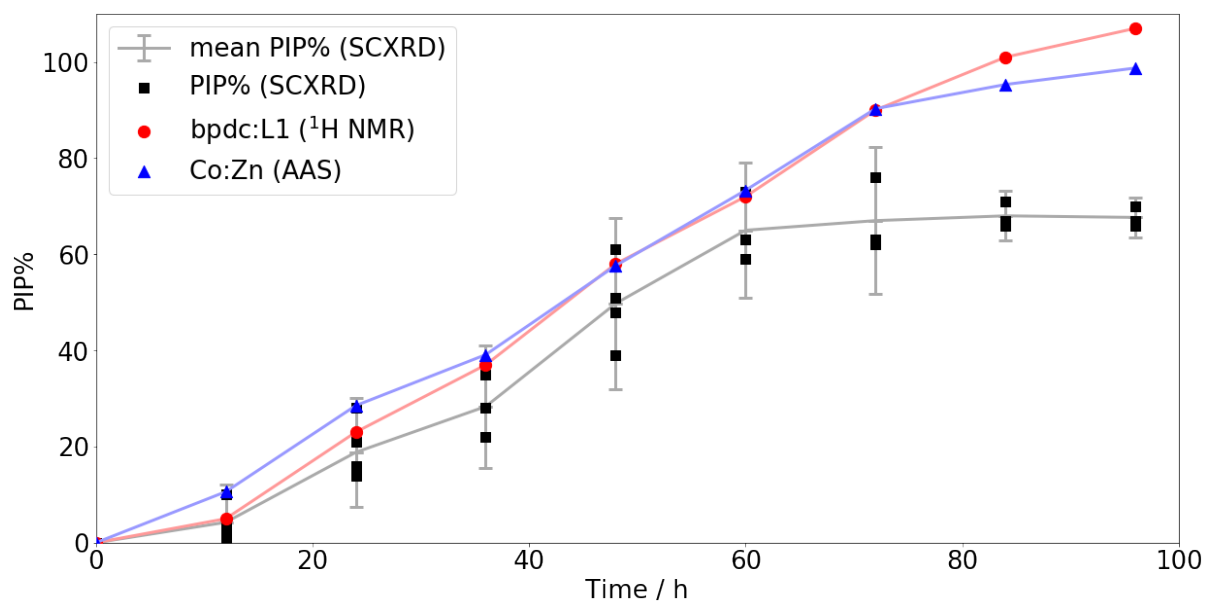


Figure 4.13: Plot of complementary characterisation data for MUF-93. Black squares represent the PIP% values obtained from SCXRD datasets collected at various time points in the growth of MUF-93. Red circles represent the ratio of BPDC to L1 as determined by ^1H -NMR and blue triangles represent the ratio of Co to Zn as determined by flame AAS, for the same digested samples of MUF-93. The grey line is drawn through the mean PIP% (from all SCXRD datasets) and the error bars correspond to the 95% confidence interval for the mean PIP% value for the sample.

Despite the potential for cobalt(II) to be incorporated into α -MUF-9, low exchange of cobalt(II) into the primary lattice during the growth of MUF-93 is expected, as the concentration of cobalt in the growth solution is much lower than that needed for rapid exchange, and the exchange process is outcompeted by the growth process.

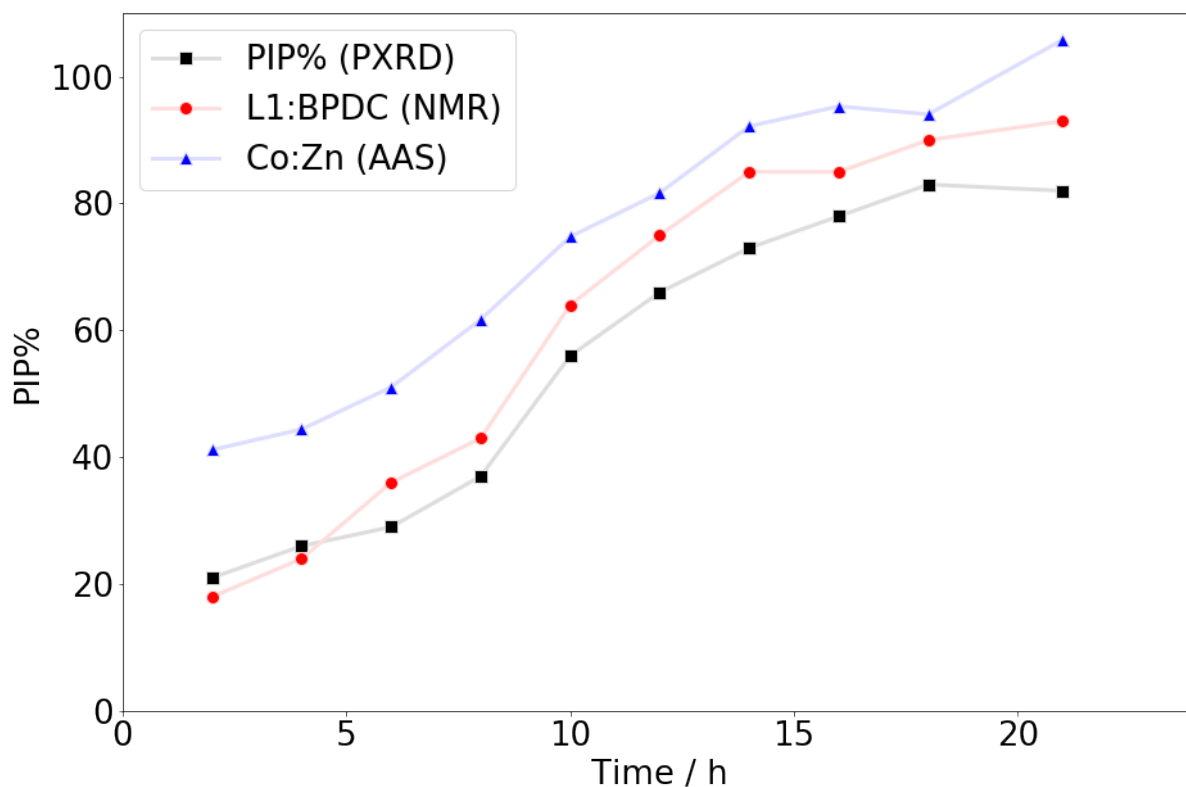


Figure 4.14: A plot of complementary characterisation data for MUF-93 prepared from powder α -MUF-9. Black squares represent the percentage of interpenetration of the sample as determined by PXR, blue triangles represent the ratio of Co : Zn as determined by flame AAS and red circles represent the ratio of BPDC : L1 as determined by ^1H -NMR, in the digested samples of powder MUF-93.

MUF-93 was also synthesised as a microcrystalline powder. Figure 4.14 shows the complementary PXR, SCXR, and AAS data for powder MUF-93. The various characterisation methods for powder MUF-93 are well correlated, although the values for the metal ratio are very high in the early stages of growth. I hypothesise that this is due to small fragments of the secondary lattice which are terminated in cobalt clusters rather than dangling ligands. That situation would be consistent with the initially high ratio of cobalt to BPDC (secondary metal to secondary ligand) which approaches parity as the growth of the second lattice continues.

Table 4.3: Crystallographic results for selected datasets obtained from MUF-93

	Low PIP% (worst data)	Medium PIP% (representative data)	High PIP% (best data)
Identification code	MUF-93-12h-4pc	MUF-93-48h-48pc	MUF-93-84h-66pc
Empirical formula	C _{85.71} H _{48.99} Co _{0.16} N ₆ O _{13.53} Zn ₄	C _{104.15} H _{59.52} Co _{1.92} N ₆ O _{19.24} Zn ₄	C _{111.57} H _{63.76} Co _{2.63} N ₆ O _{21.53} Zn ₄
Interpenetration fraction	0.04	0.48	0.66
Formula weight	1650.19	2077.31	2249.23
Temperature / K	100(2)	100(2)	100(2)
Crystal system	cubic	cubic	cubic
Space group	P-43m	P-43m	P-43m
a,b,c / Å	16.90(5)	17.101(8)	17.098(8)
α, β, γ / °	90	90	90
Volume / Å³	4827(43)	5001(7)	4998(7)
Z	1.00008	1.00008	1
ρ_{calc} / g cm⁻³	0.568	0.690	0.747
M / mm⁻¹	0.532	0.662	0.723
F(000) / e⁻	838.0	1052.0	1138.0
Radiation	Synchrotron ($\lambda = 0.7109$ Å)		Synchrotron ($\lambda = 0.7085$ Å)
2θ range for data collection / °	5.392 to 27.312	7.126 to 48.82	5.31 to 46.296
Index ranges	-11 ≤ h ≤ 11, -11 ≤ k ≤ 11, -11 ≤ l ≤ 11	-19 ≤ h ≤ 19, -19 ≤ k ≤ 14, -9 ≤ l ≤ 19	-18 ≤ h ≤ 18, -18 ≤ k ≤ 14, -11 ≤ l ≤ 18
Reflections collected	5274	14970	13070
Independent reflections	319 [Rint = 0.1635, Rsigma = 0.0493]	1605 [Rint = 0.0714, Rsigma = 0.0316]	1391 [Rint = 0.0513, Rsigma = 0.0235]
Data/restraints/parameters	319/223/55	1605/223/55	1391/223/55
Goodness-of-fit on F²	1.882	2.091	1.715
Final R indexes [I>=2σ (I)]	R ₁ = 0.2221, wR ₂ = 0.4955	R ₁ = 0.1615, wR ₂ = 0.4415	R ₁ = 0.1304, wR ₂ = 0.3709
Final R indexes [all data]	R ₁ = 0.2604, wR ₂ = 0.5260	R ₁ = 0.1807, wR ₂ = 0.4646	R ₁ = 0.1415, wR ₂ = 0.3843
Largest diff. peak/hole / e Å⁻³	0.36/-0.23	2.14/-1.27	1.12/-0.61
Flack parameter	0.42(7)	0.195(17)	0.307(14)

4.5. CONCLUSIONS

In this chapter, we show that the method for producing hetero-interpenetrated frameworks through secondary growth in α -MUF-9 introduced in Chapter 3 is generalisable to a wide variety of BPDC-based ligands as long as they meet certain demands. The main demand is that the side chain should not be too large (proline extends approximately 5 Å), and it should be on one side of the ligand only.

This method is also extensible to other metals. MUF-93 with the [Co₄O] SBU has been characterised thoroughly and we also have some evidence of success with Mg. One thing that remains to be fully determined about MUF-93 is whether each framework truly retains its identity. Although we can tell from the AAS analysis of digested samples that cobalt does not replace zinc in the primary framework on a bulk scale, we cannot completely rule out the possibility of scrambling of metals between the lattices. This question will be addressed in the next chapter.

A similar amount of variation is seen in all materials. There is considerable spread of PIP% values between individual crystals in a sample, but the bulk materials follow clear trends.

All the materials we have produced in this chapter and the preceding one reach a plateau of secondary growth. For MUF-9, we had attributed the formation of a noninterpenetrated phase to the steric unfavourability of the interpenetrated phase in the bulky solvent, and that the rate of growth of the primary framework is faster than that of the secondary framework. The inference we must take from the plateau of secondary growth is that the components of these MOFs are largely fixed in place at 95 °C in DBF. Otherwise, they could continue to rearrange and eventually reach a fully interpenetrated phase with scrambled components. Therefore, the significantly lower solubility of the components in DBF compared to DMF could also have an impact on the formation of these partially interpenetrated and hetero-interpenetrated materials.

The secondary lattices explored in this chapter may not form on their own – they are templated by the MUF-9 primary framework. This platform, therefore, provides an opportunity to study frameworks which are difficult or impossible to otherwise access.

We have also shown that it is possible to use ligands for the secondary lattice with a range of functional groups. This should give us hope that we can exploit the control we can exert over the pore chemistry in hetero-interpenetrated MOFs to tune them towards a desired application. That possibility will be explored in Chapter 6.

4.6. EXPERIMENTAL DETAILS

All CIF files relevant to this chapter are listed in Appendix B, page B-7. The files are available electronically on the included CD-ROM.

4.6.1. MOF Protocols

4.6.1.1. General synthetic method for hetero-interpenetrated MOFs (SL3 – SL6)

α -MUF-9 was synthesised in a 4 mL glass vial with a phenolic cap by a literature method⁹⁹. A stock solution of secondary ligand (1 mg mL⁻¹), Zn(NO₃)₂·4H₂O (2 mg mL⁻¹) and 2-fluorobenzoic acid (2 mg mL⁻¹) was prepared in DBF. The solvent was removed from a vial of α -MUF-9 and replaced with this stock solution, after which the vial was heated in a dry bath set to 85 °C. The stock solution was removed and replaced with fresh solution every 6 hours. At the desired stage of growth, the crystals were removed from the dry bath, cooled to room temperature, and washed several times with DBF.

4.6.1.2. Synthesis of MUF-92

α -MUF-9 was synthesised in a 4 mL glass vial with a phenolic cap by a literature method⁹⁹. A stock solution of H₂-BPDC-NH₂ (1 mg mL⁻¹), Zn(NO₃)₂·4H₂O (2 mg mL⁻¹) and 2-fluorobenzoic acid (3 mg mL⁻¹) was prepared in DBF. The solvent was removed from a vial of α -MUF-9 and replaced with this stock solution, after which the vial was heated in a dry bath set to 95 °C. The stock solution was removed and replaced with fresh solution every three hours. At the desired stage of growth, the crystals were removed from the dry bath, cooled to room temperature, and washed several times with DBF.

4.6.1.3. Synthesis of powder MUF-92

L1 (36 mg) and Zn(NO₃)₂·4H₂O (64 mg) were dissolved in DBF (4 mL) with H₂O (10 μ L) in a 25 mL Schott bottle and heated in an 85°C oven for 6 hours, shaking the mixture every hour. The resulting small crystals were then transferred to a 4 mL vial which was packed into a 50 mL centrifuge tube and centrifuged at 1000 rpm for 0.5 minutes at speed. The supernatant was replaced with 2 mL of a stock solution of H₂-BPDC-NH₂ (1 mg mL⁻¹), Zn(NO₃)₂·4H₂O (2 mg mL⁻¹) and 2-fluorobenzoic acid (3 mg

mL⁻¹) in DBF, and the crystals were heated in a dry bath set at 95 °C. At intervals of two hours, the crystals were centrifuged, a sample taken out, and the solution exchanged for fresh stock solution, then heating continued.

4.6.1.4. *Synthesis of MUF-93*

α -MUF-9 was synthesised in a 4 mL glass vial with phenolic cap by a literature method⁹⁹. A stock solution of H₂-BPDC (0.5 mg mL⁻¹), Co(NO₃)₂·6H₂O (2 mg mL⁻¹) and 2-fluorobenzoic acid (2 mg mL⁻¹) was prepared in DBF. The solvent was removed from a vial of α -MUF-9 and replaced with this stock solution, after which the vial was heated in a dry bath set to 75 °C. The stock solution was removed and replaced with fresh solution every 12 hours. At the desired stage of growth, the vial was removed from the dry bath, cooled to room temperature, and the crystals washed several times with DBF.

4.6.1.5. *Synthesis of powder MUF-93*

L1 (36 mg) and Zn(NO₃)₂·4H₂O (64 mg) were dissolved in DBF (4 mL) with H₂O (10 μ L) in a 25 mL Schott bottle and heated in an 85°C oven for 6 hours, shaking the mixture every hour. The resulting small crystals were then transferred to a 4 mL vial which was packed into a 50 mL centrifuge tube and centrifuged at 1000 rpm for 0.5 minutes at speed. The supernatant was replaced with 2 mL of a stock solution of H₂-BPDC (0.5 mg mL⁻¹), Zn(NO₃)₂·4H₂O (2 mg mL⁻¹) and 2-fluorobenzoic acid (3 mg mL⁻¹) in DBF, and the crystals were heated in a dry bath set at 95 °C. At intervals of two hours, the crystals were centrifuged, a sample taken out, and the solution exchanged for fresh stock solution, then heating continued.

4.6.1.6. *MOF digests*

For digestion, MUF-93 samples were washed with DMF three times, then acetone five times. Excess solvent was removed, and the MOF dried under vacuum overnight. To the dried MOF, 0.2 mL of a 375 mM solution of DCl in d₆-DMSO was first added, and the mixture sonicated until the MOF was dissolved, then a further 0.4 mL of d₆-DMSO

added. This solution was then used for ^1H NMR analysis before being further used for AAS.

4.6.2. $[\text{Mg}_4\text{O}(\text{bpdc})_3]$ in MUF-9

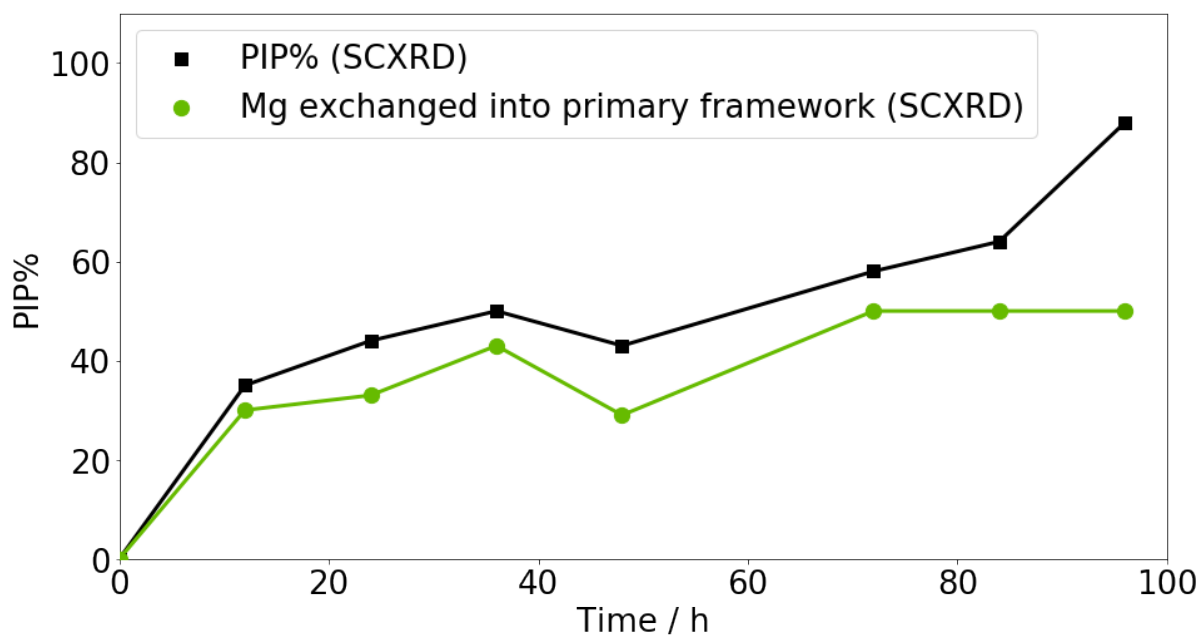


Figure 4.15: Plot of the growth of $[\text{Mg}_4\text{O}(\text{bpdc})_3]$ in α -MUF-9 over time. Black squares represent the PIP% values determined from single crystal datasets, while green circles represent the percentage of zinc in the primary lattice replaced by magnesium, determined from the same single crystal datasets.

4.6.3. PXRD patterns

4.6.3.1. Attempted syntheses with secondary precursors

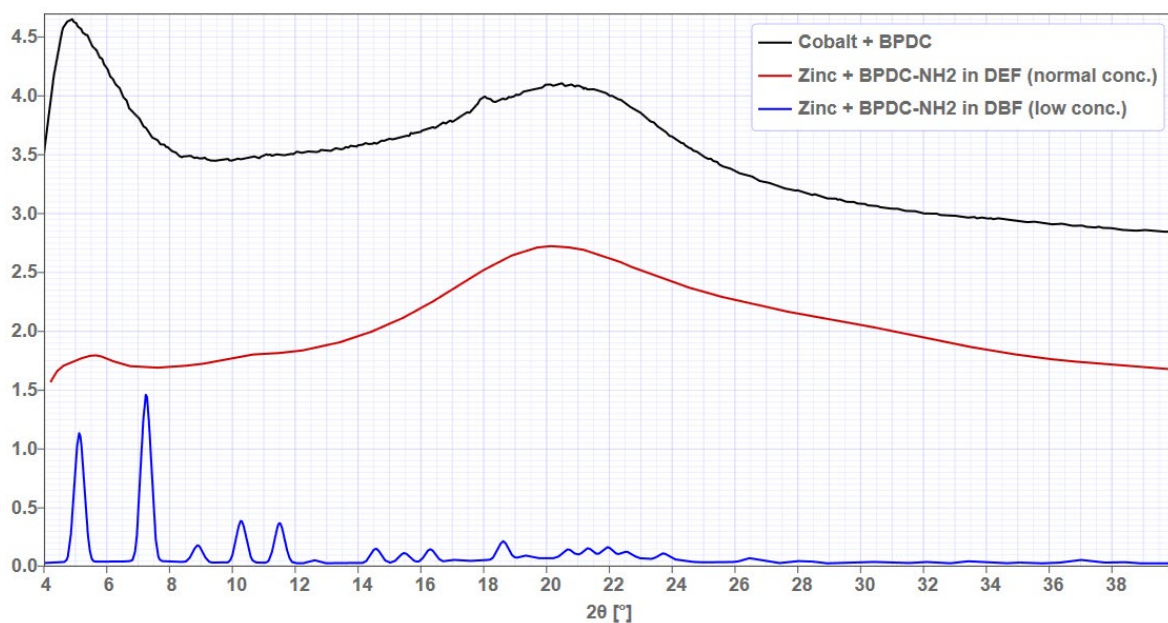


Figure 4.16: PXRD patterns of representative results of synthesis of MOFs with cobalt and BPDC (top, black), zinc and BPDC-NH₂ under ordinary synthetic conditions (middle, red), and at low concentration in DBF (bottom, blue).

4.6.3.2. Powder MUF-92

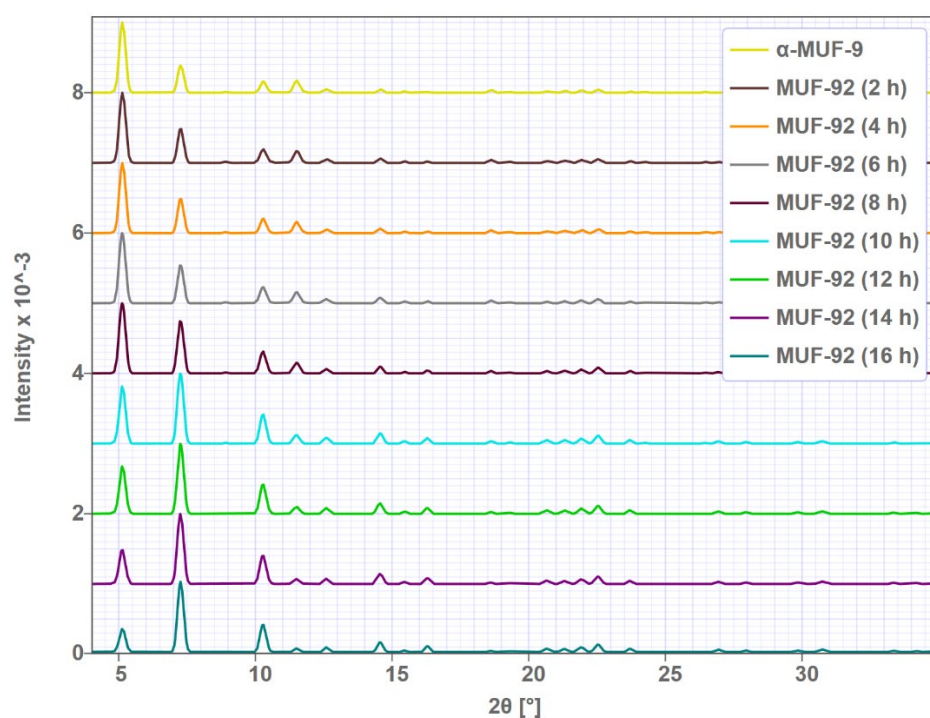


Figure 4.17: Baseline-corrected PXRD patterns of MUF-92 grown from powder α -MUF-9.

4.6.3.3. MUF-93

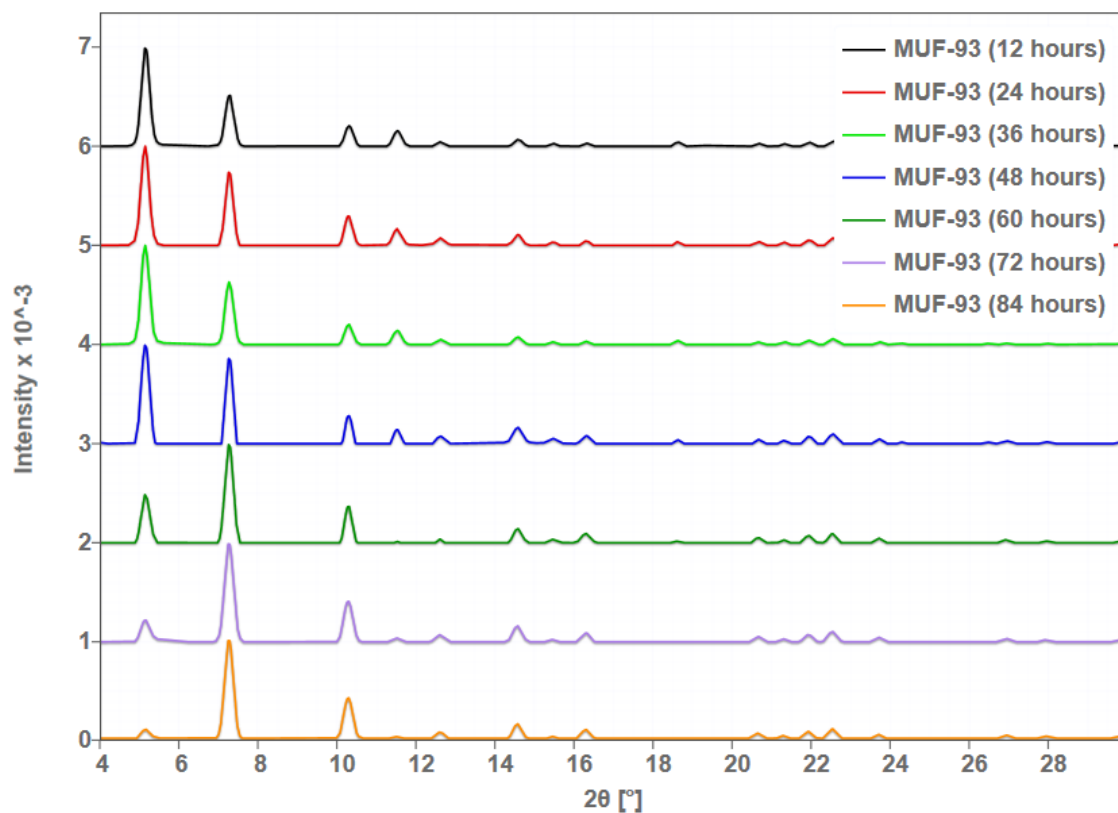


Figure 4.18: PXRD patterns of MUF-93 at various stages of growth.

4.6.3.4. Powder MUF-93

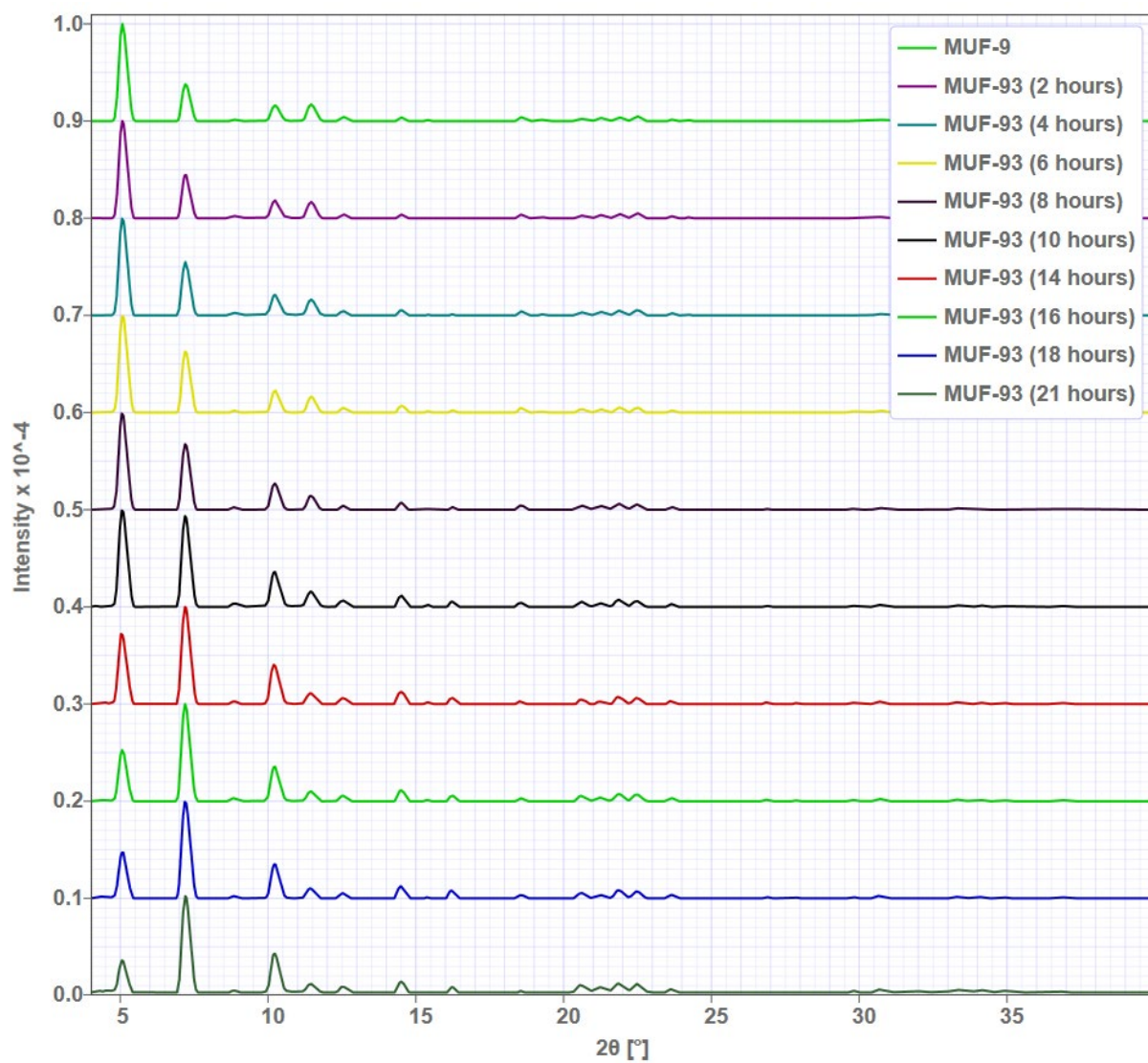


Figure 4.19: Baseline-corrected and scaled PXRD patterns of powder MUF-93 as used for interpenetration percentage determination.

4.6.4. ^1H NMR data

4.6.4.1. MUF-92

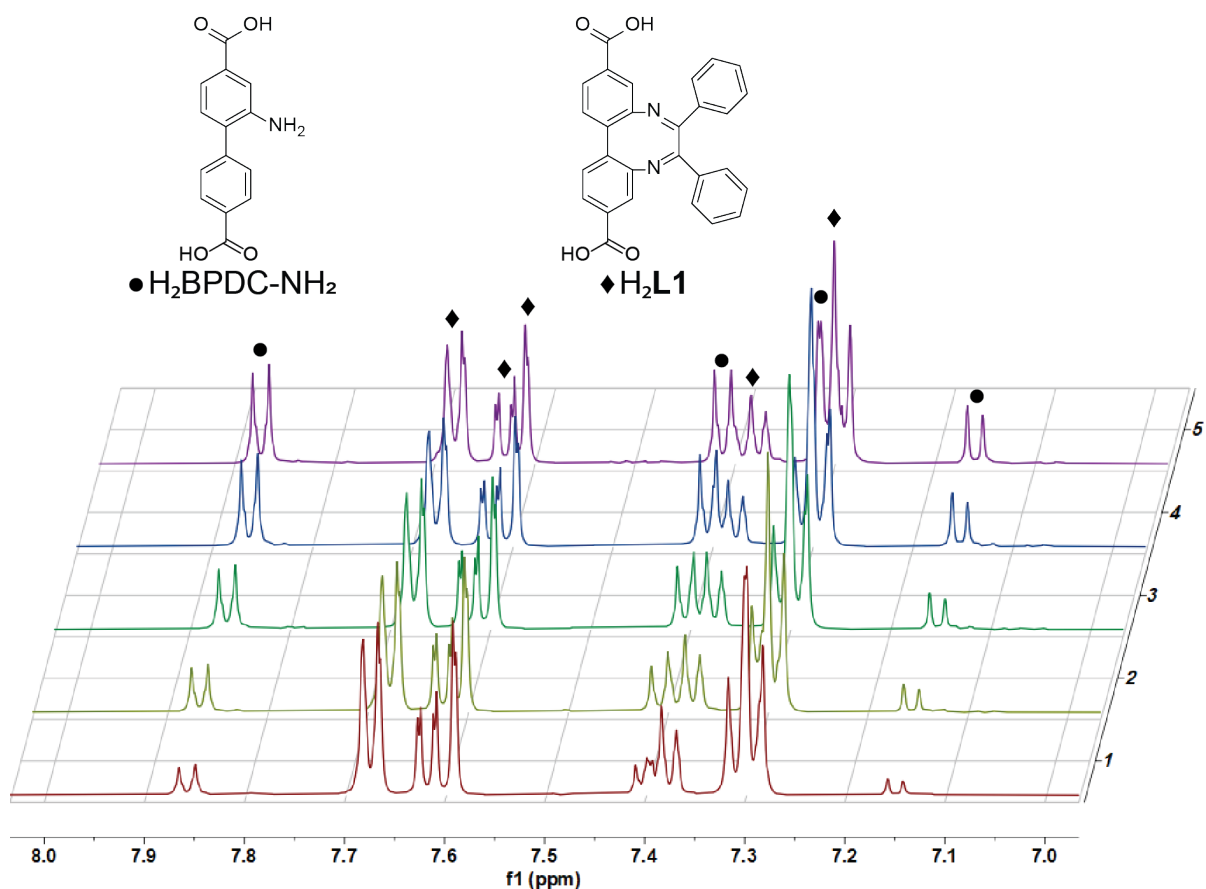


Figure 4.20: ^1H NMR spectra of digested samples of MUF-92 as the secondary lattice grows in over time. Spectra 1-5 were taken after 3, 6, 9, 12, and 15 hours of secondary growth respectively. Spectra were measured in 0.2M NaOD in D_2O .

4.6.4.2. NMR data for powder MUF-92 and -93

Table 4.4: Percentages of BPDC- NH_2 (MUF-92) or BPDC (MUF-91) to L1 as determined by ^1H NMR spectroscopy of digested samples which were prepared from a microcrystalline powder of α -MUF-9

Time / h	2	4	6	8	10	12	14	16	18
MUF-92	1	6	6	12	26	43	50	61	72
MUF-93	18	24	36	43	64	75	85	85	90

4.7. REFERENCES

30. Eddaoudi, M.; Kim, J.; Rosi, N.; Vodak, D.; Wachter, J.; O'Keeffe, M.; Yaghi, O. M., Systematic Design of Pore Size and Functionality in Isorecticular MOFs and Their Application in Methane Storage. *Science* **2002**, 295 (5554), 469–472. DOI: DOI 10.1126/science.1067208
35. Lun, D. J.; Waterhouse, G. I.; Telfer, S. G., A general thermolabile protecting group strategy for organocatalytic metal-organic frameworks. *J. Am. Chem. Soc.* **2011**, 133 (15), 5806-9. DOI: 10.1021/ja202223d
66. Liu, L.; Zhou, T.-Y.; Telfer, S. G., Modulating the Performance of an Asymmetric Organocatalyst by Tuning Its Spatial Environment in a Metal–Organic Framework. *J. Am. Chem. Soc.* **2017**, 139 (39), 13936-13943. DOI: 10.1021/jacs.7b07921
99. Ferguson, A.; Liu, L.; Tapperwijn, S. J.; Perl, D.; Coudert, F.-X.; Van Cleuvenbergen, S.; Verbiest, T.; van der Veen, M. A.; Telfer, S. G., Controlled partial interpenetration in metal–organic frameworks. *Nat. Chem.* **2016**, 8 (3), 250-257. DOI: 10.1038/nchem.2430
131. Hausdorf, S.; Baitalow, F.; Bohle, T.; Rafaja, D.; Mertens, F. O., Main-group and transition-element IRMOF homologues. *J. Am. Chem. Soc.* **2010**, 132 (32), 10978-81. DOI: 10.1021/ja1028777
132. Tonigold, M.; Lu, Y.; Bredenkötter, B.; Rieger, B.; Bahnmüller, S.; Hitzbleck, J.; Langstein, G.; Volkmer, D., Heterogeneous Catalytic Oxidation by MFU-1: A Cobalt(II)-Containing Metal-Organic Framework. *Angew. Chem. Int. Ed.* **2009**, 48 (41), 7546–7550. DOI: 10.1002/anie.200901241
133. Shen, K.; Zhang, M.; Zheng, H., Critical factors influencing the structures and properties of metal–organic frameworks. *CrystEngComm* **2015**, 17 (5), 981-991. DOI: 10.1039/c4ce02150a
134. Guillerme, V.; MasPOCH, D., Geometry Mismatch and Reticular Chemistry: Strategies To Assemble Metal-Organic Frameworks with Non-default Topologies. *J. Am. Chem. Soc.* **2019**, 141 (42), 16517-16538. DOI: 10.1021/jacs.9b08754
135. Wu, S.-H.; Wang, S.; Fang, W.-L.; Guo, X.-F.; Wang, H., An exceptionally stable Zr-based fluorescent metal–organic framework for highly selective detection of pH. *Analytical Methods* **2019**, 11 (1), 36-43. DOI: 10.1039/c8ay01998c
136. Van Zeeland, R.; Li, X.; Huang, W.; Stanley, L. M., MOF-253-Pd(OAc)₂: a recyclable MOF for transition-metal catalysis in water. *RSC Advances* **2016**, 6 (61), 56330-56334. DOI: 10.1039/c6ra12746k
137. Zhang, H.; Wu, S.; Tian, C.; Lin, Z.; Li, Z.; Lin, P.; Du, S., Two enantiomorphic 3D Zn(ii)–carboxylate MOFs with double helical structures serving as a chiral source induced by hydrogen bonding. *CrystEngComm* **2012**, 14 (12). DOI: 10.1039/c2ce25325a
138. Khansari, A.; Bryant, M. R.; Jenkinson, D. R.; Jameson, G. B.; Qazvini, O. T.; Liu, L.; Burrows, A. D.; Telfer, S. G.; Richardson, C., Interpenetration isomers in isorecticular amine-tagged zinc MOFs. *CrystEngComm* **2019**, 21 (48), 7498-7506. DOI: 10.1039/c9ce01669d
139. Deshpande, R. K.; Minnaar, J. L.; Telfer, S. G., Thermolabile groups in metal-organic frameworks: suppression of network interpenetration, post-synthetic cavity expansion, and protection of reactive functional groups. *Angew. Chem. Int. Ed.* **2010**, 49 (27), 4598-602. DOI: 10.1002/anie.200905960
140. Han, S. S.; Deng, W. Q.; Goddard, W. A., 3rd, Improved designs of metal-organic frameworks for hydrogen storage. *Angew Chem Int Ed Engl* **2007**, 46 (33), 6289-92. DOI: 10.1002/anie.200700303

141. Li, N.; Feng, R.; Zhu, J.; Chang, Z.; Bu, X.-H., Conformation versatility of ligands in coordination polymers: From structural diversity to properties and applications. *Coord. Chem. Rev.* **2018**, 375, 558-586. DOI: 10.1016/j.ccr.2018.05.016
142. Burrows, A. D.; Frost, C. G.; Mahon, M. F.; Richardson, C., Post-synthetic modification of tagged metal-organic frameworks. *Angew Chem Int Ed Engl* **2008**, 47 (44), 8482-6. DOI: 10.1002/anie.200802908
143. Brozek, C. K.; Michaelis, V. K.; Ong, T. C.; Bellarosa, L.; Lopez, N.; Griffin, R. G.; Dinca, M., Dynamic DMF Binding in MOF-5 Enables the Formation of Metastable Cobalt-Substituted MOF-5 Analogues. *ACS Central Science* **2015**, 1 (5), 252-60. DOI: 10.1021/acscentsci.5b00247

Chapter 5: SITE-SPECIFIC METAL IDENTIFICATION IN SINGLE-CRYSTAL X-RAY DIFFRACTION STRUCTURES USING ANOMALOUS DISPERSION

5.1. INTRODUCTION

Structural characterisation of materials is a crucial part of uncovering their structure-function relationships. There are many methods of structure determination but even the most powerful have some limits. Single-crystal X-ray diffraction^{144, 145} (SCXRD) gives very detailed information about the average atomic arrangements in a crystalline material, but with traditional techniques, atomic species are not directly identified. In this chapter, I will describe the development of a new method which exploits data collected at multiple X-ray wavelengths to identify specific metal species at crystallographic sites. The technique is then applied to MUF-93, to identify the metal species in each lattice.

5.1.1. Single-crystal X-ray diffraction (SCXRD)

SCXRD is the archetypal technique for determining the molecular structure of crystalline materials in general, and MOFs specifically.

Developed in the early 20th century this technique combined many earlier insights, three of which are particularly notable: 1) The observation by Nicolaus Steno in 1669 that all crystals of a given species had the same angles¹⁴⁶ between their faces, implying a regular and ordered composition. This led to early crystallography based on analysis of the macroscopic morphologies of crystals. 2) Knowledge of the diffraction of light, pioneered by Young¹⁴⁷ in his double-slit experiment in the early 19th century. This established that electromagnetic radiation could act as a wave, and more clearly explained the diffraction gratings discovered previously. 3) The discovery of X-rays by Wilhelm Röntgen¹⁴⁸ in 1895, and their characterisation as electromagnetic radiation with a short (~ 1 Å) wavelength in the decade following.

Although the science of crystallography had been slowly progressing over three centuries, almost as soon as light with wavelengths on the order of magnitude of the interatomic distances in crystals became available, X-rays were turned to study crystals. In 1912, Max von Laue demonstrated¹⁴⁹ the diffraction of X-rays through crystalline copper(II) sulphate, observing the concentric rings now known as Laue rings, from which powder X-ray diffraction (PXRD) patterns are derived. Shortly following this, Lawrence Bragg¹⁵⁰ determined the relationship between X Ray wavelength and the intensity of a beam exiting from a crystal. He had the insight that crystals would diffract X-ray beams when, and only when, the angle between the beam and the crystal determined that the interatomic spacing (at that angle) corresponds to the wavelength of the beam. The diffracted X-rays under this condition are in phase, resulting in constructive interference and the appearance of an observable X-ray “spot”. To reiterate, diffraction peaks occur wherever:

$$n\lambda = 2 d \sin \theta \quad (1)$$

Where n is a positive integer, lambda is the wavelength, d is the spacing between the planes, and theta is the angle of incidence of the beam relative to the normal of the plane. This concept is illustrated diagrammatically in Figure 5.1.

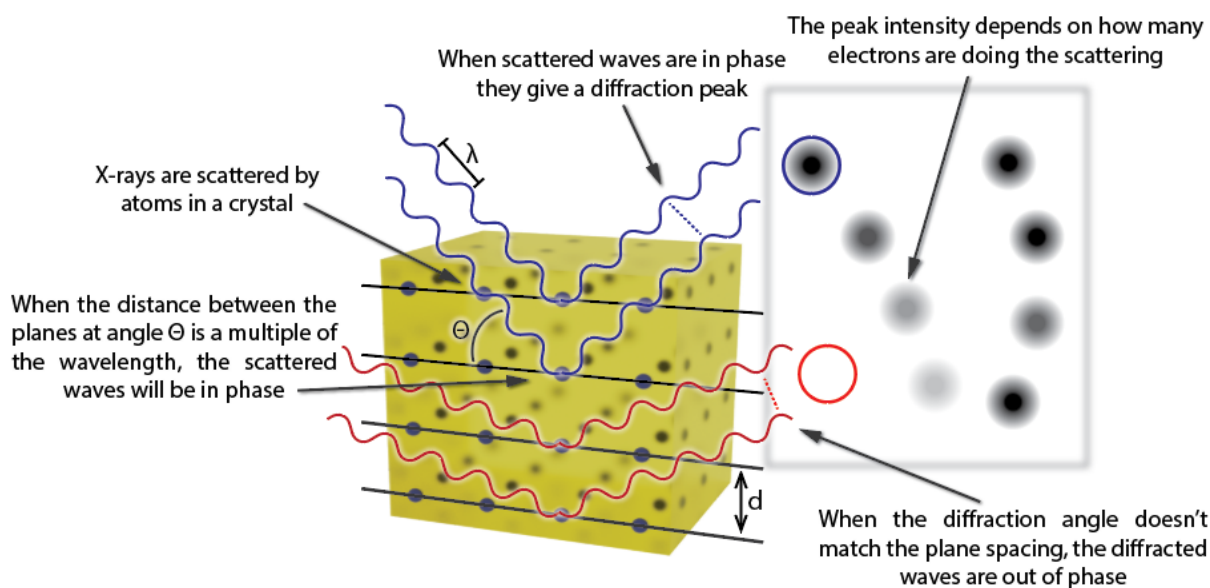


Figure 5.1: Illustration of the conditions of Bragg diffraction

Crystals are, by definition, periodic structures. What we are interested in, when trying to determine a crystal structure, is where all the atoms are in relation to the repeating unit. This is conveniently approximately the same thing as the electron density in the crystal, although the distribution of electrons is modified by bonding. The electron density in the crystal is represented as:

$$\rho(x, y, z) \quad (2)$$

Where x , y and z are coordinates relative to the unit cell origin. Because this density is periodic, it can be represented as a Fourier sum of individual structure factors for each atom:

$$\rho(x, y, z) = \frac{1}{V} \sum_h \sum_k \sum_l F_{hkl} e^{2\pi i(hx+ky+lz)} \quad (3)$$

The indices h , k and l define lattice planes through the crystal lattice. F_{hkl} is the structure factor for the plane which intersects $1/h$ on the x -axis, $1/k$ on the y -axis, and $1/l$ on the z -axis, or some multiple of each of those points. Each structure factor F_{hkl} is a Fourier sum of the scattering factors, one for each atom:

$$F_{hkl} = \sum_{j=1}^n f_j e^{2\pi i(hx_j+ky_j+lz_j)} \quad (4)$$

And an individual atom's scattering factor (f) has three components. First, the normal scattering term which is dependent on the angle (this is the Bragg diffraction described in Figure 5.1) and the number of electrons the element has (equal to its atomic number, Z). This means that for ordinary diffraction, atoms with similar Z can be difficult to tell apart, especially at higher values of Z , where the relative differences between elements are smaller. Then, there are the additional anomalous scattering factors, f' and f'' , which are dependent on wavelength:

$$f(\theta, \lambda) = f_0(\theta) + f'(\lambda) + if''(\lambda) \quad (5)$$

The observed diffraction pattern (Figure 5.1C), described as a Fourier sum of the individual reflections, is related to the electron density (as described in equation (3))

in the crystal through the Fourier transform – it is density over reciprocal space instead of density over real space.

The exponential term in Equation (4) can, using Euler's formula, also be expressed in an explicit complex number form:

$$e^{2\pi i(hx+ky+lz)} = \cos 2\pi(hx + ky + lz) + i \sin 2\pi(hx + ky + lz) \quad (6)$$

And so F_{hkl} , a sum of complex vectors, can itself be expressed as a complex vector, as illustrated in Figure 5.2. Ordinarily, a reflection (h, k, l) , and the same reflection in the opposite direction $(-h, -k, -l)$, named Friedel pairs, should have the same intensity.

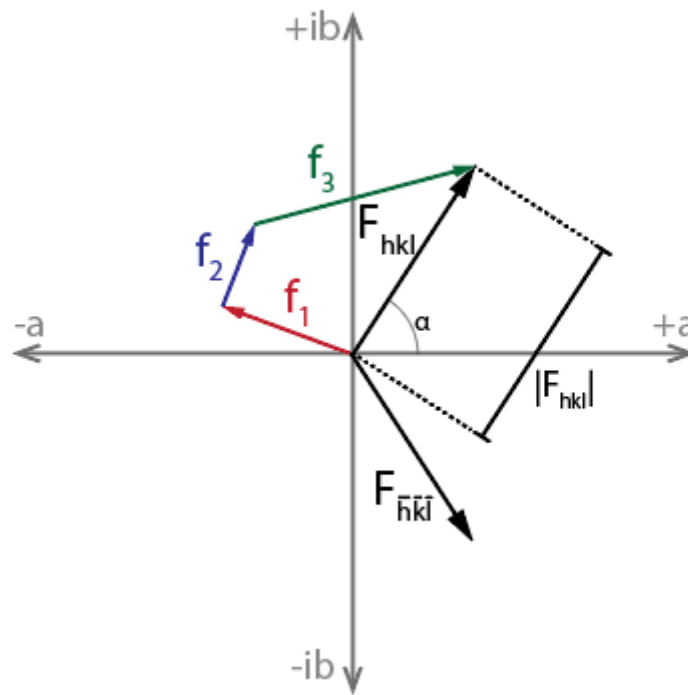


Figure 5.2: Vector representation of a structure factor.

In the diffraction pattern we measure with an X-ray detector, we do not observe the phase of each reflection (the angle α between the structure factor vector and the real number line as illustrated in Figure 5.2) only the intensity, or $|F_{hkl}|$. The position of each spot in the diffraction pattern is determined by the indices of the plane to which it corresponds, and the intensity by the electron density¹⁵¹ which repeats at the same frequency and orientation of that plane. But the phase, whose physical meaning is the relative distance¹⁵² between the location of the peak of the electron density and the

plane of the reflection doesn't show up in the diffraction pattern. From that definition, it can be intuitively understood why we should need the phase information to determine the location of the electron density in the unit cell, as well as why the phase should be opposite between F_{hkl} and $F_{\bar{h}\bar{k}\bar{l}}$, but the intensity the same.

5.1.2. Powder X-ray diffraction (PXRD)

In several circumstances, especially when large single crystals of a material are not available, or when rapid measurements (e.g., diagnostic identification of previously characterised phases; time resolved measurements) are desired, diffraction of X-rays through many crystals at once can be used instead. Because this technique is usually performed with microcrystalline samples, it is described as “powder” x-ray diffraction¹⁵³ (PXRD). The information gained from a PXRD experiment is averaged over all orientations of the crystals, instead of measured from specific angles, so one dimension of information is lost compared to SCXRD. PXRD data is usually presented as a “diffractogram”, a plot of diffraction intensity versus diffraction angle – many of these have already been displayed in previous chapters. Structures can also be determined from PXRD data collected at sufficiently high resolution: both detector resolution and scattering resolution. Structure determination by PXRD requires more complicated refinement techniques¹⁵⁴ than SCXRD, but ultimately relies on the same basis of comparing calculated diffraction by a model to the observed diffraction by the sample.

5.1.3. Contemporary synchrotron techniques

Synchrotrons are a type of circular particle accelerator, and in the context of chemical and materials research, where ‘synchrotron’ is shorthand for ‘synchrotron light source’, those particles are electrons. At ‘beamlines’, the accelerated electrons are induced to change their path by tuneable electromagnets, releasing extremely bright and focused radiation at almost any desired wavelength from microwaves to hard X-rays.

The establishment of synchrotrons to produce high-intensity, focused, X-ray beams with a wide range of accessible wavelengths, and sensitive, low-noise charge-coupled device X-ray detectors, has allowed a rapid expansion of the kinds of experiments which can successfully be performed. Some examples of the benefits of synchrotron radiation are:

- Specific wavelengths of X-rays are accessible. For example, very high energy X-rays (e.g. $\lambda < 0.5 \text{ \AA}$) allow higher resolution data to be collected, and are absorbed less, causing less damage to crystals.
- Brighter and more focused beams allow diffraction to be observed from smaller crystals.
- In-situ changes of conditions and time-resolved measurements can be made with faster detectors and shorter exposure times.

5.1.4. Anomalous scattering

Anomalous scattering (also termed anomalous diffraction or dispersion) is not, despite the name, particularly anomalous – it is simply the change to ordinary atomic scattering observed when the incident x-rays are of an appropriate energy to excite electrons in an atom's inner orbitals. This is represented by the f' (real) and f'' (imaginary) terms in equation (5). The closer the incident X-ray is to the absorption edge of the element, the larger in magnitude the anomalous scattering factors f' and f'' become.

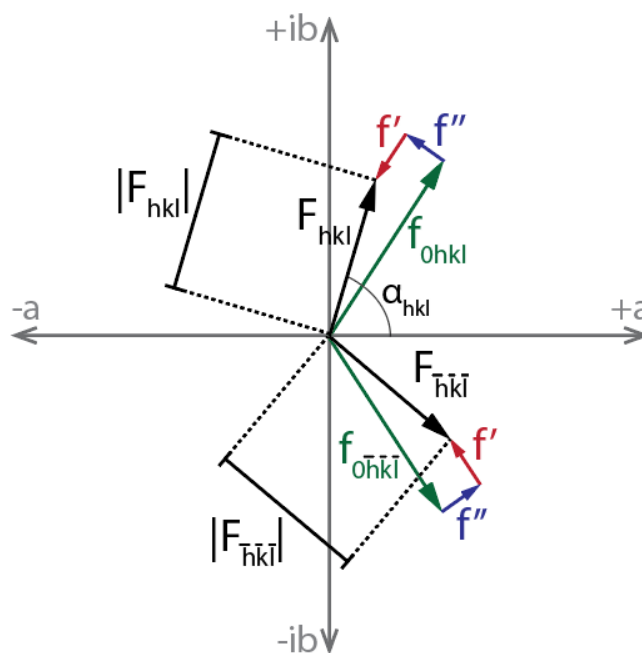


Figure 5.3: Scattering factor vectors are modified under anomalous scattering conditions. Because f'' is 90° out of phase with f_0 , the result is that Friedel mates have different intensities and phases in non-centrosymmetric crystals.

Multiwavelength anomalous dispersion¹⁵⁵⁻¹⁵⁷ (MAD) is commonly used for phase determination in biomacromolecular crystallography. It has largely supplanted earlier techniques which involved using two different crystals¹⁵⁸ where one had a heavy element added to it, because of the advantages of using datasets from an absolutely identical crystal. Because *both the real and imaginary* contributions of anomalous scattering to F_{hkl} are (approximately) constant, the result is that when the anomalous scattering is significant, Friedel pairs have *different* intensities, as illustrated in Figure 5.3.

In most protein crystallography experiments the average signal sizes (the ratio of the ordinary intensity and the anomalous scattering contribution) are roughly of 3–8% of the measured intensities¹⁵⁹ which can be limiting for some weakly diffracting, small, or not perfectly ordered protein crystals. For larger, comparatively more ordered MOF crystals, where even the weakest diffraction intensities in a synchrotron experiment are 20 times greater than the noise level, these signals ought to be intense enough to give meaningful information about the atom identities.

5.2. METHOD AND RESULTS

5.2.1. Development of a method for site-specific metal identification using multiwavelength single-crystal X-ray diffraction data

Zinc and cobalt are not clearly differentiable by ordinary single-crystal X-ray diffraction, because they have similar numbers of electrons – 28 and 25 respectively for the doubly oxidised species in MUF-93. This is especially a problem when one crystallographic site could have a mixture of the two metals, such as after cobalt exchange into the original MUF-9 lattice. For example, if ten percent of zinc ions were replaced with cobalt, the resulting crystallographic site would have, on average, 27.7 electrons compared to the 28 for zinc(II) alone.

These two metals do have significantly different peak absorption wavelengths for X-rays (Figure 5.5), and so display anomalous scattering behavior at different wavelengths. Because of this, it should be possible to distinguish zinc(II) from cobalt(II) in the structures described in the above section, using multiple SCXRD data sets collected from the same crystal at different wavelengths. Anomalous dispersion has occasionally¹⁶⁰⁻¹⁶³ been exploited to identify metals site-specifically, both in MOFs and minerals. The viability of this approach was established as early as the 1950s¹⁶⁴ when it was used to solve the crystal structure of KMnO_4 . The technique was not widely used, however, due to the limited wavelengths available from laboratory X-ray sources.

Our first approach was to use the procedure^{160, 161} demonstrated by Freedman et al., who reported a computer program entitled *Anomalous*. This software uses a model (prepared with a high quality, distant wavelength data set), along with datasets collected at appropriate wavelengths around the maximum f'' magnitude, to determine effective f' and f'' anomalous scattering factors at identified crystallographic sites for each wavelength. These values can be compared to plots of f' and f'' with respect to wavelength for each element to determine their relative

contribution. Initial results from this software were promising, but we could not verify that the software correctly handled the partial occupancies of the secondary lattice in our partially interpenetrated MUF-93 materials, and so this approach was abandoned.

We turned, then, to using the entire datasets directly in a method inspired by two techniques from protein crystallography. In an isomorphous replacement experiment, protein crystallographers collect data on two crystals with, ideally, the exact same structure (they are isomorphous) except that one has a heavy atom inserted. This could be achieved, for example, by soaking the crystal in a metal salt solution. The difference between those two datasets then reveals the location(s) of the heavy atom. Knowing those, some of the phases can be estimated, for the reflections where those heavy atoms contribute strongly. Those then reveal more of the structure, which in turn reveals the phases for the original dataset.

For centrosymmetric structures, reflection phases are always either 0 or π – there is no imaginary component to the structure factor. This is because for each atom at location (x, y, z) there must also be an atom at $(-x, -y, -z)$. We also know that $\sin(-x) = -\sin(x)$, while $\cos(-x) = \cos(x)$. So, for each contributor to the structure factor (Equation (4)) the imaginary part of the structure factor equation, which is the sine term, will cancel, while the real part will remain. With this, and using equations (4) and (6), we can express the structure factors in a dataset which is the difference of two datasets, collected at wavelengths λ_1 and λ_2 , as:

$$(F_{\lambda_1} - F_{\lambda_2}) = \sum_{j=1}^n (f_{j\lambda_1} - f_{j\lambda_2}) \cos 2\pi(hx_j + ky_j + lz_j) \quad (7)$$

And we can further note that the right-hand side of this equation only exists wherever j is an anomalous scattering atom at one of the relevant wavelengths, since otherwise the atomic scattering factors $f_{j\lambda_1}$ and $f_{j\lambda_2}$ are equal. All this is to say that the difference between two sets of scattering factors at different wavelengths becomes a set of factors of only the anomalous scattering from a crystal. This will then allow us to locate only

those atoms which are anomalous scatterers at the wavelength used, which are those of just one specific element.

β -MUF-9 is a centrosymmetric structure, and therefore MUF-93 approximates a centrosymmetric structure as it approaches high PIP%. The only differences between them are A) β -MUF-9 has a side chain in the second lattice disordered over 8 positions whereas MUF-93 has solvent and B) the replacement of zinc(II) in β -MUF-9 for cobalt(II) in the secondary lattice of MUF-93. With that in mind, the way a traditional MAD experiment approaches anomalous scattering would not be applicable in this case, since there will be no (measurable) difference between the intensities of Friedel mates. Furthermore, we already have a good model for the structure, and are not relying on this process to obtain phase information.

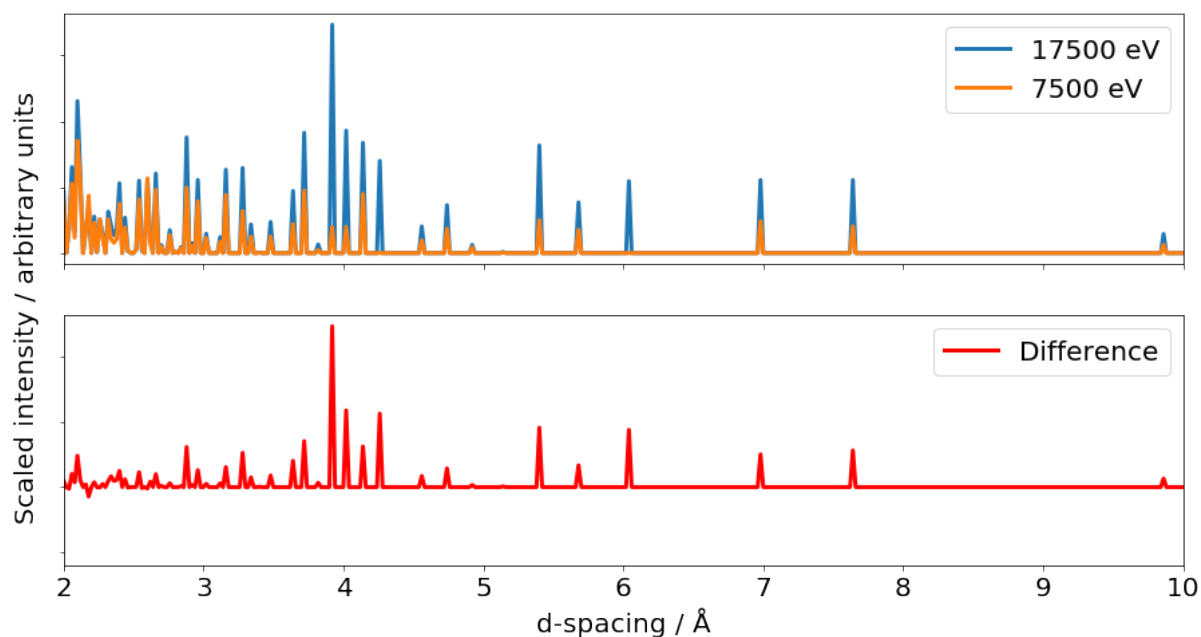


Figure 5.4: The upper panel shows intensities of x-ray reflections in MUF-93, by d-spacing, for data collected at high energy (17500 eV, 0.7084 Å) and at the cobalt(II) absorption edge (7500 eV, 1.653 Å). The lower panel shows the difference between the two datasets in the upper panel – the remaining signal is only the anomalous scattering from cobalt atoms.

Instead, we treat the dataset collected at the absorption peak of cobalt(II) as an isomorphous derivative of our original, but instead of trying to locate a “heavy” atom, we are trying to locate the anomalous scatterers in our cell, that is, the cobalt atoms. Since the datasets were collected at different wavelengths, their overall intensities will

differ. By scaling the datasets to the same average intensity, and subtracting one from the other, we obtain a new dataset where the only signal is the anomalous scattering from cobalt. Figure 5.4 illustrates this concept in a 2D format.

In Figure 5.4, I have converted two datasets collected from a single crystal of MUF-93 into profiles of intensity versus resolution, to illustrate the premise of our technique. The energies/wavelengths at which the datasets were collected are indicated on Figure 5.5. These are analogous to PXRD patterns, but are calculated by determining the d-spacing for each reflection in the SCXRD dataset, and summing all the intensities at the same d-spacing. Because datasets collected at different wavelengths have different 2θ -values for the same reflections, using resolution instead allows us to put them on the same axis.

In the upper panel of Figure 5.4, the dataset collected at 17500 eV where all atoms scatter normally is the blue line, while the orange line is the dataset collected at the absorption edge for cobalt. You can see that some of the signals in the 7500 eV dataset are significantly reduced. The difference between these datasets is only the magnitude of the anomalous scattering by cobalt. Solving this dataset by traditional direct methods and refining (using SHELXS¹²⁶ and SHELXL, as we might do for any ordinary small molecule structure) gives us the location and relative occupancy of all the cobalt atoms in the cell. Interestingly, SHELXT¹²⁹ is “too smart” for this, as it tries to make a sensible molecular structure – which this isn’t. We can also, of course, just input the locations of where we know the atoms to be.

One complication with this method is that anomalous scattering curves for metals often overlap significantly. We use the fluorescence emission maximum to find the optimum wavelength or energy to maximise the anomalous scattering signal for our element of interest. At the energy where we measured peak X-ray fluorescence emission for cobalt(II), 7500 eV, the theoretical f' for zinc (Figure 5.5, lower purple curve) is about -0.91 e-. This is likely to be relatively close to the experimental value as it is well below the absorption edge¹⁶⁵ but the position of the absorption edge and the

peak anomalous scattering coefficients at energies just above the absorption edge can shift dramatically depending on the chemical environment of the atom. That means there is a potential for zinc to interfere with the experiment, in that it may also show a small amount of anomalous scattering at the wavelength we want to use.

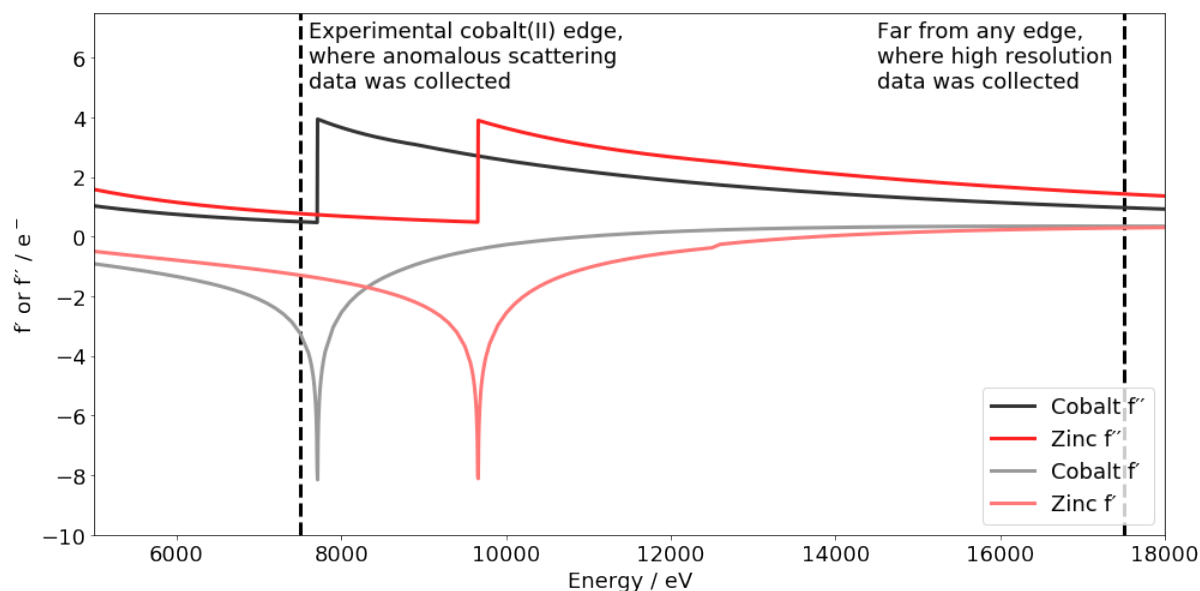


Figure 5.5: Theoretical curves of f'' (upper) and f' (lower) for zinc (red) and cobalt (black). Note that these theoretical values are not accurate very near and above the absorption edge, not least because of the effects of neighbouring atoms.

In the $[\text{Co}_4\text{O}]$ clusters in MUF-93, the absorption edge was estimated at 7500 eV, rather than the theoretical value of 7715 eV. In the worst case, significant anomalous scattering by zinc could have resulted, in a difference dataset between the cobalt edge and high energy, and collected from a material with zinc and cobalt in different sites, in an undesired signal for zinc appearing at up to approximately 15% of the strength of the cobalt peak in our electron density map. That worst case would be if the f' value for cobalt was near the experimental value, and the experimental wavelength closer to the zinc absorption peak rather than further away. But, as the real f' value for an element in an actual chemical environment is often much more negative than the theoretical value (the absorption maximum is often much more intense than the theoretical peak) the real undesired peak is likely to be much smaller than this. Fortunately we did not observe this issue in the datasets presented in Section 5.2.2, and any secondary anomalous scattering peak for zinc in our difference electron

density map was below the noise level, but this point would need to be addressed to fully realise the potential of this technique.

Ideally, one would experimentally determine the f' and f'' factors for the elements of interest in the real material, and use those values in the analysis of the difference datasets, but this requires absorption coefficients near the edge to be determined through X-ray absorption spectroscopy, specifically measurement of the X-ray absorption near edge structure (XANES), which we did not have access to. Determining the actual anomalous scattering factors becomes more important the closer the absorption maxima of elements in the material are. The absorption maxima of zinc and cobalt are far enough apart that in this case, it was sufficient to determine that only one peak appeared for our element of interest, cobalt. If there had been a weak peak at the location of the zinc node, it would have been necessary to determine the strength of anomalous scattering for zinc at that location to confirm that it was not due to exchanged cobalt. If there is no observable second peak, however, there is no evidence of cobalt at that location. Therefore, instead of measuring the XANES spectra and doing a full determination of the anomalous scattering factors to compare intensities, we compared the results obtained from MUF-93 to several materials prepared as controls, to illustrate the sufficiency of the technique for this purpose.

5.2.2. Results from the application of this method to MUF-93 and control materials

In this section, I will present several “slices” of electron density maps calculated from the difference datasets described above. These maps are calculated using the experimental intensity data from the difference between the two data sets, and the phases for each reflection supplied by the model. They are therefore referred to as (F_{obs} , Φ_{calc}) electron density maps.

Figure 5.6 illustrates how to interpret these slices. Figure 5.6 shows a hypothetical MUF-9 or MUF-93 unit cell, with the two crystallographically distinct locations of

metal atoms indicated in pink (near the corners; the secondary lattice) and blue (in the cell centre; the primary lattice). The grid indicates the (0,1,1) plane which is used for each slice, because it bisects atoms in both clusters, allowing visual comparison of the electron density at each site.

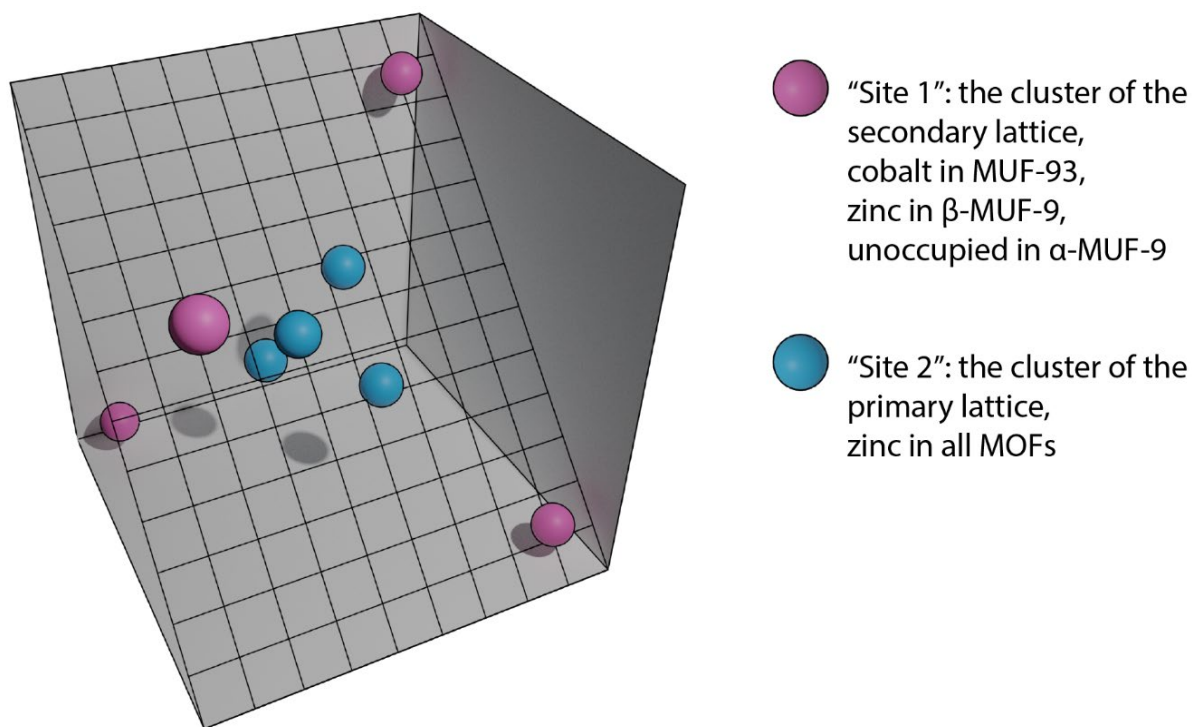


Figure 5.6: A diagram of a hypothetical MUF-9 and MUF-93 unit cell, indicating the two crystallographic sites occupied by metal atoms

The electron density map is a 3-dimensional grid, on which each point has a value representing the local electron density at that point. By integrating that map over the volume of each atom, we can determine an electron "count" for each location. These are not physical values because we don't know the total "difference in apparent electrons due to anomalous scattering" but their relative value at each site is all we need to determine the relative metal occupancy at each site for the metal of interest.

5.2.2.1. β -MUF-9, difference data between 17440 eV and zinc edge at 9670 eV

Figure 5.8 shows the (F_{obs} , Φ_{calc}) electron density map for the difference between 17440 eV and 9670 eV in β -MUF-9. Although β -MUF-9 is in the $P m \bar{3} m$ space group, this dataset was interpreted in $P \bar{4} 3 m$, to render the lattices crystallographically distinct from each other. This is necessary because otherwise both positions would be

refined as one single atom, and the resulting electron density map would have both peaks be equal by definition. The symmetries of the clusters in these two space groups are illustrated in Figure 5.7.

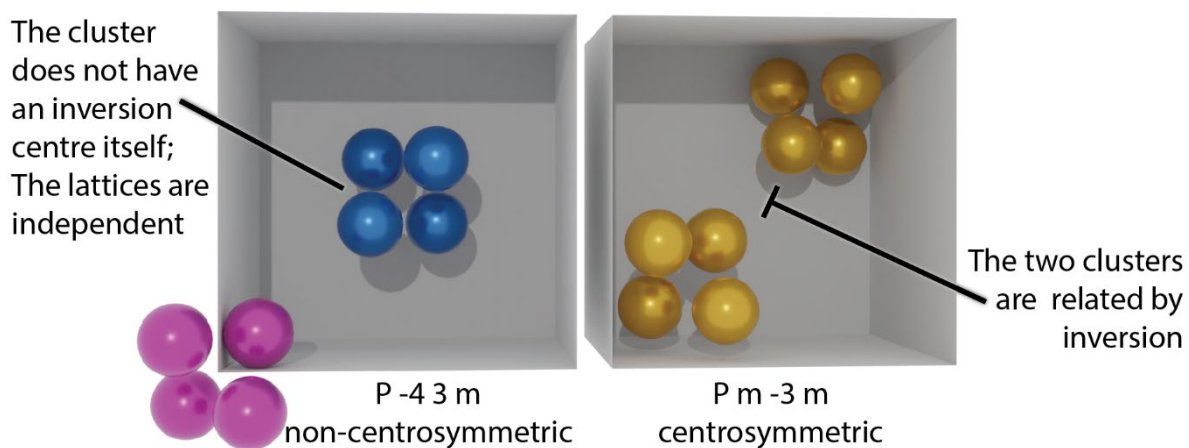


Figure 5.7: An illustration showing the location of the $[\text{Zn}_4\text{O}]$ cluster in two space groups. Left, the non-centrosymmetric space group of α -MUF-9 and its partially interpenetrated derivatives, P -4 3 m. Right, the centrosymmetric space group of β -MUF-9, P m -3 m.

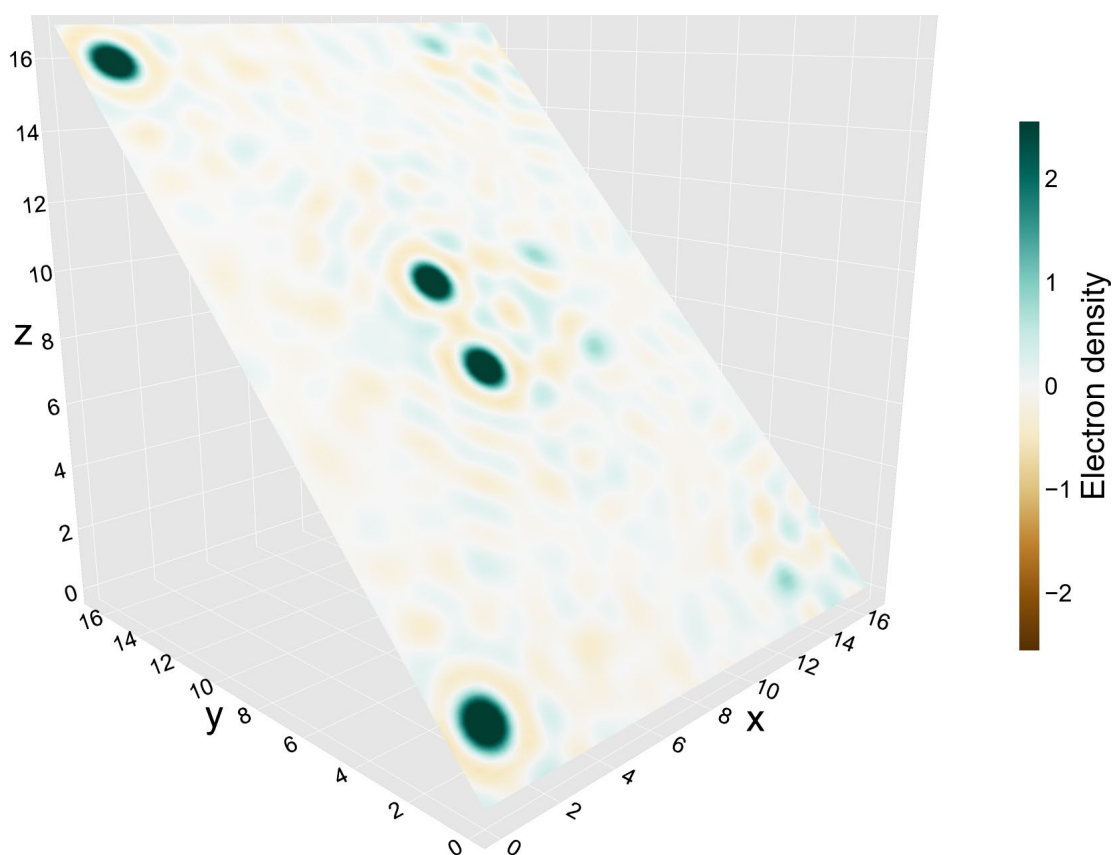


Figure 5.8: Slice of $(F_{\text{obs}}, \Phi_{\text{calc}})$ electron density map of β -MUF-9, difference data between 17440 eV and zinc edge at 9670 eV.

The appearance of strong peaks at both site 1 and site 2 indicates the presence of zinc at both locations. Summation of the intensities within the volume of a sphere of 170 pm, the average of the atomic radii of zinc and cobalt, was used to determine an electron count at each site. The integrated value of electron density at site 1 is 349.8, while integrated value at site 2 is 353.0. The ratio of those peaks is 1:0.99, close to the expected value of 1 for two identical zinc-containing lattices.

The root mean squared deviation (RMSD) for this map was 0.167, in the same arbitrary units where the maximum peak height is 4.898, for a signal-to-noise ratio of 28.9. Using this RMSD value gives us an uncertainty of approximately 2.1%, so the two peaks can therefore be considered equal within experimental uncertainty.

The signal and resolution for this sample is much better than for the following samples, because the X-rays at the zinc absorption edge of 9670 eV correspond to a wavelength of 1.282 Å, as opposed to the cobalt absorption edge of 7500 eV which corresponds to 1.653 Å.

5.2.2.2. *MUF-93, at the plateau of secondary growth*

Figure 5.9 shows the (Fobs, Φ_{calc}) electron density map for the difference between 17440 eV and 7500 eV in MUF-93, after 60 hours of secondary growth, at the beginning of the plateau. In contrast to the β -MUF-9 example above, we see a peak at only one crystallographic locus (site 1), that of the secondary lattice. This indicates that there is no observable cobalt(II) in the metal site for the primary lattice (site 2) in MUF-93 before reaching the plateau of secondary growth.

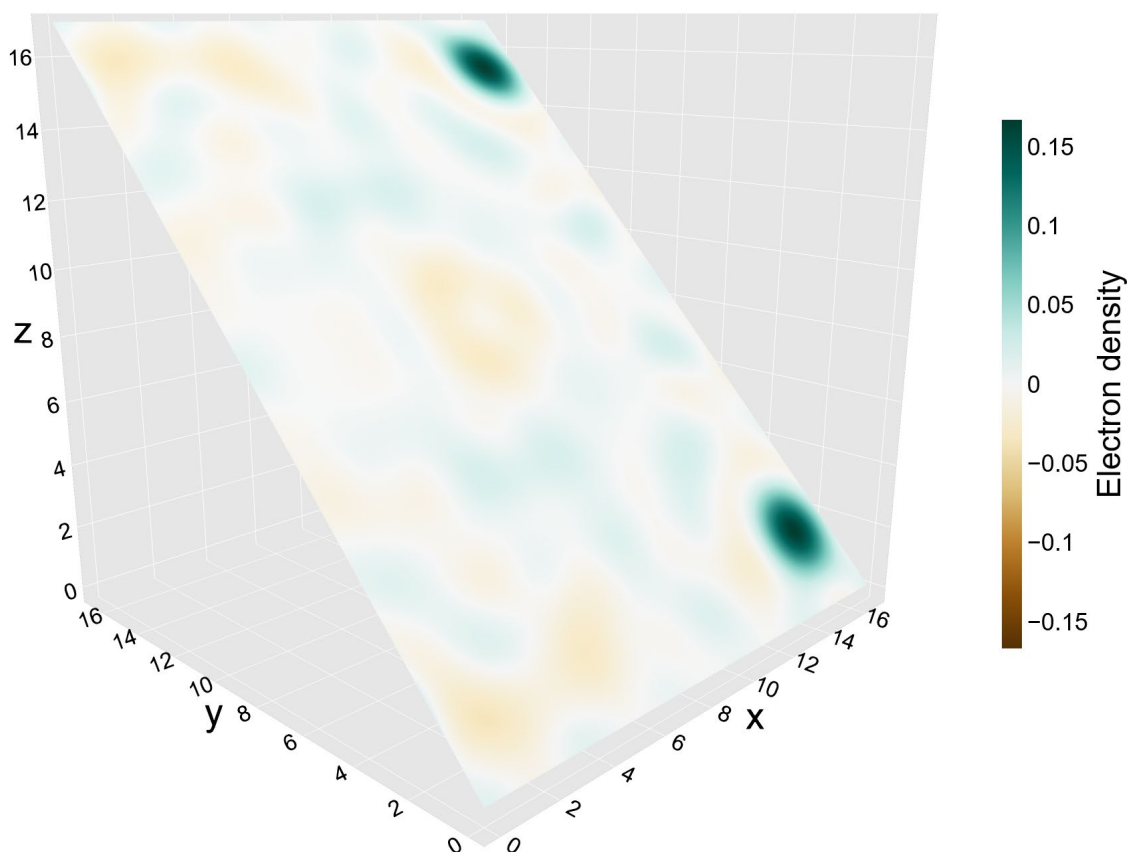


Figure 5.9: Slice of (F_{obs} , Φ_{calc}) electron density map of MUF-93 at the plateau of secondary growth after 60 hours, difference data between 17440 eV and cobalt edge at 7500 eV.

Using the RMSD of this electron density map as the noise size, the uncertainty of electron count integrals is measured at 4.7% (95% CI). This gives us an estimated exchange of cobalt(II) into the primary lattice of $2.9 \pm 4.7\%$, not significantly different from zero. This matches well with the bulk information obtained from AAS experiments in Chapter 4 and the cobalt exchange experiments in Chapter 2, which estimate an upper limit of 5% exchange at this time point.

5.2.2.3. *MUF-93, beyond the plateau of secondary growth*

Figure 5.10 shows the (F_{obs} , Φ_{calc}) electron density map for the difference between 17440 eV and 7500 eV in MUF-93, after 168 hours of secondary growth, beyond the plateau of growth of the secondary lattice. In contrast to the first MUF-93 example above, we see a peak at both crystallographic loci. The peak at site 1, of the secondary lattice, is strong, while the peak at site 2 is significantly weaker. This indicates that

after the secondary lattice stops growing, some cobalt(II) will exchange into the metal site of the primary lattice in MUF-93.

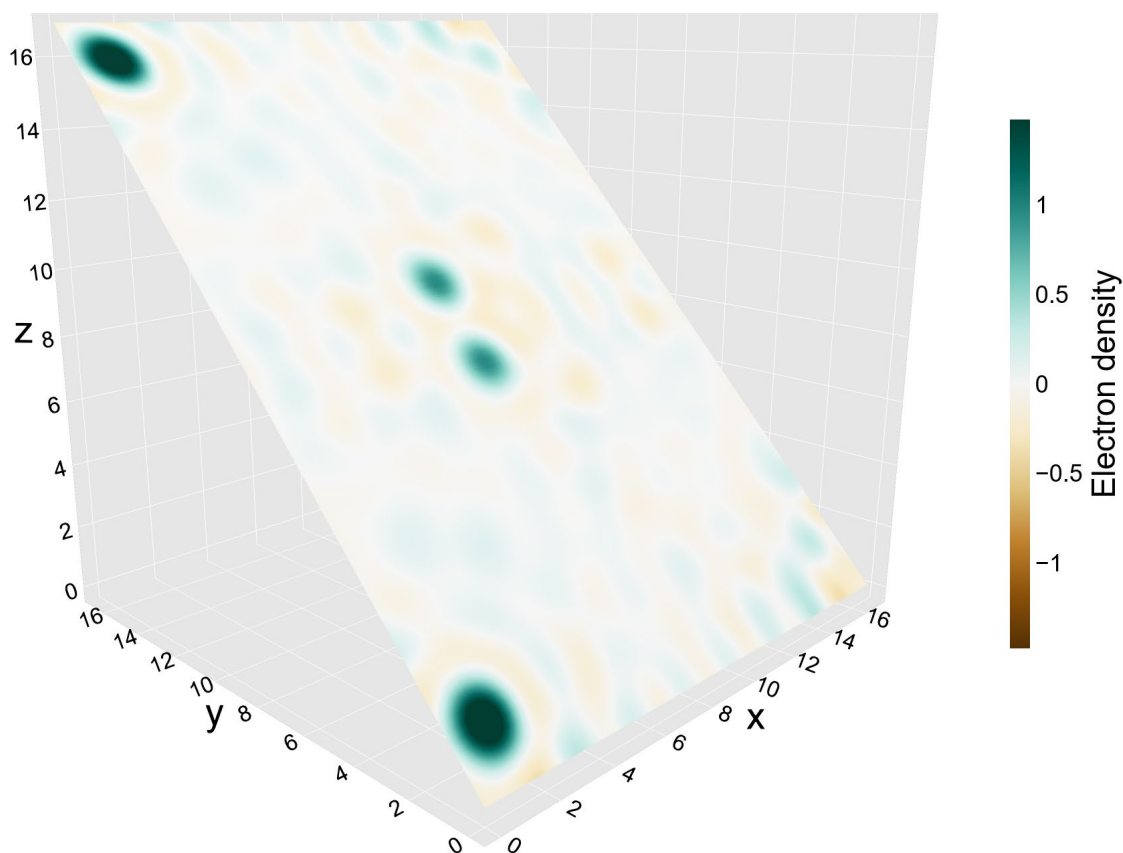


Figure 5.10: Slice of (Fobs, Φ calc) electron density map of MUF-93 beyond the plateau of secondary growth after 168 hours, difference data between 17440 eV and cobalt edge at 7500 eV.

The cobalt content at the two sites (100% cobalt in the secondary lattice of 47% occupancy and 34% cobalt in the primary lattice of 100% occupancy) approximately matches the 1.2 : 1 cobalt to zinc ratio determined for this sample by AAS. From this we can conclude that most - if not all - of the excess cobalt in samples beyond the plateau of secondary growth is due to exchange into the primary framework and not adsorption of cobalt by the MOF pores which is improperly washed out.

5.2.2.4. α -MUF-9, exchanged with cobalt

Figure 5.11 shows the (Fobs, Φ calc) electron density map for the difference between 17440 eV and 7500 eV in α -MUF-9, after exchange with cobalt(II) as described in Chapter 2. In this case, only the primary lattice is present, and a peak is observed at Site 2, the location for the primary lattice. This shows that using this method we can observe the metal exchange of cobalt into MUF-9 which was described in Chapter 2.

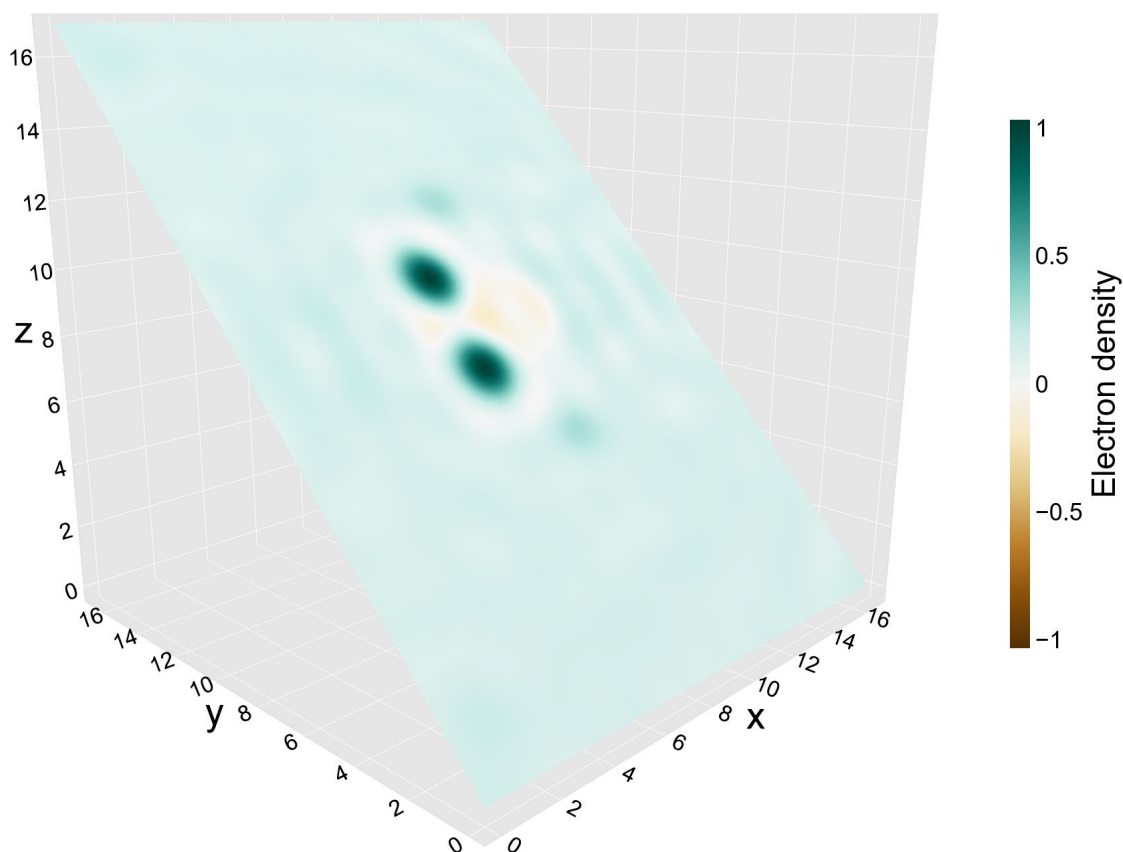


Figure 5.11: Slice of (Fobs, Φ calc) electron density map of α -MUF-9 exchanged with cobalt (as described in Chapter 2, section 2.2.5, page 43), difference data between 17440 eV and cobalt edge at 7500 eV.

5.3. DISCUSSION

The method we've developed here allows us to relatively simply identify and visualise the locations of specific kinds of atoms within a cell. Although this principle is not new, there were no standard programs available for this kind of analysis, so I had to develop this myself. Fortunately, the software libraries (like the CCTBX¹⁶⁶) for working with crystallographic datasets are well developed enough to be turned to this kind of analysis.

This technique can in principle be used for any element which displays anomalous scattering at wavelengths at which a diffraction dataset can be collected. That roughly corresponds to around iron, whose highest absorption edge is at 7.112 keV or heavier elements. At beamline MX1 of the Australian Synchrotron, at the time of carrying out these experiments, the lowest generally accessible energy is 8 keV, and down to 5.5 can be achieved with the help of the beamline staff. However, the lower the energy, the longer the wavelength, and 5.5 keV corresponds to 2.25 Å, which means the structural resolution becomes severely limited at this point. This means that with zinc (7500 eV, 1.65 Å) and cobalt (9670 eV, 1.28 Å), we were working near the lower end of the resolution range which would yield interpretable data.

This technique has wide scope for expansion to a range of different crystalline materials. Within metal-organic frameworks, there are examples¹⁶⁷ where different metals occupy distinct crystallographic locations, or catalysts^{168, 169} such as those described in Chapter 4 (page 81) which are metalated post-synthetically. This technique could be applied in those cases to determine the existence and extent of scrambling between the metal sites. That is especially important for catalysis, when it is imperative to be sure what is responsible for the catalytic activity. This technique could help to rule out, in that case, exchange of the catalytic metal into the MOF cluster, which could then also contribute to the catalytic result.

5.4. ADDITIONAL EXPERIMENTAL METHODS AND DATA

5.4.1. Python codes

All Python codes relevant to this section are provided in Appendix A. They are:

- Calculation of the difference datasets.
- Visualisation of the electron density map slices.
- Integration of electron density at each site and calculation of map statistics.

5.4.2. Determination of appropriate wavelength

An X-ray fluorescence excitation scan obtained from a single crystal of MUF-93 at the Australian Synchrotron MX1 beamline¹⁷⁰ was used to determine the optimum absorption wavelengths in MUF-93 of cobalt, the K β peak at 7500 eV and zinc, the K β peak at 9670 eV.

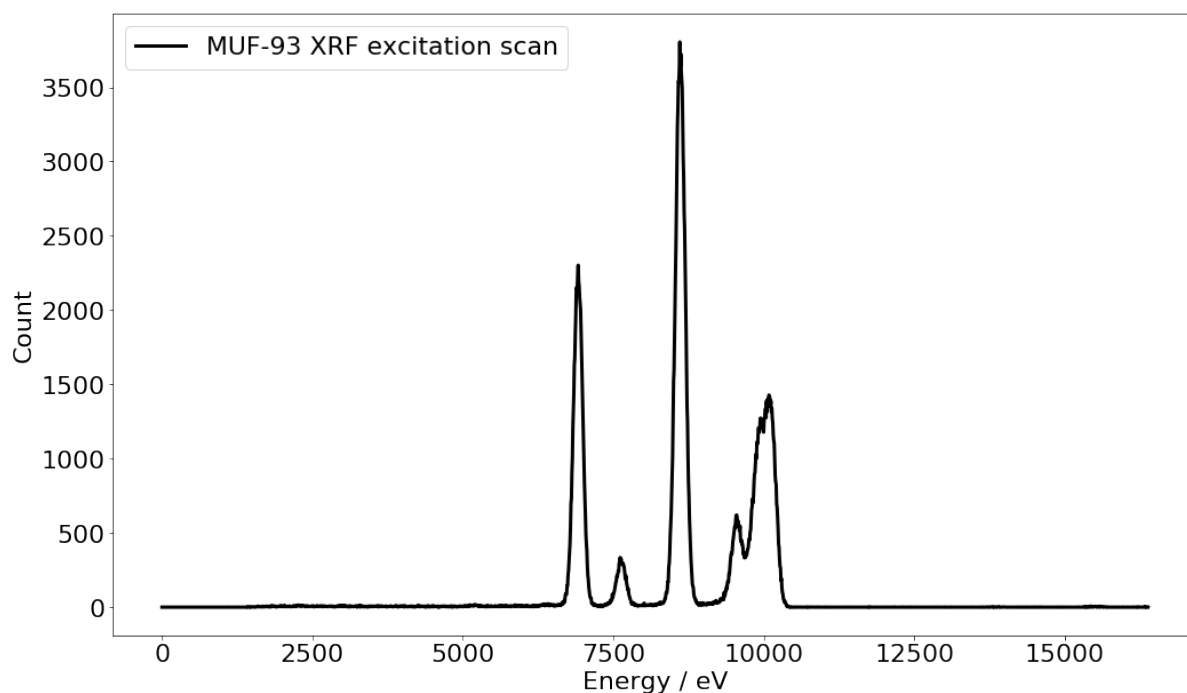


Figure S1: X-ray fluorescence excitation scan of a single crystal of MUF-93 collected at the Australian Synchrotron MX1 beamline.

5.4.3. Generation of difference dataset and Patterson map

Datasets collected from a single crystal at energies of 7500 eV (secondary absorption peak for Co) and 17500 (far from an absorption peak of any element in the material) at the Australian Synchrotron MX1 beamline¹⁷⁰ were obtained in *XDS*¹²⁵ *XDS_ASCII.HKL_p1* format, and then processed using a simple Python script making use of the *CCTBX*¹⁶⁶ toolkit.

The datasets were interpreted with a cubic cell of $a = b = c = 17.1 \text{ \AA}$ and $\alpha = \beta = \gamma = 90^\circ$ (determined from the high-resolution dataset), symmetry-equivalent reflections merged, scaled to the same average intensity, and the difference between the two datasets taken. The result was outputted as a *SHELX*¹²⁶-format *HKLF4* file, as well as the derived Patterson map as an *CCP4* format map file.

The Python libraries *Gemmi* (crystallographic data I/O for converting the *CCP4* map file to a *numpy* array) and *Plotly* were used to generate colour-mapped 2D slices from the anomalous difference Patterson map, while *pymol* can be used for 3D visualisation of the *CCP4* maps directly.

5.4.4. Solution and refinement of difference data

The difference *HKL* file can be solved using *SHELXS'* direct methods routine, finding the single atom of the cobalt SBU. The choice of cobalt in this case is arbitrary; there is no physical atom represented by this data, only the *change in the signal* from cobalt. Nonetheless, the refinement of a single atom at this position is stable, showing a clear signal that there is cobalt at this location. A small feature in the difference Fourier synthesis at the putative location of the zinc site in MUF-93 can be observed, but it is impossible to refine an atom at that position with any occupancy. When refined with a solvent mask, (which is essentially just background reduction in this case and has no physical meaning) the refinement statistics are good.

5.4.5. Generation of Plots

Using the *WinGX FFT* utility, .cube format electron density maps of F_{obs} using the supplied phases from this model were produced, and slices rendered with *Plotly*.

5.4.6. Tabulated statistics from difference datasets

“Site 1” refers to the metal atom in the cluster at the cell corner. “Site 2” refers to the metal atom in the cluster at the cell centre. Electron counts were integrated over a radius of 1.7 Å, the average of the atomic radii of zinc and cobalt. Uncertainties for the exchange percentage are calculated using the RMSD of the electron density map.

Table 5.1: SHELXL refinement results and calculated statistics for anomalous difference datasets. Integrated values at each metal atom site are proportional to the electron count of the specified metal at each site but are not absolute values, as $F(000)$ values were not determined for difference datasets.

Sample	Map RMSD	Max peak height	Integrated value at site 1	Integrated value at site 2	Ratio	Estimated exchange	R ₁	wR ₂
A	0.162	4.898	349.8	353.0	0.99 : 1	N/A	1.97 %	6.45 %
B	0.0131	0.167	356.0	10.2	1 : 0.029	2.9 ± 4.7 %	3.45 %	14.9 %
C	0.141	5.672	540.4	184.0	1 : 0.34	34 ± 2.6 %	1.36 %	5.88 %
D	N/A	N/A	N/A	N/A	N/A	N/A	4.73 %	13.0 %

Description

A	β-MUF-9, difference data between 17440 eV and zinc edge at 9670 eV
B	MUF-93, at the plateau of secondary growth after 60 hours. Sample with 50% PIP. Difference data between 17440 eV and cobalt edge at 7500 eV
C	MUF-93, beyond the plateau of secondary growth after 168 hours. Sample with 47% PIP. Difference data between 17440 eV and cobalt edge at 7500 eV
D	α-MUF-9, exchanged with cobalt(II). Difference data between 17440 eV and cobalt edge at 7500 eV

5.5. REFERENCES

125. Kabsch, W., XDS. *Acta Crystallogr D Biol Crystallogr* **2010**, 66 (Pt 2), 125-32. DOI: 10.1107/S0907444909047337
126. Sheldrick, G., Crystal structure refinement with SHELXL. *Acta Crystallogr. C* **2015**, 71 (1), 3-8. DOI: doi:10.1107/S2053229614024218
129. Sheldrick, G., SHELXT - Integrated space-group and crystal-structure determination. *Acta Crystallographica Section A* **2015**, 71 (1), 3-8. DOI: doi:10.1107/S2053273314026370
144. Hammond, C., *The Basics of Crystallography and Diffraction*. 2015. '10.1093/acprof:oso/9780198738671.001.0001: ' 10.1093/acprof:oso/9780198738671.001.0001
145. Giacovazzo, C., *Fundamentals of crystallography*. 3rd ed.; Oxford University Press: Oxford ; New York, 2011; p xxi, 842 p. '
146. Steensen, N.; Stella, I. d., *Nicolai Stenonis De solido intra solidum naturaliter contento dissertationis prodromus*. ex Typographia sub signo Stellae: 1669. '
147. Young, T., I. The Bakerian Lecture. Experiments and calculations relative to physical optics. *Philosophical Transactions of the Royal Society of London* **1804**, 94, 1-16. DOI: doi:10.1098/rstl.1804.0001
148. Röntgen, W. C., Ueber eine neue Art von Strahlen. *Annalen der Physik* **1898**, 300 (1), 12-17. DOI: 10.1002/andp.18983000103
149. Forman, P., The discovery of the diffraction of X-rays by crystals; a critique of the myths. *Archive for History of Exact Sciences* **1969**, 6 (1), 38-71. DOI: 10.1007/BF00327262
150. Bragg, W. H.; Bragg, W. L.; Duveen, A.; Chemistry, C., *X-rays and crystal structure*. G. Bell and Sons, Ltd.: London, 1915. '
151. Rhodes, G., 5 - From Diffraction Data to Electron Density. In *Crystallography Made Crystal Clear*, Rhodes, G., Ed. Academic Press: Boston, 1993; pp 83-99. '<https://doi.org/10.1016/B978-0-12-587075-7.50009-6>: '<https://doi.org/10.1016/B978-0-12-587075-7.50009-6>
152. Rhodes, G., 6 - Obtaining Phases. In *Crystallography Made Crystal Clear*, Rhodes, G., Ed. Academic Press: Boston, 1993; pp 101-129. '<https://doi.org/10.1016/B978-0-12-587075-7.50010-2>: '<https://doi.org/10.1016/B978-0-12-587075-7.50010-2>
153. Pecharsky, V. K.; Zavalij, P. Y., *Fundamentals of powder diffraction and structural characterization of materials*. 2nd ed.; Springer: New York, 2009; p xxiii, 741 p. '
154. *Rietveld Refinement in the Characterization of Crystalline Materials*. 2019. '10.3390/books978-3-03897-528-1: ' 10.3390/books978-3-03897-528-1
155. Gonzalez, A., Optimizing data collection for structure determination. *Acta Crystallogr D Biol Crystallogr* **2003**, 59 (Pt 11), 1935-42. DOI: 10.1107/s0907444903017700
156. Gonzalez, A., Faster data-collection strategies for structure determination using anomalous dispersion. *Acta Crystallogr D Biol Crystallogr* **2003**, 59 (Pt 2), 315-22. DOI: 10.1107/s0907444902022138
157. Read, R. J., As MAD as can be. *Structure* **1996**, 4 (1), 11-14. DOI: 10.1016/s0969-2126(96)00004-4

158. Smith, J. L.; Hendrickson, W. A.; Terwilliger, T. C.; Berendzen, J., MAD and MIR. *Crystallography of biological macromolecules* **2006**, 299–309. DOI:
159. Ogata, C. M., MAD phasing grows up. *Nat Struct Biol* **1998**, 5 Suppl, 638-40. DOI: 10.1038/1330
160. Brozek, C. K.; Cozzolino, A. F.; Teat, S. J.; Chen, Y.-S.; Dincă, M., Quantification of Site-Specific Cation Exchange in Metal–Organic Frameworks Using Multi-Wavelength Anomalous X-ray Dispersion. *Chem. Mater.* **2013**, 25 (15), 2998–3002. DOI: 10.1021/cm400858d
161. Freedman, D. E.; Han, T. H.; Prodi, A.; Müller, P.; Huang, Q.-Z.; Chen, Y.-S.; Webb, S. M.; Lee, Y. S.; McQueen, T. M.; Nocera, D. G., Site Specific X-ray Anomalous Dispersion of the Geometrically Frustrated Kagome Magnet, Herbertsmithite, $\text{ZnCu}_3(\text{OH})_6\text{Cl}_2$. *J. Am. Chem. Soc.* **2010**, 132 (45), 16185–16190. DOI: 10.1021/ja1070398
162. Helliwell, M.; Helliwell, J. R.; Kaucic, V.; Zabukovec Logar, N.; Teat, S. J.; Warren, J. E.; Dodson, E. J., Determination of zinc incorporation in the Zn-substituted gallophosphate ZnULM-5 by multiple wavelength anomalous dispersion techniques. *Acta Crystallogr. B* **2010**, 66 (3), 345-357. DOI: 10.1107/S0108768110011237
163. Singh, M. N.; Sinha, A. K.; Ghosh, H., Determination of transition metal ion distribution in cubic spinel $\text{Co}_{1.5}\text{Fe}_{1.5}\text{O}_4$ using anomalous x-ray diffraction. *AIP Advances* **2015**, 5 (8). DOI: 10.1063/1.4928425
164. Ramaseshan, S.; Venkatesan, K.; Mani, N. V., The use of anomalous scattering for the determination of crystal structures-KMnO₄. *Proceedings of the Indian Academy of Sciences - Section A* **1957**, 46 (2), 95-111. DOI: 10.1007/bf03045960
165. Quintana, J. P.; Butler, B. D.; Haefner, D. R., Experimentally determined anomalous scattering factors for Mn, Fe, Ni, Cu, Zn and Hg using the Kramers-Kronig relation. *J. Appl. Crystallogr.* **1991**, 24 (2), 184-187. DOI: 10.1107/s0021889890012249
166. Grosse-Kunstleve, R. W.; Sauter, N. K.; Moriarty, N. W.; Adams, P. D., The Computational Crystallography Toolbox: crystallographic algorithms in a reusable software framework. *J. Appl. Crystallogr.* **2002**, 35 (1), 126-136. DOI: doi:10.1107/S0021889801017824
167. Tu, B.; Diestel, L.; Shi, Z.-L.; Bandara, W. R. L. N.; Chen, Y.; Lin, W.; Zhang, Y.-B.; Telfer, S. G.; Li, Q., Harnessing Bottom-Up Self-Assembly To Position Five Distinct Components in an Ordered Porous Framework. *Angew. Chem. Int. Ed.* **2019**, 58 (16), 5348-5353. DOI: 10.1002/anie.201900863
168. Wang, X.; Wisser, F. M.; Canivet, J.; Fontecave, M.; Mellot-Draznieks, C., Immobilization of a Full Photosystem in the Large-Pore MIL-101 Metal-Organic Framework for CO₂ reduction. *ChemSusChem* **2018**, 11 (18), 3315-3322. DOI: 10.1002/cssc.201801066
169. Gonzalez, M. I.; Bloch, E. D.; Mason, J. A.; Teat, S. J.; Long, J. R., Single-crystal-to-single-crystal metalation of a metal-organic framework: a route toward structurally well-defined catalysts. *Inorg. Chem.* **2015**, 54 (6), 2995-3005. DOI: 10.1021/acs.inorgchem.5b00096
170. Cowieson, N. P.; Aragao, D.; Clift, M.; Ericsson, D. J.; Gee, C.; Harrop, S. J.; Mudie, N.; Panjikar, S.; Price, J. R.; Riboldi-Tunnicliffe, A.; Williamson, R.; Caradoc-Davies, T., MX1: a bending-magnet crystallography beamline serving both chemical and macromolecular crystallography communities at the Australian Synchrotron. *J Synchrotron Radiat* **2015**, 22 (1), 187-90. DOI: 10.1107/S1600577514021717

Chapter 6: APPLYING HETERO-INTERPENETRATED METAL-ORGANIC FRAMEWORKS TO CATALYSIS

6.1. INTRODUCTION

It's always nice to be able to show that some new technique or material is somehow useful, or at least that it has the potential to be. Producing a revolutionary new catalyst with practical relevance is well beyond the scope of this thesis. However, we sought to illustrate how control over the different components of hetero-interpenetrated frameworks could be exploited to impact the functionality of the resulting material, i.e., to create something greater than the sum of its components. To that end, we designed a hetero-interpenetrated catalyst where each lattice is an orthogonal contributor to the catalytic outcome.

6.1.1. Pore engineering of MOFs

As indicated earlier, one of the main reasons for the interest in MOFs is their tunability: it is possible to design^{29, 31, 34, 66, 124, 171} ligands with chemical functionalities chosen to achieve a particular result. For catalytic applications, that result might be the installation of a catalytic group on the framework structure, but it may also be modifying the pore space to provide an appropriate environment for the catalytic reaction to occur.

The characteristics of the MOF pore environment can also be varied by the guest. 'Guest' includes solvent for catalytic reactions carried out in solvent. Tuning the guest solvent is just like tuning the solvent for a conventional catalytic reaction, but the effect of a solvent can be different in a confined pore space than the bulk solvent present for a heterogeneous reaction. In a nice example, Ma et al., polymerised N-vinylpyrrolidone within the pores of a framework material catalyst.⁶⁵ The reaction outcome was similar to performing the reaction in N-methyl pyrrolidone (NMP), but

avoided a costly and environmentally unfriendly workup due to the high boiling point and toxicity of NMP.

Beyond modification of the pore space on a molecular level, the crystal growth process itself¹⁷² also provides many handles for modifying the properties of a material. Handles include heating methods, solvents, additives such as capping agents and surfactants, stirring or sonication, layer diffusion, etc., and these variables can influence the morphology, size, defects and other features of the resulting crystallites. Other means such as targeted post-synthetic modifications¹⁷³ can also modify these features.

6.1.2. MOF catalysis

Metal-organic frameworks are being explored for catalysis both for the preparation^{60, 174} of useful products and the degradation¹⁷⁵ of harmful ones. Since MOFs are constructed from a combination of metal and organic components, either of those can be exploited for a catalytic purpose.

6.1.2.1. *Metal catalysis*

The metal atoms in MOF nodes can be exploited for catalysis. Both transition metals⁶³ and lanthanides¹⁷⁶ can be used, just as in homogeneous catalysis. Although the site of the metal resembles a discrete metal complex in many ways, there are also important differences. In a MOF, the ligands generally have less conformational freedom than in a discrete complex, because they are coordinated in multiple directions within a framework. The ligands are therefore also less labile than many in discrete complexes. Thus, even for the exploitation of the metal nodes as catalysts, ligand design¹⁷⁷ is critical to allow access to the metal and provide an appropriate electronic environment for the metal.

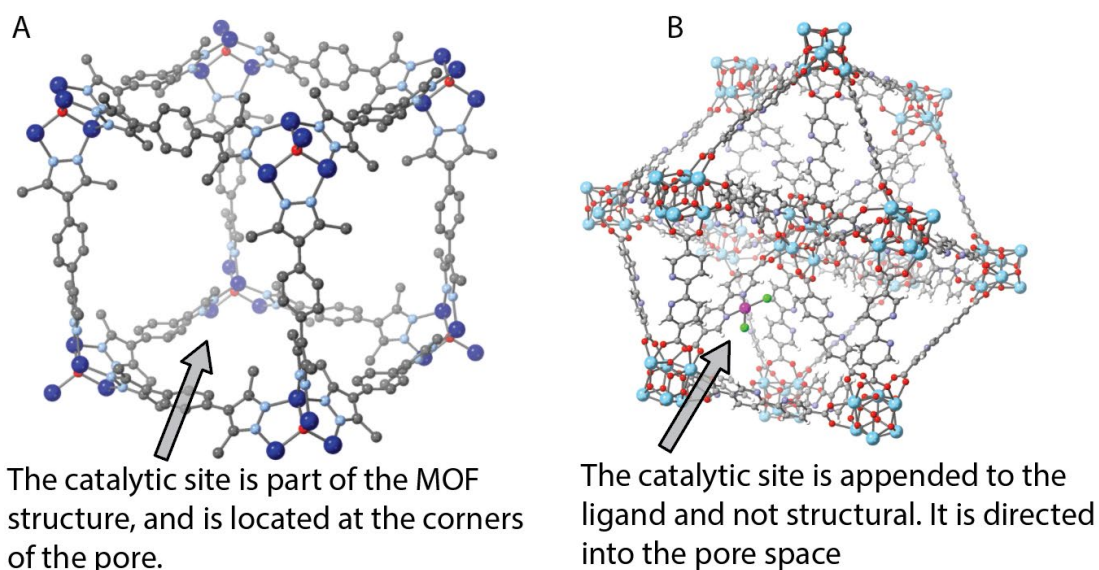


Figure 6.1: An illustration of the two classes of metal catalysis in MOFs. A) catalysis by structural metal atoms includes this example^{132, 178} of MFU-1. B) catalysis by non-structural metals includes this example¹⁶⁹ of UiO-bpydc where the catalytic metal is coordinated to the bipyridyl backbone of the ligand.

Metal catalysis can also be performed in MOFs by metals outside of the structural clusters, by using metalloligands such as porphyrins^{24, 87, 179, 180} or polypyridyl¹⁸¹ complexes. Such catalytic complexes can also be immobilised within pores by coordination to open sites on the metal cluster.

6.1.2.2. *Organocatalysis*

In some ways, organocatalysts are more attractive in MOFs than metal catalysts. It is often easier to modify the organic component than to make a MOF with the desired metal in the desired coordination environment for a catalytic application. Although it may take some clever chemistry, an organocatalytic moiety can often simply be appended to a ligand without affecting the coordinating groups which determine the MOF structure. In this way, the catalytic site is also directed into the pore space, whereas structural metal atoms are by definition in the pore corners.

Organocatalysis¹⁸²⁻¹⁸⁵ in general has a more limited scope of reactions than metal catalysis, but can still be used for a broad range of chemical transformations. Particularly famous is the enantioselective aldol reaction (or Hajos-Parrish-Eder-Sauer-Wiechert¹⁸⁶ reaction) catalysed by proline, which has found wide application in the preparation of chiral ketone-containing compounds. Organocatalysts are

particularly suited to asymmetric organic reactions, such as those required to produce many pharmaceuticals and their feedstocks.

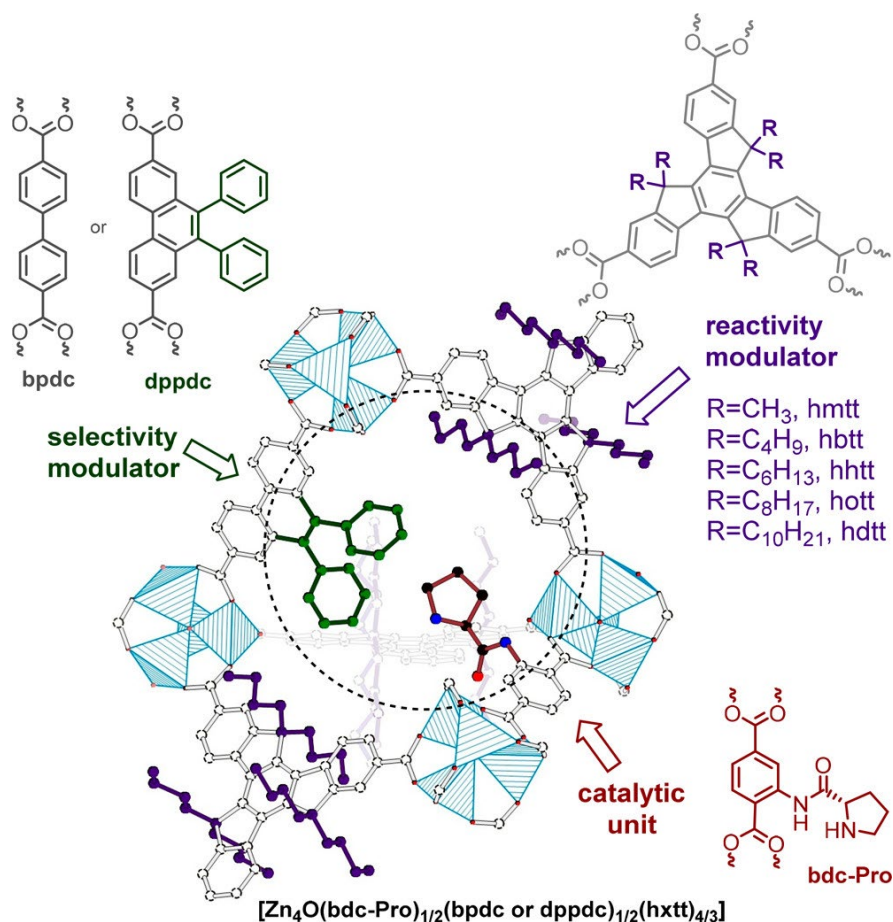


Figure 6.2 An example of modulated organocatalysis in a MOF. Figure reproduced from reference ¹⁸⁷ with permission. The catalytic unit is directed into the pore space, and other parts of the framework can be used to tune the pore properties and the resulting catalytic outcome.

Organocatalysts in MOFs are highly tuneable through the exploitation of the tunability of the MOF itself. Figure 6.2 illustrates a MOF organocatalyst reported by our group in which the outcome of catalysis by a chiral proline group on one ligand was modified by side chains on other ligands, tuning the pore environment in which the catalytic reaction occurred.

Although the strict definition of organocatalysis requires the catalyst to have a low molecular weight, it is otherwise very similar to much of enzymatic catalysis (not including metalloenzymes) in terms of the chemical groups and reactions involved.

6.1.2.3. Enzyme-like catalysis in MOFs

Much catalyst design in MOFs is inspired by biological catalysis, which is admired especially for its selectivity and mild reaction conditions. There is one major similarity between a crystalline porous nanomaterial catalyst and an enzyme, which is that the catalytic reaction takes place in a highly specific pore environment. Figure 6.1 illustrates the binding sites of an enzyme and a MOF catalyst respectively in panels A and B, and contrasts these to a homogeneous catalytic reaction surrounded by solvent in panel C. Some MOFs also replicate particular moieties from enzymes in their catalytic site, or incorporate multiple complementary functionalities to mimic natural complexes like photosystems^{188, 189}. Enzymes themselves can also be encapsulated¹⁹⁰ within MOFs to stabilise them for reactions and make them easier to handle, while allowing substrate diffusion.

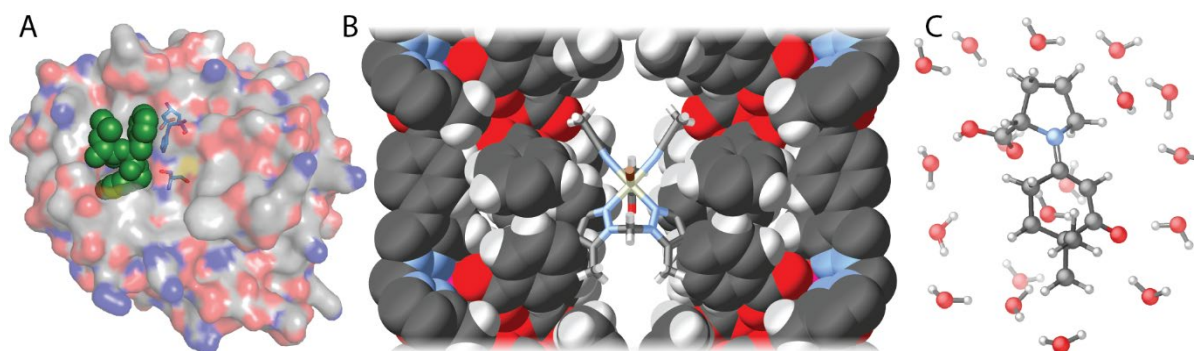


Figure 6.3: A) an inhibitor (coloured green) bound to the active site of the protein chymotrypsin. The protein surface is coloured grey for carbon, red for oxygen, blue for nitrogen, and hydrogens are omitted for clarity. The residues at the binding site are shown as sticks and coloured blue. B) the catalytic intermediate⁶⁹ $[\text{Rh}(\text{L})(\text{CH}_3\text{CN})_2(\text{CH}_3\text{CO})\text{I}]^+$ in a MOF pore, observed by SCXRD. The overall MOF structure is drawn as the van der Waals surface while the catalytic complex is shown as sticks. Carbons are grey, hydrogens white, oxygens red, nitrogens blue, rhodium cream, iodine brown. C) An enamine adduct of proline, an intermediate in a homogeneous organocatalytic reaction.

However, “enzyme-like” catalysis by MOFs is often overstated. MOFs may of course be used for the same reactions^{168, 191, 192} for which enzymes are famous, but in my opinion this is not enough to justify a description of them as enzyme-like. The above similarities between enzymes and MOFs notwithstanding, the differences are also very significant. MOFs are generally rigid, but enzymes change conformation¹⁹³ to facilitate their reactions. Enzymes dynamically bind their substrates and adopt a conformation which stabilises the transition state between the reactants and the

products. This dynamic behaviour is far more complex than anything displayed in MOFs to date. There are some recent examples of MOFs prepared with oligopeptide linkers^{194, 195} which display a wide range of conformations as the result of a complex set of interactions between different part of their components, but these are only isolated examples for now.

Despite the exaggerations sometimes seen, I will continue to use language which softly suggests the similarities between MOF catalysis and enzyme catalysis. This is not to overstate the performance or specificity of the catalysts described herein, which are rather unremarkable, nor is it to imply that these catalysts have all the mechanistic features of enzymes. I use this language because enzyme-like catalysis is the inspiration for this work, and a long-term target of the field of catalysis. In the context of this work, the deliberate introduction of specific elements of enzyme-like catalysis, new to framework materials, is much more interesting than the absolute performance of the catalyst.

6.1.3. MUF-10, a chiral analogue to MUF-9

MUF-10 is the homochiral analogue of MUF-9. **L1** has chirality due to the twist in its backbone (Figure 6.4), and its enantiomers can be resolved through co-crystallisation¹⁹⁶ with a chiral base, brucine. When enantiopure (R)- or (S)- **L1** is used to synthesise a MOF with $\text{Zn}(\text{NO}_3)_2 \cdot 4\text{H}_2\text{O}$, it behaves similarly to rac-**L1** making a $[\text{Zn}_4\text{O}(\text{L})_3]$ MOF with a pcu net. In DMF, the fully interpenetrated product results and this is referred to as β -MUF-10. Conversely, in DBF, noninterpenetrated α -MUF-10 is formed. In mixtures of DMF and DBF, partially interpenetrated PIP-MUF-10 is formed. In contrast to MUF-9, however, MUF-10 does not slowly become partially interpenetrated in DBF over long reaction times.

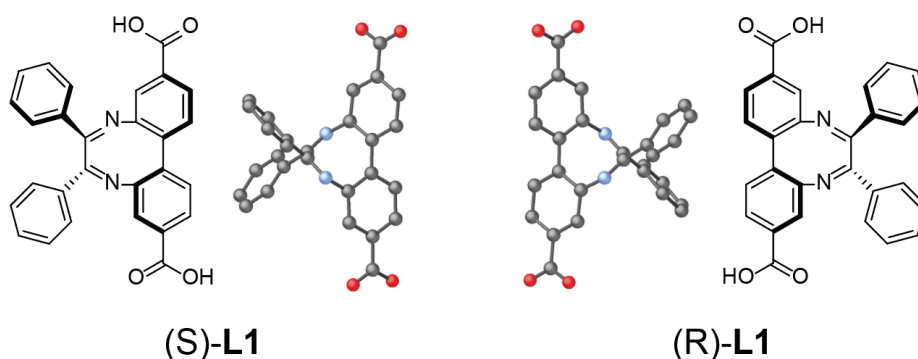


Figure 6.4: Enantiomers of L1

Our plan was to use α -MUF-10 as a chiral host template to grow an organocatalytic secondary framework, which benefits from chiral transfer from the host. The key idea was that the pore space in α -MUF-10 would act analogously to the shaped pocket in an enzyme. The chiral shape of the environment should favour the formation of one enantiomer of a reaction product over the other. Then, the secondary lattice would include a catalytic group which actually facilitates the reaction. In order to show the effect of the pore, this catalytic group should be achiral. In that case, any enantioselective reaction outcome must come from the pore environment itself.

To establish the possibility of using a hetero-interpenetrated MOF derived from MUF-10 as a catalyst, we first needed to do the same kinds of background work as we did with MUF-9 in Chapter 1. We must be sure that no other changes will befall our MUF-10 starting material under the conditions for secondary growth, or those for catalysis.

Then, we must show that secondary growth can be observed in MUF-10 as it is in MUF-9, but they are subtly different MOFs. Notably, MUF-10 does *not* show the increase in PIP% at long reaction times after synthesis. That implies that in DBF, at least, **L1** is too large to enter the MUF-10 pores. So, some more screening will be necessary to find suitable reaction conditions to prepare a hetero-interpenetrated MOF with some catalytic secondary lattice in MUF-10. We did manage to do this, with a new ligand designed for the purpose (section 6.2. page 148), and called our new hetero-interpenetrated heterogeneous catalyst ‘MUF-101’.

We trialled several different catalytic reactions with MUF-101, and ultimately found that the Henry reaction suited our needs the best as a display of the applicability of hetero-interpenetrated frameworks. The Henry (or nitroaldol) reaction is a classic carbon–carbon bond formation reaction first described in 1895. Interest in the Henry reaction was renewed almost a century later, when in 1992 the first report¹⁹⁷ of enantioselective Henry catalysis was made. Asymmetric catalysis of Henry reactions¹⁹⁸⁻²⁰⁰ is now a large field in its own right, with over five million hits for journal articles in a SciFinder search.

FURTHER CHARACTERISATION OF MUF-10

Initial tests of the ability of α -MUF-10 to undergo secondary growth were performed with zinc nitrate tetrahydrate and H₂BPDC in DBF. In that case, no change in PXRD patterns were observed, indicating the PIP% of the material was not changing from zero. This was disappointing, but not surprising: while deeply similar to MUF-9, MUF-10 does not produce partially interpenetrated phases in DBF after long synthesis times, unlike MUF-9.

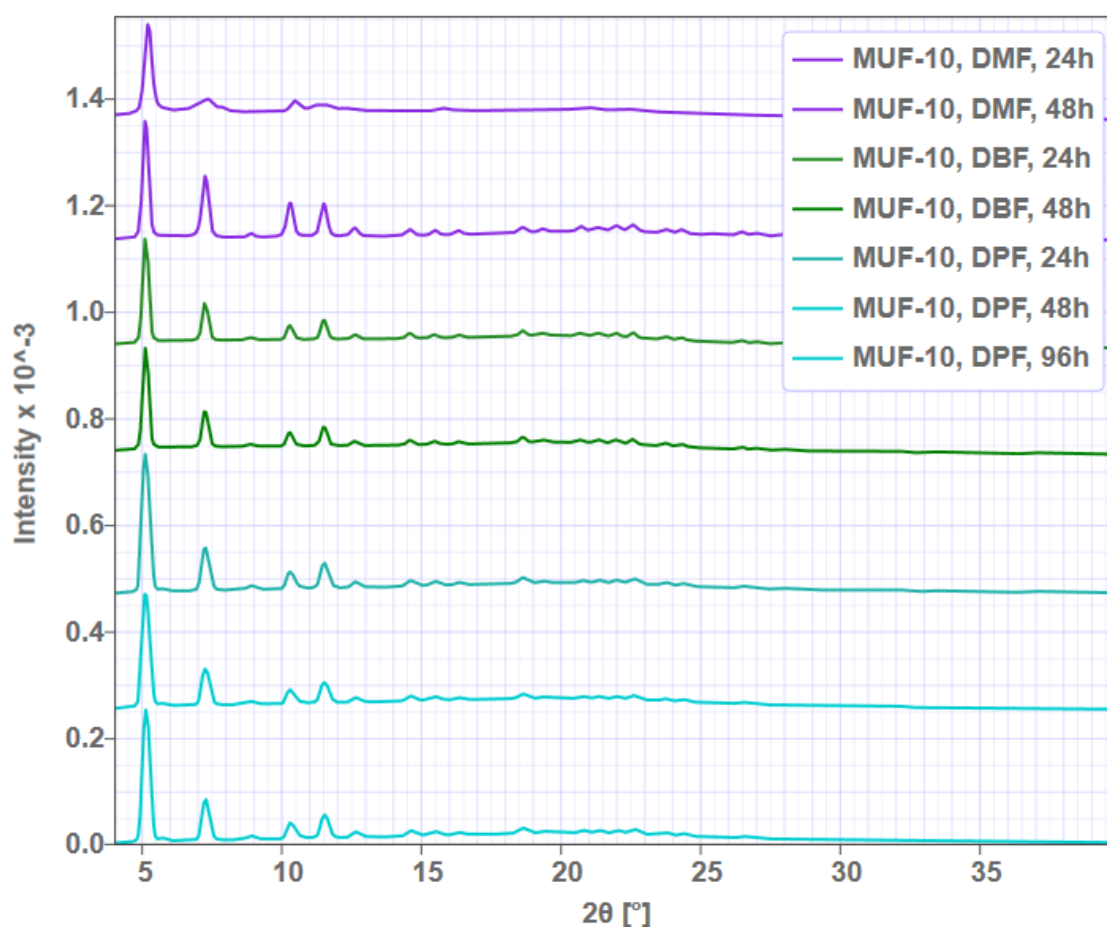


Figure 6.5: PXRD diffractograms of α -MUF-9 and α -MUF-10 heated in various solvents. Note that DBF and DPF do not cause phase changes in MUF-9 respectively, whereas smaller solvents do.

So, first, just as with MUF-9 and the MUF-9X series, it was necessary to establish which solvents would possibly be compatible with secondary growth in MUF-10. That is, we need to use a solvent which will not cause a phase change (such as autocatenation) when α -MUF-9 is heated in that solvent. Just as with the MUF-9X series, we want the

primary lattice to remain intact. Figure 6.5 shows that MUF-10 is stable when heated in N,N-di-n-propylformamide (DPF) and DBF. This is in contrast to MUF-9 which does undergo autocatenation in DPF over longer time periods. In MUF-9, out of all the solvents tested, only DBF could be used for secondary growth. With MUF-10, we have the possibility of using DPF as well.

6.2. SYNTHESIS AND CHARACTERISATION OF MUF-101

Since secondary amines are well known organocatalysts^{185, 187} for a variety of reactions which can give chiral products, and because we are subject to the same limitations of secondary ligands as in the MUF-90 series **L2**, with a methylaminomethyl group, (Figure 6.6; synthetic scheme and details in section 6.5.1) was selected as a target, as the simplest secondary amine side chain possible on BPDC. **L2** has a BPDC backbone to make it geometrically compatible with MUF-10, a small side chain that will allow it to enter the α -MUF-10 pores, and sufficient solubility in N,N-di-n-propylformamide to be used in a secondary growth solution.

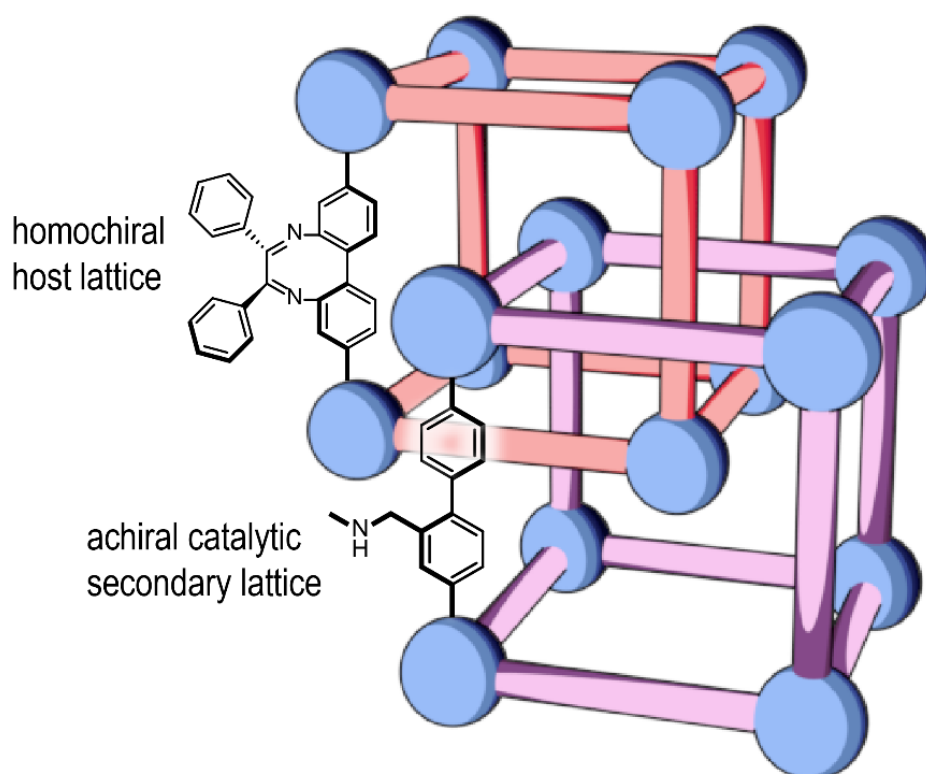


Figure 6.6: Illustration of MUF-101, showing the role of each component lattice.

Apart from tweaks to the reaction conditions (DBF as solvent, higher temperature, shorter reaction time) the synthesis of MUF-101 proceeded just as the MUF-90 series. When α -MUF-10 is heated in a solution of $\text{Zn}(\text{NO}_3)_2 \cdot 4\text{H}_2\text{O}$ and **L2**, the new components form a secondary $[\text{Zn}_4\text{O}(\text{L2})_3]$ lattice interpenetrated through MUF-10, which we call MUF-101. The solution is refreshed every two hours, to keep the concentration of new components high enough to continue forming the secondary lattice. The PXRD pattern peaks at $2\theta = 5.2$ and 7.3 decrease and increase in intensity respectively as the secondary lattice forms. This growth was tracked by PXRD, as shown in Figure 6.7. MUF-101 reaches a plateau of interpenetration at about 60% PIP, after four cycles or eight hours of exposure to the secondary growth conditions (bottom, green PXRD pattern in Figure 6.7).

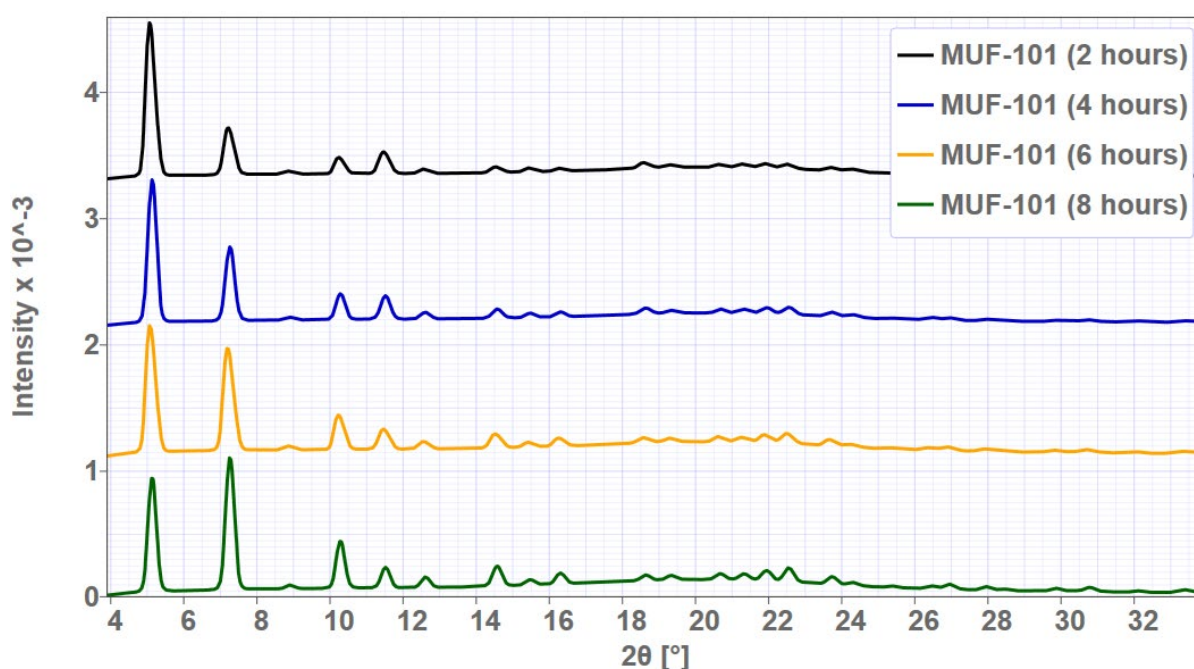


Figure 6.7: PXRD patterns of MUF-101 as it grows over time.

The growth of the secondary lattice in MOF-101 was also analysed by ^1H NMR spectroscopy of digested samples to determine the ratio of the ligands in each sample. Those NMR spectra are displayed in Figure 6.8.

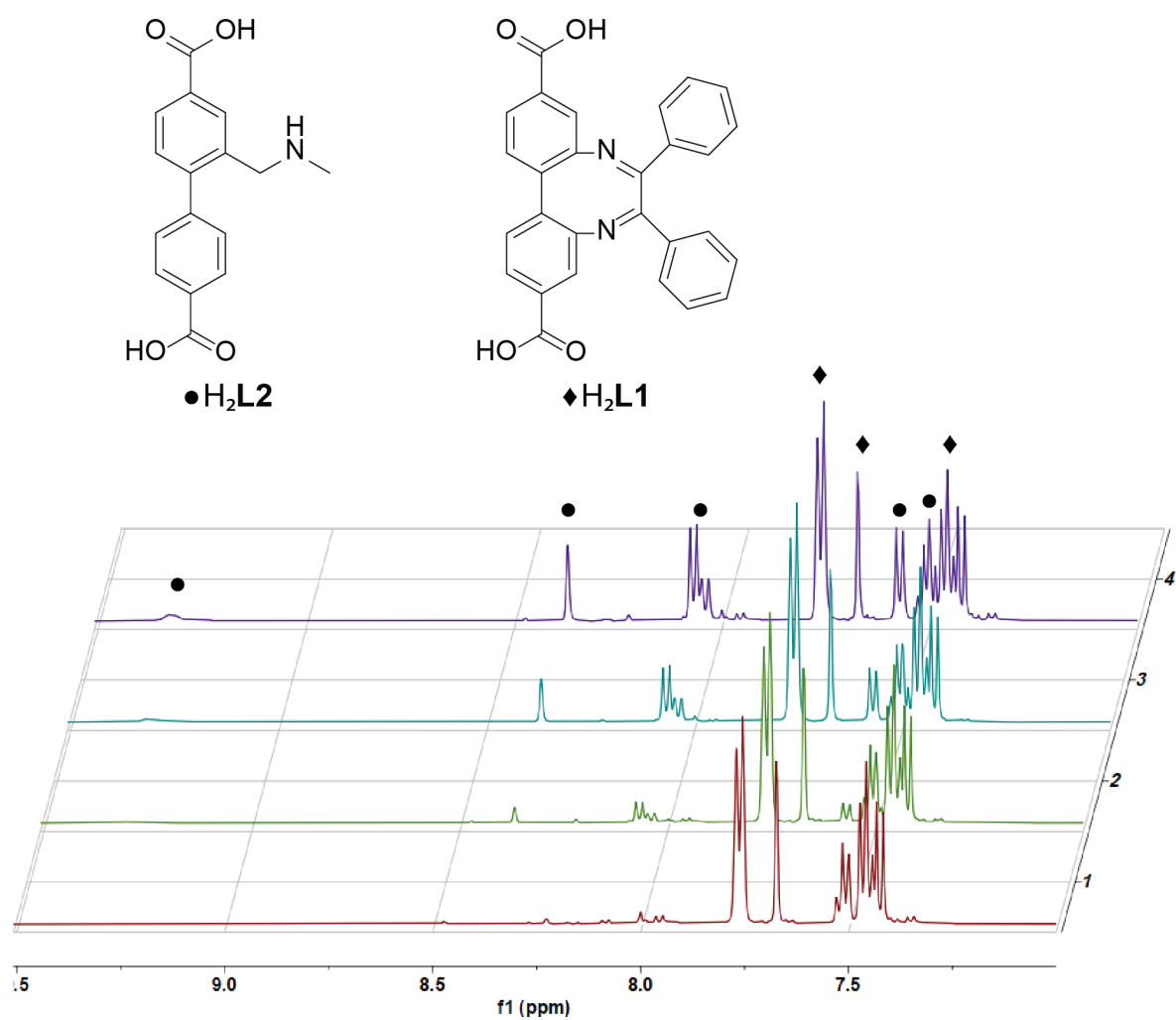
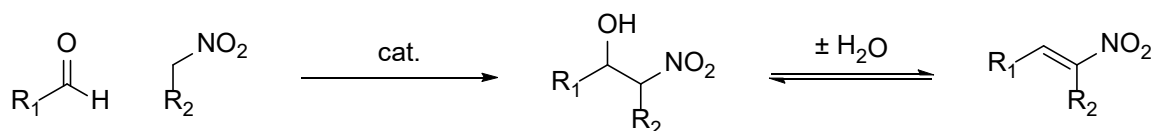


Figure 6.8: ^1H NMR spectra of digested samples of MUF-101 at various stages of growth. Spectra were recorded in a solution of 165 mM DCl in $\text{d}_6\text{-DMSO}$.

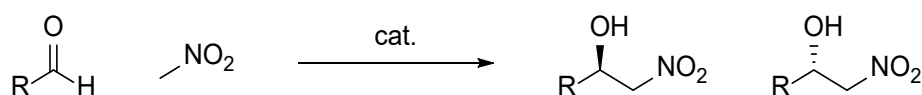
6.3. APPLICATION OF MUF-101 TO CATALYSIS

L2, and MUF-101, are active catalysts for the Henry reaction (Scheme 6.1) between m-nitrobenzaldehyde and a range of nitroalkanes, giving the expected products with comparable activity to similar catalysts^{66, 185, 201, 202} in the literature.



Scheme 6.1: A generic scheme for the Henry reaction between a nitroalkane and an aldehyde.

When the nitroalkane used is nitromethane, the product will have one new stereocentre, on the carbon with the newly formed alcohol group. This is shown in Scheme 6.2. If the reaction conditions favour one enantiomer over the other, then the resulting product will not be purely racemic, but will have an enantiomeric excess. The ratio of the two product enantiomers can be quantified because they will give distinct peaks when analysed by HPLC using a column with a chiral stationary phase. In the presence of water, the product may racemise over time (as shown in **Scheme 6.1**) through a dehydration which removes the chiral centre, followed by a hydration which is not enantioselective.



Scheme 6.2: The Henry reaction between nitromethane and an aldehyde.

We initially investigated the reaction between nitrobenzaldehyde and nitromethane, because other members of my research group had explored this reaction in their proline-based MOF catalyst, so we were familiar with the conditions for characterisation of the reaction by HPLC. MUF-101 is an active catalyst for this reaction, but no enantiomeric excess was observed in the product (Figure 6.9, top panel).

We reasoned that a possible explanation for the lack of selectivity in the reaction with nitromethane was that the substrates and products were too small to be affected by

the pore space. If the distance between the pore walls and the substrate is large enough, it will not exert a significant effect on the reaction. Therefore, we then tried using a larger substrate, nitroethane, instead. This time, we did observe an enantiomeric excess, seeing different relative peak areas for each product.

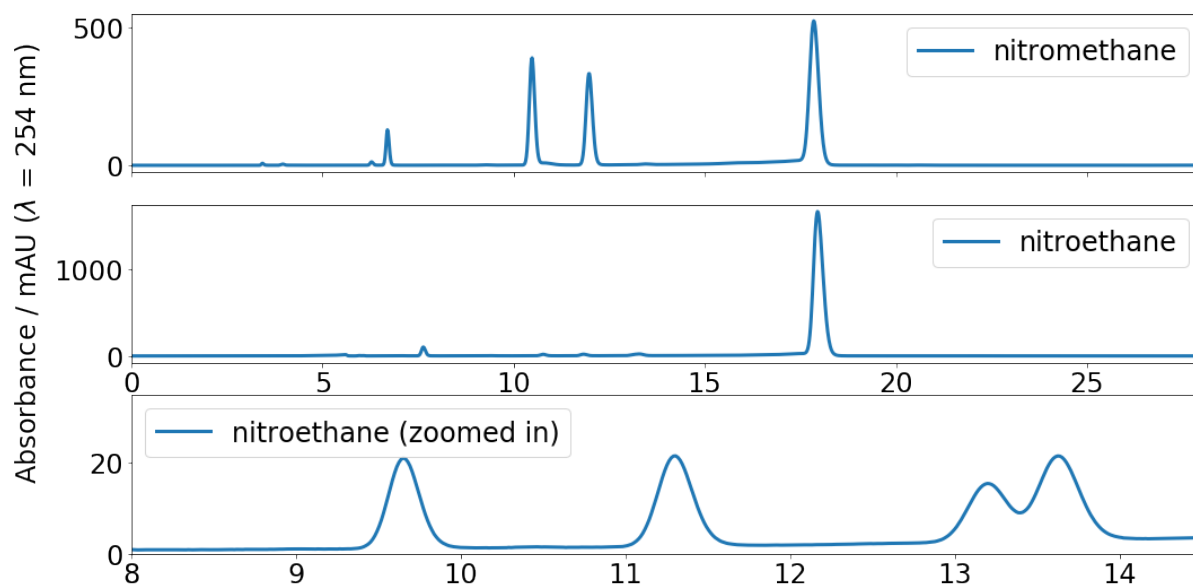


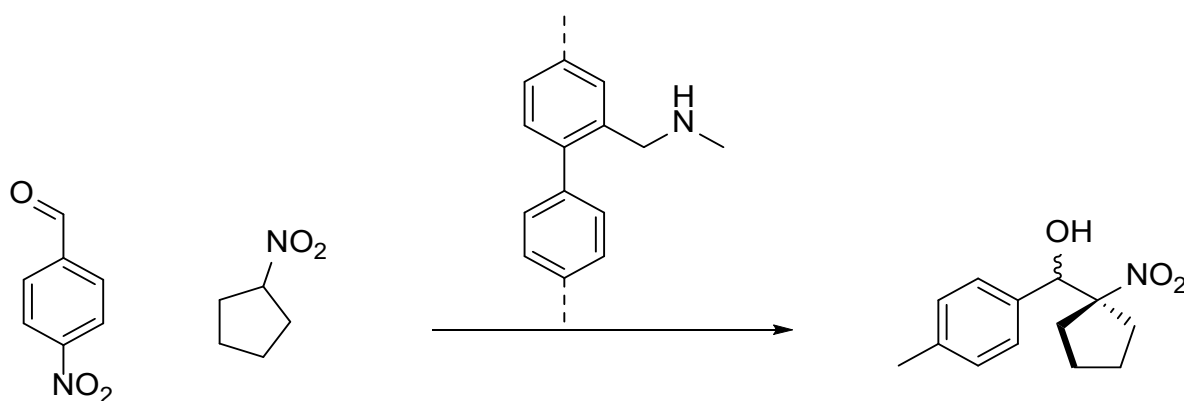
Figure 6.9: HPLC UV absorbance traces ($\lambda = 254$ nm) of the results of the Henry reaction between nitromethane or nitroethane and m-nitrobenzaldehyde, catalysed by **L2** in MUF-101. The peak at 17 minutes is the nitrobenzaldehyde starting material. The peaks between 9 and 15 minutes are the products.

Unfortunately, the products from the reaction between m-nitrobenzaldehyde and nitroethane were difficult to thoroughly characterise, since there are two diastereomeric sets of enantiomers, and a dehydration product, for five total products. We then looked at 2-nitropropane, but found that it was difficult to separate the product and reactant peaks by HPLC after exploring a range of conditions.

Looking at the outcomes of the various reactions described above, we selected m-nitrobenzaldehyde and nitrocyclopentane as substrates. We focused particularly on this reaction (Scheme 6.3) to characterise thoroughly. We considered that nitrocyclopentane had none of the major shortcomings displayed by the other substrates we tested. The products were easily separated from the aldehyde starting material by reverse phase HPLC, there are no diastereomers which form (only the two enantiomeric products), and there are no neighbouring hydrogen atoms to the newly

formed hydroxyl group, so the reaction product cannot undergo a dehydration reaction which might compromise measurement of the enantiomeric ratio of the products.

We tested Me₂L2 homogeneously for all these reactions and confirmed its activity by TLC. Unfortunately, Me₂L2 interfered with the HPLC analysis of the products, so we used NEt₃ for a homogeneous control reaction instead.



Scheme 6.3: The Henry reaction between m-nitrobenzaldehyde and nitrocyclopentane, as catalysed by **L2** in MUF-101.

Figure 6.10 shows the HPLC traces for these reactions, and the quantified outcomes are presented in Table 6.1. We observed an enantiomeric excess of $\pm 5.5\%$. The integral of each product peak (at 27.8 and 31.0 minutes respectively) were used to determine the e.e. for the reaction. The peaks were identified as the correct products using MS detection of ions with $m/z = 265.25 \pm 0.5$.

We did not assign the absolute configuration of each product peak. We assigned positive e.e. where the second-eluting peak was larger than the first eluting peak, and negative e.e. vice versa. Because enantiomers of a molecule behave the same in every way except their interactions with another chiral molecule, determining their absolute configuration is not straightforward. It is possible to determine a molecule's absolute configuration from a SCXRD structure, but to do that we would have had to isolate large enough quantities of the product to crystallise, and separating them on the scale required (rather than the few micrograms used in analytical HPLC) is also not straightforward.

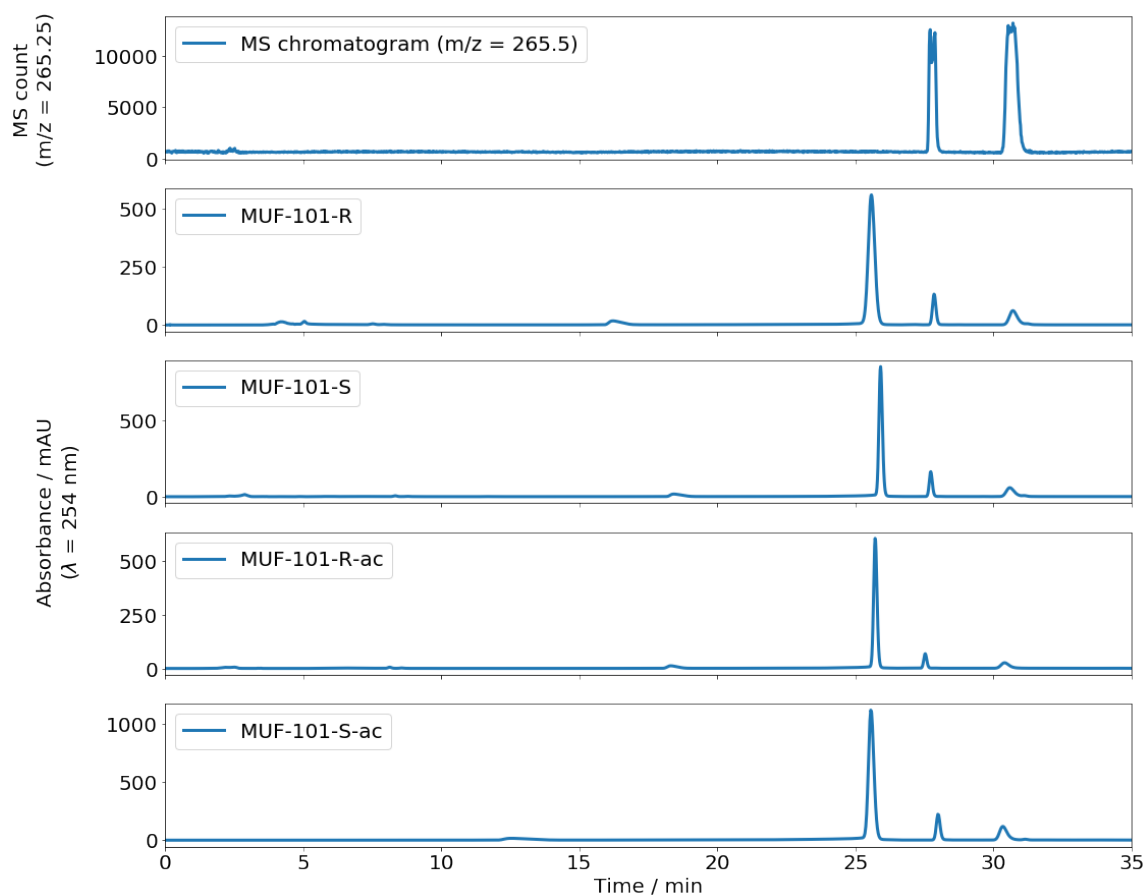


Figure 6.10: HPLC chromatograms of the results of the Henry reaction between nitrocyclopentane and m-nitrobenzaldehyde, catalysed by **L2** in MUF-101. The suffix '-ac' indicates the catalyst has been rendered fully interpenetrated through autocatenation. The peak at 26.4 minutes corresponds to the m-nitrobenzaldehyde starting material. The peaks at 27.8 and 31.0 minutes correspond to the product enantiomers, as indicated by the MS chromatogram.

As the catalytic ligand itself is achiral, the enantiomeric excess of the products must result from the chiral pore space created by the host lattice. Reversing the enantiomer of **L1** used for synthesis of the host lattice therefore also reverses the e.e. of the catalysis product. This serves as a demonstration of the capability of the individual components of a hetero-interpenetrated lattice to be orthogonal contributors to the functionality of the material.

PXRD analysis of MUF-101 (Figure 6.12, in experimental details, page 161) after its use in a catalytic reaction showed that the structure and crystallinity was maintained throughout the reaction.

Table 6.1: Results from catalysis with MUF-101 and control reactions

Catalyst	Relative area of enantiomer eluting at 28.7 min	Relative area of enantiomer eluting at 33.6 min	e.e.	Product to reactant peak ratio* at 48h	Catalyst loading [†]
NEt ₃ (homogeneous)	49.6	50.3	0	N/A	N/A
(R)-MUF-101	47.5	52.5	+5.5	0.20	5.4%
(S)-MUF-101	52.5	47.5	-5.5	0.21	5.7%
(R)-MUF-101-ac	47.5	52.5	+5.5	0.09	5.2%
(S)-MUF-101-ac	52.5	47.5	-5.5	0.11	5.6%
No catalyst	N/A	N/A	N/A	0	N/A

*The simple relative integral of the product peaks to the reactant peak in the HPLC trace.

[†]Calculated as the molar ratio of **L2** to m-nitrobenzaldehyde, using the amount of **L2** determined through by ¹H NMR analysis of the digested MOF after catalysis.

To illustrate the benefit of the hierarchical pore structure in MUF-101 for mass transport, we prepared fully-interpenetrated analogues of MUF-101 by autocatenation. By taking a crystal of MUF-101 and heating it in DMF, we observed the same single-crystal-to-single-crystal transformation as occurs with MUF-10: the rearrangement of the components into a fully interpenetrated phase. This autocatenated phase was labelled MUF-101-ac.

These frameworks have the same components as MUF-101, and were used for catalytic reactions at the same overall catalyst loading, but have no noninterpenetrated regions. Using these in the same reaction conditions as MUF-101, the same enantiomeric excess of products was observed, but the conversion at the same time point was approximately halved, showing that mass transport was hindered by the interpenetrated regions of the crystals.

6.4. CONCLUSIONS

The stepwise synthetic method we have developed for interpenetrating two different lattices has been expanded to a related framework, MUF-10. Although MUF-10 is similar to MUF-9, subtle parameters, particularly solvent choice, needed to be changed to adapt the synthetic method.

This technique has then been applied to produce an asymmetric catalyst, using a chiral host lattice to provide a chiral pore environment around an otherwise achiral catalytic ligand. This combination leads to an asymmetric catalytic outcome where each distinct lattice in MUF-101 contributes orthogonally to the function of the material. It also exploits the hierarchical pore size distribution natural to partially interpenetrated materials for increased mass transport compared to a fully interpenetrated equivalent.

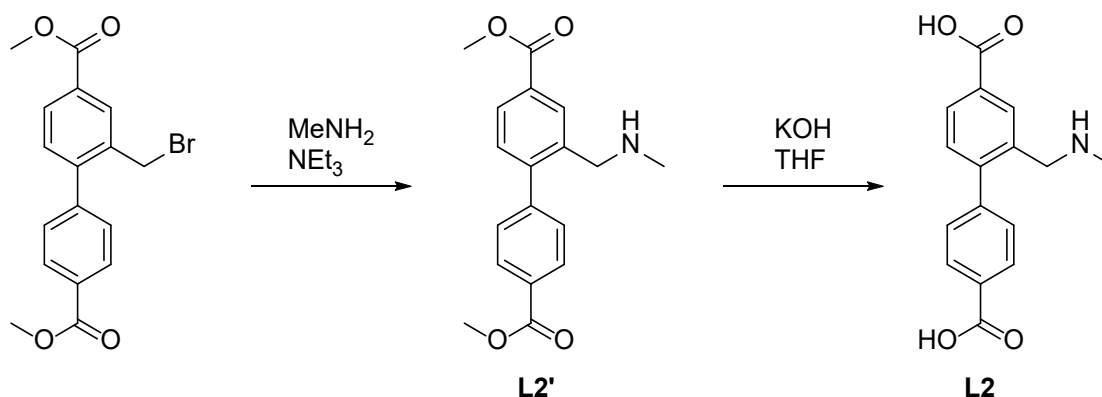
In recent work¹⁸⁷ from our group described earlier (section 6.1.2.2), modifications to ligands remote to the catalytic site in a multicomponent MOF were shown to influence reactivity and product selectivity. Here, to our knowledge for the first time, one ligand provides catalytic activity while another creates a chiral environment. To my knowledge, this is the first example of asymmetric induction by a chiral pore space around a catalytic site in a synthesised material.

This function is reminiscent of the active site in an enzyme, where the overall shape of the catalytic pocket is highly influential to its activity and selectivity.

The ability to orthogonally modify the pore shape and the catalyst could be used to tailor catalysts to specific substrates.

6.5. EXPERIMENTAL DETAILS AND SUPPLEMENTARY DATA

6.5.1. Synthesis of L2



Scheme 6.4: Synthesis of L2

Dimethyl-2-(bromomethyl)-4,4'-biphenyldicarboxylate was synthesised via a literature procedure²⁰³.

6.5.1.1. Synthesis of L2'

Dimethyl-2-(bromomethyl)-4,4'-biphenyldicarboxylate (500 mg, 1.38 mmol) was dissolved in Et_2O (30 mL) in a 100 mL round-bottom flask equipped with a magnetic stirrer. 1 M MeNH_2 in Et_2O (20 mL) and Et_3N (1 mL) were added and the mixture stirred at room temperature overnight. The reaction mixture was washed with H_2O (20 mL \times 3) and concentrated under reduced pressure, then the residue chromatographed on silica in a gradient from 1:0.01 CH_2Cl_2 : MeOH to 1:0.2 CH_2Cl_2 : MeOH to yield dimethyl-2-(methylaminomethyl)-4,4'-biphenyldicarboxylate (382 mg, 1.21 mmol, 88%)

^1H -NMR (500 MHz, CDCl_3): 8.20 (1H, s), 8.12 (2H, d, $J = 8.17$ Hz), 8.00 (1H, dd, $J = 7.98$, 1.50 Hz), 7.48 (2H, d, $J = 8.17$ Hz), 7.33 (1H, d, $J = 8.00$ Hz), 3.97 (3H, s), 3.95 (3H, s), 3.72 (2H, s), 2.36 (2H, s)

^{13}C -NMR (125 MHz, CDCl_3): 166.82, 145.46, 144.82, 130.47, 130.09, 129.89, 129.66, 129.52, 129.04, 128.41, 52.25, 52.23, 35.63

ESI-MS (-): Calc. 313.35 found 313.08 (M $^-$)

6.5.1.2. *Synthesis of L2*

Dimethyl-2-(methylaminomethyl)-4,4'-biphenyldicarboxylate (300 mg, 0.96 mmol) was dissolved in THF (15 mL) in a 50 mL round-bottom flask equipped with a stir bar. 2 M aqueous KOH (4 mL) was added and the mixture stirred vigorously overnight at room temperature. THF was removed under reduced pressure, and the mixture carefully neutralised with 1 M aqueous HCl, upon which a white precipitate formed. The precipitate was collected by filtration, washed with H₂O (5 mL × 3) and dried under high vacuum to yield 2-(methylaminomethyl)-4,4'-biphenyldicarboxylic acid (256 mg, 0.90 mmol, 94%)

¹H-NMR (500 MHz, d₆-DMSO): 10.90 (2H, s, b), 8.36 (1H, s), 8.07 (2H, d, J = 7.25 Hz), 8.03 (1H, d, J = 7.75 Hz), 7.57 (2H, d, J = 7.15 Hz), 7.49 (1H, d, J = 7.50 Hz), 4.09 (2H, s), 2.47 (3H, s)

¹³C-NMR (125 MHz, d₆-DMSO): 167.42, 146.90, 145.6, 131.26, 130.88, 130.77, 130.47, 130.11, 13.03 130.02, 49.10, 33.43

ESI-MS (+): Calc. 286.11 found 286.11 (MH⁺), (-): Calc 284.09 found 284.09 (M - H⁺)

6.5.1.3. *Synthesis of MUF-101*

α-MUF-10 was synthesised in a 4 mL glass vial with phenolic cap by a literature⁹⁹ method. A stock solution of L2 (1 mg mL⁻¹), Zn(NO₃)₂·4H₂O (2 mg mL⁻¹) and 2-fluorobenzoic acid (3 mg mL⁻¹) was prepared in N,N-di-n-propylformamide. The solvent was removed from a vial of α-MUF-10 and replaced with this stock solution, after which the vial was heated in a dry bath set to 105 °C. The stock solution was removed and replaced with fresh solution every 2 hours. At the desired stage of growth, the crystals were removed from the dry bath, cooled to room temperature, and washed several times with DBF.

6.5.1.4. *Synthesis of fully interpenetrated analogues of MUF-101 (MUF-101-ac)*

A sample of MUF-101 which had been subjected to two cycles (4 hours) of secondary growth was prepared (S4.1), then heated in DMF at 85°C for 16 hours.

Autocatenation⁹⁹ of the MUF-101 then resulted in a fully interpenetrated MOF with the same proportions of ligands as MUF-101.

6.5.1.5. *Catalytic reaction with MUF-101*

A sample of MUF-101, approximately 4 mg of MOF, which had been subjected to two cycles (4 hours) of secondary growth was prepared and washed with DBF (1 mL) then dry 1,4-dioxane (5 × 3 mL) and all excess solvent removed while being careful to limit exposure of the MOF to atmosphere. (Prepared MOF can be stored in dry dioxane for several days.) 100 µL of stock solution was then added to the vial of (R)-MUF-101. The procedure was repeated for (S)-MUF-10. Solutions were left in a dry bath set to 30°C for two days.

6.5.1.6. *HPLC conditions*

Catalytic reaction samples were diluted tenfold in 1,4-dioxane analysed by HPLC with UV detection at 254 nm and MS detection of the protonated product at $m/z = 265.25$, using a Phenomenex lux-amylose column and 35:65 MeCN:H₂O as mobile phase with a flow rate of 0.7 mL min⁻¹ over 35 minutes. The starting material *m*-nitrobenzaldehyde elutes at 26.4 minutes and the two products elute at 27.8 and 31.0 minutes.

6.5.1.7. Control HPLC chromatograms

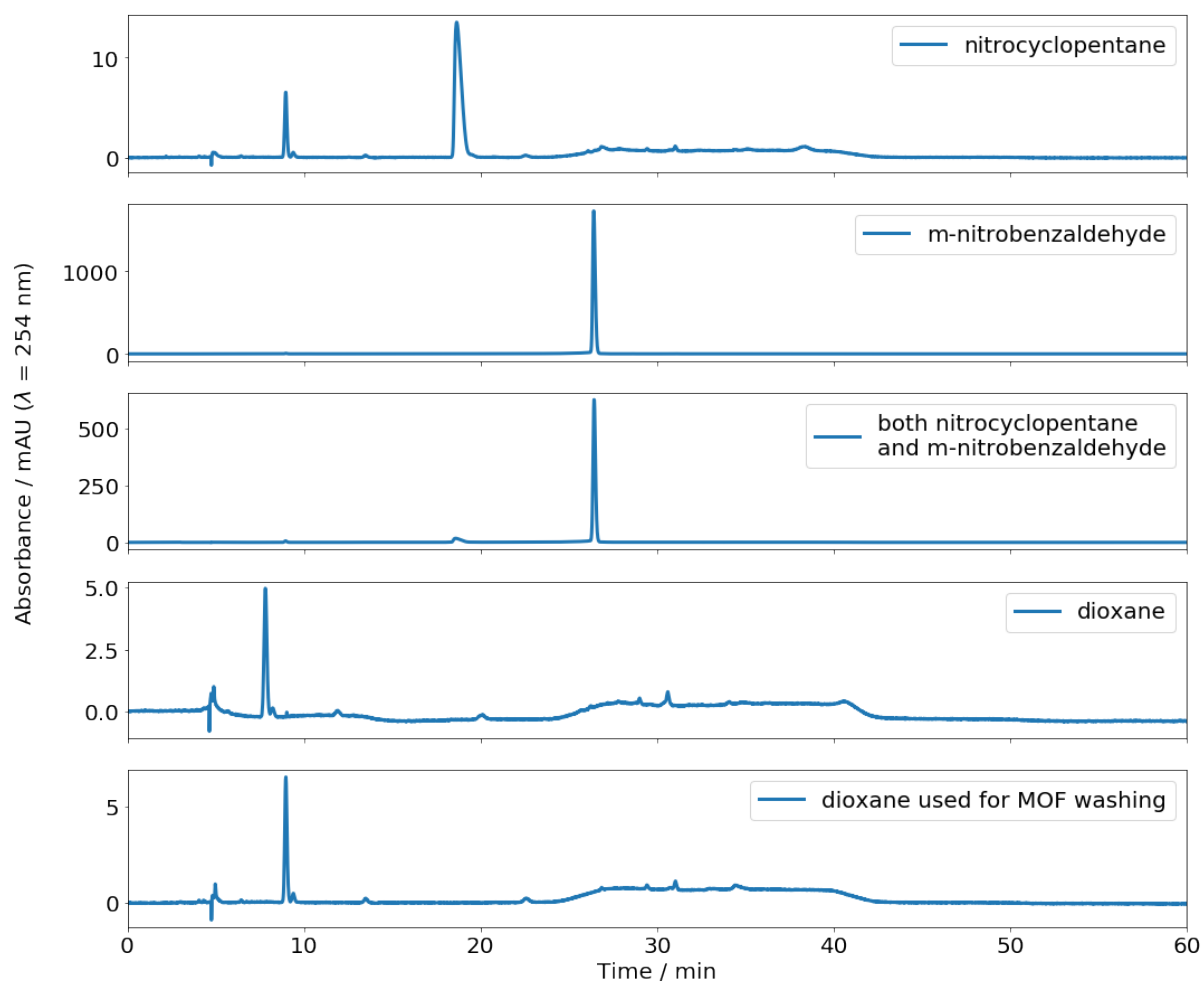


Figure 6.11: HPLC UV absorbance traces ($\lambda = 254$ nm) of various controls. Top, nitrocyclopentane in dioxane, identifying its position at 18.4 minutes. Second, m-nitrobenzaldehyde in dioxane, identifying its position at 26.4 minutes. Third, the stock solution used for the reaction, after 24 hours. Fourth, the solvent used for the reaction. The scale shows that there are no peaks. Fifth, the dioxane used to wash the MOF for the final time, showing that no material is leached from the MOF.

6.5.1.8. *PXRD patterns of MUF-101 before and after catalysis.*

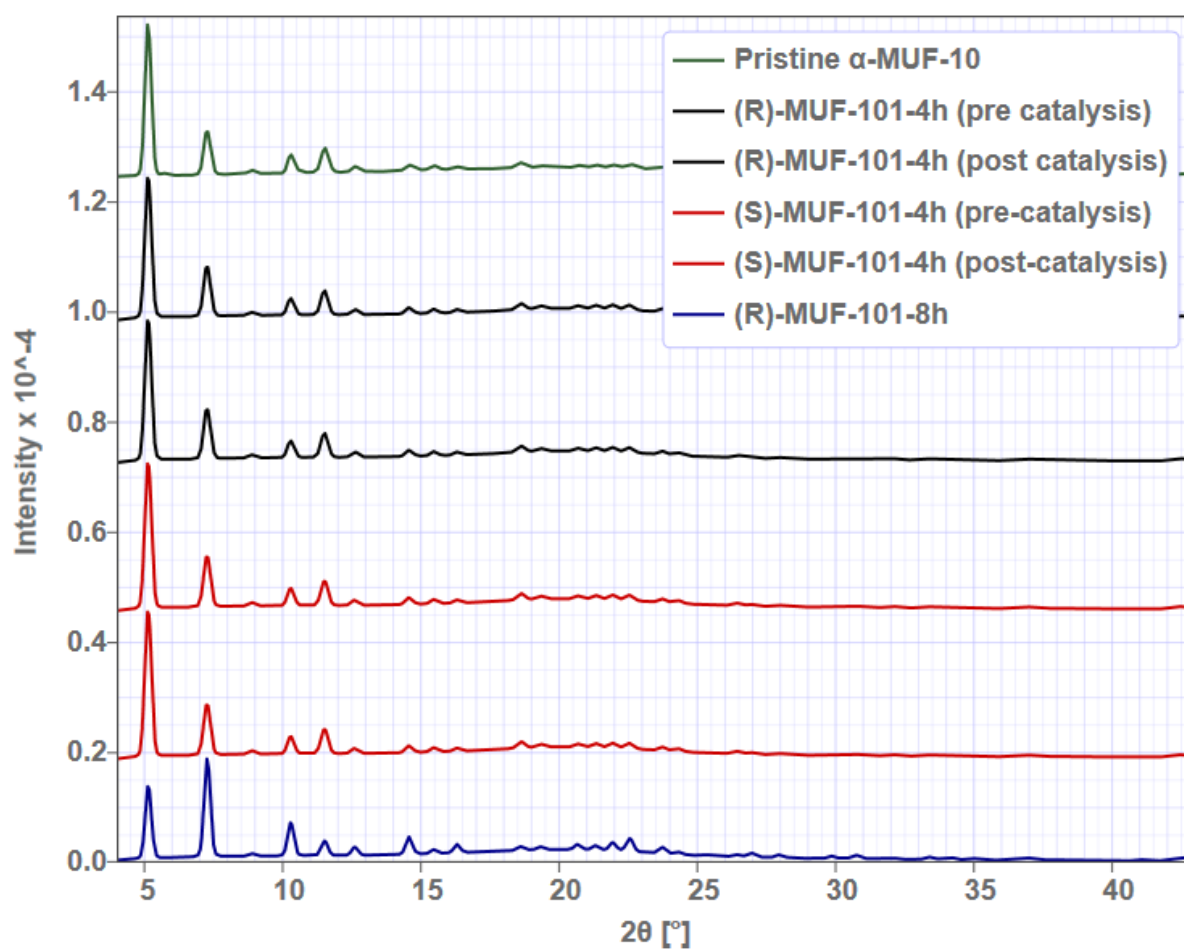


Figure 6.12: PXRD patterns of MUF-101 before and after catalysis.

6.7. REFERENCES

24. Abrahams, B. F.; Hoskins, B. F.; Michail, D. M.; Robson, R., Assembly of porphyrin building blocks into network structures with large channels. *Nature* **1994**, 369 (6483), 727-729. DOI: 10.1038/369727a0
29. Li, H.; Eddaoudi, M.; O'Keeffe, M.; Yaghi, O. M., Design and synthesis of an exceptionally stable and highly porous metal-organic framework. *Nature* **1999**, 402 (6759), 276-279. DOI: 10.1038/46248
31. Yuan, S.; Chen, Y. P.; Qin, J. S.; Lu, W.; Zou, L.; Zhang, Q.; Wang, X.; Sun, X.; Zhou, H. C., Linker Installation: Engineering Pore Environment with Precisely Placed Functionalities in Zirconium MOFs. *J. Am. Chem. Soc.* **2016**, 138 (28), 8912-9. DOI: 10.1021/jacs.6b04501
34. Lu, W.; Wei, Z.; Gu, Z. Y.; Liu, T. F.; Park, J.; Park, J.; Tian, J.; Zhang, M.; Zhang, Q.; Gentle, T., 3rd; Bosch, M.; Zhou, H. C., Tuning the structure and function of metal-organic frameworks via linker design. *Chem. Soc. Rev.* **2014**, 43 (16), 5561-93. DOI: 10.1039/c4cs00003j
60. Pascanu, V.; Gonzalez Miera, G.; Inge, A. K.; Martin-Matute, B., Metal-Organic Frameworks as Catalysts for Organic Synthesis: A Critical Perspective. *J. Am. Chem. Soc.* **2019**, 141 (18), 7223-7234. DOI: 10.1021/jacs.9b00733
63. García-García, P.; Müller, M.; Corma, A., MOF catalysis in relation to their homogeneous counterparts and conventional solid catalysts. *Chemical Science* **2014**, 5 (8), 2979. DOI: 10.1039/c4sc00265b
65. Sun, Q.; Tang, Y.; Aguila, B.; Wang, S.; Xiao, F. S.; Thallapally, P. K.; Al-Enizi, A. M.; Nafady, A.; Ma, S., Reaction Environment Modification in Covalent Organic Frameworks for Catalytic Performance Enhancement. *Angew Chem Int Ed Engl* **2019**, 58 (26), 8670-8675. DOI: 10.1002/anie.201900029
66. Liu, L.; Zhou, T.-Y.; Telfer, S. G., Modulating the Performance of an Asymmetric Organocatalyst by Tuning Its Spatial Environment in a Metal-Organic Framework. *J. Am. Chem. Soc.* **2017**, 139 (39), 13936-13943. DOI: 10.1021/jacs.7b07921
69. Burgun, A.; Coghlan, C. J.; Huang, D. M.; Chen, W.; Horike, S.; Kitagawa, S.; Alvino, J. F.; Metha, G. F.; Sumby, C. J.; Doonan, C. J., Mapping-Out Catalytic Processes in a Metal-Organic Framework with Single-Crystal X-ray Crystallography. *Angew. Chem. Int. Ed.* **2017**, 56 (29), 8412-8416. DOI: 10.1002/anie.201611254
87. Lin, Z.; Zhang, Z. M.; Chen, Y. S.; Lin, W., Highly Efficient Cooperative Catalysis by Co(III) (Porphyrin) Pairs in Interpenetrating Metal-Organic Frameworks. *Angew Chem Int Ed Engl* **2016**, 55 (44), 13739-13743. DOI: 10.1002/anie.201605802
99. Ferguson, A.; Liu, L.; Tapperwijn, S. J.; Perl, D.; Coudert, F.-X.; Van Cleuvenbergen, S.; Verbiest, T.; van der Veen, M. A.; Telfer, S. G., Controlled partial interpenetration in metal-organic frameworks. *Nat. Chem.* **2016**, 8 (3), 250-257. DOI: 10.1038/nchem.2430
124. Yin, Z.; Zhou, Y.-L.; Zeng, M.-H.; Kurmoo, M., The concept of mixed organic ligands in metal-organic frameworks: design, tuning and functions. *Dalton Trans.* **2015**, 44 (12), 5258-5275. DOI: 10.1039/c4dt04030a

132. Tonigold, M.; Lu, Y.; Bredenkötter, B.; Rieger, B.; Bahn Müller, S.; Hitzbleck, J.; Langstein, G.; Volkmer, D., Heterogeneous Catalytic Oxidation by MFU-1: A Cobalt(II)-Containing Metal-Organic Framework. *Angew. Chem. Int. Ed.* **2009**, *48* (41), 7546–7550. DOI: 10.1002/anie.200901241
168. Wang, X.; Wisser, F. M.; Canivet, J.; Fontecave, M.; Mellot-Draznieks, C., Immobilization of a Full Photosystem in the Large-Pore MIL-101 Metal-Organic Framework for CO₂ reduction. *ChemSusChem* **2018**, *11* (18), 3315–3322. DOI: 10.1002/cssc.201801066
169. Gonzalez, M. I.; Bloch, E. D.; Mason, J. A.; Teat, S. J.; Long, J. R., Single-crystal-to-single-crystal metalation of a metal-organic framework: a route toward structurally well-defined catalysts. *Inorg. Chem.* **2015**, *54* (6), 2995–3005. DOI: 10.1021/acs.inorgchem.5b00096
171. Liang, W.; Babarao, R.; Church, T. L.; D'Alessandro, D. M., Tuning the cavities of zirconium-based MIL-140 frameworks to modulate CO₂ adsorption. *Chem. Commun.* **2015**, *51* (56), 11286–9. DOI: 10.1039/c5cc02539g
172. Seoane, B.; Castellanos, S.; Dikhtiarenko, A.; Kapteijn, F.; Gascon, J., Multi-scale crystal engineering of metal organic frameworks. *Coord. Chem. Rev.* **2016**, *307*, 147–187. DOI: 10.1016/j.ccr.2015.06.008
173. Feng, L.; Yuan, S.; Zhang, L. L.; Tan, K.; Li, J. L.; Kirchon, A.; Liu, L. M.; Zhang, P.; Han, Y.; Chabal, Y. J.; Zhou, H. C., Creating Hierarchical Pores by Controlled Linker Thermolysis in Multivariate Metal-Organic Frameworks. *J. Am. Chem. Soc.* **2018**, *140* (6), 2363–2372. DOI: 10.1021/jacs.7b12916
174. Dhakshinamoorthy, A.; Li, Z.; Garcia, H., Catalysis and photocatalysis by metal organic frameworks. *Chem. Soc. Rev.* **2018**, *47* (22), 8134–8172. DOI: 10.1039/c8cs00256h
175. Jiang, D.; Xu, P.; Wang, H.; Zeng, G.; Huang, D.; Chen, M.; Lai, C.; Zhang, C.; Wan, J.; Xue, W., Strategies to improve metal organic frameworks photocatalyst's performance for degradation of organic pollutants. *Coord. Chem. Rev.* **2018**, *376*, 449–466. DOI: 10.1016/j.ccr.2018.08.005
176. Pagis, C.; Ferbinteanu, M.; Rothenberg, G.; Tanase, S., Lanthanide-Based Metal Organic Frameworks: Synthetic Strategies and Catalytic Applications. *ACS Catalysis* **2016**, *6* (9), 6063–6072. DOI: 10.1021/acscatal.6b01935
177. Zhang, Y.; Yang, X.; Zhou, H.-C., Synthesis of MOFs for heterogeneous catalysis via linker design. *Polyhedron* **2018**, *154*, 189–201. DOI: 10.1016/j.poly.2018.07.021
178. Tonigold, M.; Lu, Y.; Mavrandonakis, A.; Puls, A.; Staudt, R.; Mollmer, J.; Sauer, J.; Volkmer, D., Pyrazolate-based cobalt(II)-containing metal-organic frameworks in heterogeneous catalytic oxidation reactions: elucidating the role of entatic states for biomimetic oxidation processes. *Chemistry* **2011**, *17* (31), 8671–95. DOI: 10.1002/chem.201003173
179. Huang, N.; Yuan, S.; Drake, H.; Yang, X.; Pang, J.; Qin, J.; Li, J.; Zhang, Y.; Wang, Q.; Jiang, D.; Zhou, H. C., Systematic Engineering of Single Substitution in Zirconium Metal-Organic Frameworks toward High-Performance Catalysis. *J. Am. Chem. Soc.* **2017**, *139* (51), 18590–18597. DOI: 10.1021/jacs.7b09553
180. Johnson, J. A.; Petersen, B. M.; Kormos, A.; Echeverria, E.; Chen, Y. S.; Zhang, J., A New Approach to Non-Coordinating Anions: Lewis Acid Enhancement of Porphyrin Metal Centers in a Zwitterionic Metal-Organic Framework. *J. Am. Chem. Soc.* **2016**, *138* (32), 10293–8. DOI: 10.1021/jacs.6b05626

181. Choi, K. M.; Kim, D.; Rungtaweevoranit, B.; Trickett, C. A.; Barmanbek, J. T.; Alshammari, A. S.; Yang, P.; Yaghi, O. M., Plasmon-Enhanced Photocatalytic CO(2) Conversion within Metal-Organic Frameworks under Visible Light. *J. Am. Chem. Soc.* **2017**, *139* (1), 356-362. DOI: 10.1021/jacs.6b11027
182. van der Helm, M. P.; Klemm, B.; Eelkema, R., Organocatalysis in aqueous media. *Nature Reviews Chemistry* **2019**, *3* (8), 491-508. DOI: 10.1038/s41570-019-0116-0
183. Oliveira, V.; Cardoso, M.; Forezi, L., Organocatalysis: A Brief Overview on Its Evolution and Applications. *Catalysts* **2018**, *8* (12). DOI: 10.3390/catal8120605
184. Aleman, J.; Cabrera, S., Applications of asymmetric organocatalysis in medicinal chemistry. *Chem. Soc. Rev.* **2013**, *42* (2), 774-93. DOI: 10.1039/c2cs35380f
185. List, B., Introduction: Organocatalysis. *Chem. Rev. (Washington, DC, U. S.)* **2007**, *107* (12), 5413-5415. DOI: 10.1021/cr078412e
186. Hajos-Parrish-Eder-Sauer-Wiechert Reaction. In *Comprehensive Organic Name Reactions and Reagents*, pp 1305-1309. '10.1002/9780470638859.conrr290: ' 10.1002/9780470638859.conrr290
187. Zhou, T.-Y.; Auer, B.; Lee, S. J.; Telfer, S. G., Catalysts Confined in Programmed Framework Pores Enable New Transformations and Tune Reaction Efficiency and Selectivity. *J. Am. Chem. Soc.* **2019**, *141* (4), 1577-1582. DOI: 10.1021/jacs.8b11221
188. Lillerud, K. P.; Olsbye, U.; Tilset, M., Designing Heterogeneous Catalysts by Incorporating Enzyme-Like Functionalities into MOFs. *Top. Catal.* **2010**, *53* (13-14), 859-868. DOI: 10.1007/s11244-010-9518-4
189. Gu, Z.-Y.; Park, J.; Raiff, A.; Wei, Z.; Zhou, H.-C., Metal-Organic Frameworks as Biomimetic Catalysts. *ChemCatChem* **2014**, *6* (1), 67-75. DOI: 10.1002/cctc.201300493
190. Majewski, M. B.; Howarth, A. J.; Li, P.; Wasielewski, M. R.; Hupp, J. T.; Farha, O. K., Enzyme encapsulation in metal-organic frameworks for applications in catalysis. *CrystEngComm* **2017**, *19* (29), 4082-4091. DOI: 10.1039/c7ce00022g
191. Zheng, H. Q.; Liu, C. Y.; Zeng, X. Y.; Chen, J.; Lu, J.; Lin, R. G.; Cao, R.; Lin, Z. J.; Su, J. W., MOF-808: A Metal-Organic Framework with Intrinsic Peroxidase-Like Catalytic Activity at Neutral pH for Colorimetric Biosensing. *Inorg. Chem.* **2018**, *57* (15), 9096-9104. DOI: 10.1021/acs.inorgchem.8b01097
192. He, J.; Zhang, Y.; Zhang, X.; Huang, Y., Highly efficient Fenton and enzyme-mimetic activities of NH₂-MIL-88B(Fe) metal organic framework for methylene blue degradation. *Sci Rep* **2018**, *8* (1), 5159. DOI: 10.1038/s41598-018-23557-2
193. Gao, J., Catalysis by enzyme conformational change as illustrated by orotidine 5'-monophosphate decarboxylase. *Curr. Opin. Struct. Biol.* **2003**, *13* (2), 184-192. DOI: 10.1016/s0959-440x(03)00041-1
194. Katsoulidis, A. P.; Antypov, D.; Whitehead, G. F. S.; Carrington, E. J.; Adams, D. J.; Berry, N. G.; Darling, G. R.; Dyer, M. S.; Rosseinsky, M. J., Chemical control of structure and guest uptake by a conformationally mobile porous material. *Nature* **2019**, *565* (7738), 213-217. DOI: 10.1038/s41586-018-0820-9

195. Carrington, E. J.; Petuya, R.; Hylton, R. K.; Yan, Y.; Antypov, D.; Darling, G. R.; Dyer, M. S.; Berry, N. G.; Katsoulidis, A. P.; Rosseinsky, M. J., The Anisotropic Responses of a Flexible Metal-Organic Framework Constructed from Asymmetric Flexible Linkers and Heptanuclear Zinc Carboxylate Secondary Building Units. *Cryst. Growth Des.* **2019**, *19* (10), 5604-5618. DOI: 10.1021/acs.cgd.9b00558
196. Bell, F., The Stereochemistry of 2 : 2'-Bridged Derivatives of Diphenyl. *Journal of the Chemical Society (Resumed)* **1952**, (Notes), 1527-1528. DOI: 10.1039/jr9520001524
197. Sasai, H.; Suzuki, T.; Arai, S.; Arai, T.; Shibasaki, M., Basic character of rare earth metal alkoxides. Utilization in catalytic carbon-carbon bond-forming reactions and catalytic asymmetric nitroaldol reactions. *J. Am. Chem. Soc.* **1992**, *114* (11), 4418-4420. DOI: 10.1021/ja00037a068
198. Marqués-López, E.; Merino, P.; Tejero, T.; Herrera, R. P., Catalytic Enantioselective Aza-Henry Reactions. *Eur. J. Org. Chem.* **2009**, *2009* (15), 2401-2420. DOI: 10.1002/ejoc.200801097
199. Luzzio, F. A., The Henry reaction: recent examples. *Tetrahedron* **2001**, *57* (6), 915-945. DOI: 10.1016/s0040-4020(00)00965-0
200. Alvarez-Casao, Y.; Marques-Lopez, E.; Herrera, R. P., Organocatalytic Enantioselective Henry Reactions. *Symmetry* **2011**, *3* (2), 220-245. DOI: 10.3390/sym3020220
201. Chen, X.; Wang, J.; Zhu, Y.; Shang, D.; Gao, B.; Liu, X.; Feng, X.; Su, Z.; Hu, C., A secondary amine amide organocatalyst for the asymmetric nitroaldol reaction of alpha-ketophosphonates. *Chemistry* **2008**, *14* (35), 10896-9. DOI: 10.1002/chem.200801958
202. Luo, M.; Yan, B., Enantioselective henry reactions catalyzed by chiral N-metal complexes containing R(+)/S(-)- α -ethylphenyl amines. *Tetrahedron Lett.* **2010**, *51* (42), 5577-5580. DOI: 10.1016/j.tetlet.2010.08.055
203. Hu, Y. H.; Wang, J. C.; Yang, S.; Li, Y. A.; Dong, Y. B., CuI@UiO-67-IM: A MOF-Based Bifunctional Composite Triphase-Transfer Catalyst for Sequential One-Pot Azide-Alkyne Cycloaddition in Water. *Inorg. Chem.* **2017**, *56* (14), 8341-8347. DOI: 10.1021/acs.inorgchem.7b01025

Chapter 7: DERIVATIVE LIGANDS

7.1. INTRODUCTION

In order to probe some of the causes of the controlled partial interpenetration behaviour described in Chapters 1 and 2, and therefore also the hetero-interpenetration observed in Chapters 3 – 6, I prepared some new ligands based on **L1** to explore their properties in MOF formation.

In the analysis of the SCXRD structures presented in this chapter, the most important aspect is the effect of the interactions between side chains on the formation of the MOF. In the MOFs presented, although the specific structure that forms was not easily predicted in advance, each structural outcome can be rationalised through the tools of supramolecular chemistry²⁰⁴ – namely the identification of “motifs”, structural features common in packing arrangements.

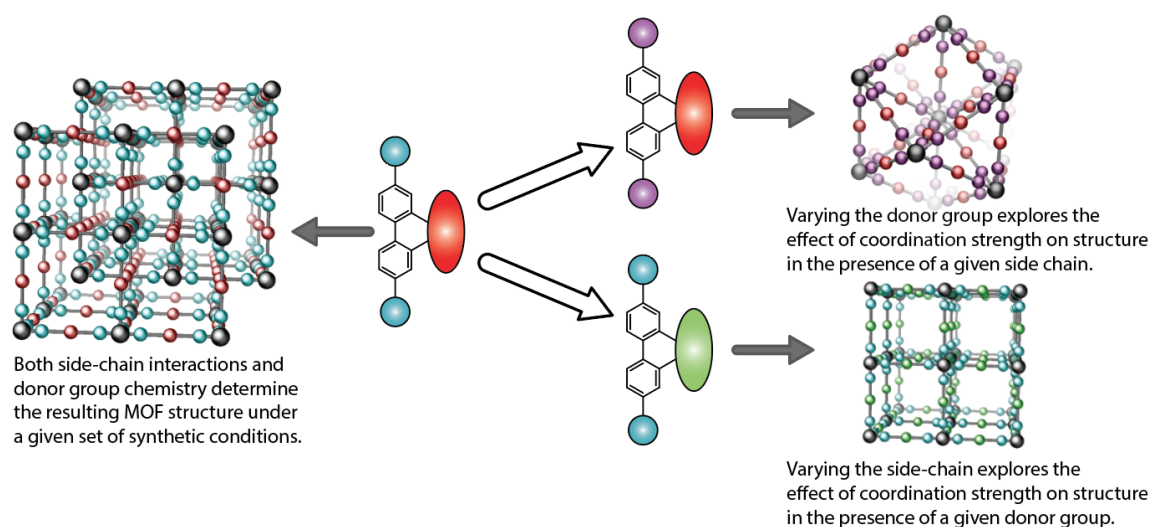


Figure 7.1: An illustration of the general ideas presented in this chapter – changing either the ligand side chain or the donor group to look at their respective influences on the resulting MOF structures.

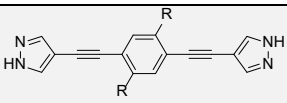
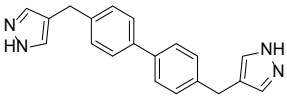
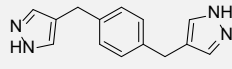
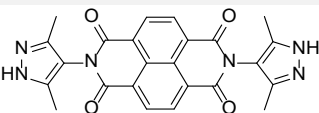
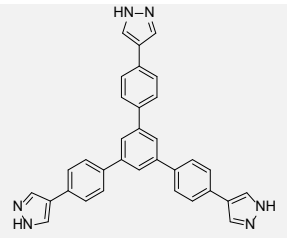
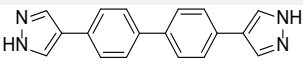
Some of these have the same BPDC backbone as **L1** (sections 7.2.1 to 7.2.2) and are used to probe the effect of varying the shape of the ligand in subtle ways. These serve to give some additional support to the theory that the specific sidechain-to-backbone interactions are responsible for the partial interpenetration behaviour of MUFs 9 – 14 (as described in Chapter 2, section 2.1. page 31).

Other sets of ligands (sections 7.2.3 and 0) are *extended* analogues of L1, with both carboxylate and pyrazolate binding groups. These ligands were chosen as targets for the purpose of giving some information about the limits of controlled partial interpenetration. With the carboxylate analogues (**L11** and **L12**) this was intended to be something like the effect of lowering the percentage of the cell volume and/or ligand atoms involved in a potential interaction leading to partial interpenetration. The pyrazolate analogue **L21** (page 180) was designed to probe the effect of a stronger ligand donor group.

Pyrazolate ligands are comparatively rare in MOFs. Out of more than 80,000 MOF structures in the Cambridge Structural Database^{23, 205} around 500 include pyrazoles coordinated to the SBU in some way. In many cases, these are unsubstituted pyrazoles capping SBUs, and the structural ligands feature other coordinating groups. MOFs with only pyrazolate ligands number under 200. Of those, only 17 MOFs (with 6 different ligands and structures, utilising different metals) have ligands longer than 1,4-benzenedipyrazolate, and these are summarised in Table 7.1. Most of these have been prepared and reported by the group of Professor Simona Galli at the University of Insubria, only reference ²⁰⁶ is from another group.

In every case listed in Table 7.1, the crystal structure was determined from PXRD data, as the materials could only be synthesised as microcrystalline powders. Pyrazolate MOFs in general, even those with smaller ligands, are difficult to synthesise as single crystals. This is directly related to their stability. The lower lability of pyrazolate-metal bonds compared to, e.g., zinc-carboxylate bonds, results in higher nucleation and less rearrangement during self-assembly, and therefore a smaller crystal size. The lower lability of the pyrazolate-metal bonds also results in higher hydrolytic stability, a desirable property in MOFs.

Table 7.1: All examples of MOFs with pyrazolate linkers greater than 13 Å in length in the CSD.

Ligand	Metal(s)	Reference(s)
	Zinc(II) Nickel(II)	207, 208
	Zinc(II) Cobalt(II) Copper(II) Cadmium(II)	209
	Zinc(II) Cobalt(II)	210
	Copper(II)	206
	Nickel(II) Copper(I,II)	211
	Nickel(II)	212-214

7.1.1. Supramolecular interactions and binding motifs

Supramolecular chemistry²¹⁵ is an area of research which, because of its breadth, is difficult to define precisely but which can be said to be “chemistry beyond the molecule”. The focus is on non-covalent bonds: the interactions between molecules leading to phenomena like host-guest recognition, self-assembly, molecular machines, and so on. Although more traditional coordination chemistry is important to the synthesis of MOFs, some aspects of their synthesis (to be elaborated upon in this chapter), and certainly their exploitation as molecular hosts, fall squarely into this realm.

Noncovalent interactions are what determine how molecules pack together²¹⁶ to form crystals. Except for ionic bonds, which will not be discussed here, probably the most

important in determining crystal packing is hydrogen bonding, simply because it is the strongest noncovalent bond. When a molecule has a possibility to hydrogen bond, there would have to be a very high number of concerted other interactions to supersede that hydrogen bond in determining the crystal packing.

Aromatic interactions²¹⁷⁻²¹⁹ are those noncovalent interactions between aromatic groups. The interactions which lead to the unusual partial interpenetration properties of MUFs 9 and 10 are aromatic interactions. Interactions between aromatic rings, or an aromatic ring and another chemical moiety, are key²²⁰ in both living and synthetic chemical recognition processes. These interactions are fundamentally the same as any other kind of van der Waals interaction (primarily resulting from attractive London dispersion forces between transient dipoles in molecules' electron clouds) but due to the highly polarisable and diffuse electron clouds in aromatic molecules, and a small permanent multipole, they are much stronger than the same interactions in aliphatic molecules and are given their own category.

Specific classes of these interactions, between types of chemical groups, are referred to in the field as motifs²²¹. The use of 'motifs' aids the design of self-assembled structures and structures which recognise and interact with guests in desired ways. Some famous examples of traditional supramolecular motifs are the binding of metal cations by crown ethers²²² and pi-pi charge transfer interactions (especially) between pyridinium groups and electron rich arenes, famously exploited for the synthesis of catenanes²²³ by Sir J. Fraser Stoddart and many others. More simply, the preferred coordination geometries of transition metal cations have been exploited²²⁴ to create many molecular shapes and cages. The application of this way of thinking, using motifs to guide self-assembly, is a direct precursor²²⁵ to the way MOF chemists think about the structures they assemble.

7.1.1.1. *Aryl embraces*

Phenyl (or aryl) embraces are a classic²²⁶⁻²²⁸ supramolecular motif characterised by "multi-armed, attractive, mutual and concerted" edge-face and offset-face-face

interactions between molecules bearing multiple aromatic groups. These kinds of interactions commonly determine the crystal packing of polyphenylphosphines^{229, 230}. The energy of these concerted interactions is a simple multiple of that of a single edge-face interaction, so between four to six phenyl rings the total can be more than 65 – 80 kJ mol⁻¹, the same order of magnitude as an ionic bond.²³⁰ It is not, therefore, difficult to see why these kinds of interactions are a significant contributor to the crystal formations observed.

Phenyl embraces typically dominate when the phenyl groups separated by an atom larger than carbon (e.g. in PPh₃, PPh₄⁺, [M(bpy)_n], etc.), while the examples here are embraces between 1,2-diphenyl compounds. These are substantially similar, certainly enough to use the same term. In both cases they are built from concerted edge-face interactions between nearby phenyl rings in a rigid structure and offset from each other within the same molecule.

7.1.2. Prediction of crystal structures

As discussed in Chapter 1, one of the great appeals of framework materials is the ease of intuitive predictions of the resulting crystal structure¹² and properties²³¹ by the chemist. Nonetheless, this “ease” is only relative, compared to the prediction of crystal packing of, say, small molecules or proteins. Although prediction of crystal structures remains complicated, significant progress has been made in the last decades, largely through the advances in speed and ease of DFT calculations.

These approaches can also be combined, by screening potential structures generated from given components for physical properties, through DFT calculations or other simulations. After describing how choosing SBUs and ligands with appropriate coordination geometries often determines the resulting MOF structure, Day and Cooper²³² write:

Arguably, such intuitive design strategies will be defeated by complexity for molecular crystals, and even “well behaved” isorecticular extended

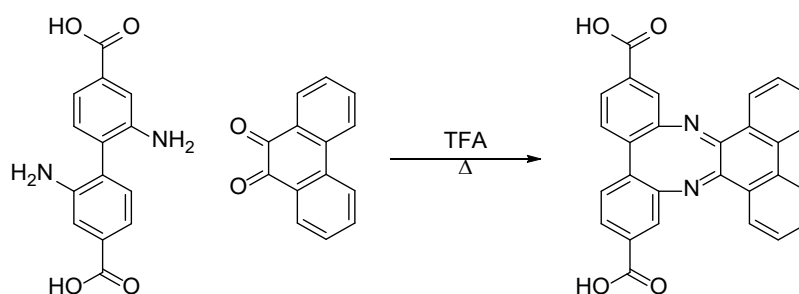
frameworks might carry an unacknowledged overhead in terms of incorporating directing functionality into materials to ensure that the components assemble directly.

That is, for results to conform to the expectations generated by the intuitive design principles of isorecticular chemistry, the frameworks must be “well behaved”. Of course, many frameworks are *not* well behaved, and particularly those with interesting functionality may not be, given that if those functionalities are interesting, they must interact with something, and if they interact with something, they might affect the structure obtained. We don’t want to be limited only to those functionalities which would certainly permit the desired structure, so we must take some of these other factors into account when thinking about MOF formation. For most synthetic chemists, detailed computational studies are not feasible. Of course, the ideal solution would be collaboration with a computational chemist, but in the absence of that possibility, using the classic tools of supramolecular chemistry expands the range of intuitive features we can use to guide our understanding of MOF formation.

7.2. RESULTS

7.2.1. Phenanthraquinone-bpdc (L3)

As an analogue to L1 which doesn't allow the rotation of pendant phenyl rings, we selected dibenzo[e,g]phenanthro[9,10-b][1,4]diazocine-3,16-dicarboxylic acid (H_2L3). It was prepared as shown in Scheme 7.1.



Scheme 7.1: Synthesis of L3.

As expected, this ligand forms a cubic $[Zn_4O]$ MOF when reacted with zinc nitrate tetrahydrate in DMF. This MOF is a noninterpenetrated **pcu** lattice, showing the result of using phenanthraquinone instead of a benzil side chain. The phenanthrene side chain is very close to the same size as the diphenylethene side chain, and also aromatic, but the pendant phenyl rings are bonded together. This side chain cannot accommodate other atoms between the two phenyl rings. Thus, it cannot form the specific interactions leading to controlled partial interpenetration in MUF-9 and its derivatives, an aryl embrace between the side chain and the backbone of its neighbouring lattice. Nor can it form the other interactions which determine some of the other structures presented in this chapter. The entire side chain is arranged perpendicular to the BPDC backbone (Figure 7.2), and only its steric bulk determines the resulting structure.

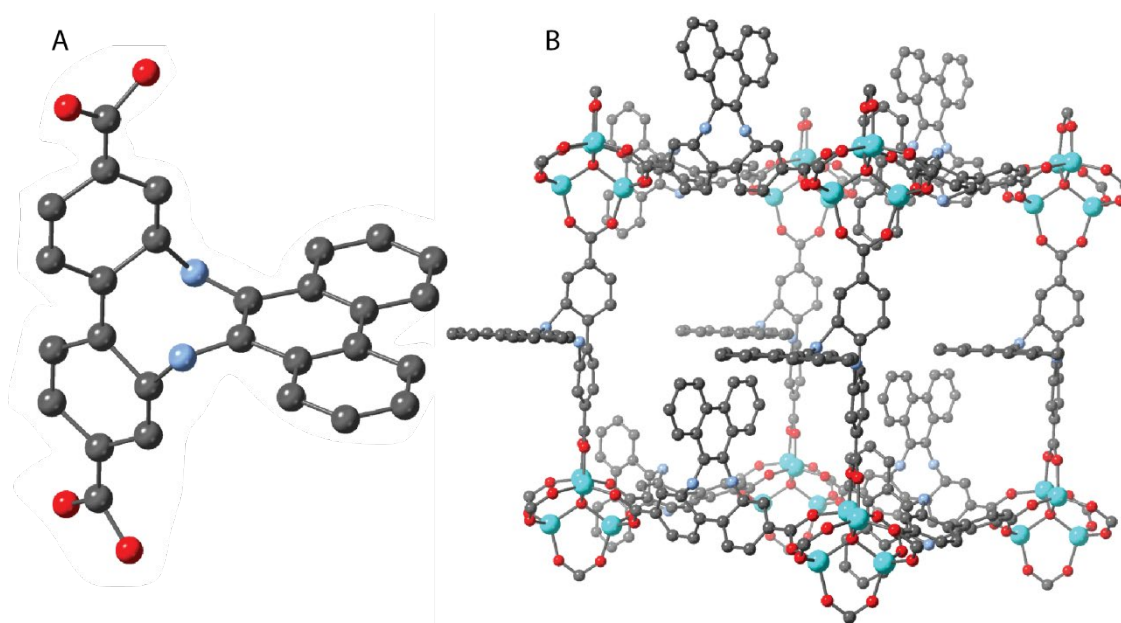
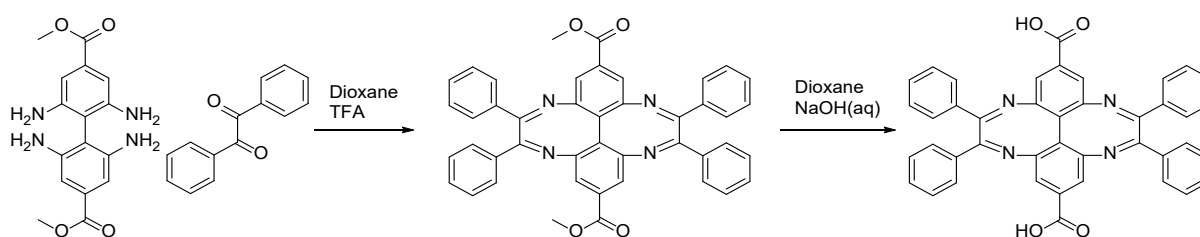


Figure 7.2: A) 3D model of **L3** as present in MOF-L3. B) the cell of MOF-L3. Disordered orientations of side chains and hydrogens have been removed for clarity. Carbon is coloured grey, oxygen red, nitrogen blue, zinc cyan.

7.2.2. Bis-benzil-bpdc (**L4**)



Scheme 7.2: Synthesis of **L4**

As an analogue to **L1** which has the same side chain, but doesn't allow access to the backbone for the contacts responsible for partial interpenetration in MUF-9, 5,6,12,13-tetraphenyl-4,7,11,14-tetraazadibenzo[fg,mn]octalene-2,9-dicarboxylic acid (**H₂L4**) was prepared as shown in Scheme 7.2. This ligand is chiral for the same reason as **L1** but was not resolved into its enantiomers and was used as the racemate for MOF synthesis.

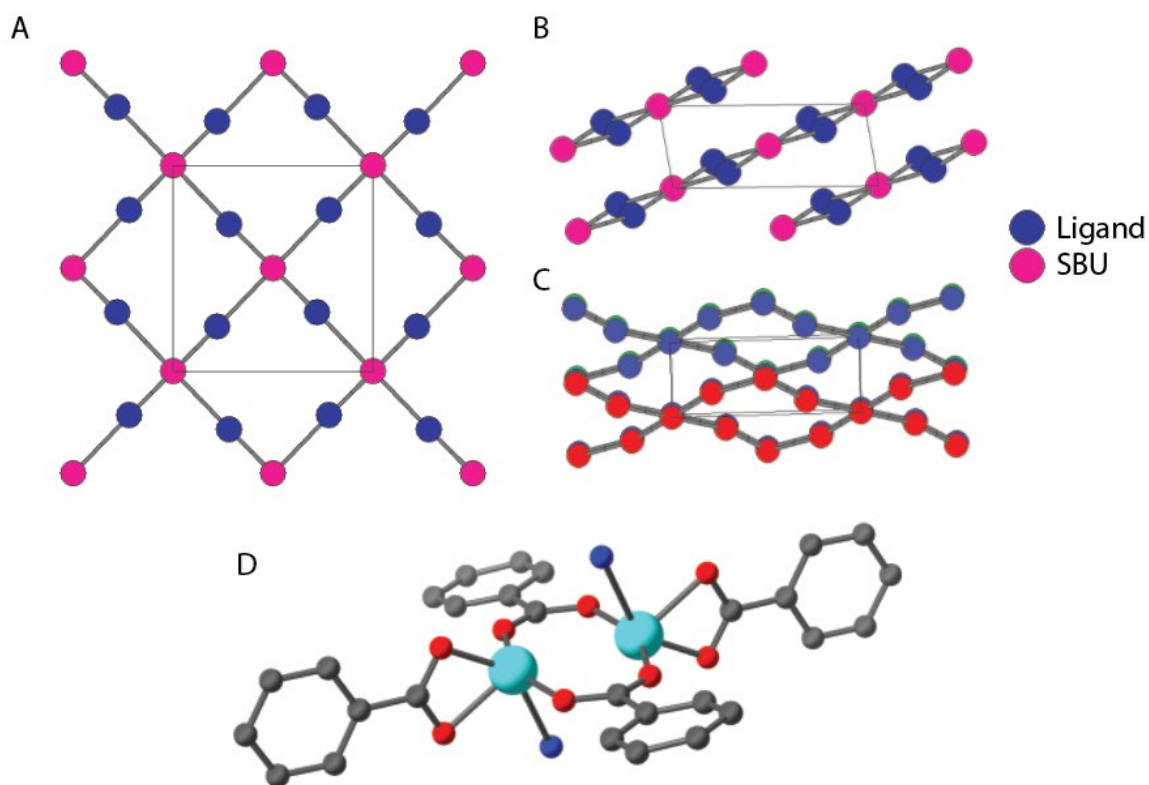


Figure 7.3: A) A simplified representation of MOF-L4 viewed from the (1,0,0) direction. B) A simplified representation of MOF-L4 viewed from the (0,1,0) direction. C) A simplified view of MOF-L4 from near the (0,0,1) direction. In panels A and B, pink circles represent the Zn_2 SBUs and the ligands, respectively. In panel C, each layer is given a different colour. D) A close-up illustration of the SBU in MOF-L4. Only the first phenyl ring of each ligand is shown. Grey spheres are carbon; blue, coordinated DMF; red, oxygen; cyan, zinc.

Unlike **L3**, **L4** does not form a **pcu** Zn_4O MOF under similar synthetic conditions in DMF (details page 192, crystallographic data page 195). Instead, it forms a 2D layered structure with each layer running diagonally through the cell, as illustrated in Figure 7.3. It has a pseudo-paddlewheel Zn_2 SBU, with each zinc (II) ion disordered over two close sites. Two of the equatorial sites are occupied by the ligand bridging two zincs, as in a traditional paddlewheel, while the other two sites are occupied by DMF. Each of the two axial sites has a ligand carboxylate group coordinated in a bidentate fashion, for an overall $\text{Zn}_2(\text{L4})_2(\text{DMF})_2$ structure. Another four DMF molecules are well located in the pores. This MOF resisted exchange of the included DMF with other solvents, preferring to collapse instead, as determined by PXRD.

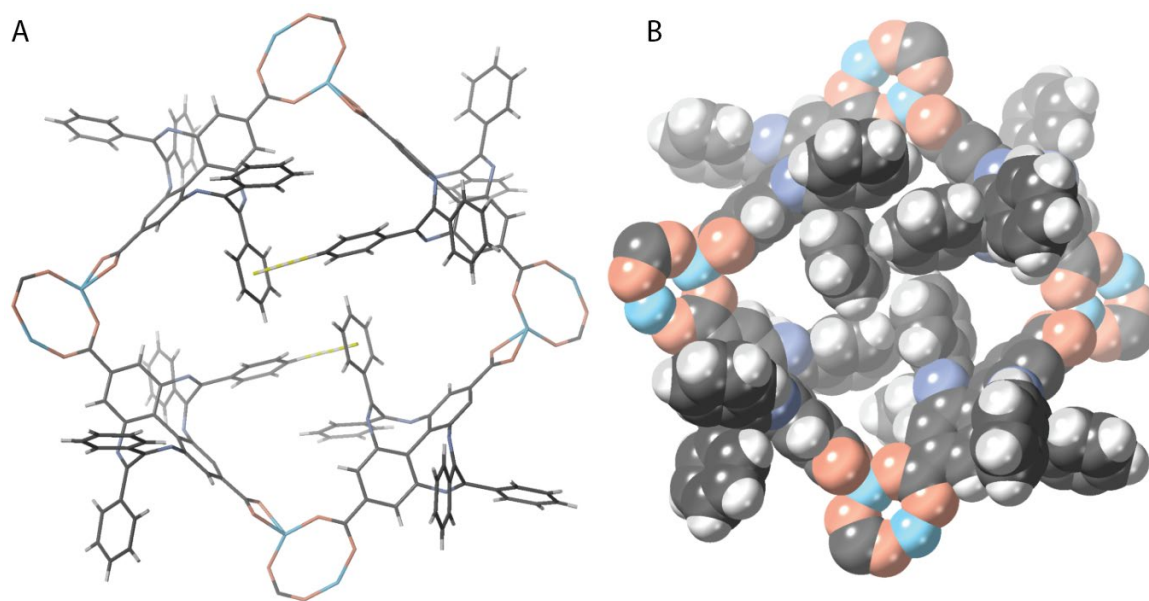


Figure 7.4: A) Stick-representation illustration of α -MOF-L4 showing the edge-face interactions as yellow sticks between side chains of **L4**. B) Space-filling illustration of α -MOF-L4 showing the offset face-face interactions between side chains of **L4**. Coordinated solvent and solvent in the pores has been omitted for clarity. For both A and B, carbon is dark grey, oxygen pale red, nitrogen blue, zinc cyan, and hydrogen white.

As with the other MOFs presented in this chapter, the presence of specific interactions between the ligand side chains determines the structure of MOF-L4. Unlike the others, it cannot be described in terms of more complex supramolecular motifs, but rather through many simple aromatic noncovalent interactions. In Figure 7.4A, a section of one layer of MOF-L4 is shown, with the edge-face interactions between pendant phenyl rings on neighbouring ligands highlighted. In Figure 7.4B, the same model rendered with space-filling atoms shows the offset face-face interactions. I suggest that the reason **L4** results in this structure, as opposed to the cubic structures usually obtained from linear dicarboxylate ligands, is that the sum of the noncovalent interactions illustrated in Figure 7.4 outweighs the difference in energy of the unusual SBU to the more common $[\text{Zn}_4\text{O}]$ cluster, or a fully coordinated paddlewheel.

In DBF, on the other hand, **L4** forms a noninterpenetrated cubic $[\text{Zn}_4\text{O}]$ MOF, β -MOF-L4, as we originally expected it to do in both DMF and DBF. The bulkier solvent doesn't allow α -MOF-L4 to form: it would neither fit in the pores, nor, if coordinated to the SBU, would the layers be able to stack as closely. The assignment of this structure for β -MOF-L4 was only by inference from the comparison of its PXRD

pattern to that of α -MUF-9, as shown in Figure 7.5; no single-crystal X-ray diffraction structure for β -MOF-L4 was obtained. The two PXRD patterns have peaks at the same angles throughout the entire range of 2θ from 4° to 45° , which allows us to make this inference with good confidence, but subtle differences cannot be ruled out without a single-crystal structure.

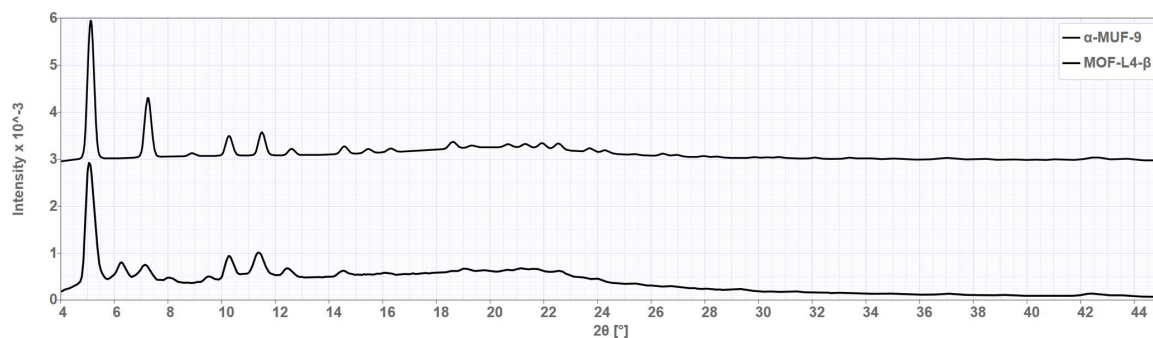
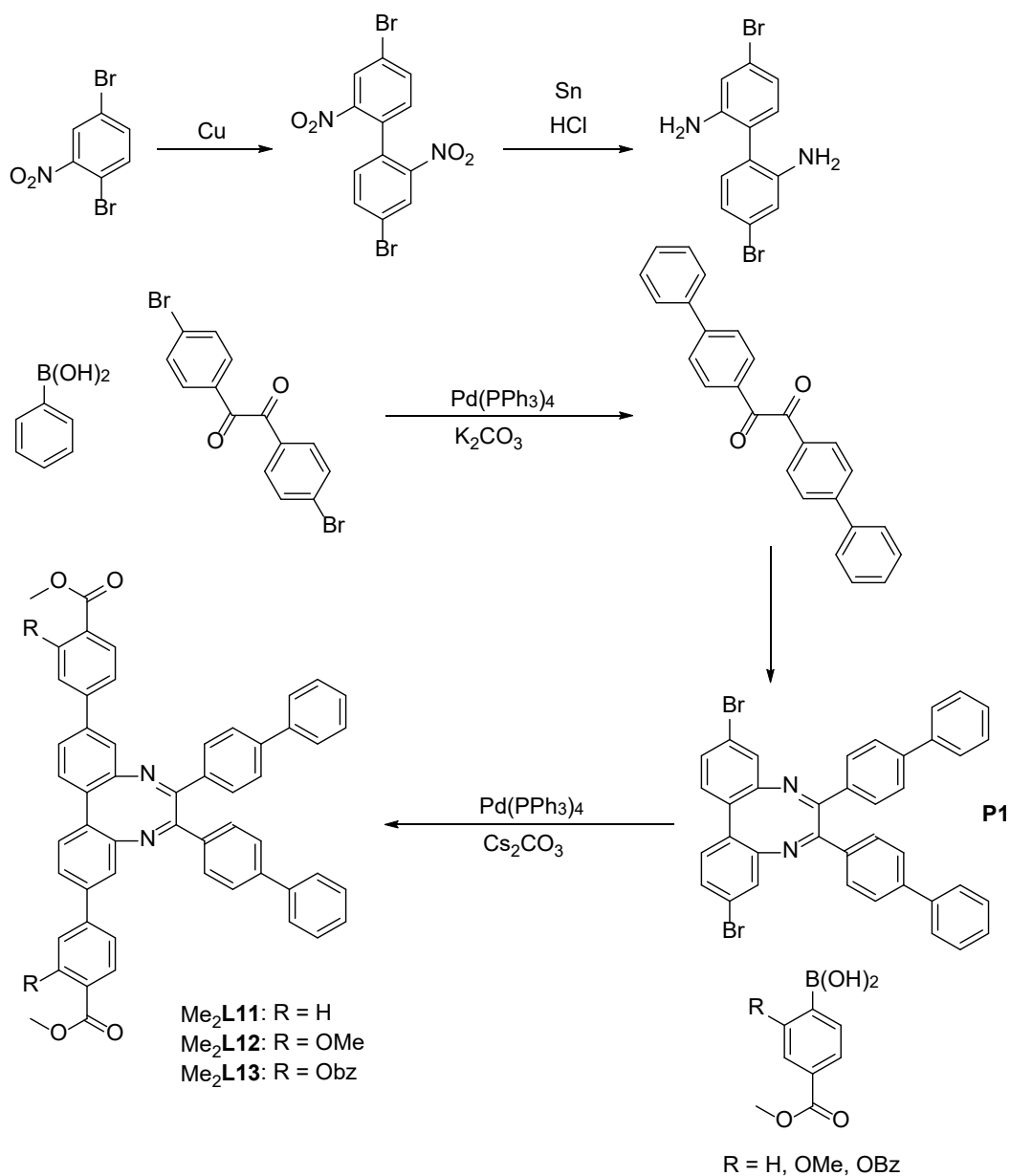


Figure 7.5: Comparison of the PXRD patterns of β -MOF-L4 (the material obtained from **L4** in DBF) and α -MUF-9.

7.2.3. Extended analogues of L1

To investigate the effect of the ligand shape, extended analogues of **L1** were synthesised. Scheme 7.3 shows the synthetic route to **L11**, **L12**, and **L13**, through the intermediate **P1** which was also used for the pyrazolate ligands described in 7.2.4. A SCXRD structure of the intermediate **P1** was obtained, which served as useful confirmation of the identity of the product beyond ^1H and ^{13}C NMR analyses, since this compound was too nonpolar for the ESI-MS available.



Scheme 7.3: Synthesis of extended analogues of **L1** with carboxylate donor groups. Full synthetic details are presented in section 7.4.3, page 187.

More importantly, the SCXRD structure of **P1** (Figure 7.6) shows that the same intermolecular interactions responsible for the behaviour of MUF-9 – the nestling of the backbone of the neighbouring molecule in the space between the pendant phenyl rings – determines the crystal packing arrangement here. This effect does not carry through to all the MOFs with ligands derived from this backbone, however – different orientations of the ligands towards each other evidently have similar enough energetics that other factors will outweigh which one occurs, as long as there is still some interaction.

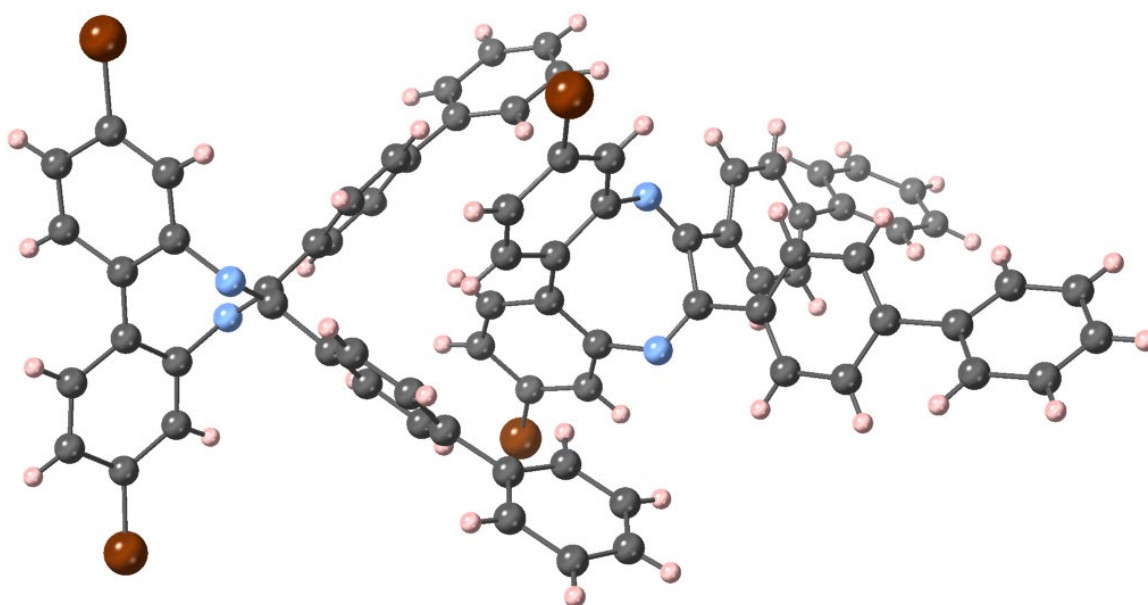


Figure 7.6: An illustration of the crystal structure of **P1**, showing the aryl embrace between the side chain on one molecule and the backbone of its neighbour. Carbons are coloured grey, nitrogen blue, hydrogen pink, and bromine brown.

A new MOF was synthesised (details in 7.4.4.1, page 192) from $\text{H}_2\text{L11}$ and zinc nitrate in DMF, and a good SCXRD structure was obtained (Table 7.4, section 7.4.5, page 194), which showed that the structure was an interpenetrated $[\text{Zn}_4\text{O}(\text{L11})_3]$ framework as expected. Unexpectedly however, the contact between the lattices was not between the side chain and the backbone, but rather between the side chains of two neighbouring lattices. This is illustrated in Figure 7.7, where (A) shows that one lattice is perfectly centred within the other (and indeed, they are crystallographically equivalent) and (B) shows the sidechains in a fourfold phenyl embrace. This difference

with β -MUF-9 – the side chains of the ligands are facing towards each other rather than towards the neighbouring backbone – results in a space group of $I -4 3 m$ compared to $P m -3 m$ for β -MUF-9.

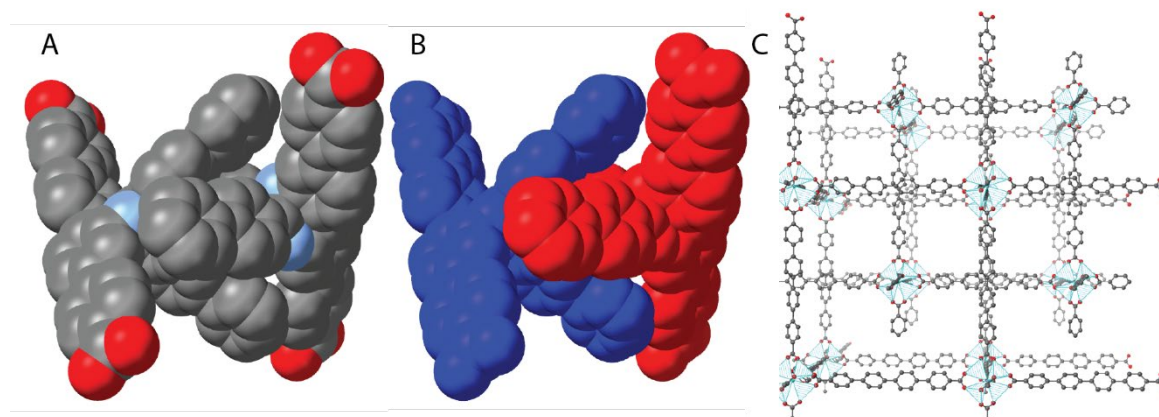
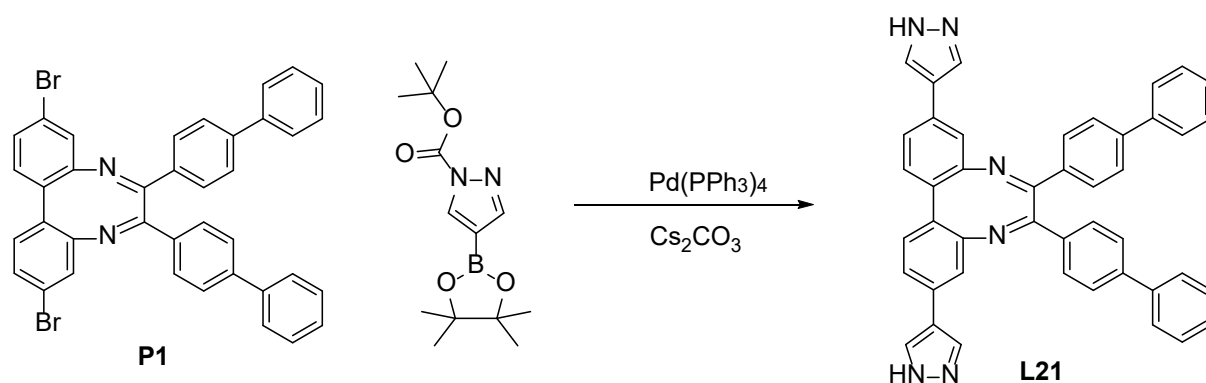


Figure 7.7: A and B) illustration of the contacts between the two lattices in MOF-L11, with hydrogens removed for clarity. In panel A, carbons are coloured grey, oxygens red, nitrogens blue. In panel B, one ligand is coloured red and the other blue. C) Overall structure of the lattices in MOF-L11, with sidechains and hydrogens removed for clarity.

L11 turned out to be insoluble in DBF, which prevented us from preparing a structure in DBF as we intended. Therefore, **L12** was prepared (section 7.4.3.5), with an additional methoxy group to aid solubility. This ligand was soluble in both DMF and DBF, but unfortunately, some screening of different conditions including $\text{Zn}(\text{NO}_3)_2$ concentration, ligand concentration, additives (benzoic acid and 2-fluorobenzoic acid), and temperature, did not yield any very crystalline materials.

7.2.4. Pyrazolate analogue of L11

To investigate the effect of the binding strength of the ligand donor group on any potential partial interpenetration, and in an attempt to produce more robust partially interpenetrated frameworks, analogues of **L1** with pyrazolate donor groups were synthesised. Scheme 7.4 shows the procedure for **L21**, with an extended benzil side chain as in **L11**.



Scheme 7.4: Synthesis of **L21**. Full synthetic details in section 7.4.3.6, page 191.

This ligand displayed some interesting behaviour – three different phases were observed with only this ligand and zinc as a metal. One of these, MOF-L21- α (experimental details in section 7.4.4.4, page 193) formed at high temperature with high modulator concentrations. MOF-L21- α was characterised by SCXRD (details page 197) and is to my knowledge the first MOF with a long pyrazolate ligand to be characterised this way. MOF-L21- α has a monoclinic cell in the space group $C2/c$, with dimensions a , b , and c of 25.31, 24.27, and 20.29 respectively. It features a 2D **sql** net. The layers are held together by the same fourfold phenyl embrace seen in MOF-L11.

Figure 7.8 shows some of the structural features of MOF-L21- α . In panels A and B, the 2D network is shown. The outer atoms of the $[Zn_3]$ SBU are disordered over two sites at a 1:2 ratio, while the inner zinc site is fully ordered. The side chains, as with MOF-L11, form a fourfold phenyl embrace motif which holds the two layers together.

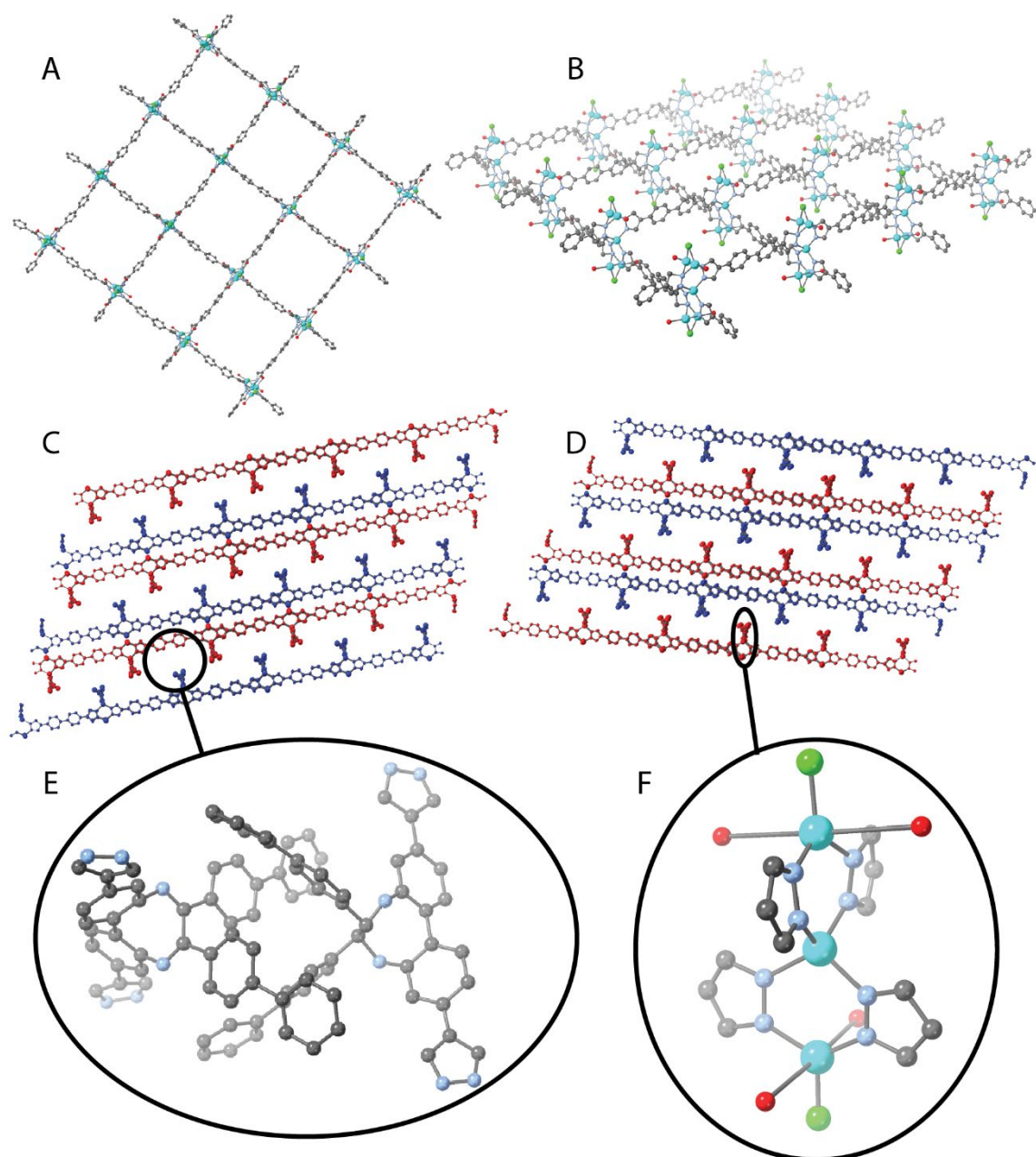


Figure 7.8: A) Simplified view of the coordination network in MOF-L21- α from the (0,1,0) view. Side chains and hydrogens are omitted for clarity. B) Simplified view of the coordination network in MOF-L21- γ at an angle, showing the alignment of ligands above and below the plane. C) and D) are views from the (1,0,0) and (0,0,1) directions respectively, showing the interdigitation of the layers in alternate directions. Side chains have been removed for clarity. E) Illustration of the fourfold phenyl embrace which joins the layers together. F) A closeup view of the $\text{Zn}_3(\text{pyz})_4\text{Cl}_2(\text{H}_2\text{O})_2$ cluster.

There has been only one other biphenyl-4,4'-dipryazolate MOF structure²¹² reported to date, a cubic framework with an octanuclear, 12-coordinated SBU and an unfunctionalised ligand backbone. Under different synthetic conditions to those which produce MOF-L21- α , namely at lower temperature and modulator

concentrations, **L21** also produced another framework, named β -MOF-21 and depicted in Figure 7.9.

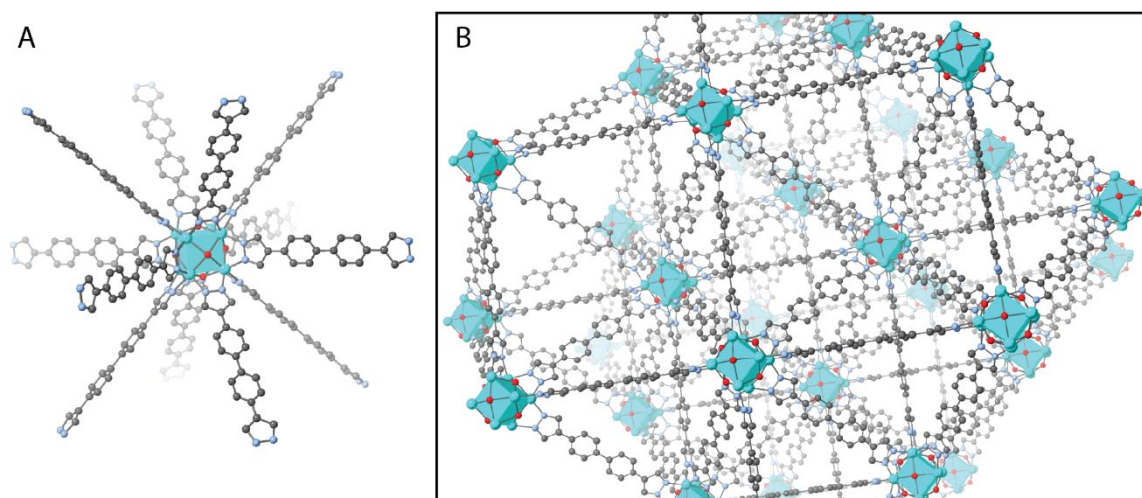


Figure 7.9: An illustration of β -MOF-21. A) the cubic Zn_8 cluster is illustrated with a cube, and the coordination of the ligands at each edge of the cube is shown. B) The overall connectivity of the lattice.

β -MOF-21 is isostructural to that reported structure: it is a cubic framework with a 12-coordinate cubic octanuclear $\text{Zn}_8(\text{OH})_4(\text{H}_2\text{O})_n$ SBU, one ligand coordinated to each edge of the SBU. This phase was identified by comparing the observed PXRD pattern to one obtained from the literature, shown in Figure 7.10.

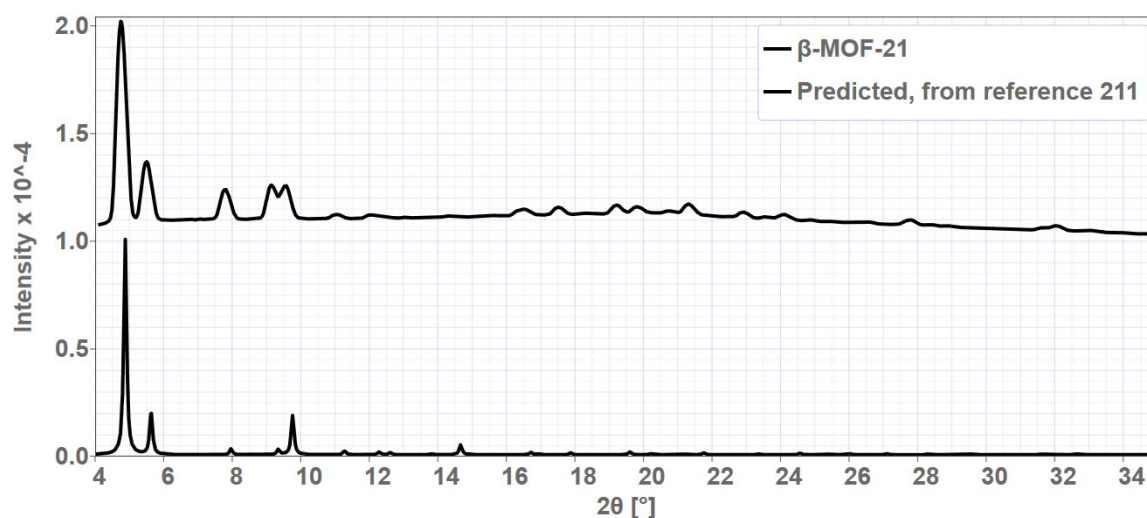


Figure 7.10: PXRD patterns of β -MOF-21 (top) and $\text{Ni}_8(\text{bdp})_6(\text{OH})_4(\text{H}_2\text{O})_n$ (bottom).

L21 also produces an unidentified third phase, which has only been characterised incompletely by PXRD and SEM – details in Appendix B. I wasn't able to determine what kind of conditions lead to its formation.

7.3. CONCLUSIONS

Despite MOFs being favoured for the predictability of structures resulting from similar precursors, and the general truth of that premise notwithstanding, it is observed that small changes in ligand structure can have dramatic consequences for the crystals that result. These consequences can, to some extent, be rationalised with the classic tools of supramolecular chemistry. After all, to paraphrase a quote I once heard at a conference, “MOFs are just coordination compounds”. When small changes in ligand structure don’t change inter-ligand interactions greatly, one can expect to get similar structures for the crystal, just as one often obtains similar crystal structures for related discrete metal complexes. When, on the other hand, the changes to the ligand strongly affect the inter-ligand interactions, they are likely to affect the crystallisation significantly.

The preferred coordination geometry of the metal atom and ligand donor group, and minimisation of pore space or maximisation of van der Waals contacts between components act together, or even compete, to determine the structure of a MOF. When specific motifs in interactions between ligand side chains result in large energetic contributions, such as with phenyl embraces, they can have considerable influence over the crystal structure observed.

The MOFs presented in this chapter share some features with traditional small molecule crystals. Specifically, they could have been better predicted and analysed using the types of techniques described in section 7.1.2 compared to most MOFs, because steric and geometric factors exert a large influence over the resultant framework architecture. This type of analysis would present an interesting avenue for further work, and some ideas are detailed in Chapter 8.

When the ligands have weaker carboxylate binding groups, such as in MOF-L3, MOF-L4, and MOF-L11, the side chain interactions control every structure observed. In MOF-L3, the steric repulsion of the awkwardly shaped ligand prevents close packing.

This is reminiscent of 9,9'-spirofluorene-2,2'-dicarboxylic acid and similar organic compounds^{233, 234} which are prevented from crystallising as pure compounds by their awkward shape, but readily form cocrystals with hydrogen-bonded guests. Whenever possible, a structure with maximum interactions between the side chains forms, but ligands can be forced apart through the use of a bulkier solvent, like DBF in β -MUF-L4, and many other MOFs^{90, 93, 235} in the literature.

When, on the other hand, the stronger pyrazolate binding groups are used, the resulting structure can be determined thermodynamically (MUF-L21- α) or kinetically (MUF-L21- γ), and involve side-chain interactions or not, respectively. At higher temperatures or modulator concentrations the most close-packed structure, MUF-L21- α , is obtained. In faster syntheses, the rapid nucleation of the octanuclear cluster in MUF-L21- γ and low lability of pyrazolate ligands results in a highly porous framework architecture where the side chains are separated from each other.

7.4. EXPERIMENTAL DETAILS

All CIF files relevant to this chapter are listed in Appendix B, page B-7. The files are available electronically on the included CD-ROM.

7.4.1. Synthesis of L2

2,2'-Diamino-4,4'-biphenyldicarboxylic acid (400 mg, 1.47 mmol), and 9,10-phenanthraquinone (397 mg, 19.1 mmol) were each separately dissolved in hot acetic acid (100 mL and 40 mL respectively). The solutions were combined and stirred at 100 °C for two hours, then left to rest overnight. Chilled H₂O (200 mL) was added to the mixture upon which a yellow-brown solid precipitated, which was collected by filtration, washed with CH₂Cl₂, and recrystallised from acetic acid-H₂O to yield dibenzo[e,g]phenanthro[9,10-b][1,4]diazocine-3,16-dicarboxylic acid (H₂L2) (102 mg, 0.22 mmol, 16%)

¹H NMR (500 MHz, d₆-DMSO): 13.2 (1H, S), 8.14 (2H, d), 7.90 (2H, d), 7.67 (4H, m), 7.47 (6H, m)

ESI-MS (-): calc. 443.10 found 443.10 (M – H⁺)

7.4.2. Synthesis of L4

2,2',6,6'-tetraamino-4,4'-biphenyldicarboxylic acid (110 mg, 0.33 mmol) and benzil (175 mg, 0.83 mmol) were dissolved in dioxane (2 mL) with TFA (0.1 mL) and heated by microwave irradiation to 130 °C for two hours. After cooling overnight, large yellow block crystals formed and were collected by filtration and washed with dioxane:H₂O (70:30) then H₂O, and dried under vacuum to give L4' (124 mg, 0.182 mmol, 55%)

¹H NMR (500 MHz, CDCl₃): 7.74 (8H, d), 7.42 (4H, s), 7.41 (4H, t), 7.35 (4H, t), 3.82 (6H, s)

This material was added to THF (10 mL), and 1M aqueous NaOH (5 mL), and the mixture heated to 50 °C and stirred overnight. THF was removed by rotary

evaporation, then the mixture was cooled and acidified with 2M aqueous HCl, the precipitate collected by filtration, washed with H₂O and dried under high vacuum to yield **L4** (108 mg, 0.179 mmol, 99%)

¹H NMR (500 MHz, d₆-DMSO): 7.55 (8H, d), 7.54 (4H, t), 7.47 (4H, t), 7.37 (4H, s)

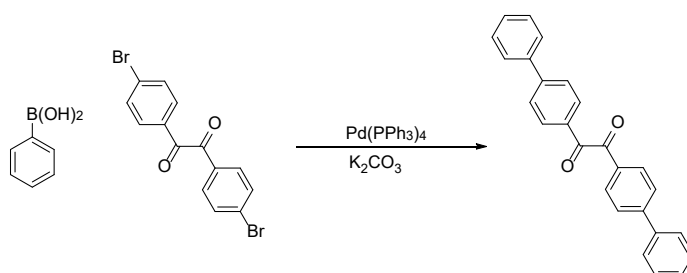
¹³C NMR (125 MHz, d₆-DMSO): 168.0, 167.1, 154.3, 133.7, 132.6, 130.2, 127.5, 120.0, 117.3, 67.1

ESI-MS (-): calc. 649.72 found 649.71 (M – H⁺)

7.4.3. Synthesis of **L11** and **L12**

2,2'-diamino-4,4'-dibromobiphenyl was synthesised by literature methods^{236, 237} from 2-nitro-1,4-dibromobenzene, by Ullmann homocoupling of 1,4-dibromo-2-nitrobenzene and reduction with Zn/HCl.

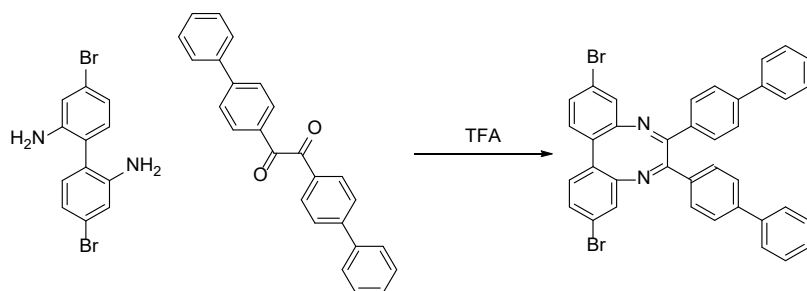
7.4.3.1. 1,2-di([1,1'-biphenyl]-4-yl)ethane-1,2-dione



Phenylboronic acid (1.52 g, 12.5 mmol), 4,4'-dibromobenzil (2.00g, 5.43 mmol), K₂CO₃ (6.0 g, 31.5 mmol) and Pd(PPh₃)₄ (620 mg, 0.50 mmol) were combined in a round-bottom flask to which 7:3 dioxane:H₂O (70 mL) was then added, and the mixture refluxed under argon overnight. H₂O (100 mL) was added, the mixture extracted with Et₂O (20 mL × 3), the organic layers combined, dried over MgSO₄, filtered, and volatiles removed under reduced pressure. The residue was chromatographed on silica in a 10:1 – 1:1 CH₂Cl₂:n-hexane gradient to yield the product (1.85 g, 5.10 mmol, 94%)

¹H NMR (500 MHz, CDCl₃): 8.10 (4H, d), 7.77 (4H, d), 7.51 (4H, t), 7.45 (2H, t)

7.4.3.2. 6,7-di([1,1'-biphenyl]-4-yl)-3,10-dibromodibenzo[e,g][1,4]diazocine



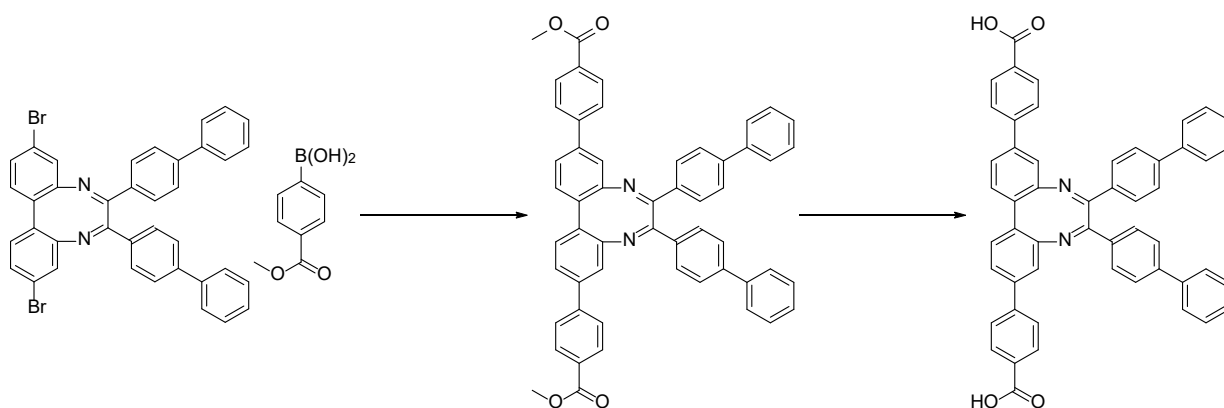
2,2'-diamino-4,4'-dibromobiphenyl (300 mg, 0.88 mmol) and 1,2-di([1,1'-biphenyl]-4-yl)ethane-1,2-dione (420 mg, 1.1 mmol) were combined in a round-bottom flask and dissolved in dry dioxane (15 mL). TFA (1.5 mL) was added and the mixture refluxed under argon overnight. After cooling to room temperature, H₂O (100 mL) was added and the mixture extracted with Et₂O (20 mL × 3), the organic layers combined, dried over MgSO₄, filtered, and volatiles removed under reduced pressure.

The residue was chromatographed on silica in 9:1 hexane:dichloromethane to yield 6,7-di([1,1'-biphenyl]-4-yl)-3,10-dibromodibenzo[e,g][1,4]diazocine (1.30 g, 2.92 mmol, 67%)

¹H NMR (500 MHz, CDCl₃): 7.88 (4H, d), 7.64 (4H, d), 7.60 (4H, d), 7.46 (4H, t), 7.39 (2H, t), 7.31, (2H + 2H, m), 7.10 (2H, d)

¹³C NMR (125 MHz, CDCl₃): 167.7, 152.7, 134.0, 132.0, 131.6, 128.9, 128.1, 128.0, 127.7, 123.6, 122.6, 26.9

7.4.3.3. 4,4'-(6,7-di([1,1'-biphenyl]-4-yl)dibenzo[e,g][1,4]diazocine-3,10-diyl)dibenzoic acid (L11')



Scheme 7.5: Synthesis of **L11'**

P1 (250 mg, 374 μmol), 3-methoxy-4-methylcarboxyphenylboronic acid (168 mg, 804 μmol), tetrakis(triphenylphosphine)palladium (42 mg, 37 μmol) and caesium carbonate (731 mg, 2.24 mmol) were combined in a 50 mL round-bottom flask with degassed dioxane (20 mL) and H_2O (2 drops) then refluxed under argon overnight. TLC confirmed consumption of starting material and the reaction mixture was filtered through Celite, washed through with dioxane (20 mL) then hexane added (50 mL) upon which a light brown precipitate **L11'** appeared, which was collected by filtration. (177 mg, 211 μmol , 57%)

7.4.3.4. *(4,4'-((5Z,7Z)-6,7-di([1,1'-biphenyl]-4-yl)dibenzo[e,g][1,4]diazocine-3,10-diyl))bis(2-methoxybenzoic acid)) (L11)*

L11' (168 mg, 200 μmol) was dissolved in THF (5 mL) to which 2M aqueous NaOH was added (5 mL) and the mixture stirred overnight at reflux. THF was removed under reduced pressure, the mixture acidified with 2 M aqueous HCl, and stirred overnight. The formed precipitate was collected by centrifugation (5 krpm, 10 min) washed with H_2O , and dried under high vacuum affording **L11** (151 mg, 184 μmol , 93%)

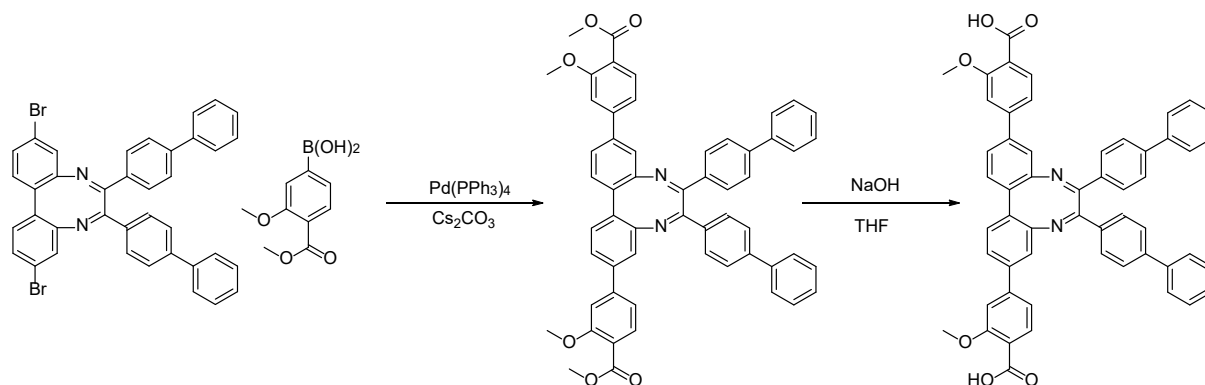
^1H NMR (500 MHz, CDCl_3): 8.00 (4H, d), 7.92 (4H, d), 7.87 (4H, d), 7.76 (4H, d), 7.65 (4H, d), 7.61 (4H, t), 7.45 (6H, m), 7.38 (2H, t)

^{13}C NMR (125 MHz, CDCl_3): 166.4, 152.1, 143.9, 139.3, 136.90, 133.9, 133.3, 131.3, 129.4, 128.7, 128.6, 127.9, 127.3, 126.9

126.3, 122.4, 120.8, 117.1

ESI-MS (-): calc. 749.24 found 749.24 ($\text{M} - \text{H}^+$)

7.4.3.5. 4,4'-(-6,7-di([1,1'-biphenyl]-4-yl)dibenzo[e,g][1,4]diazocine-3,10-diyl)bis(2-methoxybenzoic acid) (L12)



P1 (250 mg, 374 μmol), 3-methoxy-4-methylcarboxyphenylboronic acid (168 mg, 804 μmol), tetrakis(triphenyl)phosphinepalladium (42 mg, 37 μmol) and caesium carbonate (731 mg, 2.24 mmol) were combined in a 50 mL round-bottom flask with degassed dioxane (20 mL) and H₂O (2 drops) then refluxed under argon overnight. TLC confirmed consumption of starting material and the reaction mixture was filtered through celite, washed through with dioxane (20 mL) then hexane added (50 mL) upon which a light brown precipitate **L12'** appeared, which was collected by filtration. (177 mg, 211 μmol , 57%).

¹H NMR (500 MHz, CDCl₃): 7.95 (4H, d), 7.90 (2H, d), 7.62 (4H, d), 7.56 (4H, d), 7.40 (12H, m), 7.25 (2H, d), 7.21 (2H, s), 3.99 (6H, s), 3.93 (6H, s)

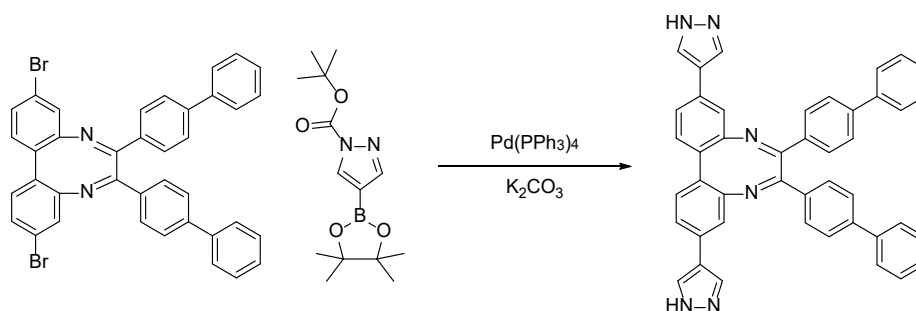
L12' (100 mg, 119 μmol) was dissolved in THF (5 mL) to which 2M aqueous NaOH was added (5 mL) and the mixture stirred overnight at reflux. THF was removed under reduced pressure, the mixture acidified with 2 M aqueous HCl, and stirred overnight. The formed precipitate was collected by centrifugation (5 krpm, 10 min) washed with H₂O, and dried under high vacuum affording **L12** (98 mg, 117 μmol).

¹H NMR (700 MHz, CDCl₃): 12.7 (2H, s), 7.93 (4H, d), 7.75 (6H, m), 7.63 (8H, m), 7.45 (6H, m), 7.38 (4H, t), 7.34 (2H, d), 3.93 (6H, s)

^{13}C NMR (175 MHz, CDCl_3): 167.5, 167.0, 159.2, 152.3, 144.4, 144.1, 140.5, 139.3, 133.2, 132.0, 131.4, 129.5, 129.2, 128.8, 128.7, 128.0, 127.3, 124.5, 120.8, 119.4, 118.9, 111.4, 56.3, 30.9

ESI-MS (-): calc. 809.27 found 809.27 ($\text{M} - \text{H}^+$)

7.4.3.6. 6,7-di([1,1'-biphenyl]-4-yl)-3,10-di(1H-pyrazol-4-yl)dibenzo[e,g][1,4]diazocine (L21)



P1 (150 mg, 224 μmol), N-boc-pyrazole-3-boronic acid pinacol ester (145 mg, 493 μmol), K_2CO_3 (248 mg, 1.80 mmol) and $\text{Pd}(\text{PPh}_3)_3$ were added to a round-bottom flask which was flushed with argon. Degassed $\text{DMF}:\text{H}_2\text{O}$ (9:1, 50 mL) was added and the mixture refluxed overnight under argon. The mixture was poured out into CH_2Cl_2 (100 mL) and washed with H_2O (50 mL \times 4) and brine (50 mL \times 2), then volatiles removed under reduced pressure and the residue chromatographed on silica in a CH_2Cl_2 to $\text{CH}_2\text{Cl}_2:\text{MeOH}$ (19:1) gradient to yield **L21** (83 mg, 129 μmol , 57%)

^1H NMR (700 MHz, $\text{d}_6\text{-DMSO}$): 12.98 (2H, s), 8.26 (2H, s), 7.97 (2H, s), 7.88 (4H, d), 7.77 (4H, d), 7.67 (4H, d), 7.46 (8H, m), 7.38 (2H, t), 7.25 (2H, d)

^{13}C NMR (175 MHz, $\text{d}_6\text{-DMSO}$): 166.4864, 152.1194, 143.9671, 139.3121, 136.9036, 133.9237, 133.3334, 131.2376, 129.4768, 128.7122, 128.6165, 127.9647, 127.3375, 126.9812, 126.3525, 122.4368, 120.8741, 117.1477, 55.3859

ESI-MS (-): calc. 641.24, found 641.24 ($\text{M} - \text{H}^+$)

7.4.4. MOF syntheses and characterisation

Note: many of the MOFs here are washed with DBF as a final step. This is primarily as an aid to room-temperature XRD data collection, because DBF is viscous and non-volatile, with the added advantage of being hydrophobic and immiscible with water, unlike DMF.

7.4.4.1. MOF-L3

L3 (7.0 mg, 12 μmol) and $\text{Zn}(\text{NO}_3)_2 \cdot 4\text{H}_2\text{O}$ (16 mg, 52 μmol) were combined in a 4 mL glass vial with poplypropylene cap and PDFE-lined PDMS septum. Anhydrous (1 mL) was added, the components dissolved by sonication, and the vial heated to 85 $^{\circ}\text{C}$ for 9 hours. After cooling to room temperature, the crystals were washed several times with anhydrous DMF, then once with DBF.

7.4.4.2. MOF-L4

L11 (5.0 mg, 9.3 μmol) and $\text{Zn}(\text{NO}_3)_2 \cdot 4\text{H}_2\text{O}$ (12 mg, 46 μmol) were combined in a 4 mL glass vial with poplypropylene cap and PDFE-lined PDMS septum. Anhydrous DMF (1 mL) was added, the components dissolved by sonication, and the vial heated to 85 $^{\circ}\text{C}$ overnight. After cooling to room temperature, the crystals were washed several times with anhydrous DMF, then once with DBF.

7.4.4.3. MOF-L11

L11 (3.0 mg, 4.0 μmol) and $\text{Zn}(\text{NO}_3)_2 \cdot 4\text{H}_2\text{O}$ (6 mg, 23 μmol) were combined in a 4 mL glass vial with poplypropylene cap and PDFE-lined PDMS septum. Anhydrous DMF (1 mL) was added, the components dissolved by sonication, and the vial heated to 85

°C for 48 hours. After cooling to room temperature, the crystals were washed several times with anhydrous DMF, then once with DBF.

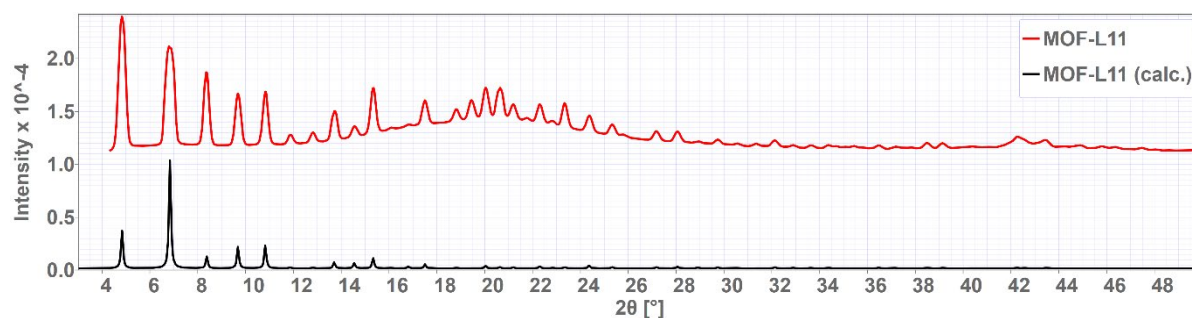


Figure 7.11: Experimental and calculated PXRD patterns for MOF-L11

7.4.4.4. *MOF-L21-α*

L21 (3.0 mg, 4.0 μmol) and $\text{Zn}(\text{NO}_3)_2 \cdot 4\text{H}_2\text{O}$ (6 mg, 23 μmol) were combined in a 4 mL glass vial with poplypropylene cap and PDFE-lined PDMS septum. Anhydrous DMF (1 mL) and 37 % HCl (10 μL) were added, the components dissolved by sonication, and the vial heated to 110 °C for 7 days. After cooling to room temperature, the crystals were washed several times with anhydrous DMF, then once with DBF.

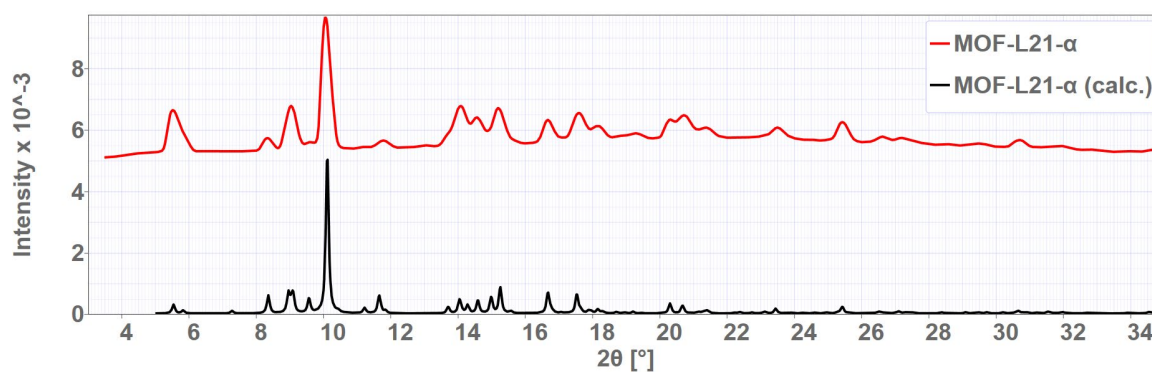


Figure 7.12: Experimental and calculated PXRD patterns for MOF-L21-α

7.4.5. Crystallographic data for MOFs

Table 7.2: Crystallographic data for MOF-L3

Identification code	MOF-L3
Empirical formula	C ₈₄ H ₃₆ N ₆ O ₁₃ Zn ₄ [Zn ₄ O(L3) ₃]
Formula weight	1598.67
Temperature/K	173
Crystal system	cubic
Space group	P-43m
a/Å	17.186(2)
b/Å	17.186(2)
c/Å	17.186(2)
α/°	90
β/°	90
γ/°	90
Volume/Å ³	5076(2)
Z	1
ρ _{calc} /cm ³	0.523
μ/mm ⁻¹	0.743
F(000)	806.0
Crystal size/mm ³	0.746 × 0.738 × 0.508
Radiation	CuKα (λ = 1.54178)
2θ range for data collection/°	5.142 to 117.692
Index ranges	-8 ≤ h ≤ 19, -8 ≤ k ≤ 8, -19 ≤ l ≤ 11
Reflections collected	7244
Independent reflections	1368 [R _{int} = 0.0920, R _{sigma} = 0.0845]
Data/restraints/parameters	1368/177/96
Goodness-of-fit on F ²	1.282
Final R indexes [I ≥ 2σ (I)]	R ₁ = 0.1211, wR ₂ = 0.3326
Final R indexes [all data]	R ₁ = 0.1575, wR ₂ = 0.3815
Largest diff. peak/hole / e Å ⁻³	0.69/-0.53
Flack parameter	0.41(5)

Table 7.3: Crystallographic data for MOF-L4

Identification code	MOF-L4
Empirical formula	$C_{102}H_{90}N_{14}O_{14}Zn_2 \mid Zn_2(L4)_2(DMF)_2 \cdot (DMF)_2$
Formula weight	1866.61
Temperature/K	108(2)
Crystal system	monoclinic
Space group	P2 ₁ /n
a/Å	9.2202(4)
b/Å	23.0308(8)
c/Å	22.7092(16)
$\alpha/^\circ$	90
$\beta/^\circ$	99.116(7)
$\gamma/^\circ$	90
Volume/Å ³	4761.4(4)
Z	2
$\rho_{\text{calc}}/\text{cm}^3$	1.302
μ/mm^{-1}	1.197
F(000)	1944.0
Crystal size/mm ³	0.554 × 0.273 × 0.231
Radiation	CuK α (λ = 1.54178)
2 Θ range for data collection/ $^\circ$	5.5 to 144.35
Index ranges	-11 ≤ h ≤ 10, -27 ≤ k ≤ 28, -27 ≤ l ≤ 28
Reflections collected	62930
Independent reflections	6565 [R _{int} = 0.0638, R _{sigma} = 0.0594]
Data/restraints/parameters	6565/50/610
Goodness-of-fit on F ²	1.265
Final R indexes [I > 2 σ (I)]	R ₁ = 0.1095, wR ₂ = 0.3169
Final R indexes [all data]	R ₁ = 0.1568, wR ₂ = 0.3747
Largest diff. peak/hole / e Å ⁻³	0.89/-0.52

Table 7.4: Crystallographic data for MOF-L11

Identification code	MOF-L11
Empirical formula	C ₁₅₆ H ₉₆ N ₆ O ₁₃ Zn ₄ [Zn ₄ O(L11) ₃]
Formula weight	2523.66
Temperature/K	293
Crystal system	cubic
Space group	I-43m
a/Å	25.8147(10)
b/Å	25.8147(10)
c/Å	25.8147(10)
$\alpha/^\circ$	90
$\beta/^\circ$	90
$\gamma/^\circ$	90
Volume/Å ³	17203(2)
Z	2.00016
$\rho_{\text{calc}}/\text{cm}^3$	0.487
μ/mm^{-1}	0.514
F(000)	2596.0
Crystal size/mm ³	0.48 × 0.47 × 0.46
Radiation	CuK α (λ = 1.54178)
2 Θ range for data collection/ $^\circ$	4.84 to 130.122
Index ranges	-27 ≤ h ≤ 19, -30 ≤ k ≤ 11, -24 ≤ l ≤ 24
Reflections collected	20962
Independent reflections	2703 [R _{int} = 0.0556, R _{sigma} = 0.0340]
Data/restraints/parameters	2703/117/164
Goodness-of-fit on F ²	1.034
Final R indexes [I>=2 σ (I)]	R ₁ = 0.0886, wR ₂ = 0.2020
Final R indexes [all data]	R ₁ = 0.0929, wR ₂ = 0.2085
Largest diff. peak/hole / e Å ⁻³	0.38/-0.30
Flack parameter	0.24(4)

Table 7.5: Crystallographic data for MOF-L21- α

Identification code	MOF-L21- α
Empirical formula	$C_{88}H_{60}Cl_2N_{12}O_2Zn_3 \mid Zn_3(L21)_2Cl_2(H_2O)_2$
Formula weight	1584.49
Temperature/K	566.3
Crystal system	monoclinic
Space group	C2/c
a/Å	25.309(13)
b/Å	24.266(12)
c/Å	20.292(12)
$\alpha/^\circ$	90
$\beta/^\circ$	123.350(15)
$\gamma/^\circ$	90
Volume/Å ³	10410(10)
Z	4
ρ_{calc}/cm^3	1.011
μ/mm^{-1}	1.613
F(000)	3248.0
Crystal size/mm ³	0.2 × 0.2 × 0.07
Radiation	CuK α (λ = 1.54178)
2 Θ range for data collection/ $^\circ$	5.22 to 88.98
Index ranges	-22 ≤ h ≤ 22, -18 ≤ k ≤ 21, -18 ≤ l ≤ 18
Reflections collected	23161
Independent reflections	3900 [R_{int} = 0.1184, R_{sigma} = 0.1299]
Data/restraints/parameters	3900/947/779
Goodness-of-fit on F ²	1.800
Final R indexes [$I \geq 2\sigma(I)$]	R_1 = 0.1727, wR_2 = 0.4324
Final R indexes [all data]	R_1 = 0.2213, wR_2 = 0.4729
Largest diff. peak/hole / e Å ⁻³	0.92/-0.55

7.5. REFERENCES

12. Diercks, C. S.; Yaghi, O. M., The atom, the molecule, and the covalent organic framework. *Science* **2017**, 355 (6328). DOI: 10.1126/science.aal1585
23. Groom, C. R.; Bruno, I. J.; Lightfoot, M. P.; Ward, S. C., The Cambridge Structural Database. *Acta Crystallogr B Struct Sci Cryst Eng Mater* **2016**, 72 (Pt 2), 171-9. DOI: 10.1107/S2052520616003954
90. Verma, G.; Butikofer, S.; Kumar, S.; Ma, S., Regulation of the Degree of Interpenetration in Metal-Organic Frameworks. *Top Curr Chem (Cham)* **2019**, 378 (1), 4. DOI: 10.1007/s41061-019-0268-x
93. Park, J. H.; Lee, W. R.; Kim, Y.; Lee, H. J.; Ryu, D. W.; Phang, W. J.; Hong, C. S., Interpenetration Control, Sorption Behavior, and Framework Flexibility in Zn(II) Metal-Organic Frameworks. *Cryst. Growth Des.* **2014**, 14 (2), 699-704. DOI: 10.1021/cg401583v
204. Steed, J. W.; Atwood, J. L., *Supramolecular chemistry*. 2nd ed.; Wiley: Chichester, UK, 2009; p xxvi, 970 p., 8 p. of plates. '
205. Moghadam, P. Z.; Li, A.; Wiggin, S. B.; Tao, A.; Maloney, A. G. P.; Wood, P. A.; Ward, S. C.; Fairen-Jimenez, D., Development of a Cambridge Structural Database Subset: A Collection of Metal-Organic Frameworks for Past, Present, and Future. *Chem. Mater.* **2017**, 29 (7), 2618-2625. DOI: 10.1021/acs.chemmater.7b00441
206. Li, Z.; Zhang, Z.; Ye, Y.; Cai, K.; Du, F.; Zeng, H.; Tao, J.; Lin, Q.; Zheng, Y.; Xiang, S., Rationally tuning host-guest interactions to free hydroxide ions within intertrimerically cuprophilic metal-organic frameworks for high OH⁻ conductivity. *Journal of Materials Chemistry A* **2017**, 5 (17), 7816-7824. DOI: 10.1039/c6ta11242k
207. Galli, S.; Maspero, A.; Giacobbe, C.; Palmisano, G.; Nardo, L.; Comotti, A.; Bassanetti, I.; Sozzani, P.; Masciocchi, N., When long bis(pyrazolates) meet late transition metals: structure, stability and adsorption of metal-organic frameworks featuring large parallel channels. *Journal of Materials Chemistry A* **2014**, 2 (31). DOI: 10.1039/c4ta01798f
208. Padial, N. M.; Quartapelle Procopio, E.; Montoro, C.; Lopez, E.; Oltra, J. E.; Colombo, V.; Maspero, A.; Masciocchi, N.; Galli, S.; Senkovska, I.; Kaskel, S.; Barea, E.; Navarro, J. A., Highly hydrophobic isorecticular porous metal-organic frameworks for the capture of harmful volatile organic compounds. *Angew Chem Int Ed Engl* **2013**, 52 (32), 8290-4. DOI: 10.1002/anie.201303484
209. Tăbăcaru, A.; Pettinari, C.; Timokhin, I.; Marchetti, F.; Carrasco-Marín, F.; Maldonado-Hódar, F. J.; Galli, S.; Masciocchi, N., Enlarging an Isorecticular Family: 3,3',5,5'-Tetramethyl-4,4'-bipyrazolato-Based Porous Coordination Polymers. *Cryst. Growth Des.* **2013**, 13 (7), 3087-3097. DOI: 10.1021/cg400495w
210. Tabacaru, A.; Pettinari, C.; Masciocchi, N.; Galli, S.; Marchetti, F.; Angiellari, M., Pro-porous coordination polymers of the 1,4-bis((3,5-dimethyl-1H-pyrazol-4-yl)-methyl)benzene ligand with late transition metals. *Inorg. Chem.* **2011**, 50 (22), 11506-13. DOI: 10.1021/ic2013705
211. Tăbăcaru, A.; Galli, S.; Pettinari, C.; Masciocchi, N.; McDonald, T. M.; Long, J. R., Nickel(ii) and copper(i,ii)-based metal-organic frameworks incorporating an extended tris-pyrazolate linker. *CrystEngComm* **2015**, 17 (27), 4992-5001. DOI: 10.1039/c5ce00561b

212. Masciocchi, N.; Galli, S.; Colombo, V.; Maspero, A.; Palmisano, G.; Seyyedi, B.; Lamberti, C.; Bordiga, S., Cubic octanuclear Ni(II) clusters in highly porous polypyrazolyl-based materials. *J. Am. Chem. Soc.* **2010**, *132* (23), 7902-4. DOI: 10.1021/ja102862j
213. Timokhin, I.; Pettinari, C.; Marchetti, F.; Pettinari, R.; Condello, F.; Galli, S.; Alegria, E. C. B. A.; Martins, L. M. D. R. S.; Pombeiro, A. J. L., Novel Coordination Polymers with (Pyrazolato)-Based Tectons: Catalytic Activity in the Peroxidative Oxidation of Alcohols and Cyclohexane. *Cryst. Growth Des.* **2015**, *15* (5), 2303-2317. DOI: 10.1021/acs.cgd.5b00083
214. Mino, L.; Colombo, V.; Vitillo, J. G.; Lamberti, C.; Bordiga, S.; Gallo, E.; Glatzel, P.; Maspero, A.; Galli, S., Spectroscopic and adsorptive studies of a thermally robust pyrazolato-based PCP. *Dalton Trans.* **2012**, *41* (14), 4012-9. DOI: 10.1039/c2dt12121b
215. Lehn, J. M., Toward complex matter: supramolecular chemistry and self-organization. *Proc. Natl. Acad. Sci. U. S. A.* **2002**, *99* (8), 4763-8. DOI: 10.1073/pnas.072065599
216. Beran, G. J. O.; Heit, Y. N.; Hartman, J. D., Chapter 10 - Noncovalent Interactions in Molecular Crystals. In *Non-Covalent Interactions in Quantum Chemistry and Physics*, Otero de la Roza, A.; DiLabio, G. A., Eds. Elsevier: 2017; pp 303-331. '<https://doi.org/10.1016/B978-0-12-809835-6.00012-8>:' '<https://doi.org/10.1016/B978-0-12-809835-6.00012-8>
217. Martinez, C. R.; Iverson, B. L., Rethinking the term “pi-stacking”. *Chemical Science* **2012**, *3* (7), 2191. DOI: 10.1039/c2sc20045g
218. Fischer, F. R.; Schweizer, W. B.; Diederich, F., Substituent effects on the aromatic edge-to-face interaction. *Chem. Commun.* **2008**, (34), 4031-3. DOI: 10.1039/b809058k
219. Hunter, C. A.; Lawson, K. R.; Perkins, J.; Urch, C. J., Aromatic interactions. *Journal of the Chemical Society, Perkin Transactions 2* **2001**, (5), 651-669. DOI: 10.1039/b008495f
220. Meyer, E. A.; Castellano, R. K.; Diederich, F., Interactions with aromatic rings in chemical and biological recognition. *Angew Chem Int Ed Engl* **2003**, *42* (11), 1210-50. DOI: 10.1002/anie.200390319
221. Schneider, H. J., Binding mechanisms in supramolecular complexes. *Angew Chem Int Ed Engl* **2009**, *48* (22), 3924-77. DOI: 10.1002/anie.200802947
222. Gokel, G. W.; Leevy, W. M.; Weber, M. E., Crown ethers: sensors for ions and molecular scaffolds for materials and biological models. *Chem Rev* **2004**, *104* (5), 2723-50. DOI: 10.1021/cr020080k
223. Stoddart, J. F., Mechanically Interlocked Molecules (MIMs)-Molecular Shuttles, Switches, and Machines (Nobel Lecture). *Angew Chem Int Ed Engl* **2017**, *56* (37), 11094-11125. DOI: 10.1002/anie.201703216
224. Lindoy, L. F.; Park, K. M.; Lee, S. S., Metals, macrocycles and molecular assemblies - macrocyclic complexes in metallo-supramolecular chemistry. *Chem. Soc. Rev.* **2013**, *42* (4), 1713-27. DOI: 10.1039/c2cs35218d
225. Nguyen, S. T.; Gin, D. L.; Hupp, J. T.; Zhang, X., Supramolecular chemistry: functional structures on the mesoscale. *Proc. Natl. Acad. Sci. U. S. A.* **2001**, *98* (21), 11849-50. DOI: 10.1073/pnas.201373898
226. Atwood, J. L.; Steed, J. W., *Encyclopedia of Supramolecular Chemistry*. 2004. '10.1081/e-esmc: ' 10.1081/e-esmc

227. Dance, I.; Scudder, M., Molecules embracing in crystals. *CrystEngComm* **2009**, *11* (11). DOI: 10.1039/b904479e
228. Dance, I.; Scudder, M., The sextuple phenyl embrace, a ubiquitous concerted supramolecular motif. *J. Chem. Soc., Chem. Commun.* **1995**, (10). DOI: 10.1039/c39950001039
229. Dance, I.; Scudder, M., Crystal supramolecularity: sixfold phenyl embraces between PPh₃ ligands, forming extended nets in one-, two-, and three-dimensions. *Journal of the Chemical Society, Dalton Transactions* **2000**, (10), 1587-1594. DOI: 10.1039/A909330C
230. Dance, I.; Scudder, M., Supramolecular Motifs: Concerted Multiple Phenyl Embraces between Ph₄ P(+) Cations Are Attractive and Ubiquitous. *Chemistry* **1996**, *2* (5), 481-486. DOI: 10.1002/chem.19960020505
231. Ohrstrom, L., Framework Chemistry Transforming our Perception of the Solid State. *ACS Cent Sci* **2017**, *3* (6), 528-530. DOI: 10.1021/acscentsci.7b00230
232. Day, G. M.; Cooper, A. I., Energy-Structure-Function Maps: Cartography for Materials Discovery. *Adv Mater* **2018**, *30* (37), e1704944. DOI: 10.1002/adma.201704944
233. Weber, E., Molecular recognition: designed crystalline inclusion complexes of carboxylic hosts. *Journal of Molecular Graphics* **1989**, *7* (1), 12-27. DOI: 10.1016/0263-7855(89)80053-0
234. Weber, E.; Csoeregh, I.; Ahrendt, J.; Finge, S.; Czugler, M., Design of roof-shaped clathrate hosts. Inclusion properties and x-ray crystal structures of a free host and of inclusion compounds with 1-butenol and DMF. *J. Org. Chem.* **1988**, *53* (25), 5831-5839. DOI: 10.1021/jo00260a007
235. Yang, G. S.; Lang, Z. L.; Zang, H. Y.; Lan, Y. Q.; He, W. W.; Zhao, X. L.; Yan, L. K.; Wang, X. L.; Su, Z. M., Control of interpenetration in S-containing metal-organic frameworks for selective separation of transition metal ions. *Chem Commun (Camb)* **2013**, *49* (11), 1088-90. DOI: 10.1039/c2cc36894c
236. Liou, S.-Y.; Ke, C.-S.; Chen, J.-H.; Luo, Y.-W.; Kuo, S.-Y.; Chen, Y.-H.; Fang, C.-C.; Wu, C.-Y.; Chiang, C.-M.; Chan, Y.-H., Tuning the Emission of Semiconducting Polymer Dots from Green to Near-Infrared by Alternating Donor Monomers and Their Applications for in Vivo Biological Imaging. *ACS Macro Letters* **2015**, *5* (1), 154-157. DOI: 10.1021/acsmacrolett.5b00842
237. Tian, Z.; Yang, X.; Liu, B.; Zhong, D.; Zhou, G., Photophysical properties and optical power limiting ability of Pt(II) polyynes bearing fluorene-type ligands with ethynyl units at different positions. *J. Organomet. Chem.* **2019**, *895*, 28-36. DOI: 10.1016/j.jorganchem.2019.05.022

Chapter 8: PERSPECTIVE AND CONCLUSIONS

Now I will summarize some of the key findings of the previous seven chapters and opine on some directions that this work might lead.

In this work we have looked at the ligand **L1** and the MOFs it forms, MUF-9 and MUF-10. We have seen how the same interactions that lead to the formation of PIP-MUF-9 can be used to deliberately prepare new hetero-interpenetrated MOFs, MUF-91, -92, -93, and -101. A new method was developed for locating metal atoms of specific elements in a crystallographic cell. MUF-101 was used as a catalyst where the host lattice imparted chirality while the secondary lattice imparted activity. Finally, some ligands related to **L1** also yielded frameworks where the interactions between the side chains controlled the structural outcome.

8.1. CHAPTERS 2 & 3 – WHAT FURTHER INFORMATION COULD WE GET?

In Chapters 2 and 3 we described how the features which made MUF-9 interesting could be exploited to yield hetero-interpenetrated frameworks by design. The noncovalent interactions between the side chain of **L1** with the backbone of another biphenyl-based ligand encourage that other ligand to form a secondary lattice interpenetrated through α -MUF-9 to the exclusion of other processes. In Chapter 2, an upper bound was put on those other processes, exchange of components or autocatenation of the starting material, through a series of control experiments. In Chapter 3, we established a stepwise method for producing hetero-interpenetrated materials termed secondary growth. MUF-91 was prepared, through secondary growth of $[\text{Zn}_4\text{O}(\text{bpd})_3]$ interpenetrated through MUF-9. MUF-91 was characterised through a variety of complementary methods to verify that the aforementioned other processes were not taking place. Comparison of the results of ^1H NMR spectroscopic analysis of digested samples of MUF-91 with information about the interpenetration

percentage obtained from SCXRD structures showed that the content of the new ligand increased at the expected rate for secondary framework growth.

It's never possible to get every single kind of analysis and piece of information about a material. In our investigation of MUF-9, MUF-91, and other materials, we prioritised the information we needed to make confident assessments of these novel structures, but there remain many interesting questions.

MOFs are often used for their interaction with gases, and the gas uptake properties of MUF-9 are almost completely unknown. It would be fascinating to look at how the interpenetration percentage affects its sorption properties. One factor which complicates this is the propensity of α -MUF-9 to autocatenate into β -MUF-9 on the removal of solvent, a necessary step in measuring the gas uptake.

We have started to explore means of activating MUF-9 without causing autocatenation. Many MOFs are sensitive to their activation conditions¹⁰⁸ and it is known that activation with supercritical CO₂ will sometimes allow the activation of otherwise delicate materials without disrupting their structure. Preliminary trials were not very successful, but one attempt at activating MUF-9 with liquid CO₂ at low temperature was promising. Relevant experimental data are appended and can be found on page B-6.

In the original paper⁹⁹ on MUF-9, second-harmonic generation microscopy was used to characterise the various levels of interpenetration. This type of nonlinear optical microscopy²³⁸ is a powerful tool for characterising MOF materials because it distinguishes between centrosymmetric and noncentrosymmetric structures. For MUF-9, it allowed us to establish a lower bound on the domain size of interpenetrated regions. In MUFs 91-93, it could be used to better resolve the distribution of interpenetrated regions of the crystals. In principle, it should allow us to image, and therefore determine accurately, how far the secondary lattice penetrates into the crystals.

8.2. CHAPTERS 4 & 5 – HOW COULD THESE TECHNIQUES BE EXTENDED?

8.2.1. Chapter 4

In Chapter 4, we showed that the method for secondary growth of new lattices interpenetrated through MUF-9 was amenable to a variety of BPDC-based ligands, as well as two different metals.

The examples of secondary phases mentioned in Chapter 4 probably broadly represents most of the realm of what is possible with secondary growth MUF-9. Of course, there is an almost infinite number of small variations one could make to the BPDC backbone which may be compatible with our method for secondary growth. Nonetheless, some of the limits established are strict, especially that the size of the side chain must be small and located on one side of the ligand backbone.

We could get much more information out of these structures themselves. Of course, any of the examples presented in our initial exploration of possible secondary lattices could be characterised thoroughly in the way we have done for MUF-92 and MUF-93. The additional possible characterisation methods mentioned in the preceding section could also be applied to the diverse range of MOFs.

However, to really go further in the exploration of rationally designed hetero-interpenetrated MOFs, I think we need to identify more robust potential starting materials with larger pores. That would allow us to overcome the limits of MUF-9.

8.2.2. Chapter 5

In Chapter 5 I detailed a new implementation of a method to specifically identify the location of an element of choice in a SCXRD structure. This method exploits the preferential absorption of X-rays by the element of interest at a specific wavelength. By taking the difference of two datasets, one where that element absorbs a significant amount of radiation, and another where it doesn't, a dataset is generated where the location of that element is revealed.

This method for site-specific metal identification using anomalous scattering was considerably simplified because we were working with a pseudocentrosymmetric structure in a cubic unit cell. All of the basic crystallographic manipulations are compatible with other symmetries, but my routine for extracting statistics from the electron density maps would need to be extended significantly to be used for non-cubic cells.

If those expansions were made, the components could be combined into a complete program. Perhaps a suitable manifestation of such a program would be an add-on to an existing popular crystallography toolkit such as OLEX2¹³⁰ which is already built on Python, the language I used. That would allow this technique to be used by scientists without specific programming language expertise.

If the data processing used for this technique were more accessible, it would be almost trivial to extend it to more metals, more materials, and more situations.

8.3. CHAPTER 6 – HOW COULD THESE MATERIALS BE FURTHER EXPLOITED?

In Chapter 6, we turned our method for producing hetero-interpenetrated materials towards designing a framework tuned to a specific application. We prepared MUF-101, through the secondary growth of an achiral catalytic lattice interpenetrated through the homochiral starting material MUF-10. MUF-101 catalyses the Henry reaction between m-nitrobenzaldehyde and nitrocyclopentane, and gives a product with measurable enantiomeric excess. This enantioselectivity is a result of the chiral pore space surrounding the catalytic unit.

One shortcoming of our understanding of the catalysis presented in Chapter 6 is that we don't really know how the catalytic substrates and products fit into the MUF-101 pore. We successfully realised our aim of producing a catalyst where the chirality of the product is imparted by the host lattice, by applying intuitive reasoning about the size of the substrate. It should be large enough to interact with the pore walls, but small enough to diffuse in and out of the pores.

In the future, the development of such catalysts could be aided by modelling. Molecular dynamics simulations have often been applied to catalytic systems²³⁹, and to guest diffusion in MOFs.^{240, 241} Application of those established simulation techniques should allow the screening of MOFs for potential substrates, or conversely, modifications to the side chains which would result in a pore shape suited to a specific catalytic reaction.

We know the exact orientations of the ligands to each other in the hetero-interpenetrated MOFs based on MUF-9. We also know can change their functional groups without affecting the orientation of the rings towards each other, as the ligands are fixed in place by the MOF structure. This makes hetero-interpenetrated MOFs based on MUF-9 a potential platform for investigating the interactions between ligands. An example of that could be a charge transfer interaction between an electron-rich side chain on one lattice and an electron-poor backbone on the other, or vice versa. One could imagine that if such a charge transfer process took place, that MOF might be photoconductive as a function of its PIP%.

The pyrolysis of MOFs has led to unique porous carbon based hybrid materials,^{242, 243} including some produced in work by other members our group incorporating multimetallic nanoparticles. Due to their complex structure, hetero-interpenetrated materials might yield interesting carbon materials on pyrolysis. For example, since the secondary lattice exists mainly around the outside of the crystal, pyrolysis of these products could yield pore-shell porous carbon materials.

8.4. CHAPTER 7 – WHAT MORE CAN WE FIND OUT ABOUT LIGAND-LIGAND INTERACTIONS?

In Chapter 7 we explored some new frameworks, using ligands analogous to L1, but with varied side chains and binding groups. In all of these frameworks, where the side chains have multiple aromatic rings, those side chains exert a strong influence over the MOF they form. Sometimes, the influence of the side chain even overrides the

isorecticular principle, that the geometry of the binding groups and the identity of the metal cluster should determine the topology of the resulting MOF.

Several of the MOF structures in Chapter 7 involve an aryl embrace between the two enantiomers of the ligand. It would be worthwhile to resolve the enantiomers of the extended ligands **L11** and **L21** to determine which structures would occur when that specific embrace is not possible.

To investigate the interactions between ligands with the most possible detail, it would be best to do in-situ diffraction and spectroscopy experiments during crystal growth.

The results from a continuation of this work might help us to produce the more robust MOFs needed for expanding other areas.

8.5. FINAL WORDS

The directions described above all inform each other. Developing new characterisation tools, or new ways of implementing them, will allow us to discover more about these materials. Knowing more about the fundamental behaviours of partially interpenetrated frameworks, and the interactions between ligands as they form, will allow us to prepare them more easily and cleanly, and tune them more precisely. Being able to tune them more precisely will allow us to be better able to turn them towards desired applications.

8.6. REFERENCES

99. Ferguson, A.; Liu, L.; Tapperwijn, S. J.; Perl, D.; Coudert, F.-X.; Van Cleuvenbergen, S.; Verbiest, T.; van der Veen, M. A.; Telfer, S. G., Controlled partial interpenetration in metal–organic frameworks. *Nat. Chem.* **2016**, *8* (3), 250-257. DOI: 10.1038/nchem.2430
108. Howarth, A. J.; Peters, A. W.; Vermeulen, N. A.; Wang, T. C.; Hupp, J. T.; Farha, O. K., Best Practices for the Synthesis, Activation, and Characterization of Metal–Organic Frameworks. *Chem. Mater.* **2016**, *29* (1), 26-39. DOI: 10.1021/acs.chemmater.6b02626
130. Dolomanov, O. V.; Bourhis, L. J.; Gildea, R. J.; Howard, J. A. K.; Puschmann, H., OLEX2: a complete structure solution, refinement and analysis program. *J. Appl. Crystallogr.* **2009**, *42* (2), 339-341. DOI: doi:10.1107/S0021889808042726
238. van der Veen, M. A.; Verbiest, T.; De Vos, D. E., Probing microporous materials with second-harmonic generation. *Microporous Mesoporous Mater.* **2013**, *166*, 102-108. DOI: 10.1016/j.micromeso.2012.04.051
239. Farah, K.; Muller-Plathe, F.; Bohm, M. C., Classical reactive molecular dynamics implementations: state of the art. *ChemPhysChem* **2012**, *13* (5), 1127-51. DOI: 10.1002/cphc.201100681
240. Amirjalayer, S.; Tafipolsky, M.; Schmid, R., Molecular dynamics simulation of benzene diffusion in MOF-5: importance of lattice dynamics. *Angew Chem Int Ed Engl* **2007**, *46* (3), 463-6. DOI: 10.1002/anie.200601746
241. Greathouse, J. A.; Allendorf, M. D., The interaction of water with MOF-5 simulated by molecular dynamics. *J. Am. Chem. Soc.* **2006**, *128* (33), 10678-9. DOI: 10.1021/ja063506b
242. Yang, H.; Bradley, S. J.; Chan, A.; Waterhouse, G. I.; Nann, T.; Kruger, P. E.; Telfer, S. G., Catalytically Active Bimetallic Nanoparticles Supported on Porous Carbon Capsules Derived From Metal–Organic Framework Composites. *J. Am. Chem. Soc.* **2016**, *138* (36), 11872-81. DOI: 10.1021/jacs.6b06736
243. Yang, H.; Kruger, P. E.; Telfer, S. G., Metal-organic framework nanocrystals as sacrificial templates for hollow and exceptionally porous titania and composite materials. *Inorg. Chem.* **2015**, *54* (19), 9483-90. DOI: 10.1021/acs.inorgchem.5b01352

APPENDIX A - PYTHON CODES

Python codes are provided here for review and the convenience of anyone wanting to replicate or improve upon this work. They have no license attached and may be used, adapted, modified, or redistributed for any purpose, commercial or not, without attribution. These codes are provided "as is", without warranty of any kind, express or implied, including, fitness for a particular purpose and noninfringement. In no event shall the authors or copyright holders be liable for any claim, damages or other liability, arising from use of the software.

A.1. Correction of baselines for PXRD patterns

This code is in two parts. PXRD_process.py handles the files. It runs on all Rigaku .asc format files in a folder named 'input' and writes baseline corrected .xy files to a folder named output. It uses the algorithm in sonneveld.py as a dependency.

sonneveld.py

```
#Modified Sonneveld-Visser Baseline Removal Algorithm
#inputs is a single numpy 2Darray containing xy format PXRD data
#Sonneveld algorithm selects baseline points by choosing ones where the gradient to the next
point is small
#then a polynomial fit to those points is subtracted from the pattern
#as described in J. Appl. Crystallogr. (1975), 8, p1
import numpy as np
import random

def remove_baseline(inputs,step,iter,maxpeak,poly_order):
    input = inputs[1]
    maximum = max(input)
    print(maximum)
    points = list(range(int(len(input)*0.7)))[1::step]
    for j in range(iter):
        change = False
        for i in range(len(points)-1):
            if (abs(input[points[i]]-input[points[i+1]]) > (maxpeak * maximum)):
                print("large change detected at " + str(i))
                change = True
                for k in range(i,len(points)):
                    points[k] += step
                    if points[k] >= len(input): points[k] =
random.choice(range(int(len(input)*0.7)))
                if not change: break
            print("reiterating, attempt " + str(j))
        x = list([inputs[0][i] for i in points])
        y = list([inputs[1][i] for i in points])
        fit = np.polyfit(x,y,poly_order)
        print(fit)
        f = np.poly1d(fit)
        outputdata = [(inputs[1][i] - f(inputs[0][i])) for i in range(len(inputs[0]))]
        outputdata = [max(i,0) for i in outputdata]

    return [inputs[0],outputdata]
```

PXRD_process.py

```
import os
import re
import sonneveld
import numpy as np
#import all files from /input folder
filelist = os.listdir("./input/")
print(filelist)

def convert_to_xy(f):
    start = 0
    stop = 0
    step = 0
    count = 0
    data = []
    for i in range(len(f)):
        if "*START" in f[i]: start = float(re.findall("\d+\.\d+", f[i])[0])
        if "*STOP" in f[i]: stop = float(re.findall("\d+\.\d+", f[i])[0])
        if "*STEP" in f[i]: step = float(re.findall("\d+\.\d+", f[i])[0])

        if "*COUNT " in f[i]:
            count = int(re.findall("\d+", f[i])[0])
            for j in [(x + i + 1) for x in range(count)]:
                data.append(float(f[j]))
    points = ([round((start+i*step),2) for i in range(int((stop - start)/step))])
    return [points,data]

def scale(input,endmax):
    firstmax = max(input[1])
    scalefactor = endmax/firstmax
    out=[x * scalefactor for x in input[1]]
    return [input[0],out]

#main routine
for i in range(len(filelist)):
    print("processing "+filelist[i])
    ftext = open("./input/"+filelist[i], 'r').read().splitlines()
    xyf = convert_to_xy(ftext)
    xyf[1].pop()
    print(len(xyf[0]))
    print(len(xyf[1]))
    xyf = sonneveld.remove_baseline(xyf,10,200,0.05,10)
    xyf = scale(xyf,1000)
    outname = filelist[i][:-4] + ".txt"
    otext = open("./output/"+outname, 'w')
    for j in range(len(xyf[0])):
        print(str(xyf[0][j]) + " " + str(xyf[1][j]), file=otext)
```

A.2. Interpenetration percentage determination

Takes a folder of sample data in .xy format, a fully interpenetrated PXRD pattern, and a noninterpenetrated PXRD pattern as command line arguments. Returns as console output the percentage contribution of the interpenetrated pattern for each sample in the input folder, as determined by the linear mixture of interpenetrated and noninterpenetrated patterns with the least squared-differences to the sample pattern.

```
import numpy as np
import sys
import os

folder = "."+sys.argv[1]+"/"
samples = os.listdir(folder)

def scale(input,endmax):
    firstmax = max(input)
    scalefactor = endmax/firstmax
    return [x * scalefactor for x in input]

def importArray(filename):
    ftext = open(filename, 'r').read().splitlines()
    list1 = []
    for x in ftext:
        tmp = x.split()
        cur = float(tmp[0])
        #RANGE OF 2-THETA TO USE - for MUF-9 this works best with the two first peaks
        if 4.7 < cur < 8:
            list1.append(float(tmp[1]))
    return np.array(scale(list1,1000))

def mix(array1,array2,contribution):
    return np.add(np.multiply(array1,1-contribution),np.multiply(array2,contribution))

def getSSD(reference,sample):
    sample_scaled = sample * (reference.max() / sample.max())
    squares = (reference - sample_scaled) ** 2
    return np.sum(squares)

nonint_array = importArray(sys.argv[2])
int_array = importArray(sys.argv[3])

def refine(samplename):
    test_array = importArray(folder + samplename)
    contribution = 0.0
    step = 0.01
    improvement = True
    ssd = getSSD(mix(nonint_array,int_array,contribution),test_array)

    while improvement:
        contribution += step
        old_ssd = ssd
        ssd = getSSD(mix(nonint_array,int_array,contribution),test_array)
        if ssd > old_ssd:
            improvement = False

    return contribution

for sample in samples:
    print(sample, refine(sample))
```

A.3. Generation of difference data

Must be run in a cctbx.python environment. Takes the high-energy and metal absorption edge datasets as first and second command line arguments respectively.

```
from iotbx.reflection_file_reader import any_reflection_file
from cctbx import miller
from cctbx import crystal
from cctbx.array_family import flex
from iotbx.command_line import patterson_map
import sys

#Cell and symmetry data for the datasets - no way to obtain these from SHELX .hkl files, but
could be extracted from other filetypes
symm = crystal.symmetry(
    space_group_symbol="P-43m",
    unit_cell=(17.1,17.1,17.1,90,90,90))

print "Reading reflection files, merging equivalents \n\n\n"
#read and format high-energy dataset
hkl_in_native = any_reflection_file(file_name=sys.argv[1]+"=hk1f4")
miller_set_native = miller(hkl_in_native.as_miller_arrays()[0].customized_copy(crystal_symmetry=symm,anomalous_flag=False)
).merge_equivalents().array()
miller_set_native.show_summary()

print "\n"
#read and format high-energy dataset
hkl_in_derivative = any_reflection_file(file_name=sys.argv[2]+"=hk1f4")
miller_set_derivative = miller(hkl_in_derivative.as_miller_arrays()[0].customized_copy(crystal_symmetry=symm,anomalous_flag=False)
).merge_equivalents().array()
miller_set_derivative.show_summary()

print "\n\n Scaling reflection files and finding common reflections \n\n\n"
#Use only the reflections available in the derivative (lower resolution) dataset
miller_set_native, miller_set_derivative = miller_set_native.common_sets(other=miller_set_derivative)
miller_set_derivative = miller_set_native.multiscale(other=miller_set_derivative)
delta_f = miller_set_native.customized_copy(data=miller_set_derivative.data() - miller_set_derivative.data())

#print some stats for sanity checking
miller_set_native.show_summary()
print list(miller_set_native.data())[0:20]
print "\n"
miller_set_derivative.show_summary()
print list(miller_set_derivative.data().as_float())[0:20]

#output SHELX-format hkl file, and CCP4-format patterson map
print "\n writing difference hkl file \n"
f = open("delta_f.hkl", "w")
delta_f.export_as_shelx_hklf(file_object=f)
f.close()
pmap = patterson_map.calculate_patterson_map(data=delta_f, params=params)
pmap.as_ccp4_map(file_name="delta_f_patterson")
```

A.4. Integration of difference data

Generates various information and statistics from Gaussian .cube format electron density maps.

This depends on the *cubetools* library written by P. R. Vaidyanathan and published at <https://gist.github.com/aditya95sriram/8d1fccbb91dae93c4edf31cd6a22510f> under the MIT license. This library is appended below for convenience.

Atom locations and sizes are obtained from the refinement of signals in difference datasets (S4.1.3) and hardcoded into this script, which counts the total peak intensity over the volume of a sphere at each location in the cube map, the maximum peak height at each atom site, and the noise level as root mean squared deviation of each map, and returns these as console output.

electron_density_integration.py

```
import numpy as np
import math
import cubetools
from scipy.spatial import distance

def is_in_sphere(origin, radius, point):
    if (distance.euclidean(origin, point) <= radius):
        #print (origin, radius, point)
        #print ("distance ", distance.euclidean(origin, point), ">=> true")
        return True
    else:
        #print (origin, radius, point)
        #print ("distance ", distance.euclidean(origin, point), ">=> false")
        return False

def integrate_atom(location, radius, cell_size, emap):
    #location should be a triple (x,y,z) in fractional coordinates,
    #radius and cell_size should be in Angstroms
    sites = []
    min_i = int(( location[0] - (radius / cell_size) ) * emap.shape[0])
    max_i = int(( location[0] + (radius / cell_size) ) * emap.shape[0])
    min_j = int(( location[1] - (radius / cell_size) ) * emap.shape[1])
    max_j = int(( location[1] + (radius / cell_size) ) * emap.shape[1])
    min_k = int(( location[2] - (radius / cell_size) ) * emap.shape[2])
    max_k = int(( location[2] + (radius / cell_size) ) * emap.shape[2])
    print("integrating from x = "+str(min_i)+" to "+str(max_i)+", y = "+str(min_j)+" to "+str(max_j)+", z = "+str(min_k)+" to "+str(max_k))
    for i in range(min_i, max_i):
        for j in range(min_j, max_j):
            for k in range(min_k, max_k):
                x = (i/emap.shape[0])
                y = (j/emap.shape[1])
                z = (k/emap.shape[2])
                if is_in_sphere(location, radius/cell_size, (x,y,z)): sites.append(emap[i,j,k])
    return sites

fo_emap = cubetools.read_cube("MUF-93-72h-fobs.cube")
fo_emap_array = fo_emap[0]
fo_min_fc_emap = cubetools.read_cube("MUF-93-72h-fobs-min-fcalc.cube")
fo_min_fc_emap_array = fo_min_fc_emap[0]

atom_1 = (integrate_atom((ATOM_COORDINATES), ATOM_SIZE, CELL_LENGTH, fo_emap_array))
```

```

atom_2 = (integrate_atom((ATOM_COORDINATES), ATOM_SIZE, CELL_LENGTH, fo_emap_array))
print (atom_1, atom_2)
print(sum(atom_1), sum(atom_2))

print(fo_emap_array.shape)
print(fo_emap_array)
print(fo_min_fc_emap_array.shape)
print(fo_min_fc_emap_array)

def map_rmsd(emap_arr):
    emap_mean = emap_arr.mean(axis=None)
    print ("mean value:",emap_mean,"min value:",emap_arr.min(),"max value:",emap_arr.max())
    emap_disp = emap_arr - emap_mean
    emap_disp_sq = np.square(emap_disp)
    emap_mean_disp_sq = emap_disp_sq.mean()
    print ("mean squared displacement: " + str(emap_mean_disp_sq))
    emap_rmsd = math.sqrt(emap_mean_disp_sq)
    print ("root mean squared displacement: " + str(emap_rmsd))
    return emap_rmsd

print("Statistics for (Fobs, phi) electron density map:")
noise_fobs = map_rmsd(fo_emap_array)
print("")
print("Statistics for (Fobs - Fcalc, phi) electron density map:")
noise_diff = map_rmsd(fo_min_fc_emap_array)
print("")
print("meax peak height at location 1:", max(atom_1))
print("meax peak height at location 2:", max(atom_2))
print("integrated electron density at locations 1 & 2:", sum(atom_1), sum(atom_2))
print("ratio of peak integrals:", sum(atom_2)/sum(atom_1)*100, "%")
print("")
print("signal to noise ratio for main peak (noise calculated from (Fobs, phi) = ",
max(atom_1)/noise_fobs)
print("signal to noise ratio for main peak (noise calculated from (Fobs - Fcalc, phi)) = ",
max(atom_1)/noise_diff)
print("")

```

cubetools.py

```
#-----
# Module: cubetools
#-----
#
# Description:
# Module to work with Gaussian cube format files
# (see http://paulbourke.net/dataformats/cube/)
#
#-----
#
# What does it do:
# * Read/write cube files to/from numpy arrays (dtype=float*)
# * Read/write pairse of cube files to/from numpy arrays (dtype=complex*)
# * Provides a CubeFile object, to be used when cubefiles with
#   constant and static data is required. It simulates the readline method
#   of a file object with a cube file opened, without creating a file
#
#-----
#
# Dependency: numpy
#
#-----
#
# Author: P. R. Vaidyanathan (aditya95sriram <at> gmail <dot> com)
# Date: 25th June 2017
#
#-----
#
# MIT License
#
# Copyright (c) 2019 P. R. Vaidyanathan
#
# Permission is hereby granted, free of charge, to any person obtaining a copy
# of this software and associated documentation files (the "Software"), to deal
# in the Software without restriction, including without limitation the rights
# to use, copy, modify, merge, publish, distribute, sublicense, and/or sell
# copies of the Software, and to permit persons to whom the Software is
# furnished to do so, subject to the following conditions:
#
# The above copyright notice and this permission notice shall be included in all
# copies or substantial portions of the Software.
#
# THE SOFTWARE IS PROVIDED "AS IS", WITHOUT WARRANTY OF ANY KIND, EXPRESS OR
# IMPLIED, INCLUDING BUT NOT LIMITED TO THE WARRANTIES OF MERCHANTABILITY,
# FITNESS FOR A PARTICULAR PURPOSE AND NONINFRINGEMENT. IN NO EVENT SHALL THE
# AUTHORS OR COPYRIGHT HOLDERS BE LIABLE FOR ANY CLAIM, DAMAGES OR OTHER
# LIABILITY, WHETHER IN AN ACTION OF CONTRACT, TORT OR OTHERWISE, ARISING FROM,
# OUT OF OR IN CONNECTION WITH THE SOFTWARE OR THE USE OR OTHER DEALINGS IN THE
# SOFTWARE.
#-----

import numpy as np

if name == ' __main__':
    DEBUGMODE = True
else:
    DEBUGMODE = False

def _debug(*args):
    global DEBUGMODE
    if DEBUGMODE:
        print " ".join(map(str, args))

class CubeFile(object):
    """
    Object which mimics a cube file opened as a file object
    by returning output in the correct format, matching the
    metadata of the source cube file and replacing volumetric
    data with static data provided as arg to the constructor.
    Doesn't copy atoms metadata, retains number of atoms, but
    returns dummy atoms
    Mimics file object's readline method.
    """
```

```

params:
    srcname: source file to copy metadata from
    const: numeric value to return instead of volumetric data

returns: CubeFile object
"""

def __init__(self, srcname, const=1):
    self.cursor = 0
    self.const = const
    self.src = src = open(srcname)
    src.readline(); src.readline(); # comments
    _debug(srcname)
    self.lines = [" Cubefile created by cubetools.py\n",
                  "   source: {0}\n".format(srcname)]
    self.lines.append(src.readline()) # read natm and origin
    self.natm = int(self.lines[-1].strip().split()[0])
    # read cube dim and vectors along 3 axes
    self.lines.extend(src.readline() for i in range(3))
    self.src.close()
    self.nx, self.ny, self.nz = [int(l.strip().split()[0]) for l in self.lines[3:6]]
    self.remvals = self.nz
    self.remrows = self.nx*self.ny
    for i in range(self.natm):
        self.lines.append("{0:^ 8d}".format(1) + "{0:< 12.6f}".format(0)*4 + '\n')

def __del__(self):
    self.src.close()

def readline(self):
    """ Mimic readline method of file object with cube file opened """
    try:
        retval = self.lines[self.cursor]
    except IndexError:
        if not self.remrows:
            return ""
        if self.remvals <= 6:
            nval = min(6, self.remvals)
            self.remrows -= 1
            self.remvals = self.nz
        else:
            nval = 6
            self.remvals -= nval
        return " {0: .5E}".format(self.const)*nval + "\n"
    else:
        self.cursor += 1
        return retval

def _getline(cube):
    """
    Read a line from cube file where first field is an int
    and the remaining fields are floats.

    params:
        cube: file object of the cube file

    returns: (int, list<float>)
    """
    l = cube.readline().strip().split()
    return int(l[0]), map(float, l[1:])

def _putline(*args):
    """
    Generate a line to be written to a cube file where
    the first field is an int and the remaining fields are floats.

    params:
        *args: first arg is formatted as int and remaining as floats

    returns: formatted string to be written to file with trailing newline
    """
    s = "{0:^ 8d}".format(args[0])
    s += "".join("{0:< 12.6f}".format(arg) for arg in args[1:])
    return s + "\n"

def read_cube(fname):

```

```

"""
Read cube file into numpy array

params:
    fname: filename of cube file

returns: (data: np.array, metadata: dict)
"""
meta = {}
with open(fname, 'r') as cube:
    cube.readline(); cube.readline() # ignore comments
    natm, meta['org'] = _getline(cube)
    nx, meta['xvec'] = _getline(cube)
    ny, meta['yvec'] = _getline(cube)
    nz, meta['zvec'] = _getline(cube)
    meta['atoms'] = [_getline(cube) for i in range(natm)]
    data = np.zeros((nx*ny*nz))
    idx = 0
    for line in cube:
        for val in line.strip().split():
            data[idx] = float(val)
            idx += 1
data = np.reshape(data, (nx, ny, nz))
return data, meta

def read_imcube(rfname, ifname = ""):
    """
    Convenience function to read in two cube files at once,
    where one contains the real part and the other contains the
    imag part. If only one filename given, other filename is inferred.

    params:
        rfname: filename of cube file of real part
        ifname: optional, filename of cube file of imag part

    returns: np.array (real part + j*imag part)
    """
    ifname = ifname or rfname.replace('real', 'imag')
    _debug("reading from files", rfname, "and", ifname)
    re, im = read_cube(rfname), read_cube(ifname)
    fin = np.zeros(re[0].shape, dtype='complex128')
    if re[1] != im[1]:
        _debug("warning: meta data mismatch, real part metadata retained")
    fin += re[0]
    fin += 1j*im[0]
    return fin, re[1]

def write_cube(data, meta, fname):
    """
    Write volumetric data to cube file along

    params:
        data: volumetric data consisting real values
        meta: dict containing metadata with following keys
            atoms: list of atoms in the form (mass, [position])
            org: origin
            xvec, yvec, zvec: lattice vector basis
        fname: filename of cubefile (existing files overwritten)

    returns: None
    """
    with open(fname, "w") as cube:
        # first two lines are comments
        cube.write(" Cubefile created by cubetools.py\n source: none\n")
        natm = len(meta['atoms'])
        nx, ny, nz = data.shape
        cube.write(_putline(natm, *meta['org'])) # 3rd line #atoms and origin
        cube.write(_putline(nx, *meta['xvec']))
        cube.write(_putline(ny, *meta['yvec']))
        cube.write(_putline(nz, *meta['zvec']))
        for atom_mass, atom_pos in meta['atoms']:
            cube.write(_putline(atom_mass, *atom_pos)) #skip the newline
        for i in range(nx):
            for j in range(ny):
                for k in range(nz):
                    if (i or j or k) and k%6==0:
                        cube.write("\n")

```

```

        cube.write(" {0: .5E}".format(data[i,j,k]))

def write_incube(data, meta, rfname, ifname=""):
    """
    Convenience function to write two cube files from complex valued
    volumetric data, one for the real part and one for the imaginary part.
    Data about atoms, origin and lattice vectors are kept same for both.
    If only one filename given, other filename is inferred.

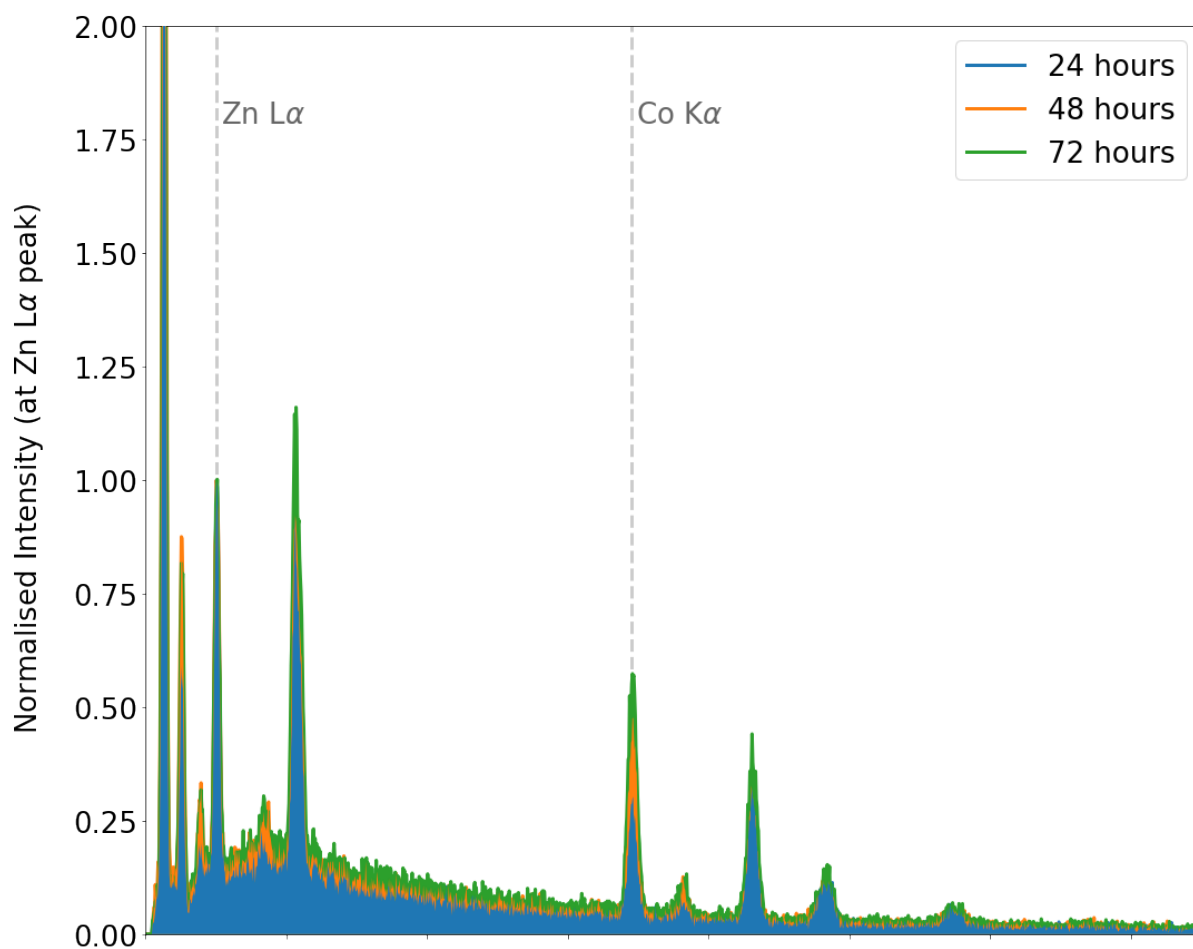
    params:
        data: volumetric data consisting complex values
        meta: dict containing metadata with following keys
            atoms: list of atoms in the form (mass, [position])
            org: origin
            xvec,yvec,zvec: lattice vector basis
        rfname: filename of cube file containing real part
        ifname: optional, filename of cube file containing imag part

    returns: None
    """
    ifname = ifname or rfname.replace('real', 'imag')
    _debug("writing data to files", rfname, "and", ifname)
    write_cube(data.real, meta, rfname)
    write_cube(data.imag, meta, ifname)

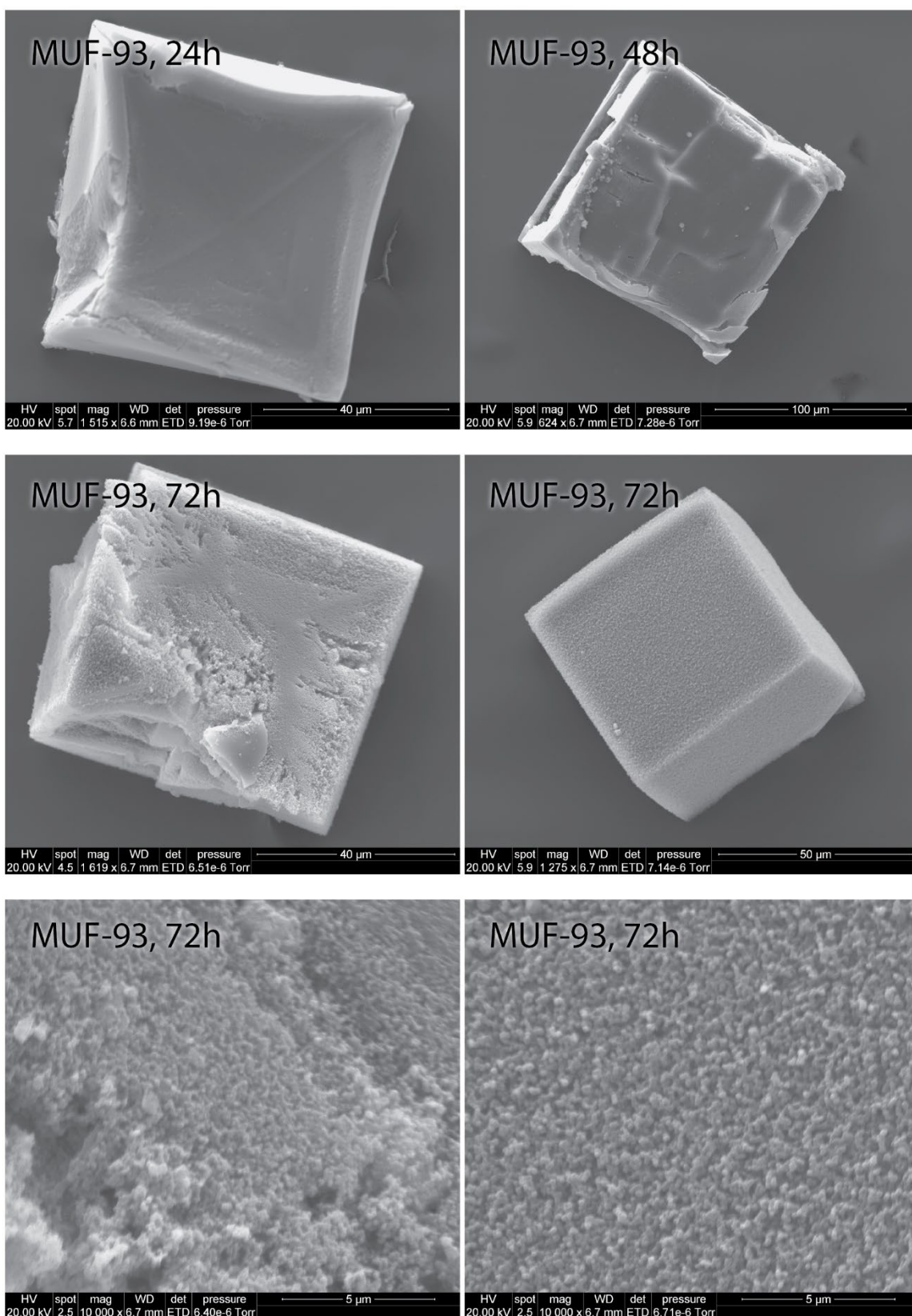
```

APPENDIX B - OTHER EXPERIMENTAL DATA

B.1. Data for MUF-93

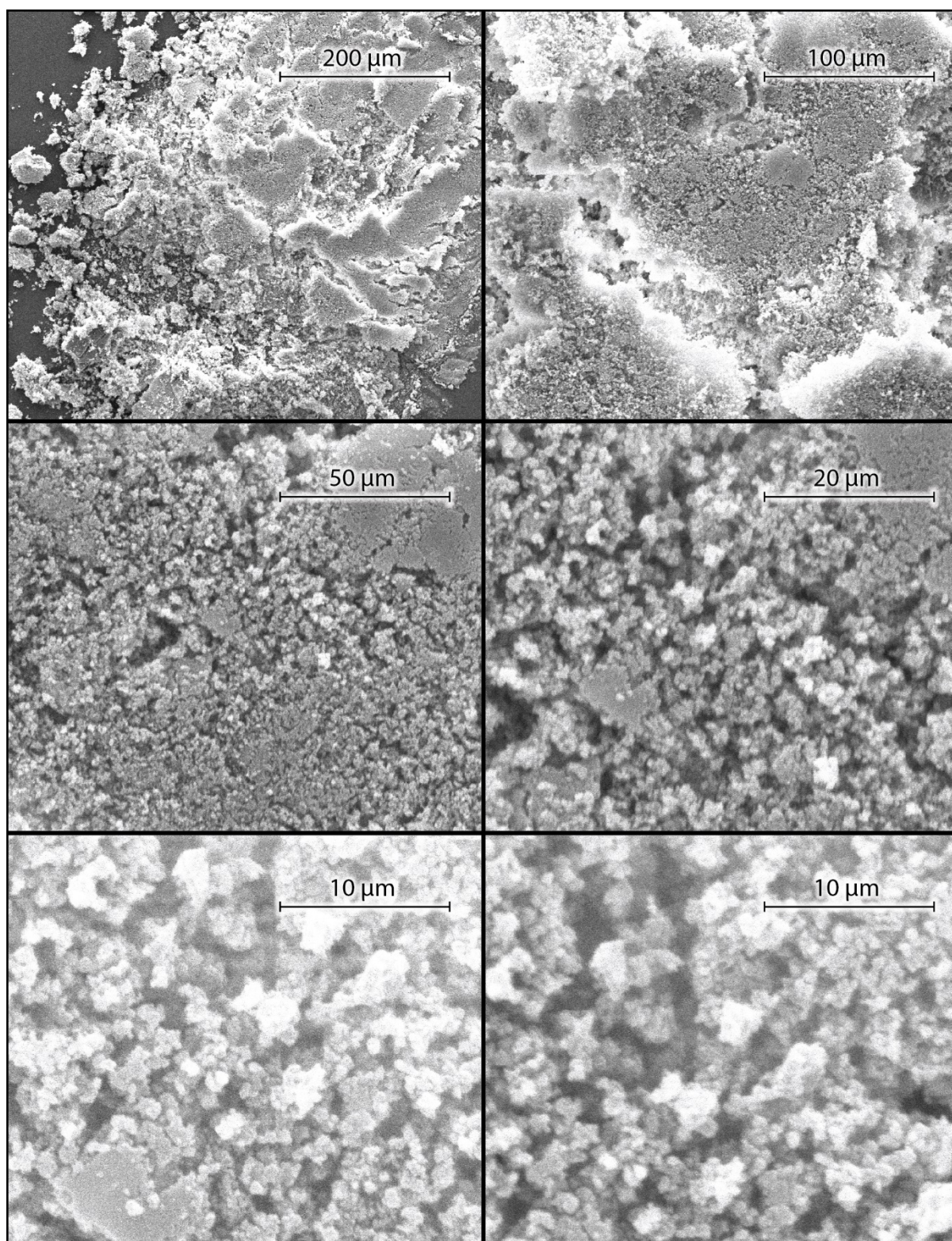


Appended Figure B.1: EDS spectra of MUF-93 at various time points of secondary growth, normalised to the intensity of the Zn Lα peak.

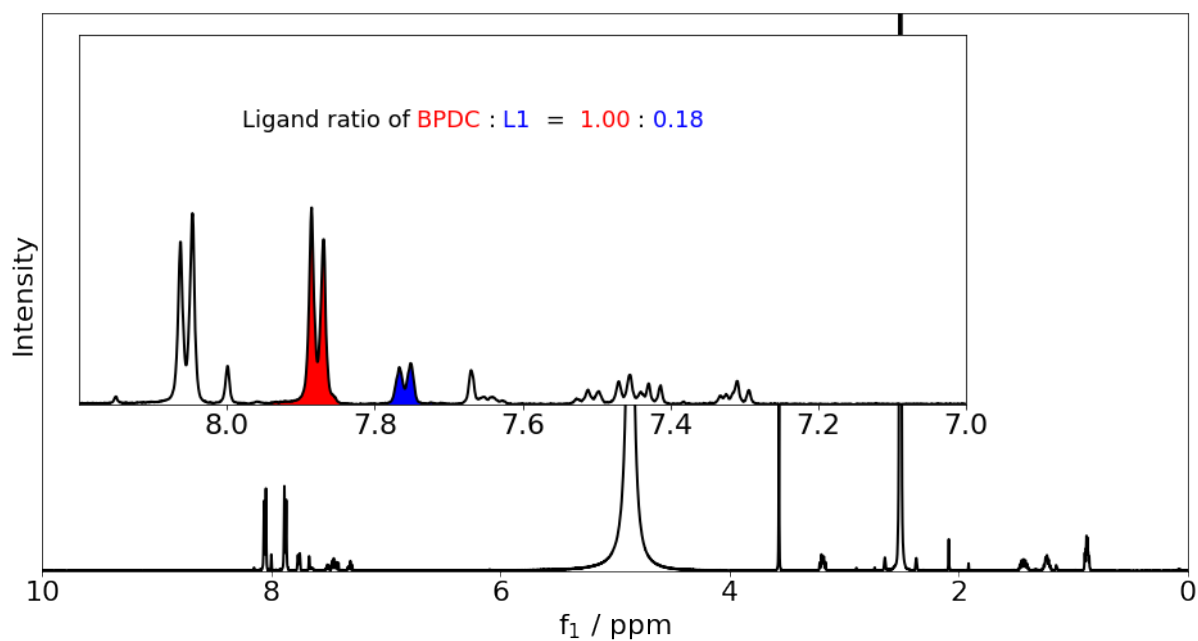


Appended Figure B.2: SEM images of MUF-93 crystals at various time points

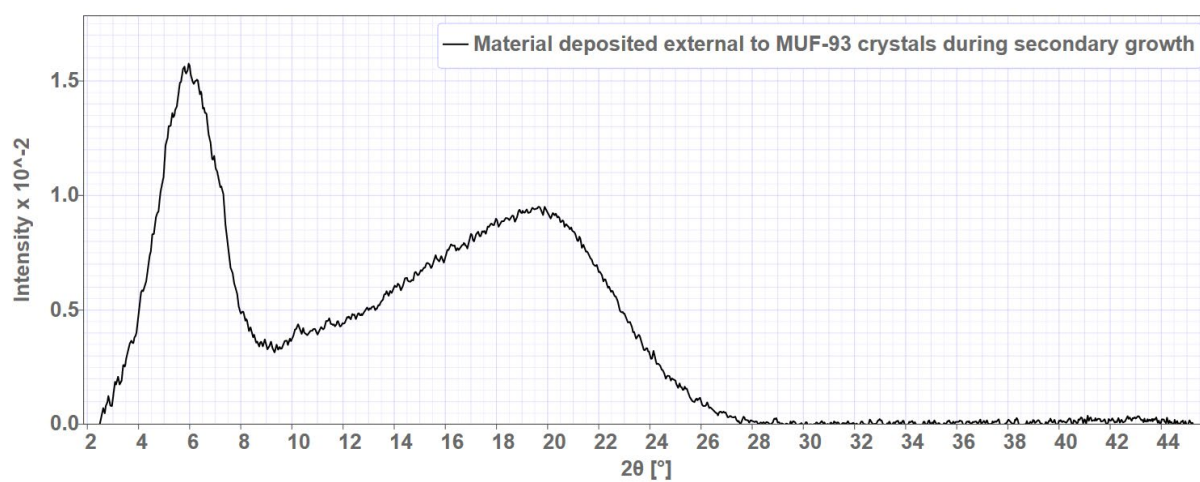
B.2. Data for external phase deposited on MUF-93



Appended Figure B.3: SEM images of the external phase deposited during MUF-93 growth

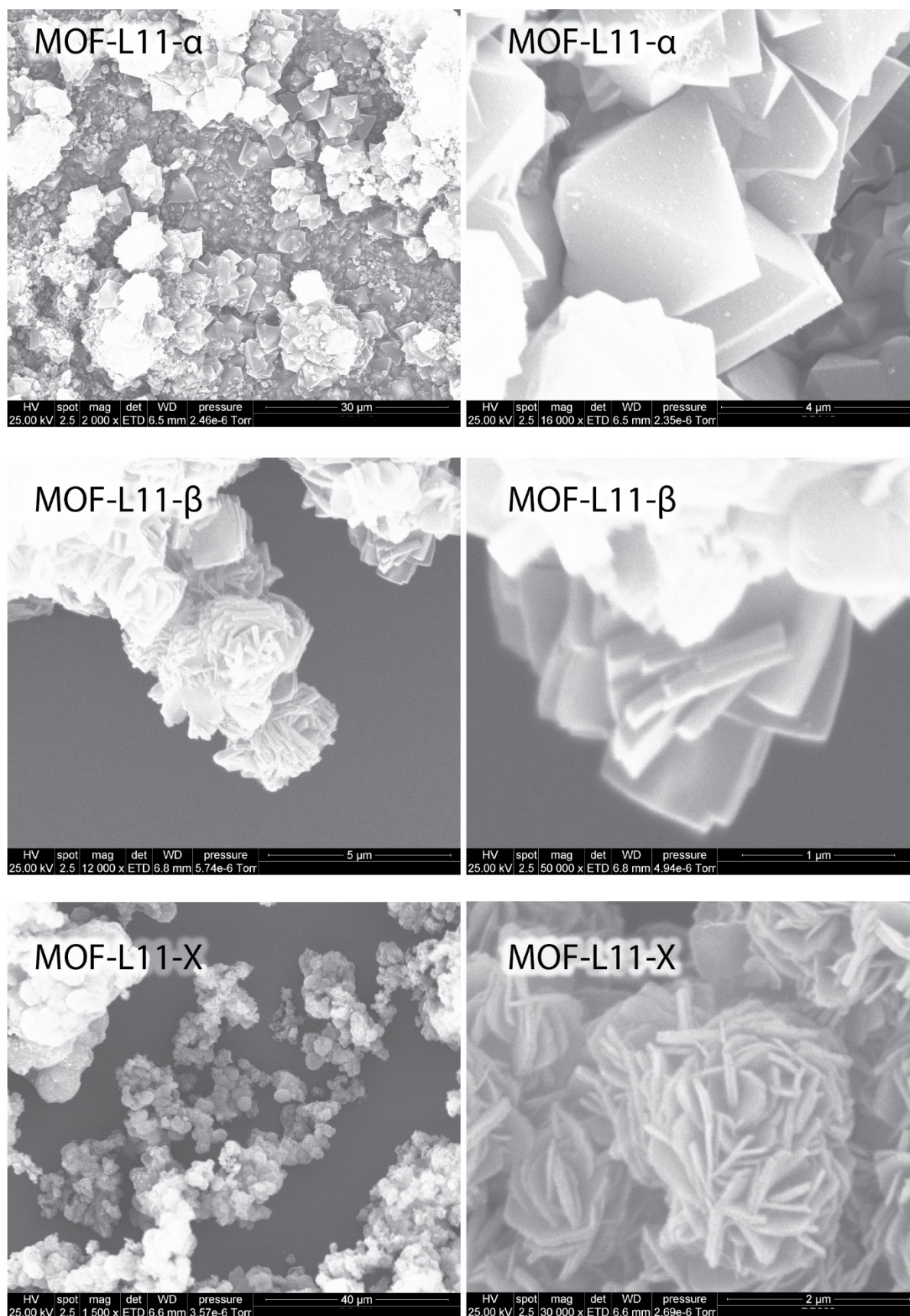


Appended Figure B.4: ^1H NMR spectrum of a digested sample of the external phase deposited on MUF-93 during secondary growth. 18% L1 is due to contamination with small MUF-9 crystals.



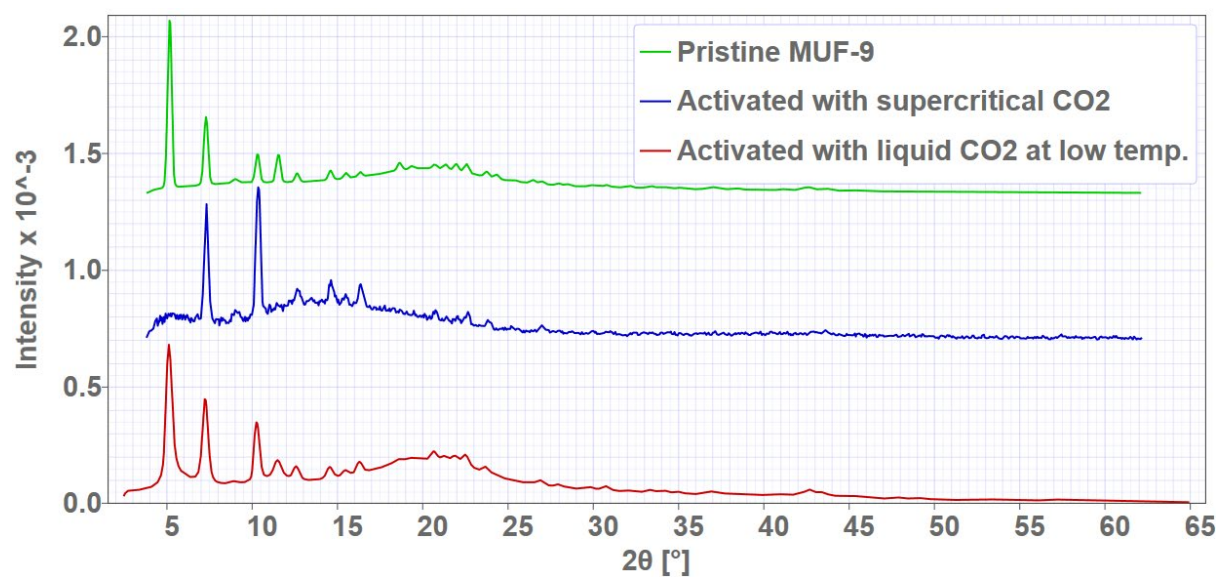
Appended Figure B.5: PXRD pattern of the uncharacterised phase which forms external to the MUF-93 crystals during secondary growth.

B.3. Data for new MOFs from Chapter 7



Appended Figure B.6: SEM images of MOF-L21-α, MOF-L21-β and an unidentified phase.

B.4. Data relating to the activation of MUF-9



Appended Figure B.7: PXRD patterns of MUF-9 activated by various means.

B.5. List of SCXRD datasets available electronically:

All CIF files listed here are available electronically on the included CD-ROM.

Chapter 2:

- MUF-91-12h-57pc.cif
- MUF-91-12h-71pc.cif
- MUF-91-15h-51pc.cif
- MUF-91-15h-58pc.cif
- MUF-91-15h-68pc.cif
- MUF-91-18h-46pc.cif
- MUF-91-1h-12pc.cif
- MUF-91-3h-23pc.cif
- MUF-91-3h-27pc.cif
- MUF-91-3h-38pc.cif
- MUF-91-3h-41pc.cif
- MUF-91-6h-50pc.cif
- MUF-91-6h-52pc.cif
- MUF-91-9h-51pc.cif
- MUF-91-9h-64pc.cif
- MUF-91-9h-76pc.cif

Chapter 3:

Structures from preliminary trials:

- SL3_in_MUF-9.cif
- SL5_in_MUF-9.cif
- SL6_in_MUF-9.cif
- MgBPDC_in_MUF-9_12h.cif
- MgBPDC_in_MUF-9_24h.cif
- MgBPDC_in_MUF-9_36h.cif
- MgBPDC_in_MUF-9_48h.cif
- MgBPDC_in_MUF-9_72h.cif
- MgBPDC_in_MUF-9_84h.cif
- MgBPDC_in_MUF-9_96h.cif

MUF-92:

- MUF-92-3h-41pc.cif
- MUF-92-3h-47pc.cif
- MUF-92-3h-50pc.cif
- MUF-92-6h-53pc.cif
- MUF-92-6h-63pc.cif
- MUF-92-6h-65pc.cif
- MUF-92-9h-63pc.cif
- MUF-92-9h-65pc.cif

- MUF-92-9h-71pc.cif
- MUF-92-12h-68pc.cif
- MUF-92-12h-71pc.cif
- MUF-92-12h-81pc.cif
- MUF-92-15h-71pc.cif
- MUF-92-15h-77pc-2.cif
- MUF-92-15h-77pc.cif

MUF-93:

Growth of MUF-93 over time:

- MUF-93-12h-01pc.cif
- MUF-93-12h-02pc.cif
- MUF-93-12h-10pc.cif
- MUF-93-12h-4pc.cif
- MUF-93-24h-14pc.cif
- MUF-93-24h-15pc.cif
- MUF-93-24h-16pc.cif
- MUF-93-24h-21pc.cif
- MUF-93-24h-28pc.cif
- MUF-93-36h-22pc.cif
- MUF-93-36h-28pc.cif
- MUF-93-48h-39pc.cif
- MUF-93-48h-48pc.cif
- MUF-93-48h-51pc.cif
- MUF-93-48h-61pc.cif
- MUF-93-60h-59pc.cif
- MUF-93-60h-63pc.cif
- MUF-93-60h-73pc.cif
- MUF-93-72h-62pc.cif
- MUF-93-72h-63pc.cif
- MUF-93-72h-76pc.cif
- MUF-93-84h-66pc.cif
- MUF-93-84h-67pc.cif
- MUF-93-84h-71pc.cif
- MUF-93-96h-66pc.cif
- MUF-93-96h-67pc.cif
- MUF-93-96h-70pc.cif

Scanning across a single crystal:

- MUF-93-scan1-pos1-72pc.cif
- MUF-93-scan1-pos3-59pc.cif
- MUF-93-scan1-pos4-52pc.cif

- MUF-93-scan1-pos5-31pc.cif
- MUF-93-scan1-pos6-23pc.cif
- MUF-93-scan1-pos7-21pc.cif
- MUF-93-scan1-pos8-23pc.cif
- MUF-93-scan1-pos9-26pc.cif
- MUF-93-scan1-pos10-31pc.cif
- MUF-93-scan1-pos11-47pc.cif
- MUF-93-scan1-pos12-59pc.cif
- MUF-93-scan1-pos13-65pc.cif
- MUF-93-scan1-pos14-73pc.cif
- MUF-93-scan1-pos15-73pc.cif

Chapter 7:

- MOF-L3.cif
- MOF-L4.cif
- MOF-L11.cif
- MOF-L21-a.cif
- P1.cif

SCXRD results for preliminary trials in Chapter 4:

Appended table 1: Crystallographic data for initial attempts at secondary growth in MUF-9, from chapter 4.

Identification code	SL3_in_MUF-9	SL5_in_MUF-9	SL6_in_MUF-9
Empirical formula	C _{109.01} H _{62.3} N _{9.57} O _{20.75} Zn _{6.38}	C _{106.66} H _{60.95} N _{7.62} O _{16.51} SZn _{5.08}	C _{118.43} I _{0.78} N ₆ O _{19.78} Zn _{6.09}
Formula weight	2255.08	2077.44	2319.97
Temperature/K	100.15	292.15	292.15
Crystal system	cubic	cubic	cubic
Space group	P-43m	P-43m	P-43m
a, b, c /Å	17.10(5)	17.20(5)	17.10(5)
Volume/Å³	5000(44)	5088(44)	5000(44)
Z	1	1	1
ρ_{calc}/cm³	0.749	0.678	0.770
μ/mm⁻¹	0.791	1.039	0.877
F(000)	1141.0	1055.0	1135.0
Radiation	Synchrotron (λ = 0.7085)		
2θ range for data collection/°	5.818 to 41.464	11.504 to 72.486	5.322 to 34.41
Index ranges	-16 ≤ h ≤ 17, -15 ≤ k ≤ 17, -12 ≤ l ≤ 17	-8 ≤ h ≤ 12, -12 ≤ k ≤ 13, -13 ≤ l ≤ 13	-14 ≤ h ≤ 13, -12 ≤ k ≤ 14, -12 ≤ l ≤ 14
Reflections collected	9718	4616	5649
Independent reflections	1033 [R _{int} = 0.0572, R _{sigma} = 0.0248]	506 [R _{int} = 0.0518, R _{sigma} = 0.0242]	622 [R _{int} = 0.0626, R _{sigma} = 0.0256]
Data/restraints/parameters	1033/313/130	506/27/21	622/35/35
Goodness-of-fit on F²	1.831	1.762	1.738
Final R indexes [I>=2σ (I)]	R ₁ = 0.1421, wR ₂ = 0.3812	R ₁ = 0.1377, wR ₂ = 0.3548	R ₁ = 0.1335, wR ₂ = 0.3425
Final R indexes [all data]	R ₁ = 0.1546, wR ₂ = 0.3925	R ₁ = 0.1416, wR ₂ = 0.3610	R ₁ = 0.1364, wR ₂ = 0.3484
Largest diff. peak/hole / e Å⁻³	1.40/-0.84	0.51/-0.29	0.64/-0.34
Flack parameter	0.23(2)	0.02(6)	0.30(3)

Bibliography

1. Furukawa, H.; Muller, U.; Yaghi, O. M., "Heterogeneity within order" in metal-organic frameworks. *Angew Chem Int Ed Engl* **2015**, *54* (11), 3417-30. DOI: 10.1002/anie.201410252
2. Furukawa, H.; Cordova, K. E.; O'Keeffe, M.; Yaghi, O. M., The Chemistry and Applications of Metal-Organic Frameworks. *Science* **2013**, *341* (6149), 1230444. DOI: 10.1126/science.1230444
3. Yaghi, O. M., Metal-organic Frameworks: A tale of two entanglements. *Nat. Mater.* **2007**, *6* (2), 92-93. DOI: 10.1038/nmat1824
4. Kitagawa, S.; Kitaura, R.; Noro, S.-i., Functional Porous Coordination Polymers. *Angew. Chem. Int. Ed.* **2004**, *43* (18), 2334-2375. DOI: 10.1002/anie.200300610
5. Cavka, J. H.; Jakobsen, S.; Olsbye, U.; Guillou, N.; Lamberti, C.; Bordiga, S.; Lillerud, K. P., A new zirconium inorganic building brick forming metal organic frameworks with exceptional stability. *J. Am. Chem. Soc.* **2008**, *130* (42), 13850-1. DOI: 10.1021/ja8057953
6. Yaghi, O. M.; Li, G.; Li, H., Selective binding and removal of guests in a microporous metal-organic framework. *Nature* **1995**, *378* (6558), 703-706. DOI: DOI 10.1038/378703a0
7. Batten, S. R.; Champness, N. R.; Chen, X.-M.; Garcia-Martinez, J.; Kitagawa, S.; Öhrström, L.; O'Keeffe, M.; Suh, M. P.; Reedijk, J., Coordination polymers, metal-organic frameworks and the need for terminology guidelines. *CrystEngComm* **2012**, *14* (9), 3001-3004. DOI: 10.1039/c2ce06488j
8. Chui, S. S.; Lo, S. M.; Charmant, J. P.; Orpen, A. G.; Williams, I. D., A chemically functionalizable nanoporous material. *Science* **1999**, *283* (5405), 1148-50. DOI: 10.1126/science.283.5405.1148
9. Ferey, G.; Mellot-Draznieks, C.; Serre, C.; Millange, F.; Dutour, J.; Surble, S.; Margiolaki, I., A chromium terephthalate-based solid with unusually large pore volumes and surface area. *Science* **2005**, *309* (5743), 2040-2. DOI: 10.1126/science.1116275
10. Hoskins, B. F.; Robson, R., Design and construction of a new class of scaffolding-like materials comprising infinite polymeric frameworks of 3D-linked molecular rods. A reappraisal of the zinc cyanide and cadmium cyanide structures and the synthesis and structure of the diamond-related frameworks [N(CH₃)₄][CuI₂ZnII(CN)₄] and CuI[4,4',4'',4'''-tetracyanotetraphenylmethane]BF₄.x C₆H₅NO₂. *J. Am. Chem. Soc.* **1990**, *112* (4), 1546-1554. DOI: 10.1021/ja00160a038
11. Rosi, N. L.; Kim, J.; Eddaoudi, M.; Chen, B.; O'Keeffe, M.; Yaghi, O. M., Rod packings and metal-organic frameworks constructed from rod-shaped secondary building units. *J. Am. Chem. Soc.* **2005**, *127* (5), 1504-18. DOI: 10.1021/ja045123o
12. Diercks, C. S.; Yaghi, O. M., The atom, the molecule, and the covalent organic framework. *Science* **2017**, *355* (6328). DOI: 10.1126/science.aal1585
13. Stewart, D.; Antypov, D.; Dyer, M. S.; Pitcher, M. J.; Katsoulidis, A. P.; Chater, P. A.; Blanc, F.; Rosseinsky, M. J., Stable and ordered amide frameworks synthesised under reversible conditions which facilitate error checking. *Nat Commun* **2017**, *8* (1), 1102. DOI: 10.1038/s41467-017-01423-5

14. Zhang, Y. B.; Su, J.; Furukawa, H.; Yun, Y.; Gandara, F.; Duong, A.; Zou, X.; Yaghi, O. M., Single-crystal structure of a covalent organic framework. *J. Am. Chem. Soc.* **2013**, *135* (44), 16336-9. DOI: 10.1021/ja409033p
15. Li, Y.; Tang, S.; Yusov, A.; Rose, J.; Borrforss, A. N.; Hu, C. T.; Ward, M. D., Hydrogen-bonded frameworks for molecular structure determination. *Nat Commun* **2019**, *10* (1), 4477. DOI: 10.1038/s41467-019-12453-6
16. Lin, R. B.; He, Y.; Li, P.; Wang, H.; Zhou, W.; Chen, B., Multifunctional porous hydrogen-bonded organic framework materials. *Chem. Soc. Rev.* **2019**, *48* (5), 1362-1389. DOI: 10.1039/c8cs00155c
17. O'Keeffe, M.; Yaghi, O. M., Deconstructing the crystal structures of metal-organic frameworks and related materials into their underlying nets. *Chem Rev* **2012**, *112* (2), 675-702. DOI: 10.1021/cr200205j
18. Kim, D.; Liu, X.; Lah, M. S., Topology analysis of metal-organic frameworks based on metal-organic polyhedra as secondary or tertiary building units. *Inorganic Chemistry Frontiers* **2015**, *2* (4), 336-360. DOI: 10.1039/c4qi00236a
19. Ockwig, N. W.; Delgado-Friedrichs, O.; O'Keeffe, M.; Yaghi, O. M., Reticular chemistry: occurrence and taxonomy of nets and grammar for the design of frameworks. *Acc. Chem. Res.* **2005**, *38* (3), 176-82. DOI: 10.1021/ar020022l
20. Yazaydin, A. O.; Snurr, R. Q.; Park, T. H.; Koh, K.; Liu, J.; Levan, M. D.; Benin, A. I.; Jakubczak, P.; Lanuza, M.; Galloway, D. B.; Low, J. J.; Willis, R. R., Screening of metal-organic frameworks for carbon dioxide capture from flue gas using a combined experimental and modeling approach. *J. Am. Chem. Soc.* **2009**, *131* (51), 18198-9. DOI: 10.1021/ja9057234
21. Farha, O. K.; Yazaydin, A. O.; Eryazici, I.; Malliakas, C. D.; Hauser, B. G.; Kanatzidis, M. G.; Nguyen, S. T.; Snurr, R. Q.; Hupp, J. T., De novo synthesis of a metal-organic framework material featuring ultrahigh surface area and gas storage capacities. *Nat Chem* **2010**, *2* (11), 944-8. DOI: 10.1038/nchem.834
22. Buser, H. J.; Schwarzenbach, D.; Petter, W.; Ludi, A., The crystal structure of Prussian Blue: Fe₄[Fe(CN)₆]₃·xH₂O. *Inorg. Chem.* **2002**, *16* (11), 2704-2710. DOI: 10.1021/ic50177a008
23. Groom, C. R.; Bruno, I. J.; Lightfoot, M. P.; Ward, S. C., The Cambridge Structural Database. *Acta Crystallogr B Struct Sci Cryst Eng Mater* **2016**, *72* (Pt 2), 171-9. DOI: 10.1107/S2052520616003954
24. Abrahams, B. F.; Hoskins, B. F.; Michail, D. M.; Robson, R., Assembly of porphyrin building blocks into network structures with large channels. *Nature* **1994**, *369* (6483), 727-729. DOI: 10.1038/369727a0
25. Kondo, M.; Yoshitomi, T.; Matsuzaka, H.; Kitagawa, S.; Seki, K., Three-Dimensional Framework with Channeling Cavities for Small Molecules: {[M₂(4,4'-bpy)₃(NO₃)₄]·xH₂O}_n (M = Co, Ni, Zn). *Angew. Chem., Int. Ed. Engl.* **1997**, *36* (16), 1725-1727. DOI: 10.1002/anie.199717251
26. Yaghi, O. M.; Li, G., Mutually Interpenetrating Sheets and Channels in the Extended Structure of [Cu(4,4'-bpy)Cl]. *Angew. Chem., Int. Ed. Engl.* **1995**, *34* (2), 207-209. DOI: 10.1002/anie.199502071
27. Fujita, M.; Kwon, Y. J.; Washizu, S.; Ogura, K., Preparation, Clathration Ability, and Catalysis of a Two-Dimensional Square Network Material Composed of Cadmium(II) and 4,4'-Bipyridine. *J. Am. Chem. Soc.* **1994**, *116* (3), 1151-1152. DOI: 10.1021/ja00082a055

28. Yaghi, O. M.; Li, H.; Groy, T. L., Construction of Porous Solids from Hydrogen-Bonded Metal Complexes of 1,3,5-Benzenetricarboxylic Acid. *J. Am. Chem. Soc.* **1996**, *118* (38), 9096–9101. DOI: DOI 10.1021/ja960746q
29. Li, H.; Eddaoudi, M.; O'Keeffe, M.; Yaghi, O. M., Design and synthesis of an exceptionally stable and highly porous metal-organic framework. *Nature* **1999**, *402* (6759), 276-279. DOI: 10.1038/46248
30. Eddaoudi, M.; Kim, J.; Rosi, N.; Vodak, D.; Wachter, J.; O'Keeffe, M.; Yaghi, O. M., Systematic Design of Pore Size and Functionality in Isoreticular MOFs and Their Application in Methane Storage. *Science* **2002**, *295* (5554), 469–472. DOI: DOI 10.1126/science.1067208
31. Yuan, S.; Chen, Y. P.; Qin, J. S.; Lu, W.; Zou, L.; Zhang, Q.; Wang, X.; Sun, X.; Zhou, H. C., Linker Installation: Engineering Pore Environment with Precisely Placed Functionalities in Zirconium MOFs. *J. Am. Chem. Soc.* **2016**, *138* (28), 8912-9. DOI: 10.1021/jacs.6b04501
32. Liu, L.; Telfer, S. G., Systematic ligand modulation enhances the moisture stability and gas sorption characteristics of quaternary metal-organic frameworks. *J. Am. Chem. Soc.* **2015**, *137* (11), 3901-9. DOI: 10.1021/jacs.5b00365
33. Dau, P. V.; Cohen, S. M., A bifunctional, site-isolated metal-organic framework-based tandem catalyst. *Inorg. Chem.* **2015**, *54* (7), 3134-8. DOI: 10.1021/ic502316v
34. Lu, W.; Wei, Z.; Gu, Z. Y.; Liu, T. F.; Park, J.; Park, J.; Tian, J.; Zhang, M.; Zhang, Q.; Gentle, T., 3rd; Bosch, M.; Zhou, H. C., Tuning the structure and function of metal-organic frameworks via linker design. *Chem. Soc. Rev.* **2014**, *43* (16), 5561-93. DOI: 10.1039/c4cs00003j
35. Lun, D. J.; Waterhouse, G. I.; Telfer, S. G., A general thermolabile protecting group strategy for organocatalytic metal-organic frameworks. *J. Am. Chem. Soc.* **2011**, *133* (15), 5806-9. DOI: 10.1021/ja202223d
36. Gascon, J.; Aktay, U.; Hernandezalonso, M.; Vanklink, G.; Kapteijn, F., Amino-based metal-organic frameworks as stable, highly active basic catalysts. *J. Catal.* **2009**, *261* (1), 75-87. DOI: 10.1016/j.jcat.2008.11.010
37. Stock, N.; Biswas, S., Synthesis of Metal-Organic Frameworks (MOFs): Routes to Various MOF Topologies, Morphologies, and Composites. *Chem. Rev.* **2012**, *112* (2), 933–969. DOI: 10.1021/cr200304e
38. Schaate, A.; Roy, P.; Godt, A.; Lippke, J.; Waltz, F.; Wiebcke, M.; Behrens, P., Modulated synthesis of Zr-based metal-organic frameworks: from nano to single crystals. *Chemistry* **2011**, *17* (24), 6643-51. DOI: 10.1002/chem.201003211
39. Hausdorf, S.; Baitalow, F.; Seidel, J.; Mertens, F. O. R. L., Gaseous Species as Reaction Tracers in the Solvothermal Synthesis of the Zinc Oxide Terephthalate MOF-5. *The Journal of Physical Chemistry A* **2007**, *111* (20), 4259-4266. DOI: 10.1021/jp0708291
40. Férey, G.; Haouas, M.; Loiseau, T.; Taulelle, F., Nanoporous Solids: How Do They Form? An In Situ Approach. *Chem. Mater.* **2013**, *26* (1), 299-309. DOI: 10.1021/cm4019875
41. Van Vleet, M. J.; Weng, T.; Li, X.; Schmidt, J. R., In Situ, Time-Resolved, and Mechanistic Studies of Metal-Organic Framework Nucleation and Growth. *Chem Rev* **2018**, *118* (7), 3681-3721. DOI: 10.1021/acs.chemrev.7b00582

42. Denny Jr, M. S.; Moreton, J. C.; Benz, L.; Cohen, S. M., Metal-organic frameworks for membrane-based separations. *Nature Reviews Materials* **2016**, 1 (12), 16078. DOI: 10.1038/natrevmats.2016.78
43. Vellingiri, K.; Deep, A.; Kim, K. H., Metal-Organic Frameworks as a Potential Platform for Selective Treatment of Gaseous Sulfur Compounds. *ACS Appl. Mater. Interfaces* **2016**, 8 (44), 29835-29857. DOI: 10.1021/acsami.6b10482
44. Frameworks for commercial success. *Nat. Chem.* **2016**, 8 (11), 987-987. DOI: 10.1038/nchem.2661
45. Kim, H.; Yang, S.; Rao, S. R.; Narayanan, S.; Kapustin, E. A.; Furukawa, H.; Umans, A. S.; Yaghi, O. M.; Wang, E. N., Water harvesting from air with metal-organic frameworks powered by natural sunlight. *Science* **2017**, 356 (6336), eaam8743. DOI: 10.1126/science.aam8743
46. Chen, Q.; Ma, Y.; Song, W. C.; Chang, Z.; Li, J. R.; Zhang, J.; Sun, H. W.; Balbuena, P. B.; Bu, X. H., Why Porous Materials Have Selective Adsorptions: A Rational Aspect from Electrodynamics. *Inorg. Chem.* **2017**, 56 (5), 2614-2620. DOI: 10.1021/acs.inorgchem.6b02746
47. Nandasiri, M. I.; Jambovane, S. R.; McGrail, B. P.; Schaef, H. T.; Nune, S. K., Adsorption, separation, and catalytic properties of densified metal-organic frameworks. *Coord. Chem. Rev.* **2016**, 311, 38-52. DOI: 10.1016/j.ccr.2015.12.004
48. Carrington, E. J.; Vitorica-Yrezabal, I. J.; Brammer, L., Crystallographic studies of gas sorption in metal-organic frameworks. *Acta Crystallogr. B* **2014**, 70 (Pt 3), 404-22. DOI: 10.1107/S2052520614009834
49. Nugent, P.; Belmabkhout, Y.; Burd, S. D.; Cairns, A. J.; Luebke, R.; Forrest, K.; Pham, T.; Ma, S.; Space, B.; Wojtas, L.; Eddaoudi, M.; Zaworotko, M. J., Porous materials with optimal adsorption thermodynamics and kinetics for CO₂ separation. *Nature* **2013**, 495 (7439), 80-4. DOI: 10.1038/nature11893
50. Yang, C.; Wang, X.; Omary, M. A., Crystallographic observation of dynamic gas adsorption sites and thermal expansion in a breathable fluororous metal-organic framework. *Angew. Chem. Int. Ed.* **2009**, 48 (14), 2500-5. DOI: 10.1002/anie.200804739
51. Lin, R.-B.; Xiang, S.; Zhou, W.; Chen, B., Microporous Metal-Organic Framework Materials for Gas Separation. *Chem* **2019**. DOI: 10.1016/j.chempr.2019.10.012
52. Zhao, X.; Wang, Y.; Li, D. S.; Bu, X.; Feng, P., Metal-Organic Frameworks for Separation. *Adv Mater* **2018**, 30 (37), e1705189. DOI: 10.1002/adma.201705189
53. Senkovska, I.; Kaskel, S., Ultrahigh porosity in mesoporous MOFs: promises and limitations. *Chem. Commun.* **2014**, 50 (54), 7089-98. DOI: 10.1039/c4cc00524d
54. Kim, J. Y.; Oh, H.; Moon, H. R., Hydrogen Isotope Separation in Confined Nanospaces: Carbons, Zeolites, Metal-Organic Frameworks, and Covalent Organic Frameworks. *Adv Mater* **2019**, 31 (20), e1805293. DOI: 10.1002/adma.201805293
55. Huang, J.; Han, X.; Yang, S.; Cao, Y.; Yuan, C.; Liu, Y.; Wang, J.; Cui, Y., Microporous 3D Covalent Organic Frameworks for Liquid Chromatographic Separation of Xylene Isomers and Ethylbenzene. *J. Am. Chem. Soc.* **2019**, 141 (22), 8996-9003. DOI: 10.1021/jacs.9b03075

56. Alaerts, L.; Maes, M.; Giebel, L.; Jacobs, P. A.; Martens, J. A.; Denayer, J. F.; Kirschhock, C. E.; De Vos, D. E., Selective adsorption and separation of ortho-substituted alkylaromatics with the microporous aluminum terephthalate MIL-53. *J. Am. Chem. Soc.* **2008**, *130* (43), 14170-8. DOI: 10.1021/ja802761z
57. Yu, J.; Xie, L. H.; Li, J. R.; Ma, Y.; Seminario, J. M.; Balbuena, P. B., CO₂ Capture and Separations Using MOFs: Computational and Experimental Studies. *Chem Rev* **2017**, *117* (14), 9674-9754. DOI: 10.1021/acs.chemrev.6b00626
58. Pullumbi, P.; Brandani, F.; Brandani, S., Gas separation by adsorption: technological drivers and opportunities for improvement. *Current Opinion in Chemical Engineering* **2019**, *24*, 131-142. DOI: 10.1016/j.coche.2019.04.008
59. Adil, K.; Belmabkhout, Y.; Pillai, R. S.; Cadiau, A.; Bhatt, P. M.; Assen, A. H.; Maurin, G.; Eddaoudi, M., Gas/vapour separation using ultra-microporous metal-organic frameworks: insights into the structure/separation relationship. *Chem. Soc. Rev.* **2017**, *46* (11), 3402-3430. DOI: 10.1039/c7cs00153c
60. Pascanu, V.; Gonzalez Miera, G.; Inge, A. K.; Martin-Matute, B., Metal-Organic Frameworks as Catalysts for Organic Synthesis: A Critical Perspective. *J. Am. Chem. Soc.* **2019**, *141* (18), 7223-7234. DOI: 10.1021/jacs.9b00733
61. Jiao, L.; Wang, Y.; Jiang, H. L.; Xu, Q., Metal-Organic Frameworks as Platforms for Catalytic Applications. *Adv Mater* **2018**, *30* (37), e1703663. DOI: 10.1002/adma.201703663
62. Foo, M. L.; Matsuda, R.; Kitagawa, S., Functional Hybrid Porous Coordination Polymers. *Chem. Mater.* **2014**, *26* (1), 310-322. DOI: 10.1021/cm402136z
63. García-García, P.; Müller, M.; Corma, A., MOF catalysis in relation to their homogeneous counterparts and conventional solid catalysts. *Chemical Science* **2014**, *5* (8), 2979. DOI: 10.1039/c4sc00265b
64. Chen, T.-H.; Popov, I.; Kaveevivitchai, W.; Miljanić, O. Š., Metal–Organic Frameworks: Rise of the Ligands. *Chem. Mater.* **2014**, *26* (15), 4322-4325. DOI: 10.1021/cm501657d
65. Sun, Q.; Tang, Y.; Aguila, B.; Wang, S.; Xiao, F. S.; Thallapally, P. K.; Al-Enizi, A. M.; Nafady, A.; Ma, S., Reaction Environment Modification in Covalent Organic Frameworks for Catalytic Performance Enhancement. *Angew Chem Int Ed Engl* **2019**, *58* (26), 8670-8675. DOI: 10.1002/anie.201900029
66. Liu, L.; Zhou, T.-Y.; Telfer, S. G., Modulating the Performance of an Asymmetric Organocatalyst by Tuning Its Spatial Environment in a Metal–Organic Framework. *J. Am. Chem. Soc.* **2017**, *139* (39), 13936-13943. DOI: 10.1021/jacs.7b07921
67. Alkas, A.; Cornelio, J.; Telfer, S. G., Tritopic Triazatruxene Ligands for Multicomponent Metal-Organic Frameworks. *Chem. Asian. J.* **2019**, *14* (8), 1167-1174. DOI: 10.1002/asia.201801546
68. Liu, L.; Li, L.; DeGayner, J. A.; Winegar, P. H.; Fang, Y.; Harris, T. D., Harnessing Structural Dynamics in a 2D Manganese-Benzoquinoid Framework To Dramatically Accelerate Metal Transport in Diffusion-Limited Metal Exchange Reactions. *J. Am. Chem. Soc.* **2018**, *140* (36), 11444-11453. DOI: 10.1021/jacs.8b06774

69. Burgun, A.; Coghlan, C. J.; Huang, D. M.; Chen, W.; Horike, S.; Kitagawa, S.; Alvino, J. F.; Metha, G. F.; Sumby, C. J.; Doonan, C. J., Mapping-Out Catalytic Processes in a Metal-Organic Framework with Single-Crystal X-ray Crystallography. *Angew. Chem. Int. Ed.* **2017**, *56* (29), 8412-8416. DOI: 10.1002/anie.201611254
70. Metzger, E. D.; Comito, R. J.; Hendon, C. H.; Dinca, M., Mechanism of Single-Site Molecule-Like Catalytic Ethylene Dimerization in Ni-MFU-4l. *J. Am. Chem. Soc.* **2017**, *139* (2), 757-762. DOI: 10.1021/jacs.6b10300
71. Lucier, B. E. G.; Chen, S.; Huang, Y., Characterization of Metal-Organic Frameworks: Unlocking the Potential of Solid-State NMR. *Acc. Chem. Res.* **2018**, *51* (2), 319-330. DOI: 10.1021/acs.accounts.7b00357
72. Sutrisno, A.; Huang, Y., Solid-state NMR: a powerful tool for characterization of metal-organic frameworks. *Solid State Nucl. Magn. Reson.* **2013**, *49-50*, 1-11. DOI: 10.1016/j.ssnmr.2012.09.003
73. Wong, Y. T. A.; Martins, V.; Lucier, B. E. G.; Huang, Y., Solid-State NMR Spectroscopy: A Powerful Technique to Directly Study Small Gas Molecules Adsorbed in Metal-Organic Frameworks. *Chemistry* **2019**, *25* (8), 1848-1853. DOI: 10.1002/chem.201803866
74. Vukotic, V. N.; Harris, K. J.; Zhu, K.; Schurko, R. W.; Loeb, S. J., Metal-organic frameworks with dynamic interlocked components. *Nat Chem* **2012**, *4* (6), 456-60. DOI: 10.1038/nchem.1354
75. Liu, L.; Chen, Z.; Wang, J.; Zhang, D.; Zhu, Y.; Ling, S.; Huang, K. W.; Belmabkhout, Y.; Adil, K.; Zhang, Y.; Slater, B.; Eddaoudi, M.; Han, Y., Imaging defects and their evolution in a metal-organic framework at sub-unit-cell resolution. *Nat Chem* **2019**, *11* (7), 622-628. DOI: 10.1038/s41557-019-0263-4
76. Gong, Y.-N.; Zhong, D.-C.; Lu, T.-B., Interpenetrating metal-organic frameworks. *CrystEngComm* **2016**, *18* (15), 2596-2606. DOI: 10.1039/c6ce00371k
77. Zhu, R.; Ding, J.; Jin, L.; Pang, H., Interpenetrated structures appeared in supramolecular cages, MOFs, COFs. *Coord. Chem. Rev.* **2019**, *389*, 119-140. DOI: 10.1016/j.ccr.2019.03.002
78. Batten, S. R., Topology of interpenetration. *CrystEngComm* **2001**, *3* (18), 67-72. DOI: 10.1039/b102400k
79. Wu, H.; Yang, J.; Su, Z. M.; Batten, S. R.; Ma, J. F., An exceptional 54-fold interpenetrated coordination polymer with 10(3)-srs network topology. *J. Am. Chem. Soc.* **2011**, *133* (30), 11406-9. DOI: 10.1021/ja202303b
80. Schaate, A.; Roy, P.; Preusse, T.; Lohmeier, S. J.; Godt, A.; Behrens, P., Porous interpenetrated zirconium-organic frameworks (PIZOFs): a chemically versatile family of metal-organic frameworks. *Chemistry* **2011**, *17* (34), 9320-5. DOI: 10.1002/chem.201101015
81. Murray, L. J.; Dinca, M.; Long, J. R., Hydrogen storage in metal-organic frameworks. *Chem. Soc. Rev.* **2009**, *38* (5), 1294-314. DOI: 10.1039/b802256a
82. Ma, S.; Sun, D.; Ambrogio, M.; Fillinger, J. A.; Parkin, S.; Zhou, H. C., Framework-catenation isomerism in metal-organic frameworks and its impact on hydrogen uptake. *J. Am. Chem. Soc.* **2007**, *129* (7), 1858-9. DOI: 10.1021/ja067435s

83. Maji, T. K.; Matsuda, R.; Kitagawa, S., A flexible interpenetrating coordination framework with a bimodal porous functionality. *Nat. Mater.* **2007**, *6* (2), 142-8. DOI: 10.1038/nmat1827
84. Han, S. S.; Jung, D.-H.; Heo, J., Interpenetration of Metal Organic Frameworks for Carbon Dioxide Capture and Hydrogen Purification: Good or Bad? *J. Phys. Chem. C* **2012**, *117* (1), 71-77. DOI: 10.1021/jp308751x
85. Sezginel, K. B.; Asinger, P. A.; Babaei, H.; Wilmer, C. E., Thermal Transport in Interpenetrated Metal–Organic Frameworks. *Chem. Mater.* **2018**, *30* (7), 2281-2286. DOI: 10.1021/acs.chemmater.7b05015
86. Ma, L.; Lin, W., Unusual interlocking and interpenetration lead to highly porous and robust metal-organic frameworks. *Angew Chem Int Ed Engl* **2009**, *48* (20), 3637-40. DOI: 10.1002/anie.200806227
87. Lin, Z.; Zhang, Z. M.; Chen, Y. S.; Lin, W., Highly Efficient Cooperative Catalysis by Co(III) (Porphyrin) Pairs in Interpenetrating Metal-Organic Frameworks. *Angew Chem Int Ed Engl* **2016**, *55* (44), 13739-13743. DOI: 10.1002/anie.201605802
88. Wang, R.; Zhang, M.; Liu, X.; Zhang, L.; Kang, Z.; Wang, W.; Wang, X.; Dai, F.; Sun, D., Tuning the Dimensionality of Interpenetration in a Pair of Framework-Catenation Isomers To Achieve Selective Adsorption of CO₂ and Fluorescent Sensing of Metal Ions. *Inorg. Chem.* **2015**, *54* (13), 6084-6. DOI: 10.1021/acs.inorgchem.5b00934
89. Shekhah, O.; Wang, H.; Paradinas, M.; Ocal, C.; Schüpbach, B.; Terfort, A.; Zacher, D.; Fischer, R. A.; Wöll, C., Controlling interpenetration in metal–organic frameworks by liquid-phase epitaxy. *Nat. Mater.* **2009**, *8* (6), 481–484. DOI: 10.1038/nmat2445
90. Verma, G.; Butikofer, S.; Kumar, S.; Ma, S., Regulation of the Degree of Interpenetration in Metal-Organic Frameworks. *Top Curr Chem (Cham)* **2019**, *378* (1), 4. DOI: 10.1007/s41061-019-0268-x
91. Chae, H. K.; Siberio-Perez, D. Y.; Kim, J.; Go, Y.; Eddaoudi, M.; Matzger, A. J.; O’Keeffe, M.; Yaghi, O. M., A route to high surface area, porosity and inclusion of large molecules in crystals. *Nature* **2004**, *427* (6974), 523-7. DOI: 10.1038/nature02311
92. Deng, H.; Grunder, S.; Cordova, K. E.; Valente, C.; Furukawa, H.; Hmadeh, M.; Gandara, F.; Whalley, A. C.; Liu, Z.; Asahina, S.; Kazumori, H.; O’Keeffe, M.; Terasaki, O.; Stoddart, J. F.; Yaghi, O. M., Large-pore apertures in a series of metal-organic frameworks. *Science* **2012**, *336* (6084), 1018-23. DOI: 10.1126/science.1220131
93. Park, J. H.; Lee, W. R.; Kim, Y.; Lee, H. J.; Ryu, D. W.; Phang, W. J.; Hong, C. S., Interpenetration Control, Sorption Behavior, and Framework Flexibility in Zn(II) Metal–Organic Frameworks. *Cryst. Growth Des.* **2014**, *14* (2), 699-704. DOI: 10.1021/cg401583v
94. Kim, J.; Yang, S.-T.; Choi, S. B.; Sim, J.; Kim, J.; Ahn, W.-S., Control of catenation in CuTATB-n metal–organic frameworks by sonochemical synthesis and its effect on CO₂ adsorption. *J. Mater. Chem.* **2011**, *21* (9). DOI: 10.1039/c0jm03318a
95. Feldblyum, J. I.; Wong-Foy, A. G.; Matzger, A. J., Non-interpenetrated IRMOF-8: synthesis, activation, and gas sorption. *Chem. Commun.* **2012**, *48* (79), 9828-9828. DOI: 10.1039/c2cc34689c
96. Yazdanparast, M. S.; Day, V. W.; Gadzikwa, T., Hydrogen-Bonding Linkers Yield a Large-Pore, Non-Catenated, Metal-Organic Framework with pcu Topology. *Molecules* **2020**, *25* (3). DOI: 10.3390/molecules25030697

97. O'Nolan, D.; Madden, D. G.; Kumar, A.; Chen, K. J.; Pham, T.; Forrest, K. A.; Patyk-Kazmierczak, E.; Yang, Q. Y.; Murray, C. A.; Tang, C. C.; Space, B.; Zaworotko, M. J., Impact of partial interpenetration in a hybrid ultramicroporous material on C₂H₂/C₂H₄ separation performance. *Chem Commun (Camb)* **2018**, 54 (28), 3488-3491. DOI: 10.1039/C8CC01627E
98. Verma, G.; Kumar, S.; Pham, T.; Niu, Z.; Wojtas, L.; Perman, J. A.; Chen, Y.-S.; Ma, S., Partially Interpenetrated NbO Topology Metal–Organic Framework Exhibiting Selective Gas Adsorption. *Cryst. Growth Des.* **2017**, 17 (5), 2711-2717. DOI: 10.1021/acs.cgd.7b00198
99. Ferguson, A.; Liu, L.; Tapperwijn, S. J.; Perl, D.; Coudert, F.-X.; Van Cleuvenbergen, S.; Verbiest, T.; van der Veen, M. A.; Telfer, S. G., Controlled partial interpenetration in metal–organic frameworks. *Nat. Chem.* **2016**, 8 (3), 250-257. DOI: 10.1038/nchem.2430
100. Yang, S.; Lin, X.; Lewis, W.; Suyetin, M.; Bichoutskaia, E.; Parker, J. E.; Tang, C. C.; Allan, D. R.; Rizkallah, P. J.; Hubberstey, P.; et al., A partially interpenetrated metal–organic framework for selective hysteretic sorption of carbon dioxide. *Nat. Mater.* **2012**, 11 (8), 710–716. DOI: 10.1038/nmat3343
101. Ding, J.-G.; Yin, C.; Zheng, L.-Y.; Han, S.-S.; Li, B.-L.; Wu, B., Tuning cadmium coordination architectures using 1,4-bis(1,2,4-triazol-1-ylmethyl)benzene and sulfoisophthalate. *RSC Advances* **2014**, 4 (47), 24594. DOI: 10.1039/c4ra02291b
102. Yao, X.-Q.; Cao, D.-P.; Hu, J.-S.; Li, Y.-Z.; Guo, Z.-J.; Zheng, H.-G., Chiral and Porous Coordination Polymers Based on an N-Centered Triangular Rigid Ligand. *Cryst. Growth Des.* **2011**, 11 (1), 231–239. DOI: 10.1021/cg1011764
103. Xu, H.; Bao, W.; Xu, Y.; Liu, X.; Shen, X.; Zhu, D., An unprecedented 3D/3D hetero-interpenetrated MOF built from two different nodes, chemical composition, and topology of networks. *CrystEngComm* **2012**, 14 (18), 5720-5720. DOI: 10.1039/c2ce25739d
104. Carlucci, L.; Ciani, G.; Maggini, S.; Proserpio, D. M., A New Polycatenated 3D Array of Interlaced 2D Brickwall Layers and 1D Molecular Ladders in [Mn₂(bix)₃(NO₃)₄]·2CHCl₃[bix = 1,4-bis(imidazol-1-ylmethyl)benzene] That Undergoes Supramolecular Isomerization upon Guest Removal. *Cryst. Growth Des.* **2008**, 8 (1), 162-165. DOI: 10.1021/cg700884q
105. Kwon, O.; Park, S.; Zhou, H. C.; Kim, J., Computational prediction of hetero-interpenetration in metal-organic frameworks. *Chem. Commun.* **2017**, 53 (12), 1953-1956. DOI: 10.1039/c6cc08940b
106. Sezginel, K. B.; Feng, T.; Wilmer, C. E., Discovery of hypothetical hetero-interpenetrated MOFs with arbitrarily dissimilar topologies and unit cell shapes. *CrystEngComm* **2017**, 19 (31), 4497-4504. DOI: 10.1039/c7ce00290d
107. Yuan, S.; Feng, L.; Wang, K.; Pang, J.; Bosch, M.; Lollar, C.; Sun, Y.; Qin, J.; Yang, X.; Zhang, P.; Wang, Q.; Zou, L.; Zhang, Y.; Zhang, L.; Fang, Y.; Li, J.; Zhou, H. C., Stable Metal-Organic Frameworks: Design, Synthesis, and Applications. *Adv Mater* **2018**, 30 (37), e1704303. DOI: 10.1002/adma.201704303
108. Howarth, A. J.; Peters, A. W.; Vermeulen, N. A.; Wang, T. C.; Hupp, J. T.; Farha, O. K., Best Practices for the Synthesis, Activation, and Characterization of Metal–Organic Frameworks. *Chem. Mater.* **2016**, 29 (1), 26-39. DOI: 10.1021/acs.chemmater.6b02626
109. Allinger, N. L.; Youngdale, G. A., Reduction of 6,7-Diphenyldibenzo[e,g] [1,4]diazocine. An Unusual Nucleophilic Aromatic Substitution 1. *J. Org. Chem.* **1959**, 24 (3), 306-308. DOI: DOI 10.1021/jo01085a004

110. Cornelio, J.; Zhou, T. Y.; Alkas, A.; Telfer, S. G., Systematic Tuning of the Luminescence Output of Multicomponent Metal-Organic Frameworks. *J. Am. Chem. Soc.* **2018**, *140* (45), 15470-15476. DOI: 10.1021/jacs.8b09887
111. Tranchemontagne, D. J.; Hunt, J. R.; Yaghi, O. M., Room temperature synthesis of metal-organic frameworks: MOF-5, MOF-74, MOF-177, MOF-199, and IRMOF-0. *Tetrahedron* **2008**, *64* (36), 8553-8557. DOI: 10.1016/j.tet.2008.06.036
112. Wang, Y.; Cheng, L.; Wang, K. J.; Perry, Z.; Jia, W.; Chen, R.; Wang, Z. L.; Pang, J., Temperature-Controlled Degree of Interpenetration in a Single-Crystal-to-Single-Crystal Transformation within Two Co(II)-Triazole Frameworks. *Inorg. Chem.* **2019**, *58* (1), 18-21. DOI: 10.1021/acs.inorgchem.8b01339
113. Zhang, J.; Wojtas, L.; Larsen, R. W.; Eddaoudi, M.; Zaworotko, M. J., Temperature and concentration control over interpenetration in a metal-organic material. *J. Am. Chem. Soc.* **2009**, *131* (47), 17040-1. DOI: 10.1021/ja906911q
114. Brozek, C. K.; Dinca, M., Cation exchange at the secondary building units of metal-organic frameworks. *Chem. Soc. Rev.* **2014**, *43* (16), 5456-67. DOI: 10.1039/c4cs00002a
115. Borycz, J.; Tiana, D.; Haldoupis, E.; Sung, J. C.; Farha, O. K.; Siepmann, J. I.; Gagliardi, L., CO₂ Adsorption in M-IRMOF-10 (M = Mg, Ca, Fe, Cu, Zn, Ge, Sr, Cd, Sn, Ba). *J. Phys. Chem. C* **2016**, *120* (23), 12819-12830. DOI: 10.1021/acs.jpcc.6b02235
116. Hicks, J. M.; Desgranges, C.; Delhomme, J., Characterization and Comparison of the Performance of IRMOF-1, IRMOF-8, and IRMOF-10 for CO₂ Adsorption in the Subcritical and Supercritical Regimes. *J. Phys. Chem. C* **2012**, *116* (43), 22938-22946. DOI: 10.1021/jp307319u
117. Babarao, R.; Jiang, J., Molecular screening of metal-organic frameworks for CO₂ storage. *Langmuir* **2008**, *24* (12), 6270-8. DOI: 10.1021/la800369s
118. Yang, L.-M.; Ravindran, P.; Vajeeston, P.; Tilset, M., Ab initio investigations on the crystal structure, formation enthalpy, electronic structure, chemical bonding, and optical properties of experimentally synthesized isorecticular metal-organic framework-10 and its analogues: M-IRMOF-10 (M = Zn, Cd, Be, Mg, Ca, Sr and Ba). *RSC Adv.* **2012**, *2* (4), 1618-1631. DOI: 10.1039/c1ra00187f
119. Farha, O. K.; Mulfort, K. L.; Thorsness, A. M.; Hupp, J. T., Separating solids: purification of metal-organic framework materials. *J. Am. Chem. Soc.* **2008**, *130* (27), 8598-9. DOI: 10.1021/ja803097e
120. Lee, J. S.; Kapustin, E. A.; Pei, X.; Llopis, S.; Yaghi, O. M.; Toste, F. D., Architectural Stabilization of a Gold(III) Catalyst in Metal-Organic Frameworks. *Chem* **2020**, *6* (1), 142-152. DOI: 10.1016/j.chempr.2019.10.022
121. Deria, P.; Mondloch, J. E.; Karagiari, O.; Bury, W.; Hupp, J. T.; Farha, O. K., Beyond post-synthesis modification: evolution of metal-organic frameworks via building block replacement. *Chem. Soc. Rev.* **2014**, *43* (16), 5896-912. DOI: 10.1039/c4cs00067f
122. Karagiari, O.; Bury, W.; Mondloch, J. E.; Hupp, J. T.; Farha, O. K., Solvent-assisted linker exchange: an alternative to the de novo synthesis of unattainable metal-organic frameworks. *Angew Chem Int Ed Engl* **2014**, *53* (18), 4530-40. DOI: 10.1002/anie.201306923

123. Brozek, C. K.; Bellarosa, L.; Soejima, T.; Clark, T. V.; Lopez, N.; Dinca, M., Solvent-dependent cation exchange in metal-organic frameworks. *Chemistry* **2014**, *20* (23), 6871-4. DOI: 10.1002/chem.201402682
124. Yin, Z.; Zhou, Y.-L.; Zeng, M.-H.; Kurmoo, M., The concept of mixed organic ligands in metal-organic frameworks: design, tuning and functions. *Dalton Trans.* **2015**, *44* (12), 5258–5275. DOI: 10.1039/c4dt04030a
125. Kabsch, W., XDS. *Acta Crystallogr D Biol Crystallogr* **2010**, *66* (Pt 2), 125-32. DOI: 10.1107/S0907444909047337
126. Sheldrick, G., Crystal structure refinement with SHELXL. *Acta Crystallogr. C* **2015**, *71* (1), 3-8. DOI: doi:10.1107/S2053229614024218
127. Sonneveld, E. J.; Visser, J. W., Automatic collection of powder data from photographs. *J. Appl. Crystallogr.* **1975**, *8* (1), 1-7. DOI: doi:10.1107/S0021889875009417
128. McPhillips, T. M.; McPhillips, S. E.; Chiu, H.-J.; Cohen, A. E.; Deacon, A. M.; Ellis, P. J.; Garman, E.; Gonzalez, A.; Sauter, N. K.; Phizackerley, R. P.; et al., Blu-Ice and the Distributed Control System: software for data acquisition and instrument control at macromolecular crystallography beamlines. *J. Synchrotron Rad.* **2002**, *9* (6), 401–406. DOI: 10.1107/S0909049502015170
129. Sheldrick, G., SHELXT - Integrated space-group and crystal-structure determination. *Acta Crystallographica Section A* **2015**, *71* (1), 3-8. DOI: doi:10.1107/S2053273314026370
130. Dolomanov, O. V.; Bourhis, L. J.; Gildea, R. J.; Howard, J. A. K.; Puschmann, H., OLEX2: a complete structure solution, refinement and analysis program. *J. Appl. Crystallogr.* **2009**, *42* (2), 339-341. DOI: doi:10.1107/S0021889808042726
131. Hausdorf, S.; Baitalow, F.; Bohle, T.; Rafaja, D.; Mertens, F. O., Main-group and transition-element IRMOF homologues. *J. Am. Chem. Soc.* **2010**, *132* (32), 10978-81. DOI: 10.1021/ja1028777
132. Tonigold, M.; Lu, Y.; Bredenkötter, B.; Rieger, B.; Bahn Müller, S.; Hitzbleck, J.; Langstein, G.; Volkmer, D., Heterogeneous Catalytic Oxidation by MFU-1: A Cobalt(II)-Containing Metal-Organic Framework. *Angew. Chem. Int. Ed.* **2009**, *48* (41), 7546–7550. DOI: 10.1002/anie.200901241
133. Shen, K.; Zhang, M.; Zheng, H., Critical factors influencing the structures and properties of metal-organic frameworks. *CrystEngComm* **2015**, *17* (5), 981-991. DOI: 10.1039/c4ce02150a
134. Guillermin, V.; MasPOCH, D., Geometry Mismatch and Reticular Chemistry: Strategies To Assemble Metal-Organic Frameworks with Non-default Topologies. *J. Am. Chem. Soc.* **2019**, *141* (42), 16517-16538. DOI: 10.1021/jacs.9b08754
135. Wu, S.-H.; Wang, S.; Fang, W.-L.; Guo, X.-F.; Wang, H., An exceptionally stable Zr-based fluorescent metal-organic framework for highly selective detection of pH. *Analytical Methods* **2019**, *11* (1), 36-43. DOI: 10.1039/c8ay01998c
136. Van Zeeland, R.; Li, X.; Huang, W.; Stanley, L. M., MOF-253-Pd(OAc)₂: a recyclable MOF for transition-metal catalysis in water. *RSC Advances* **2016**, *6* (61), 56330-56334. DOI: 10.1039/c6ra12746k
137. Zhang, H.; Wu, S.; Tian, C.; Lin, Z.; Li, Z.; Lin, P.; Du, S., Two enantiomorphic 3D Zn(ii)-carboxylate MOFs with double helical structures serving as a chiral source induced by hydrogen bonding. *CrystEngComm* **2012**, *14* (12). DOI: 10.1039/c2ce25325a

138. Khansari, A.; Bryant, M. R.; Jenkinson, D. R.; Jameson, G. B.; Qazvini, O. T.; Liu, L.; Burrows, A. D.; Telfer, S. G.; Richardson, C., Interpenetration isomers in isorecticular amine-tagged zinc MOFs. *CrystEngComm* **2019**, 21 (48), 7498-7506. DOI: 10.1039/c9ce01669d
139. Deshpande, R. K.; Minnaar, J. L.; Telfer, S. G., Thermolabile groups in metal-organic frameworks: suppression of network interpenetration, post-synthetic cavity expansion, and protection of reactive functional groups. *Angew. Chem. Int. Ed.* **2010**, 49 (27), 4598-602. DOI: 10.1002/anie.200905960
140. Han, S. S.; Deng, W. Q.; Goddard, W. A., 3rd, Improved designs of metal-organic frameworks for hydrogen storage. *Angew Chem Int Ed Engl* **2007**, 46 (33), 6289-92. DOI: 10.1002/anie.200700303
141. Li, N.; Feng, R.; Zhu, J.; Chang, Z.; Bu, X.-H., Conformation versatility of ligands in coordination polymers: From structural diversity to properties and applications. *Coord. Chem. Rev.* **2018**, 375, 558-586. DOI: 10.1016/j.ccr.2018.05.016
142. Burrows, A. D.; Frost, C. G.; Mahon, M. F.; Richardson, C., Post-synthetic modification of tagged metal-organic frameworks. *Angew Chem Int Ed Engl* **2008**, 47 (44), 8482-6. DOI: 10.1002/anie.200802908
143. Brozek, C. K.; Michaelis, V. K.; Ong, T. C.; Bellarosa, L.; Lopez, N.; Griffin, R. G.; Dinca, M., Dynamic DMF Binding in MOF-5 Enables the Formation of Metastable Cobalt-Substituted MOF-5 Analogues. *ACS Central Science* **2015**, 1 (5), 252-60. DOI: 10.1021/acscentsci.5b00247
144. Hammond, C., *The Basics of Crystallography and Diffraction*. 2015. '10.1093/acprof:oso/9780198738671.001.0001: ' 10.1093/acprof:oso/9780198738671.001.0001
145. Giacovazzo, C., *Fundamentals of crystallography*. 3rd ed.; Oxford University Press: Oxford ; New York, 2011; p xxi, 842 p. '
146. Steensen, N.; Stella, I. d., *Nicolai Stenonis De solido intra solidum naturaliter contento dissertationis prodromus*. ex Typographia sub signo Stellae: 1669. '
147. Young, T., I. The Bakerian Lecture. Experiments and calculations relative to physical optics. *Philosophical Transactions of the Royal Society of London* **1804**, 94, 1-16. DOI: doi:10.1098/rstl.1804.0001
148. Röntgen, W. C., Ueber eine neue Art von Strahlen. *Annalen der Physik* **1898**, 300 (1), 12-17. DOI: 10.1002/andp.18983000103
149. Forman, P., The discovery of the diffraction of X-rays by crystals; a critique of the myths. *Archive for History of Exact Sciences* **1969**, 6 (1), 38-71. DOI: 10.1007/BF00327262
150. Bragg, W. H.; Bragg, W. L.; Duveen, A.; Chemistry, C., *X-rays and crystal structure*. G. Bell and Sons, Ltd.: London, 1915. '
151. Rhodes, G., 5 - From Diffraction Data to Electron Density. In *Crystallography Made Crystal Clear*, Rhodes, G., Ed. Academic Press: Boston, 1993; pp 83-99. <https://doi.org/10.1016/B978-0-12-587075-7.50009-6>: '<https://doi.org/10.1016/B978-0-12-587075-7.50009-6>
152. Rhodes, G., 6 - Obtaining Phases. In *Crystallography Made Crystal Clear*, Rhodes, G., Ed. Academic Press: Boston, 1993; pp 101-129. '<https://doi.org/10.1016/B978-0-12-587075-7.50010-2>: '<https://doi.org/10.1016/B978-0-12-587075-7.50010-2>

153. Pecharsky, V. K.; Zavalij, P. Y., *Fundamentals of powder diffraction and structural characterization of materials*. 2nd ed.; Springer: New York, 2009; p xxiii, 741 p. '
154. *Rietveld Refinement in the Characterization of Crystalline Materials*. 2019. '10.3390/books978-3-03897-528-1: ' 10.3390/books978-3-03897-528-1
155. Gonzalez, A., Optimizing data collection for structure determination. *Acta Crystallogr D Biol Crystallogr* **2003**, 59 (Pt 11), 1935-42. DOI: 10.1107/s0907444903017700
156. Gonzalez, A., Faster data-collection strategies for structure determination using anomalous dispersion. *Acta Crystallogr D Biol Crystallogr* **2003**, 59 (Pt 2), 315-22. DOI: 10.1107/s0907444902022138
157. Read, R. J., As MAD as can be. *Structure* **1996**, 4 (1), 11-14. DOI: 10.1016/s0969-2126(96)00004-4
158. Smith, J. L.; Hendrickson, W. A.; Terwilliger, T. C.; Berendzen, J., MAD and MIR. *Crystallography of biological macromolecules* **2006**, 299-309. DOI:
159. Ogata, C. M., MAD phasing grows up. *Nat Struct Biol* **1998**, 5 Suppl, 638-40. DOI: 10.1038/1330
160. Brozek, C. K.; Cozzolino, A. F.; Teat, S. J.; Chen, Y.-S.; Dincă, M., Quantification of Site-Specific Cation Exchange in Metal–Organic Frameworks Using Multi-Wavelength Anomalous X-ray Dispersion. *Chem. Mater.* **2013**, 25 (15), 2998–3002. DOI: 10.1021/cm400858d
161. Freedman, D. E.; Han, T. H.; Prodi, A.; Müller, P.; Huang, Q.-Z.; Chen, Y.-S.; Webb, S. M.; Lee, Y. S.; McQueen, T. M.; Nocera, D. G., Site Specific X-ray Anomalous Dispersion of the Geometrically Frustrated Kagome Magnet, Herbertsmithite, $\text{ZnCu}_3(\text{OH})_6\text{Cl}_2$. *J. Am. Chem. Soc.* **2010**, 132 (45), 16185–16190. DOI: 10.1021/ja1070398
162. Helliwell, M.; Helliwell, J. R.; Kaucic, V.; Zabukovec Logar, N.; Teat, S. J.; Warren, J. E.; Dodson, E. J., Determination of zinc incorporation in the Zn-substituted gallophosphate ZnULM-5 by multiple wavelength anomalous dispersion techniques. *Acta Crystallogr. B* **2010**, 66 (3), 345-357. DOI: 10.1107/S0108768110011237
163. Singh, M. N.; Sinha, A. K.; Ghosh, H., Determination of transition metal ion distribution in cubic spinel $\text{Co}_{1.5}\text{Fe}_{1.5}\text{O}_4$ using anomalous x-ray diffraction. *AIP Advances* **2015**, 5 (8). DOI: 10.1063/1.4928425
164. Ramaseshan, S.; Venkatesan, K.; Mani, N. V., The use of anomalous scattering for the determination of crystal structures-KMnO₄. *Proceedings of the Indian Academy of Sciences - Section A* **1957**, 46 (2), 95-111. DOI: 10.1007/bf03045960
165. Quintana, J. P.; Butler, B. D.; Haeffner, D. R., Experimentally determined anomalous scattering factors for Mn, Fe, Ni, Cu, Zn and Hg using the Kramers-Kronig relation. *J. Appl. Crystallogr.* **1991**, 24 (2), 184-187. DOI: 10.1107/s0021889890012249
166. Grosse-Kunstleve, R. W.; Sauter, N. K.; Moriarty, N. W.; Adams, P. D., The Computational Crystallography Toolbox: crystallographic algorithms in a reusable software framework. *J. Appl. Crystallogr.* **2002**, 35 (1), 126-136. DOI: doi:10.1107/S0021889801017824
167. Tu, B.; Diestel, L.; Shi, Z.-L.; Bandara, W. R. L. N.; Chen, Y.; Lin, W.; Zhang, Y.-B.; Telfer, S. G.; Li, Q., Harnessing Bottom-Up Self-Assembly To Position Five Distinct Components in an Ordered Porous Framework. *Angew. Chem. Int. Ed.* **2019**, 58 (16), 5348-5353. DOI: 10.1002/anie.201900863

168. Wang, X.; Wisser, F. M.; Canivet, J.; Fontecave, M.; Mellot-Draznieks, C., Immobilization of a Full Photosystem in the Large-Pore MIL-101 Metal-Organic Framework for CO₂ reduction. *ChemSusChem* **2018**, *11* (18), 3315-3322. DOI: 10.1002/cssc.201801066
169. Gonzalez, M. I.; Bloch, E. D.; Mason, J. A.; Teat, S. J.; Long, J. R., Single-crystal-to-single-crystal metalation of a metal-organic framework: a route toward structurally well-defined catalysts. *Inorg. Chem.* **2015**, *54* (6), 2995-3005. DOI: 10.1021/acs.inorgchem.5b00096
170. Cowieson, N. P.; Aragao, D.; Clift, M.; Ericsson, D. J.; Gee, C.; Harrop, S. J.; Mudie, N.; Panjikar, S.; Price, J. R.; Riboldi-Tunnicliffe, A.; Williamson, R.; Caradoc-Davies, T., MX1: a bending-magnet crystallography beamline serving both chemical and macromolecular crystallography communities at the Australian Synchrotron. *J Synchrotron Radiat* **2015**, *22* (1), 187-90. DOI: 10.1107/S1600577514021717
171. Liang, W.; Babarao, R.; Church, T. L.; D'Alessandro, D. M., Tuning the cavities of zirconium-based MIL-140 frameworks to modulate CO₂ adsorption. *Chem. Commun.* **2015**, *51* (56), 11286-9. DOI: 10.1039/c5cc02539g
172. Seoane, B.; Castellanos, S.; Dikhtiarenko, A.; Kapteijn, F.; Gascon, J., Multi-scale crystal engineering of metal organic frameworks. *Coord. Chem. Rev.* **2016**, *307*, 147-187. DOI: 10.1016/j.ccr.2015.06.008
173. Feng, L.; Yuan, S.; Zhang, L. L.; Tan, K.; Li, J. L.; Kirchon, A.; Liu, L. M.; Zhang, P.; Han, Y.; Chabal, Y. J.; Zhou, H. C., Creating Hierarchical Pores by Controlled Linker Thermolysis in Multivariate Metal-Organic Frameworks. *J. Am. Chem. Soc.* **2018**, *140* (6), 2363-2372. DOI: 10.1021/jacs.7b12916
174. Dhakshinamoorthy, A.; Li, Z.; Garcia, H., Catalysis and photocatalysis by metal organic frameworks. *Chem. Soc. Rev.* **2018**, *47* (22), 8134-8172. DOI: 10.1039/c8cs00256h
175. Jiang, D.; Xu, P.; Wang, H.; Zeng, G.; Huang, D.; Chen, M.; Lai, C.; Zhang, C.; Wan, J.; Xue, W., Strategies to improve metal organic frameworks photocatalyst's performance for degradation of organic pollutants. *Coord. Chem. Rev.* **2018**, *376*, 449-466. DOI: 10.1016/j.ccr.2018.08.005
176. Pagis, C.; Ferbinteanu, M.; Rothenberg, G.; Tanase, S., Lanthanide-Based Metal Organic Frameworks: Synthetic Strategies and Catalytic Applications. *ACS Catalysis* **2016**, *6* (9), 6063-6072. DOI: 10.1021/acscatal.6b01935
177. Zhang, Y.; Yang, X.; Zhou, H.-C., Synthesis of MOFs for heterogeneous catalysis via linker design. *Polyhedron* **2018**, *154*, 189-201. DOI: 10.1016/j.poly.2018.07.021
178. Tonigold, M.; Lu, Y.; Mavrandonakis, A.; Puls, A.; Staudt, R.; Mollmer, J.; Sauer, J.; Volkmer, D., Pyrazolate-based cobalt(II)-containing metal-organic frameworks in heterogeneous catalytic oxidation reactions: elucidating the role of entatic states for biomimetic oxidation processes. *Chemistry* **2011**, *17* (31), 8671-95. DOI: 10.1002/chem.201003173
179. Huang, N.; Yuan, S.; Drake, H.; Yang, X.; Pang, J.; Qin, J.; Li, J.; Zhang, Y.; Wang, Q.; Jiang, D.; Zhou, H. C., Systematic Engineering of Single Substitution in Zirconium Metal-Organic Frameworks toward High-Performance Catalysis. *J. Am. Chem. Soc.* **2017**, *139* (51), 18590-18597. DOI: 10.1021/jacs.7b09553
180. Johnson, J. A.; Petersen, B. M.; Kormos, A.; Echeverria, E.; Chen, Y. S.; Zhang, J., A New Approach to Non-Coordinating Anions: Lewis Acid Enhancement of Porphyrin Metal Centers in a

Zwitterionic Metal-Organic Framework. *J. Am. Chem. Soc.* **2016**, *138* (32), 10293-8. DOI: 10.1021/jacs.6b05626

181. Choi, K. M.; Kim, D.; Rungtaweeworant, B.; Trickett, C. A.; Barmanbek, J. T.; Alshammari, A. S.; Yang, P.; Yaghi, O. M., Plasmon-Enhanced Photocatalytic CO(2) Conversion within Metal-Organic Frameworks under Visible Light. *J. Am. Chem. Soc.* **2017**, *139* (1), 356-362. DOI: 10.1021/jacs.6b11027

182. van der Helm, M. P.; Klemm, B.; Eelkema, R., Organocatalysis in aqueous media. *Nature Reviews Chemistry* **2019**, *3* (8), 491-508. DOI: 10.1038/s41570-019-0116-0

183. Oliveira, V.; Cardoso, M.; Forezi, L., Organocatalysis: A Brief Overview on Its Evolution and Applications. *Catalysts* **2018**, *8* (12). DOI: 10.3390/catal8120605

184. Aleman, J.; Cabrera, S., Applications of asymmetric organocatalysis in medicinal chemistry. *Chem. Soc. Rev.* **2013**, *42* (2), 774-93. DOI: 10.1039/c2cs35380f

185. List, B., Introduction: Organocatalysis. *Chem. Rev. (Washington, DC, U. S.)* **2007**, *107* (12), 5413-5415. DOI: 10.1021/cr078412e

186. Hajos-Parrish-Eder-Sauer-Wiechert Reaction. In *Comprehensive Organic Name Reactions and Reagents*, pp 1305-1309. '10.1002/9780470638859.conrr290: ' 10.1002/9780470638859.conrr290

187. Zhou, T.-Y.; Auer, B.; Lee, S. J.; Telfer, S. G., Catalysts Confined in Programmed Framework Pores Enable New Transformations and Tune Reaction Efficiency and Selectivity. *J. Am. Chem. Soc.* **2019**, *141* (4), 1577-1582. DOI: 10.1021/jacs.8b11221

188. Lillerud, K. P.; Olsbye, U.; Tilset, M., Designing Heterogeneous Catalysts by Incorporating Enzyme-Like Functionalities into MOFs. *Top. Catal.* **2010**, *53* (13-14), 859-868. DOI: 10.1007/s11244-010-9518-4

189. Gu, Z.-Y.; Park, J.; Raiff, A.; Wei, Z.; Zhou, H.-C., Metal-Organic Frameworks as Biomimetic Catalysts. *ChemCatChem* **2014**, *6* (1), 67-75. DOI: 10.1002/cctc.201300493

190. Majewski, M. B.; Howarth, A. J.; Li, P.; Wasielewski, M. R.; Hupp, J. T.; Farha, O. K., Enzyme encapsulation in metal-organic frameworks for applications in catalysis. *CrystEngComm* **2017**, *19* (29), 4082-4091. DOI: 10.1039/c7ce00022g

191. Zheng, H. Q.; Liu, C. Y.; Zeng, X. Y.; Chen, J.; Lu, J.; Lin, R. G.; Cao, R.; Lin, Z. J.; Su, J. W., MOF-808: A Metal-Organic Framework with Intrinsic Peroxidase-Like Catalytic Activity at Neutral pH for Colorimetric Biosensing. *Inorg. Chem.* **2018**, *57* (15), 9096-9104. DOI: 10.1021/acs.inorgchem.8b01097

192. He, J.; Zhang, Y.; Zhang, X.; Huang, Y., Highly efficient Fenton and enzyme-mimetic activities of NH₂-MIL-88B(Fe) metal organic framework for methylene blue degradation. *Sci Rep* **2018**, *8* (1), 5159. DOI: 10.1038/s41598-018-23557-2

193. Gao, J., Catalysis by enzyme conformational change as illustrated by orotidine 5'-monophosphate decarboxylase. *Curr. Opin. Struct. Biol.* **2003**, *13* (2), 184-192. DOI: 10.1016/s0959-440x(03)00041-1

194. Katsoulidis, A. P.; Antypov, D.; Whitehead, G. F. S.; Carrington, E. J.; Adams, D. J.; Berry, N. G.; Darling, G. R.; Dyer, M. S.; Rosseinsky, M. J., Chemical control of structure and guest uptake by a

conformationally mobile porous material. *Nature* **2019**, 565 (7738), 213-217. DOI: 10.1038/s41586-018-0820-9

195. Carrington, E. J.; Petuya, R.; Hylton, R. K.; Yan, Y.; Antypov, D.; Darling, G. R.; Dyer, M. S.; Berry, N. G.; Katsoulidis, A. P.; Rosseinsky, M. J., The Anisotropic Responses of a Flexible Metal-Organic Framework Constructed from Asymmetric Flexible Linkers and Heptanuclear Zinc Carboxylate Secondary Building Units. *Cryst. Growth Des.* **2019**, 19 (10), 5604-5618. DOI: 10.1021/acs.cgd.9b00558

196. Bell, F., The Stereochemistry of 2 : 2'-Bridged Derivatives of Diphenyl. *Journal of the Chemical Society (Resumed)* **1952**, (Notes), 1527-1528. DOI: 10.1039/jr9520001524

197. Sasai, H.; Suzuki, T.; Arai, S.; Arai, T.; Shibasaki, M., Basic character of rare earth metal alkoxides. Utilization in catalytic carbon-carbon bond-forming reactions and catalytic asymmetric nitroaldol reactions. *J. Am. Chem. Soc.* **1992**, 114 (11), 4418-4420. DOI: 10.1021/ja00037a068

198. Marqués-López, E.; Merino, P.; Tejero, T.; Herrera, R. P., Catalytic Enantioselective Aza-Henry Reactions. *Eur. J. Org. Chem.* **2009**, 2009 (15), 2401-2420. DOI: 10.1002/ejoc.200801097

199. Luzzio, F. A., The Henry reaction: recent examples. *Tetrahedron* **2001**, 57 (6), 915-945. DOI: 10.1016/s0040-4020(00)00965-0

200. Alvarez-Casao, Y.; Marques-Lopez, E.; Herrera, R. P., Organocatalytic Enantioselective Henry Reactions. *Symmetry* **2011**, 3 (2), 220-245. DOI: 10.3390/sym3020220

201. Chen, X.; Wang, J.; Zhu, Y.; Shang, D.; Gao, B.; Liu, X.; Feng, X.; Su, Z.; Hu, C., A secondary amine amide organocatalyst for the asymmetric nitroaldol reaction of alpha-ketophosphonates. *Chemistry* **2008**, 14 (35), 10896-9. DOI: 10.1002/chem.200801958

202. Luo, M.; Yan, B., Enantioselective henry reactions catalyzed by chiral N-metal complexes containing R(+)/S(-)- α -ethylphenyl amines. *Tetrahedron Lett.* **2010**, 51 (42), 5577-5580. DOI: 10.1016/j.tetlet.2010.08.055

203. Hu, Y. H.; Wang, J. C.; Yang, S.; Li, Y. A.; Dong, Y. B., CuI@UiO-67-IM: A MOF-Based Bifunctional Composite Triphase-Transfer Catalyst for Sequential One-Pot Azide-Alkyne Cycloaddition in Water. *Inorg. Chem.* **2017**, 56 (14), 8341-8347. DOI: 10.1021/acs.inorgchem.7b01025

204. Steed, J. W.; Atwood, J. L., *Supramolecular chemistry*. 2nd ed.; Wiley: Chichester, UK, 2009; p xxvi, 970 p., 8 p. of plates. '

205. Moghadam, P. Z.; Li, A.; Wiggin, S. B.; Tao, A.; Maloney, A. G. P.; Wood, P. A.; Ward, S. C.; Fairen-Jimenez, D., Development of a Cambridge Structural Database Subset: A Collection of Metal-Organic Frameworks for Past, Present, and Future. *Chem. Mater.* **2017**, 29 (7), 2618-2625. DOI: 10.1021/acs.chemmater.7b00441

206. Li, Z.; Zhang, Z.; Ye, Y.; Cai, K.; Du, F.; Zeng, H.; Tao, J.; Lin, Q.; Zheng, Y.; Xiang, S., Rationally tuning host-guest interactions to free hydroxide ions within intertrimerically cuprophilic metal-organic frameworks for high OH⁻ conductivity. *Journal of Materials Chemistry A* **2017**, 5 (17), 7816-7824. DOI: 10.1039/c6ta11242k

207. Galli, S.; Maspero, A.; Giacobbe, C.; Palmisano, G.; Nardo, L.; Comotti, A.; Bassanetti, I.; Sozzani, P.; Masciocchi, N., When long bis(pyrazolates) meet late transition metals: structure, stability

and adsorption of metal–organic frameworks featuring large parallel channels. *Journal of Materials Chemistry A* **2014**, 2 (31). DOI: 10.1039/c4ta01798f

208. Padial, N. M.; Quartapelle Procopio, E.; Montoro, C.; Lopez, E.; Oltra, J. E.; Colombo, V.; Maspero, A.; Masciocchi, N.; Galli, S.; Senkovska, I.; Kaskel, S.; Barea, E.; Navarro, J. A., Highly hydrophobic isorecticular porous metal-organic frameworks for the capture of harmful volatile organic compounds. *Angew Chem Int Ed Engl* **2013**, 52 (32), 8290-4. DOI: 10.1002/anie.201303484

209. Tăbăcaru, A.; Pettinari, C.; Timokhin, I.; Marchetti, F.; Carrasco-Marín, F.; Maldonado-Hódar, F. J.; Galli, S.; Masciocchi, N., Enlarging an Isorecticular Family: 3,3',5,5'-Tetramethyl-4,4'-bipyrazolato-Based Porous Coordination Polymers. *Cryst. Growth Des.* **2013**, 13 (7), 3087-3097. DOI: 10.1021/cg400495w

210. Tabacaru, A.; Pettinari, C.; Masciocchi, N.; Galli, S.; Marchetti, F.; Angiellari, M., Pro-porous coordination polymers of the 1,4-bis((3,5-dimethyl-1H-pyrazol-4-yl)-methyl)benzene ligand with late transition metals. *Inorg. Chem.* **2011**, 50 (22), 11506-13. DOI: 10.1021/ic2013705

211. Tăbăcaru, A.; Galli, S.; Pettinari, C.; Masciocchi, N.; McDonald, T. M.; Long, J. R., Nickel(ii) and copper(i,ii)-based metal-organic frameworks incorporating an extended tris-pyrazolate linker. *CrystEngComm* **2015**, 17 (27), 4992-5001. DOI: 10.1039/c5ce00561b

212. Masciocchi, N.; Galli, S.; Colombo, V.; Maspero, A.; Palmisano, G.; Seyyedi, B.; Lamberti, C.; Bordiga, S., Cubic octanuclear Ni(II) clusters in highly porous polypyrazolyl-based materials. *J. Am. Chem. Soc.* **2010**, 132 (23), 7902-4. DOI: 10.1021/ja102862j

213. Timokhin, I.; Pettinari, C.; Marchetti, F.; Pettinari, R.; Condello, F.; Galli, S.; Alegria, E. C. B. A.; Martins, L. M. D. R. S.; Pombeiro, A. J. L., Novel Coordination Polymers with (Pyrazolato)-Based Tectons: Catalytic Activity in the Peroxidative Oxidation of Alcohols and Cyclohexane. *Cryst. Growth Des.* **2015**, 15 (5), 2303-2317. DOI: 10.1021/acs.cgd.5b00083

214. Mino, L.; Colombo, V.; Vitillo, J. G.; Lamberti, C.; Bordiga, S.; Gallo, E.; Glatzel, P.; Maspero, A.; Galli, S., Spectroscopic and adsorptive studies of a thermally robust pyrazolato-based PCP. *Dalton Trans.* **2012**, 41 (14), 4012-9. DOI: 10.1039/c2dt12121b

215. Lehn, J. M., Toward complex matter: supramolecular chemistry and self-organization. *Proc. Natl. Acad. Sci. U. S. A.* **2002**, 99 (8), 4763-8. DOI: 10.1073/pnas.072065599

216. Beran, G. J. O.; Heit, Y. N.; Hartman, J. D., Chapter 10 - Noncovalent Interactions in Molecular Crystals. In *Non-Covalent Interactions in Quantum Chemistry and Physics*, Otero de la Roza, A.; DiLabio, G. A., Eds. Elsevier: 2017; pp 303-331. '<https://doi.org/10.1016/B978-0-12-809835-6.00012-8>: '<https://doi.org/10.1016/B978-0-12-809835-6.00012-8>

217. Martinez, C. R.; Iverson, B. L., Rethinking the term “pi-stacking”. *Chemical Science* **2012**, 3 (7), 2191. DOI: 10.1039/c2sc20045g

218. Fischer, F. R.; Schweizer, W. B.; Diederich, F., Substituent effects on the aromatic edge-to-face interaction. *Chem. Commun.* **2008**, (34), 4031-3. DOI: 10.1039/b809058k

219. Hunter, C. A.; Lawson, K. R.; Perkins, J.; Urch, C. J., Aromatic interactions. *Journal of the Chemical Society, Perkin Transactions 2* **2001**, (5), 651-669. DOI: 10.1039/b008495f

220. Meyer, E. A.; Castellano, R. K.; Diederich, F., Interactions with aromatic rings in chemical and biological recognition. *Angew Chem Int Ed Engl* **2003**, 42 (11), 1210-50. DOI: 10.1002/anie.200390319

221. Schneider, H. J., Binding mechanisms in supramolecular complexes. *Angew Chem Int Ed Engl* **2009**, 48 (22), 3924-77. DOI: 10.1002/anie.200802947
222. Gokel, G. W.; Leevy, W. M.; Weber, M. E., Crown ethers: sensors for ions and molecular scaffolds for materials and biological models. *Chem Rev* **2004**, 104 (5), 2723-50. DOI: 10.1021/cr020080k
223. Stoddart, J. F., Mechanically Interlocked Molecules (MIMs)-Molecular Shuttles, Switches, and Machines (Nobel Lecture). *Angew Chem Int Ed Engl* **2017**, 56 (37), 11094-11125. DOI: 10.1002/anie.201703216
224. Lindoy, L. F.; Park, K. M.; Lee, S. S., Metals, macrocycles and molecular assemblies - macrocyclic complexes in metallo-supramolecular chemistry. *Chem. Soc. Rev.* **2013**, 42 (4), 1713-27. DOI: 10.1039/c2cs35218d
225. Nguyen, S. T.; Gin, D. L.; Hupp, J. T.; Zhang, X., Supramolecular chemistry: functional structures on the mesoscale. *Proc. Natl. Acad. Sci. U. S. A.* **2001**, 98 (21), 11849-50. DOI: 10.1073/pnas.201373898
226. Atwood, J. L.; Steed, J. W., *Encyclopedia of Supramolecular Chemistry*. 2004. '10.1081/e-esmc: ' 10.1081/e-esmc
227. Dance, I.; Scudder, M., Molecules embracing in crystals. *CrystEngComm* **2009**, 11 (11). DOI: 10.1039/b904479e
228. Dance, I.; Scudder, M., The sextuple phenyl embrace, a ubiquitous concerted supramolecular motif. *J. Chem. Soc., Chem. Commun.* **1995**, (10). DOI: 10.1039/c39950001039
229. Dance, I.; Scudder, M., Crystal supramolecularity: sixfold phenyl embraces between PPh₃ ligands, forming extended nets in one-, two-, and three-dimensions. *Journal of the Chemical Society, Dalton Transactions* **2000**, (10), 1587-1594. DOI: 10.1039/A909330C
230. Dance, I.; Scudder, M., Supramolecular Motifs: Concerted Multiple Phenyl Embraces between Ph₄ P(+) Cations Are Attractive and Ubiquitous. *Chemistry* **1996**, 2 (5), 481-486. DOI: 10.1002/chem.19960020505
231. Ohrstrom, L., Framework Chemistry Transforming our Perception of the Solid State. *ACS Cent Sci* **2017**, 3 (6), 528-530. DOI: 10.1021/acscentsci.7b00230
232. Day, G. M.; Cooper, A. I., Energy-Structure-Function Maps: Cartography for Materials Discovery. *Adv Mater* **2018**, 30 (37), e1704944. DOI: 10.1002/adma.201704944
233. Weber, E., Molecular recognition: designed crystalline inclusion complexes of carboxylic hosts. *Journal of Molecular Graphics* **1989**, 7 (1), 12-27. DOI: 10.1016/0263-7855(89)80053-0
234. Weber, E.; Csoeregh, I.; Ahrendt, J.; Finge, S.; Czugler, M., Design of roof-shaped clathrate hosts. Inclusion properties and x-ray crystal structures of a free host and of inclusion compounds with 1-butenol and DMF. *J. Org. Chem.* **1988**, 53 (25), 5831-5839. DOI: 10.1021/jo00260a007
235. Yang, G. S.; Lang, Z. L.; Zang, H. Y.; Lan, Y. Q.; He, W. W.; Zhao, X. L.; Yan, L. K.; Wang, X. L.; Su, Z. M., Control of interpenetration in S-containing metal-organic frameworks for selective separation of transition metal ions. *Chem Commun (Camb)* **2013**, 49 (11), 1088-90. DOI: 10.1039/c2cc36894c

236. Liou, S.-Y.; Ke, C.-S.; Chen, J.-H.; Luo, Y.-W.; Kuo, S.-Y.; Chen, Y.-H.; Fang, C.-C.; Wu, C.-Y.; Chiang, C.-M.; Chan, Y.-H., Tuning the Emission of Semiconducting Polymer Dots from Green to Near-Infrared by Alternating Donor Monomers and Their Applications for in Vivo Biological Imaging. *ACS Macro Letters* **2015**, 5 (1), 154-157. DOI: 10.1021/acsmacrolett.5b00842
237. Tian, Z.; Yang, X.; Liu, B.; Zhong, D.; Zhou, G., Photophysical properties and optical power limiting ability of Pt(II) polyyne bearing fluorene-type ligands with ethynyl units at different positions. *J. Organomet. Chem.* **2019**, 895, 28-36. DOI: 10.1016/j.jorganchem.2019.05.022
238. van der Veen, M. A.; Verbiest, T.; De Vos, D. E., Probing microporous materials with second-harmonic generation. *Microporous Mesoporous Mater.* **2013**, 166, 102-108. DOI: 10.1016/j.micromeso.2012.04.051
239. Farah, K.; Muller-Plathe, F.; Bohm, M. C., Classical reactive molecular dynamics implementations: state of the art. *ChemPhysChem* **2012**, 13 (5), 1127-51. DOI: 10.1002/cphc.201100681
240. Amirjalayer, S.; Tafipolsky, M.; Schmid, R., Molecular dynamics simulation of benzene diffusion in MOF-5: importance of lattice dynamics. *Angew Chem Int Ed Engl* **2007**, 46 (3), 463-6. DOI: 10.1002/anie.200601746
241. Greathouse, J. A.; Allendorf, M. D., The interaction of water with MOF-5 simulated by molecular dynamics. *J. Am. Chem. Soc.* **2006**, 128 (33), 10678-9. DOI: 10.1021/ja063506b
242. Yang, H.; Bradley, S. J.; Chan, A.; Waterhouse, G. I.; Nann, T.; Kruger, P. E.; Telfer, S. G., Catalytically Active Bimetallic Nanoparticles Supported on Porous Carbon Capsules Derived From Metal-Organic Framework Composites. *J. Am. Chem. Soc.* **2016**, 138 (36), 11872-81. DOI: 10.1021/jacs.6b06736
243. Yang, H.; Kruger, P. E.; Telfer, S. G., Metal-organic framework nanocrystals as sacrificial templates for hollow and exceptionally porous titania and composite materials. *Inorg. Chem.* **2015**, 54 (19), 9483-90. DOI: 10.1021/acs.inorgchem.5b01352